FACULTY OF SCIENCES

PLASMA-ENHANCED ATOMIC LAYER DEPOSITION OF TRANSITION METAL PHOSPHATES

Thesis submitted for the degree of
Doctor in Sciences: Physics

THOMAS DOBBELAERE
September 2017

Promotor:	Prof. Dr. Christophe Detavernier
Co-Promotor:	Prof. Dr. Philippe Vereecken
Members of the Jury:	Prof. Dr. Natalie Jachowicz (UGent, chair)
	Dr. Jolien Dendooven (UGent)
	Prof. Dr. Katrien Strubbe (UGent)
	Prof. Dr. Adriana Creatore (TU Eindhoven)
	Prof. Dr. Christophe Lethien (IEMN)

This research was supported by the Research Foundation-Flanders (FWO-Vlaanderen).

GHENT UNIVERSITY

Ghent University
Faculty of Sciences
Department of Solid State Sciences
Krijgslaan 281/S1, 9000 Gent, Belgium

PREFACE

This PhD thesis presents a study on the plasma-enhanced atomic layer deposition of transition metal phosphates and explores their application as lithium-ion battery electrode materials. The research was started in August 2013, and results up to June 2017 are included. The bulk of the experimental work took place at the Department of Solid State Sciences of Ghent University. The provision of 3D substrates and the analysis of selected samples by ERD were courtesies of imec, Leuven.

The thesis is paper-based and contains five original research articles, each of which has been published in a peer-reviewed journal, reformatted, and included as a stand-alone chapter. These papers are preceded by an introductory chapter, providing research context to the reader, and an experimental chapter, explaining the multitude of experimental techniques that were used. The final chapter presents a critical discussion of the results along with general conclusions.

I hope that I have succeeded in presenting my findings in a clear way, and that this thesis may pave the way for future researchers to continue working in this fascinating field.

Thomas Dobbelaere
Gent, September 2017

TABLE OF CONTENTS

NEDERLANDSTALIGE SAMENVATTING

INLEIDING

Dit doctoraatsproefschrift omvat een studie van de plasmaversterkte atoomlaagdepositie van transitiemetaalfosfaten en verkent de toepassing van deze materialen als lithium-ionbatterijelektrodes.

Atoomlaagdepositie (ALD) is een dunne-filmdepositietechniek die gebaseerd is op chemische oppervlaktereacties. De techniek kan beschouwd worden als een variant van chemische dampdepositie (CVD); net zoals bij CVD geschiedt de depositie van de dunne film door het binnenbrengen van chemische precursordampen in een vacuümkamer. In tegenstelling tot bij CVD gebeurt de reactie echter niet continu. In een ALD-proces wordt een eerste precursor binnengelaten en veroorzaakt deze een eerste halfreactie aan het substraatoppervlak; van zodra alle oppervlaktegroepen met de precursor gereageerd hebben, is deze reactie afgelopen. Vervolgens wordt de overtollige precursor weggepompt, waarna een tweede precursor binnengelaten wordt. De tweede precursor beschikt nu over geschikte oppervlaktegroepen om de tweede halfreactie van het ALD-proces te laten doorgaan. Eens alle groepen op het oppervlak gereageerd hebben met de tweede precursor, is deze reactie eveneens afgelopen, en wordt de tweede precursor weggepompt.

Na de opeenvolging van deze twee halfreacties, ook bekend als één ALD-cyclus, is er een zeer dunne laag (in de grootteorde van één atoomlaag) van het gewenste materiaal afgezet, die bovendien bedekt is met oppervlaktegroepen die opnieuw kunnen reageren met de eerste precursor. Het herhalen van deze cycli resulteert in het "atoomlaag per atoomlaag" opbouwen van de gewenste dunne film. De laagdikte afgezet in één cyclus staat bekend als de groei per cyclus (GPC).

Bij plasmaversterkte atoomlaagdepositie (PEALD) wordt minstens één van de precursorblootstellingen vervangen door een plasma. Het plasma levert extra energie en kan reacties laten doorgaan die normaliter niet (of slechts bij een veel hogere temperatuur) zouden gebeuren. De nieuwe processen die als deel van deze thesis ontwikkeld zijn, maken allemaal gebruik van een plasma van trimethylfosfaat (TMP). Op deze manier konden verscheidene metaalfosfaten gegroeid worden. Vijf van deze processen werden als artikel in een internationaal tijdschrijft gepubliceerd en

als hoofdstuk in dit proefschrift opgenomen; hieronder volgt een korte bespreking van elk proces.

ARTIKEL I: ALUMINIUMFOSFAAT

Het eerste artikel in dit proefschrift beschrijft de groei van aluminiumfosfaat met PEALD op basis van een inductief gekoppeld trimethylfosfaatplasma. Dit plasma heeft merkwaardige eigenschappen en de studie begint dan ook met een karakterisatie hiervan. Via optische emissiespectroscopie en massaspectrometrie wordt aangetoond dat de structuur van de TMP-molecule in het plasma deels afgebroken en geherconfigureerd wordt. Dit gaat o.a. gepaard met de productie van waterstofgas. Bij lage substraattemperaturen polymeriseert het plasma en wordt continu een organofosfaatlaag afgezet. Door dit vervolgens bloot te stellen aan zuurstofplasma wordt koolstof verwijderd ("weggebrand") en ontstaat er (poly-)fosforzuur. Dit kan op zijn beurt reageren met een metaalprecursor zoals TMA, waardoor aluminiumfosfaat gevormd wordt. Door de substraattemperatuur op te drijven boven de 300 °C stopt de spontane polymerisatie maar is er wel nog zelflimiterende groei; hierdoor gaat het proces over van een PECVD-regime naar een PEALD-regime. Het proces heeft een GPC van 0.37 nm/cyclus en produceert amorf aluminiumpyrofosfaat ($Al_4P_6O_{21}$). De amorfe laag kan via thermische annealing omgezet worden naar kristallijn aluminiumorthofosfaat ($AlPO_4$).

ARTIKEL II: ZINKFOSFAAT

Door in het aluminiumfosfaatproces de aluminiumprecursor te vervangen door een zinkprecursor, in dit geval diethylzink, kan zinkfosfaat afgezet worden. Onderzoek van de filmgroei met in-situ ellipsometrie brengt een lineaire en gesatureerde filmgroei aan het licht, in overeenstemming met de verwachte eigenschappen van PEALD. Het optisch model levert een opmerkelijk lage brekingsindex van 1.3. De GPC bedraagt 0.92 nm/cyclus. Het gedeponeerde materiaal is amorf en bovendien zeer hygroscopisch; deze laatste eigenschap kan in verband gebracht worden met het fosforrijke karakter van het materiaal. Via thermische annealing kunnen verschillende kristallijne vormen van zinkpyrofosfaat ($Zn_2P_2O_7$) gevormd worden.

ARTIKEL III: IJZERFOSFAAT

Dit artikel beschrijft de groei, karakterisatie, en elektrochemische lithiatie van ijzerfosfaat geproduceerd via een PEALD-proces bestaande uit her-

haalde en sequentiële blootstellingen aan TMP plasma, zuurstofplasma, en *tert*-butylferroceen. Bij een optimale substraattemperatuur van 300 °C vertoont het proces lineaire groei zonder nucleatie-effecten. Het heeft een uitzonderlijk hoge GPC van 1.1 nm/cyclus. Het gedeponeerde materiaal is amorf, heeft een dichtheid van 3.1 g/cm^3, en een empirische stoichiometrie van $FeP_{1.5}O_{4.7}$ met zeer weinig onzuiverheden (0.9% waterstof en geen detecteerbaar koolstof). Thermische annealing in lucht resulteert in de vorming van trigonaal $FePO_4$, terwijl dezelfde anneal in een heliumatmosfeer elementair fosfor oplevert. De conformaliteit van het proces is niet perfect, maar voldoende om micropilaren volledig te bedekken. Het gedeponeerde materiaal kan elektrochemisch gelithieerd worden; na een "activatie" bestaande uit de volledige reductie van Fe^{3+} naar Fe^0 en de vorming van een SEI, in gang gezet door een potentiaal beneden de 0.5 V vs. Li^+/Li aan te leggen, en een oxidatie van Fe^0 terug naar Fe^{3+}, kan de film als kathodemateriaal gebruikt worden in een gebied rond 3 V vs. Li^+/Li. Hierbij kunnen lithiumionen reversibel in en uit het materiaal gaan, gepaard met de overgang van ijzer tussen Fe^{3+} (gedelithieerd) en Fe^{2+} (gelithieerd). Een capaciteit van 0.7 μAh/cm^2 wordt behouden gedurende 200 op- en ontlaadcycli. Door dezelfde film op een substraat met micropilaren te deponeren kan de capaciteit aanzienlijk verhoogd worden en behoudt de elektrode dezelfde goede kinetiek als op een vlak substraat.

ARTIKEL IV: TITANIUMFOSFAAT

Via een PEALD-proces bestaande uit blootstellingen aan TMP plasma, zuurstofplasma, en titaniumisopropoxide kunnen dunne filmen van titaniumfosfaat geproduceerd worden. Net zoals bij de voorgaande processen treedt er bij een substraattemperatuur van 300 °C gesatureerde en lineaire groei op met een GPC van 0.66 nm/cyclus. Het gedeponeerde materiaal is amorf en heeft een empirische stoichiometrie van $TiP_{1.7}O_{5.6}$, met 4% waterstof als enige onzuiverheid. Door annealing kan het gekristalliseerd worden tot titanium(IV)pyrofosfaat (TiP_2O_7). De conformaliteit van de coating werd gekarakteriseerd door depositie op micropilaren; hieruit blijkt dat de hoeveelheden fosfor en zuurstof enigszins afnemen naarmate er dieper in de pilaren gegaan wordt, maar dat de hoeveelheid titanium wel constant blijft. Het titaniumfosfaat kan elektrochemisch gelithieerd en gedelithieerd worden bij een potentiaal rond 2.7 V vs. Li^+/Li; deze activiteit wordt toegewezen aan de reductie en oxidatie van titanium tussen Ti^{4+} (gedelithieerd) en Ti^{3+} (gelithieerd). Een capaciteit van 1.0 μAh/cm^2 wordt behouden gedurende 100 op- en ontlaadcycli. Dit materiaal werd eveneens op micropilaren gedeponeerd met een aanzienlijke capaciteitsverhoging tot gevolg.

ARTIKEL V: VANADIUMFOSFAAT

In de zoektocht naar een PEALD-proces voor vanadiumfosfaat werden twee verschillende vanadiumprecursors getest, namelijk VTIP en TEMAV. Bij de benodigde substraattemperatuur van 300 °C (deze temperatuur is nodig om plasmapolymerisatie van TMP, dus een CVD-component, tegen te gaan) vertonen beide precursors thermische decompositie. Merkwaardig genoeg wordt deze decompositie in het geval van TEMAV onderdrukt door de aanwezigheid van fosfaatgroepen op het substraatoppervlak; dit effect treedt niet op bij VTIP. Op die manier werd een PEALD-proces voor vanadiumfosfaat ontwikkeld, bestaande uit blootstellingen aan TMP plasma, zuurstofplasma, en TEMAV. Het proces vertoont saturatiegedrag en kent een lineaire groei met een GPC van 0.8 nm/cyclus. Het gedeponeerde materiaal heeft een empirische stoichiometrie van $VP_{1.1}O_{4.3}$. Het kan elektrochemisch gelithieerd en gedelithieerd worden in een potentiaalgebied tussen 1.4 V en 3.6 V vs. Li^+/Li, met een volumetrische capaciteit van 630 mAh/cm^3 die gedurende 100 op- en ontlaadcycli behouden blijft. In een breder potentiaalgebied, tussen 0.5 V en 4.3 V, is er een aanzienlijk grotere volumetrische capaciteit van 1.9 Ah/cm^3 beschikbaar; deze begint echter na 40 op- en ontlaadcycli reeds te degraderen. In beide gevallen vertoont het elektrodemateriaal een hoge coulometrische efficiëntie en een uitstekende kinetiek, waarbij aan een rate van 100C nog 60% van de 1C-capaciteit behouden blijft.

CO/NI FOSFAAT EN CO/NI/FE FOSFIDE

Naar analogie met de voorgaande fosfaatprocessen werden processen voor kobalt- en nikkelfosfaat ontwikkeld op basis van hun respectievelijke metalloceenprecursors. Hoewel de groei van kobaltfosfaat op basis van kobaltoceen merkwaardige niet-lineariteiten vertoont, is er toch saturatie, en kan er een gemiddelde GPC van 0.8 nm/cyclus bepaald worden. Het gedeponeerde materiaal is amorf en heeft een empirische stoichiometrie van $CoP_{2.3}O_{6.7}$. In tegenstelling tot alle voorgaande fosfaatfilms heeft het kobaltfostaat een aanzienlijke oppervlakteruwheid. Via thermische annealing kan kristallijn $Co_2P_2O_7$ gevormd worden.

Nikkelfosfaat kon gedeponeerd worden met nikkeloceen; hierbij werd eveneens saturatiegedrag geobserveerd. Een amorfe laag met een empirische stoichiometrie van $NiP_{1.4}O_{5.3}$ werd afgezet. Inspectie onder de microscoop bracht echter aan het licht dat deze bedekt was met microscopisch kleine schilfers. Deze bleken afkomstig van de (vaste) nikkeloceenprecursor als decompositieproduct. In een poging om dit probleem op te lossen werden de alternatieve precursoren dimethylnikkeloceen en

diethylnikkeloceen uitgeprobeerd, maar deze bleken onvoldoende stabiel om praktisch bruikbaar te zijn.

Via thermische annealing in een waterstofhoudende atmosfeer bleek het mogelijk om kobalt-, nikkel-, en ijzerfosfaat om te zetten in resp. kobaltfosfide (Co_2P), nikkelfosfide ($Ni_{12}P_5$), en ijzerfosfide (Fe_2P). Deze materialen zijn potentieel interessant voor toepassingen in de elektrokatalyse.

LIST OF FIGURES

LIST OF TABLES

LIST OF ABBREVIATIONS

AFM	Atomic Force Microscopy
ALD	Atomic Layer Deposition
ALE	Atomic Layer Epitaxy
CE	Counter Electrode
CV	Cyclic voltammetry
CVD	Chemical Vapor Deposition
DC	Direct Current
DEPA	Diethyl Phosphoramidate
DEZn	Diethylzinc
DMC	Dimethyl Carbonate
EC	Ethylene Carbonate
EDX	Energy-Dispersive X-ray Spectroscopy
EIS	Electrochemical Impedance Spectroscopy
ERD	Elastic Recoil Detection
ETD	Everhart-Thornley Detector
FTIR	Fourier Transform Infrared Spectroscopy
GPC	Growth Per Cycle
HER	Hydrogen Evolution Reaction
ICP	Inductively Coupled Plasma
MS	Mass Spectrometry
MSE	Mean Square Error
OCP	Open-Circuit Potential
OER	Oxygen Evolution Reaction
OES	Optical Emission Spectroscopy
PC	Propylene Carbonate

PE	Plasma-Enhanced
PID	Proportional-Integral-Derivative
PTFE	Polytetrafluoroethylene
PVD	Physical Vapor Deposition
RBS	Rutherford Backscattering Spectrometry
RE	Reference Electrode
RF	Radio Frequency
SE	Sense Electrode
SEI	Solid-Electrolyte Interphase
SEM	Scanning Electron Microscope
TBF	*tert*-Butylferrocene
TDMAP	Tris-dimethylaminophosphorus
TEMAV	Tetrakisethylmethylamido Vanadium
TMA	Trimethylaluminium
TEP	Triethyl Phosphate
TMP	Trimethyl Phosphate
TTIP	Titanium Tetraisopropoxide
UHV	Ultra-High Vacuum
VTIP	Vanadium Triisopropoxide
WE	Working Electrode
XPS	X-Ray Photoelectron Spectroscopy
XRD	X-Ray Diffraction
XRR	X-Ray Reflectivity/Reflectometry

1

INTRODUCTION

1.1 RESEARCH CONTEXT

The research performed in this PhD thesis can be situated within two distinct fields of current scientific interest: on the one hand, plasma-enhanced atomic layer deposition (PEALD), and on the other hand, lithium-ion battery electrode materials. The idea is to not only develop new materials by the PEALD method, but also to explore the use of these materials as battery electrodes. This introductory chapter aims to to familiarize the reader with these fields in order to provide a broader context to the research results in the following chapters.

1.2 ATOMIC LAYER DEPOSITION

Atomic layer deposition (ALD), also known as atomic layer epitaxy (ALE)[1] is a thin-film deposition method where the growth of the desired material is based on chemical reactions taking place on the substrate surface, starting from chemical precursors in the vapor phase.[2, 3] It can be regarded as a variant of chemical vapor deposition (CVD). Unlike CVD, where the chemical reactions which synthesize the desired thin-film material take place continuously, ALD operates discontinuously using alternating pulses of precursors which are separated by pumping or purging steps. Each precursor exposure invokes a certain half-reaction which is self-terminating. The growth progresses by alternating these exposures and thus combining the half-reactions into a complete reaction, which produces a (sub)monolayer of the desired material. This is referred to as one ALD cycle. The thickness of the (sub)monolayer is known as the growth per cycle (GPC). Although it may vary over about two orders of magnitude depending on the particular process, typical values for the GPC are in the order of 0.1 nm, which is similar to the length scale of interatomic distances; hence the *"atomic layer"* aspect of the deposition technique. For

1 The technique has an interesting naming history: it was first pioneered as "molecular layering" by Soviet scientists in the sixties, then unknown to the rest of the world. In the late seventies, it was independently discovered by Finnish researchers who gave it the name of ALE. It later appeared that the same technique also worked in case of non-epitaxial (even amorphous) films, so it was renamed to the more general term ALD.[1]

a particular process, the GPC is usually accurately known and constant. This allows for the controlled deposition of a precise film thickness by simply repeating these cycles, offering "digital" thickness control by varying the number of cycles.

1.2.1 *An example ALD process*

The typical reaction chemistry of an ALD process is best explained by means of a well-understood example, namely the thermal ALD of aluminium oxide from trimethylaluminium ($Al(CH_3)_3$, TMA) and water.[4] This process is based on the following reaction sequence:

1. TMA vapor is brought into the deposition chamber, and reacts with the hydroxyl ($-OH$) groups which are assumed to be present on the substrate surface. The TMA molecule chemisorbs onto the surface, releasing CH_4 (methane gas) as a reaction product:

   $$-OH\,(s) + Al(CH_3)_3\,(g) \longrightarrow -O-Al(CH_3)_2\,(s) + CH_4\,(g)$$

   where the (g) and (s) suffixes denote resp. gas and surface species.

2. Once all $-OH$ sites have reacted with TMA, no further reaction will take place; the first half-reaction has self-terminated. The excess TMA as well as the CH_4 exhaust product is removed by either evacuating the deposition chamber or purging it with an inert gas flow.

3. Water vapor is brought into the deposition chamber, and reacts with the methyl ($-CH_3$) group terminations that originated from the TMA adsorbed onto the surface. This results in the chemisorption of water, creating $-OH$ terminations and again releasing CH_4 as a reaction product:

   $$-Al(CH_3)_2\,(s) + 2\,H_2O\,(g) \longrightarrow -Al(OH)_2\,(s) + 2\,CH_4\,(g)$$

4. Once all $-CH_3$ sites have reacted with H_2O, no further reaction takes place and the second half-reaction has terminated. The excess H_2O is removed from the chamber. The substrate is now covered with a monolayer of aluminium oxide, terminated by $-OH$ groups. The cycle can now be repeated, given that the requirement of step 1 (a hydroxyl-covered surface) is satisfied.

The process is graphically illustrated in figure 1.1. It should be noted that this picture is heavily simplified and merely serves to sketch the concept; it ignores important details, e.g. misrepresenting the stoichiometry of the resulting Al_2O_3 film and ignoring incomplete reactions due to steric hindrance.

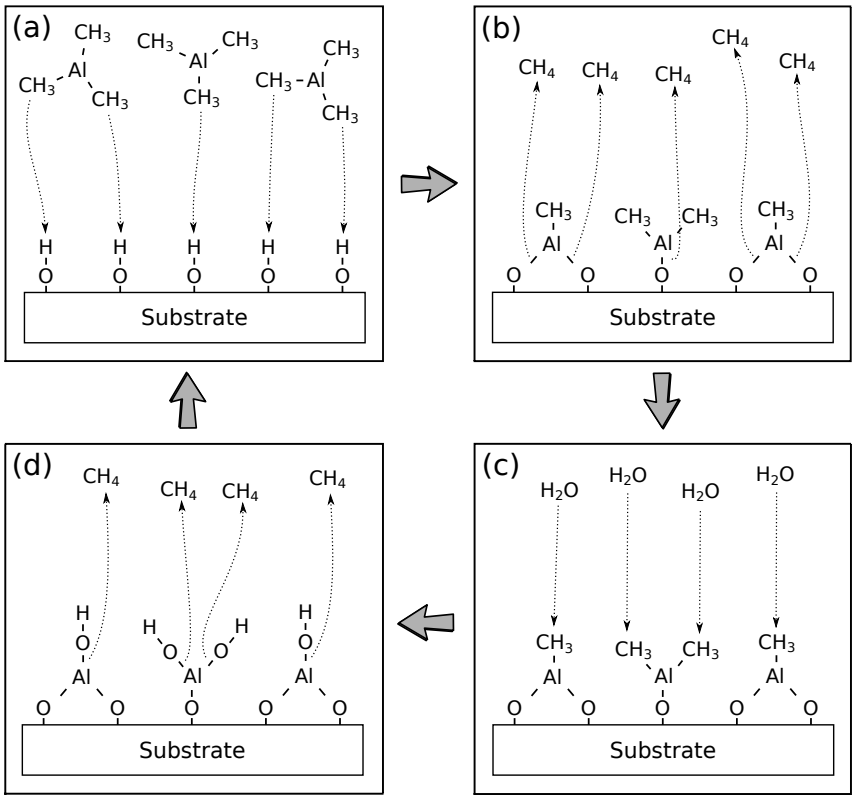

Figure 1.1: Schematic illustration of thermal ALD of aluminium oxide based on TMA and water as vapor-phase precursors, showing the substeps within one cycle: (a) TMA exposure; (b) purge; (c) H_2O exposure; (d) purge.

1.2.2 *Growth characteristics*

LINEARITY The constancy of the GPC implies that the deposited film thickness is proportional to the number of cycles, with the GPC as the proportionality constant:

$$[\text{Film thickness}] = [\text{GPC}] \times [\text{Number of cycles}]$$

In other words, there is linear growth, as illustrated in figure 1.2a. It should be noted that in some cases, nucleation effects can occur which result in a different GPC in the initial growth stage compared to the "steady-state" growth; this depends both on the nature of the substrate and on the deposited material. More details about this can be found in literature.[5]

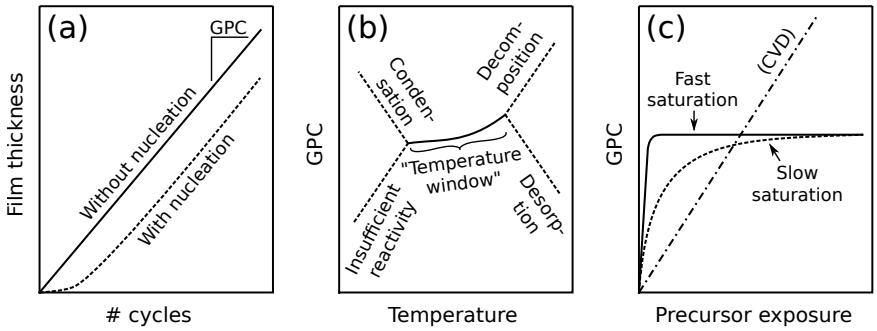

Figure 1.2: Simplified graphs showing typical ALD growth characteristics: (a) growth linearity; (b) temperature dependency; (c) GPC saturation.

TEMPERATURE DEPENDENCY Given that ALD growth is governed by chemical reactions and that temperature is generally an important factor determining the rate of chemical reactions, it can be expected that the substrate temperature is an important variable in an ALD process. Although the details depend on the particular process, some typically expected temperature effects on the GPC are sketched in figure 1.2b.

On the low-temperature side, the chemical reactions might not have enough thermal activation energy to proceed, resulting in a decreased GPC due to insufficient reactivity. On the other hand, low temperatures might cause the precursor to physically condense on the substrate surface, leading to an increased GPC due to CVD side reactions.

On the high-temperature side, some precursors may thermally decompose. In that case, the substrate temperature is so high that there is enough thermal energy to break up the precursor molecule without requiring any other reactants. This results in the continuous deposition of a thin film by a single precursor, i.e. CVD growth,[2] and is paired with an increasing GPC due to the extra CVD contribution. On the other hand, in some other cases, functional groups may desorb from the substrate surface at elevated temperatures, resulting in a decreased GPC.

In between those temperature extremes, there is a "temperature window" within which the ALD reactions proceed optimally. In some cases, the GPC is constant within the temperature window, but this is not generally true, as is deliberately depicted in fig. 1.2b.[4] The real criterion for

2 Which is a perfectly good deposition method by itself, although it does not share some of the desired properties of ALD (e.g. film purity and conformality). Hence, if one is interested in doing ALD, CVD is regarded as an undesirable side reaction.

ALD-type growth is in fact self-saturation, as will be discussed in the next paragraph.

SATURATION In order to satisfy ALD growth, by definition, the half-reactions invoked by the precursor exposures need to be self-limiting. This implies that the GPC "saturates" with increasing precursor exposure.[3] As shown in the typical saturation curves of fig. 1.2c, the GPC initially rises with precursor exposure, until the half-reaction is completed; once completed, further exposure does not result in further reactions, resulting in a flattening of the GPC. While the point of saturation may be reached very quickly for certain (very reactive) precursors, it may take more time for others, resulting in slow saturation. In case of CVD-type growth, the deposition proceeds continuously and does not saturate, resulting in a linearly increasing GPC with precursor exposure. In case of ALD-type growth with a CVD contribution (e.g. thermal decomposition or another side reaction), the flat part of the saturation curve will no longer be flat but have an upwards slope instead.

1.2.3 *Advantages and limitations*

Thin-film deposition by ALD has some unique and desirable properties, including:

- The possibility of depositing a wide range of materials, including oxides, nitrides, sulfides, fluorides, phosphates, various semiconductors, and metals
- Precise control over the film thickness down to the atomic level
- Excellent film thickness uniformity over large substrates
- Excellent conformality on complex (three-dimensional) structures
- Inherent insensitivity to process variations
- Low deposition temperatures, enabling deposition on temperature-sensitive substrates such as polymers

The fourth item is perhaps the most unique quality of ALD compared to competing thin-film deposition methods. The near-ideal conformality of the coating is a result of the self-limiting nature of the half-reactions, so that even hard-to-reach surfaces (e.g. walls and trenches), which locally receive lower precursor fluxes, will eventually be coated with the same

3 The precursor exposure can be defined as the integral of the precursor pressure over time; with constant vapor pressure, the exposure is proportional to the time duration.

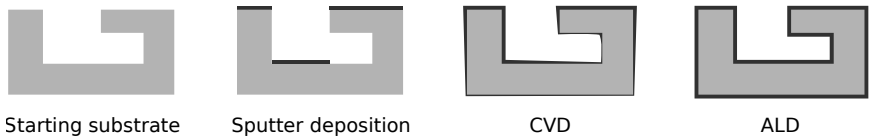

Figure 1.3: Diagrammatic illustration of coating conformality, showing an irregularly shaped substrate coated by different deposition methods.

layer thickness as the line-of-sight surfaces if a sufficient exposure time is allowed. As illustrated in figure 1.3, this is in contrast to e.g. sputter deposition, where material is deposited strictly line-of-sight, and to CVD, where the deposited film thickness is proportional to the local precursor flux (which tends to be lower in "hard-to-reach" places).

However, these properties come at a (literal) cost: ALD is expensive and slow. Given a typical GPC of 0.1 nm/cycle (e.g. for the TMA-H_2O process), and cycle times between a few seconds and one minute (depending on the deposition hardware), it can take between an hour and a full day to deposit a 100 nm film. Furthermore, the precursors are often expensive chemicals, and scaling up (which is traditionally a way to decrease costs) only increases the costs of the vacuum equipment. For this reason, one often resorts to ALD only when no other deposition method fits the requirements, e.g. for very thin metal oxide films in microelectronics. Otherwise, non-vacuum-based thin-film deposition techniques (e.g. sol-gel deposition, electrodeposition, plating, etc.) are preferable due to the much lower cost and much better scalability.

1.2.4 *Plasma-enhanced ALD*

In plasma-enhanced ALD (PEALD), one or more of the vapor-phase precursor exposures is replaced by a plasma exposure. The energy imparted by the plasma essentially enables chemical reactions which would not take place otherwise, i.e. if only thermal activation energy were available. The plasma can deliver this energy in various forms, including ions, radicals, and ultraviolet light, which may all contribute to the breaking and reconfiguring of chemical bonds.

As an instructive example, we once again consider the growth of aluminium oxide, this time using a PEALD process consisting of alternating TMA and O_2 plasma exposures. Compared to the thermal process discussed earlier, the water vapor pulse has been replaced with O_2 plasma. The function of the water pulse was to react with the $-CH_3$ terminations left behind from the first half-reaction, converting them to $-OH$ and

producing CH_4 as a gaseous byproduct. The oxygen plasma fulfills the same purpose, converting $-CH_3$ to $-OH$ groups, but this time through a combustion-type reaction with CO_2 and H_2O as byproducts:

$$-Al(CH_3)\,(s) + 2\,O_2{}^* \longrightarrow -Al(OH)\,(s) + CO_2\,(g) + H_2O\,(g)$$

where the asterisk (*) denotes plasma activation.

Despite the increased cost and complexity of a PEALD system compared to a thermal one, PEALD may be preferred because it results in lower-temperature processing, better film properties, or faster nucleation. Most importantly, it enables certain processes which would otherwise not be possible at all due to insufficient reactivity of the precursors; plasma activation is sometimes the only way to make certain chemical reactions happen.

The main limitation of PEALD is arguably the limited conformality that can be achieved with it compared to thermal ALD.[6] In the case of thermal ALD, given enough time for the vapor-phase precursors to diffuse into a structure, the self-limited nature of the reactions results in the same film thickness being deposited everywhere, even inside deep trench-like structures. In the case of PEALD, however, the radicals produced by the plasma have only a finite litefime until they spontaneously recombine. This imposes an upper limit on the penetration depth inside a trench structure: while descending into the trench, more and more radicals recombine; at some point, the remaining amount of radicals will be insufficient, resulting in a decreasing film thickness.

For the interested reader, a more extensive discussion of PEALD can be found in literature,[7] and an excellent database of PEALD processes and publications hand-curated by an anonymous author can be found online.[8]

1.2.5 *ALD of phosphates*

Metal oxides are by far the most popular class of materials to be deposited by ALD. In principle, turning an oxide into a phosphate is only a matter of adding phosphorus atoms, so one would expect plenty of literature reports from authors whom have developed processes that come down to this. In practice, however, this is not the case. The difficulty lies in finding a phosphorus precursor which is (1) chemically reactive towards the desired organometallic precursor (e.g. TMA) and (2) which can be vaporized.

At first sight, a straightforward choice would be phosphoric acid (H_3PO_4): just like water, it has $-OH$ terminations, which are reactive towards

e.g. the $-CH_3$ ligands of TMA. However, unfortunately, it does not satisfy requirement (2). As shown in figure 1.4, upon heating, phosphoric acid drives off water and condenses into various polymerized forms, generally referred to as polyphosphoric acids. In other words, rather than evaporating the acid, the act of heating only tends to concentrate the acid and evaporates water. This makes phosphoric acid unusable as an ALD precursor. One thus has to resort to alternative chemistries.

Interestingly, phosphates were historically amongst the first materials to be synthesized in an ALD-like fashion by Soviet scientists in the late 60's, who knew the technique as "molecular layering" long before it was independently discovered in the West. Using alternating cycles of phosphorus trichloride (PCl_3, fig. 1.5a) and water, the group of Prof. Kol'tsov could make monolayers of phosphorus pentoxide (P_2O_5);[9] combining this with monolayers of titanium oxide made from titanium tetrachloride ($TiCl_4$) and water, they essentially synthesized titanium phosphate.[10] In a later report, they combined the P_2O_5 with chromium oxide monolayers made from chromyl chloride (CrO_2Cl_2) and H_2O to result in chromium phosphate.[11]

Although PCl_3 satisfies requirements (1) and (2), no other authors have described ALD processes using PCl_3 as the phosphorus precursor since then, perhaps because of a reluctancy to work with this corrosive and very toxic chemical.

In the late 90's, two separate reports described the use of P_2O_5 (fig. 1.5b) as a precursor for the growth of aluminium phosphate.[12, 13] Although cheap and less toxic than PCl_3, the trouble with P_2O_5 is that it is technically difficult to use because it needs to be heated to very high temperatures

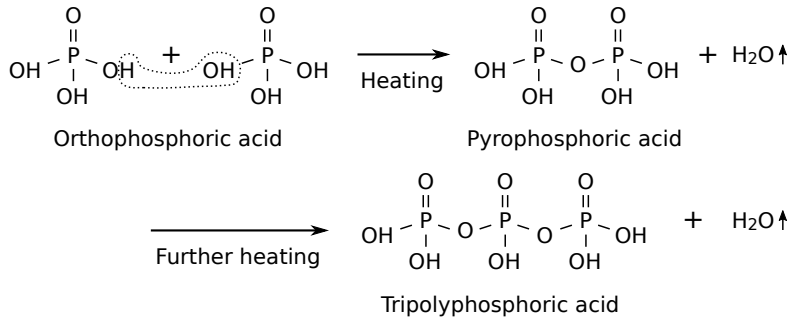

Figure 1.4: Dehydration of phosphoric acid upon heating, illustrating the impossibility of using it as an ALD precursor.

in order to vaporize it. Sublimation temperatures ranging from 170 °C to 330 °C are specified, which is significantly higher than what many ALD reactors (or rather, their evaporators) are able to withstand.

The most popular phosphate precursor in "modern" ALD work is, by far, trimethyl phosphate (TMP, fig. 1.5c). It is technically a great ALD precursor because it is cheap, stable, reasonably non-toxic and most importantly easy to evaporate (source temperatures below 70 °C are usually sufficient). It has been the basis of ALD processes for aluminium phosphate,[14, 15], titanium phosphate,[14, 16] calcium phosphate,[17, 18] lithium phosphate,[19, 20] lanthanum phosphate,[21] iron phosphate,[22, 23], lithium iron phosphate,[24] and europium titanium phosphate.[25] One paper describes the use of a closely related compound, triethyl phosphate (TEP, fig. 1.5d), for the deposition of alumium phosphate.[26] An amine-substituted variety of this precursor, diethyl phosphoramidate (DEPA, fig. 1.5e), has recently been used by two different authors to deposit nitrogen-doped lithium phosphate.[27, 28] The same material has also recently been deposited using tris-dimethylaminophosphorus (TDMAP).[29]

The limitation of TMP as an ALD precursor is that it is difficult to satisfy requirement (1). The stability of the compound, which is convenient when handling it, is inconvenient when trying to produce an ALD reaction. Due to its $-CH_3$ terminations, it will not directly react with most metalorganic precursors. In the aforementioned reports, in order to circumvent this issue, TMP is either directly reacted with chloride-based precursors, or combined with ozone (O_3) as a reactant in order to "burn away" its $-CH_3$ groups.

The work in this PhD thesis presents an alternative method of getting TMP to react, namely by making it into a plasma. The working hypothesis is

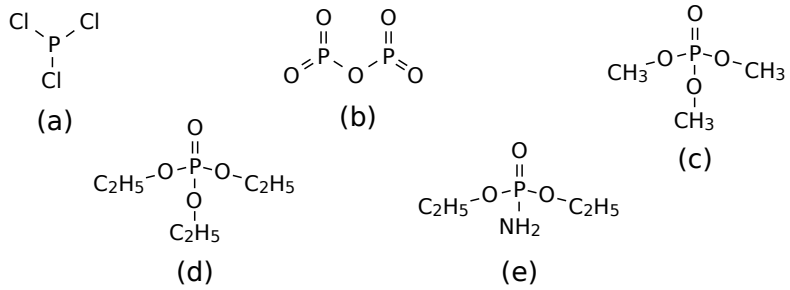

Figure 1.5: Chemical structures of ALD phosphorus precursors: (a) PCl_3; (b) P_2O_5; (c) TMP; (d) TEP; (e) DEPA

Table 1.1: Overview of published literature on the atomic layer deposition of phosphates. Entries that are part of this PhD thesis are highlighted in bold.

Ref.	Year	Metal (source)	Phosphorus source	Temperature (°C)
[10]	1969	Titanium (-Cl_4)	PCl_3	180
[11]	1980	Chromium (CrO_2Cl_2)	PCl_3	180
[12]	1995	Aluminium (-Cl_3)	P_2O_5, TMP	500
[13]	1998	Aluminium (-Cl_3, n-propoxide)	P_2O_5	450 - 500
[17]	2009	Calcium (-$(thd)_2$)	TMP	300
[19]	2012	Lithium (-HMDS)	TMP	225 - 300
[19]	2012	Lithium (-O^{t}Bu)	TMP	275 - 350
[16]	2012	Titanium (-Cl_4)	TMP	150 - 300
[14]	2012	Aluminium (-Cl_3)	TMP	150 - 400
[14]	2012	Titanium (-Cl_4)	TMP	275 - 450
[15]	2013	Aluminium (TMA)	TMP	150
[26]	2013	Aluminium (TMA)	TEP	250
[22]	2013	Iron (-$(thd)_3$)	TMP	200 - 380
[18]	2013	Calcium (-$(thd)_2$)	TMP	300
[21]	2014	Lanthanum (-$(thd)_3$)	TMP	250 - 300
[30]	**2014**	**Aluminium (TMA)**	**TMP plasma**	**320**
[24]	2014	Iron (-$(Cp)_2$) + Lithium (-O^{t}Bu)	TMP	300
[23]	2015	Iron (-$(Cp)_2$)	TMP	200 - 350
[20]	2015	Lithium (-O^{t}Bu)	TMP	250
[27]	2015	Lithium (-HMDS)	DEPA	270 - 310
[31]	**2016**	**Zinc (DEZn)**	**TMP plasma**	**300**
[32]	**2016**	**Iron (TBF)**	**TMP plasma**	**300**
[29]	2016	Lithium (-O^{t}Bu)	TDMAP	400 - 500
[25]	2017	Europium (-$(thd)_3$) + Titanium (-Cl_4)	TMP	300
[33]	**2017**	**Titanium (TTIP)**	**TMP plasma**	**300**
[28]	2017	Lithium (-O^{t}Bu)	DEPA	250 - 300
[34]	**2017**	**Vanadium (TEMAV)**	**TMP plasma**	**300**

that the plasma activation breaks up the molecule and reconfigures the bonds to give it $-OH$ terminations, thereby making it more similar to phosphoric acid and making it easy to react with many organometallic precursors. This topic is elaborately investigated and discussed in Paper I, and forms the basis of the processes developed in Papers II-V.

To place this work within a literature context, table 1.1 provides an overview of publications where ALD processes for phosphates were reported. This table can be regarded as an extended version of table 3.1 from Paper I, which was made in 2014 and so does not contain any work that has been published after that date. The new table makes it immediately obvious that the atomic layer deposition of phosphates is attracting growing research attention, especially for applications in lithium-ion batteries.

1.3 Lithium-ion batteries

Lithium-ion batteries represent the current state of the art of high-energy-density electrochemical energy storage. First commercialized by Sony in the early 90's to power their portable video cameras, they quickly became the preferred battery option for laptops, cell phones, and eventually almost any portable electronic device. Continued development also made them suitable for more "heavy-duty" applications, e.g. power tools and electric vehicles, and their steadily decreasing cost has even driven the technology towards large-scale applications such as off-grid storage.

When compared to other battery technologies, as is done in table 1.2, it becomes apparent that lithium-ion batteries are gifted with the unique combination of being based on a non-aqueous electrolyte (enabling a high cell voltage, and thus a high energy density) and also being rechargeable. Rather than using metallic lithium, which grows dendrites upon recharging that eventually result in catastrophic short-circuits, the lithium-ion cell

Table 1.2: Types of batteries.

	Aqueous electrolyte (low voltage)	Non-aqueous electrolyte (high voltage)
Primary battery (disposable)	Zinc-Carbon dry cell, Alkaline dry cell	Metallic lithium
Secondary battery (rechargeable)	Lead-Acid, Nickel-Cadmium, Nickel-Metal Hydride	Lithium-ion

(just like its name implies) uses only lithium ions, which migrate between the positive electrode (cathode) and the negative electrode (anode) upon charging and discharging.

For a more complete understanding, some notions of electrochemistry and battery terminology are in order. A short overview is given below.

1.3.1 *Battery basics*

A battery can be defined as an electrochemical charge storage device which uses reduction and oxidation reactions to convert stored chemical energy into electrical energy. In case of a primary battery, this process is irreversible (i.e. the battery is "single use"); in case of a secondary (or rechargeable) battery, electrical energy can be converted back into stored chemical energy by reversing the current flow.

1.3.1.1 *Anodes and cathodes*

Batteries consist of one or more electrochemical cells. An electrochemical cell has two electrodes; the one that sustains the oxidation reaction is defined as the anode, while the other (sustaining the reduction reaction) is defined as the cathode. The flow of electrons from the anode to the cathode is directed through an external circuit. This implies that the rate of the reaction is externally controlled, as opposed to many other types of redox reactions (e.g. corrosion) where electrons are directly transferred.

In case of a primary battery, the anode is always the negative terminal, i.e. the one that releases the electrons going into the external circuit. The anode can be be a metal, e.g. zinc in alkaline batteries or lithium in lithium cells. The cathode is the positive terminal, which receives the electrons from the external circuit. The electrodes are internally separated by the electrolyte. It conducts ions, but not electrons (otherwise there would be an internal short-circuit). Liquid electrolytes are often acids, bases or salts dissolved in water or another kind of solvent. Solid electrolytes also exist.

In case of a secondary battery, the anode and cathode are defined in the same way; when discharging, the situation is identical to the primary battery, as sketched in figure 1.6a. Upon charging, however, the current flow is reversed, and so are the electrode reactions. The negative electrode now receives electrons from the external circuit, invoking reduction, so that it is now the cathode; the positive electrode similarly becomes the anode. This is illustrated in figure 1.6b.

Despite this definition, in the context of rechargeable batteries, positive electrode materials are often referred to as "cathode materials" and nega-

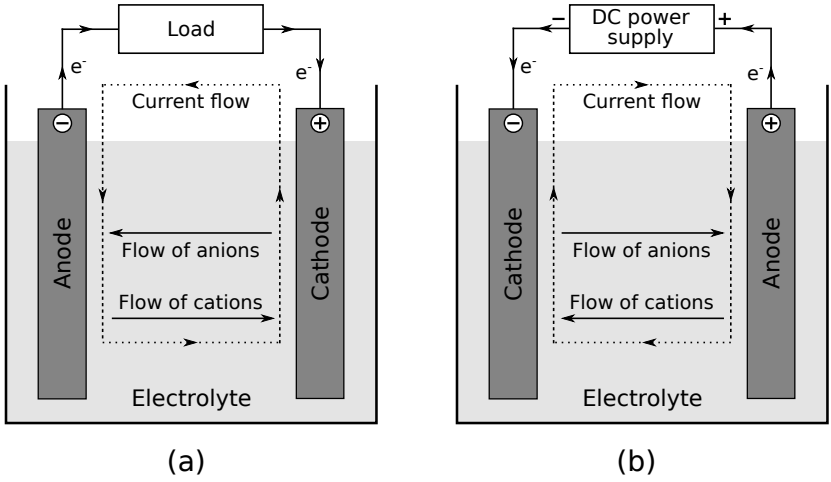

Figure 1.6: Generalized working principle of a secondary battery consisting of a single cell: (a) during discharge; (b) during charge.

tive electrode materials as "anode materials". In other words, the naming convention assumes the discharge phase.

Inside the cell, the current path is completed by ions flowing through the electrolyte. Cations (positive ions) follow the direction of the current and move from the negative to the positive electrode, while anions (negative ions) do the opposite.

1.3.1.2 *Cell chemistries*

Depending on the choice of anode, cathode, and electrolyte, many different types of primary and secondary batteries can be constructed. Table 1.3 provides a brief overview of a few cell chemistries which are in wide use today.

1.3.1.3 *Example: the Daniell cell*

The Daniell cell was invented in the 19th century and can be historically considered as one of the first practical batteries. Although it is no longer used today because it has been superseded by better technologies, it still serves as an instructive example because it is based on simple half-reactions. The cell consists of a metallic zinc anode, submerged in a zinc sulfate electrolyte, and a metallic copper cathode, submerged in a copper sulfate electrolyte. The electrolytes are separated by a porous membrane,

Table 1.3: Overview of popular primary and secondary cell chemistries. Secondary cells are described in their fully charged states.

Type	Name	Anode	Cathode	Electrolyte
Prim.	Zinc-Carbon	Zinc	MnO_2	NH_4Cl, $ZnCl_2$
Prim.	Alkaline	Zinc	MnO_2	KOH
Prim.	Lithium	Lithium	MnO_2 [(a)]	Li salt [(b)]
Sec.	Lead-Acid	Lead	PbO_2	H_2SO_4
Sec.	NiCd	Cadmium	NiOOH	KOH
Sec.	NiMH	Metal hydride	NiOOH	KOH
Sec.	Li-ion	Li_yC_6	$Li_{1-x}CoO_2$ [(a)]	Li salt [(b)]

(a) Many alternative materials are possible.

(b) Dissolved in a non-aqueous solvent.

allowing the transfer of ions (more specifically, SO_4^{2-} anions) without mixing the liquids.

At the anode side, the zinc metal is oxidised to Zn^{2+}, liberating two electrons into the external circuit. This yields the following anodic half-reaction:

$$Zn\,(s) \longrightarrow Zn^{2+}\,(aq) + 2\,e^-$$

At the cathode side, Cu^{2+} (from the copper sulfate solution) is reduced to copper metal, with the aid of two electrons from the external circuit. The cathodic half-reaction is thus:

$$Cu^{2+}\,(aq) + 2\,e^- \longrightarrow Cu\,(s)$$

The total cell reaction is then given by:

$$Zn\,(s) + Cu^{2+}\,(aq) \longrightarrow Zn^{2+}\,(aq) + Cu\,(s)$$

1.3.1.4 *Cell voltage*

The cell voltage (i.e. the potential difference between the electrodes) under standard conditions[4] can be found by taking the difference between the standard reduction potentials of the anode and cathode half-reactions:

$$\Delta U^0_{\text{cell}} = U^0_{\text{cathode}} - U^0_{\text{anode}}$$

4 Standard conditions mean a temperature of 25 °C, reagent concentrations of 1 M, gas pressures of 1 bar and metals in their pure state.

The standard reduction potential of a half-reaction is a measure of the amount of energy per unit charge that is released following the reduction of a chemical species. Tabulated values can be found in literature.[35] For instance, the standard reduction potential of the Cu^{2+}/Cu redox couple is +0.34 V and that of the Zn^{2+}/Zn redox couple is −0.76 V, yielding a standard cell voltage of $\Delta U^0 = 0.34\,\mathrm{V} - (-0.76\,\mathrm{V}) = 1.10\,\mathrm{V}$ for the Daniell cell.

In the context of lithium-ion batteries, the potential is often reported and/or measured relative to the Li^+/Li redox couple.

1.3.1.5 *Capacity*

The amount of charge stored in a battery. Often expressed in units of Ah (amp-hour), defined as the amount of charge transferred by a current of 1 A during one hour:

$$1\,\mathrm{Ah} = 1\,\mathrm{C/s} \times 3600\,\mathrm{s} = 3600\,\mathrm{C}$$

Units of milliamp-hour (mAh) are also commonly used, with 1 mAh being equivalent to 3.6 C.

1.3.1.6 *Specific energy*

The amount of energy (expressed in watt-hours, Wh) stored in a battery is found by multiplying its capacity (in Ah) by its cell voltage (in V). The ratio of this number over the mass of the battery yields the (gravimetric) *specific energy*, expressed in e.g. Wh/kg. The low atomic weight of lithium, together with the high cell voltage, explains why lithium-ion batteries can achieve high specific energies.

1.3.1.7 *C-rate*

The charge or discharge rate is often expressed in terms of C, the current necessary to reach the cell's theoretical capacity in one hour. For instance, for a battery with a capacity of 1000 mAh, a charge rate of 1C means a current of 1000 mA during 1 hour. 2C would be 2000 mA during 1/2 hour, and C/10 would be 100 mA during 10 hours.

1.3.2 *The "original" lithium-ion battery*

Although modern lithium-ion batteries come in many varieties and cell chemistries, they all share the basic working principle of the "original"

lithium-ion battery invented by Akira Yoshino in the 1980's and first commercialized by Sony in 1991. This type of battery is schematically shown in figure 1.7. It consists of a $LiCoO_2$ positive electrode and a (graphitic) carbon negative electrode, separated by a non-aqueous electrolyte containing a lithium salt.

Contrary to primary batteries (and in fact, many secondary ones), lithium-ion cells are first assembled in the discharged state. Upon initial charging, electrons are pulled from the positive electrode into the external circuit. This oxidizes the cobalt atoms in $LiCoO_2$ from Co^{3+} to Co^{4+}, causing lithium ions (Li^+) to be extracted from the positive electrode and thereby releasing them into the electrolyte:

$$LiCoO_2 \longrightarrow Li_{1-x}CoO_2 + x\,Li^+ + x e^-$$

where x is a continuous variable. After migrating through the electrolyte, the extracted Li^+ ions are inserted into the carbon negative electrode, charge-balanced by electrons from the external circuit:

$$C_6 + y\,Li^+ + y\,e^- \longrightarrow Li_yC_6$$

The "continuous" insertion/extraction of Li^+ proceeds through a process called intercalation; both the carbon anode and the $LiCoO_2$ cathode are referred to as intercalation-type materials. These materials accommodate

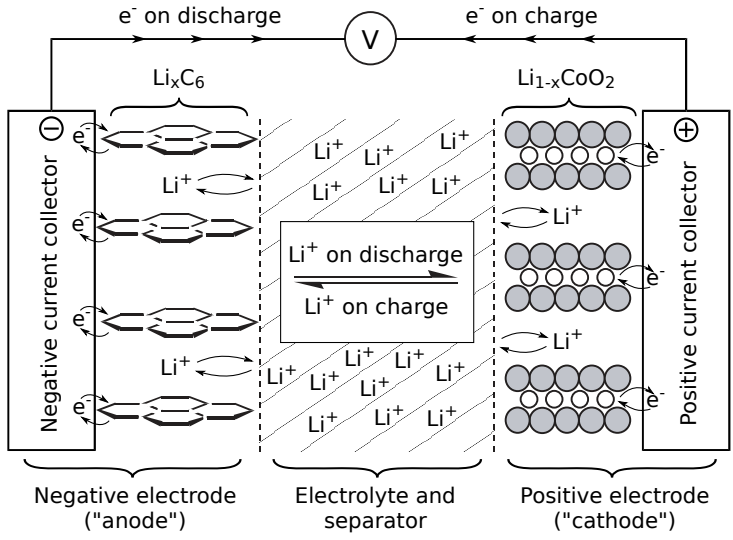

Figure 1.7: Schematic diagram showing the working principle of a lithium-ion cell.

Li^+ in the interstitial spaces in their crystalline lattices, through which the lithium ions can move freely. The $LiCoO_2$ cathode is conventionally delithiated up to $Li_{0.5}CoO_2$ (i.e. $x = 0.5$) to maintain reversibility; although it can in principle be delithiated all the way to CoO_2 ($x = 1$), this process is irreversible.[36] At $x = 0.5$ and $y = 1$, the battery is considered fully charged and has a cell voltage of 4.2 V.[37]

During discharge, the same reactions proceed in the opposite direction. The lithium ions are now extracted (deintercalated) from the carbon negative electrode, releasing electrons; they move through the electrolyte, and are then intercalated back into the $Li_{1-x}CoO_2$ positive electrode.

The overall reaction can be written as follows:

$$2\,Li_{0.5}CoO_2 + LiC_6 \underset{\text{Charge}}{\overset{\text{Discharge}}{\rightleftharpoons}} 2\,LiCoO_2 + C_6$$

The above notation highlights the fact that the lithium ions move back and forth between the positive and the negative electrode upon oxidation and reduction of the electrode materials during charging and discharging. Batteries based on this principle are said to have a "rocking-chair" configuration.

1.3.3 *Electrode materials and the role of phosphates*

Lithium-ion batteries are nowadays manufactured using a wide range of cathode materials, a small overview of which is given in table 1.4. The listed materials are all intercalation-based, but have different crystalline

Table 1.4: List of selected lithium-ion cathode materials together with their abbreviations and main properties. The listed specific capacities represent the experimentally determined values.[38]

Material	Structure	Potential (V vs. Li^+/Li)	Specific capacity (mAh/g)
$LiCoO_2$ (LCO)	Layered	3.8	150
$LiMn_2O_4$ (LMO)	Spinel	4.1	120
$LiFePO_4$ (LFP)	Olivine	3.4	165
$LiNi_{1/3}Mn_{1/3}Co_{1/3}O_2$ (NMC)	Layered	3.7	160
$LiNi_{0.8}Co_{0.15}Al_{0.05}O_2$ (NCA)	Layered	3.7	200

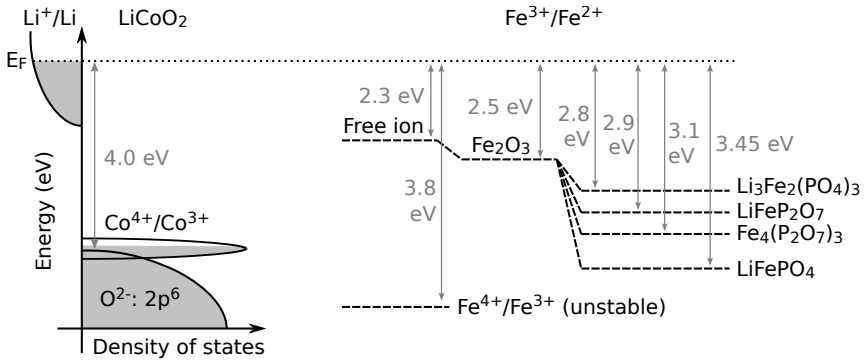

Figure 1.8: Diagram showing the energy levels of Co^{4+}/Co^{3+} in $LiCoO_2$ (left), and of Fe^{3+}/Fe^{2+} as a free ion, in an oxide, and in phosphate hosts (right), illustrating the shift in redox potential due to the inductive effect.

structures. Aside from differences in the average potentials and specific capacities, the materials may also differ in cost, longevity (cycle life), power handling (rate capability), safety, toxicity, and other aspects. The best compromise between these properties is application-specific.

Of particular relevance to the work in this PhD thesis is the only phosphate listed in the table, namely $LiFePO_4$. It was discovered by John Goodenough's group in the late 90's in search of a cathode material that was abundant, low-cost, environmentally benign, and safer than $LiCoO_2$.[39]

The issue with $LiCoO_2$ is that, although it is perfectly safe when charged properly, it does not resist abuse in the form of overcharging. This behavior finds its origin in the position of the energy levels of the Co^{4+}/Co^{3+} redox couple relative to the oxygen $2p^6$ levels, as illustrated in figure 1.8 (left). The Co energy levels overlap with the top of the O 2p band, located 4.0 eV below the Fermi level of Li^+/Li. Upon charging, Li^+ ions are extracted along with electrons from the cobalt levels, which is the intended behavior of the cathode material. However, when overcharged ($x > 0.5$ in $Li_{1-x}CoO_2$), due to the overlap with the 2p levels of oxygen, electrons are not only extracted from the cobalt, but also from the oxygen. This decomposes the cathode material and releases O_2 gas, thereby damaging the cell.

Given the low cost, non-toxicity, and abundancy of iron, initial efforts were focused on replacing $LiCoO_2$ with iron oxides (e.g. $LiFeO_2$ which has the same layered structure as $LiCoO_2$). However, it soon became apparent that these were not suitable as cathode materials. As shown in figure 1.8

(right), the redox energy of the Fe^{3+}/Fe^{2+} couple lies significantly higher than the Co^{4+}/Co^{3+} couple in $LiCoO_2$, resulting in a much lower potential against Li^+/Li. This limits the attainable specific energy. Making use of the Fe^{4+}/Fe^{3+} couple would result in a much higher potential, were it not for the fact that Fe^{4+} is unstable and results in a collapse of the structure.

The solution to this problem is to use a polyanion-based material rather than an oxide. Possible polyanions include e.g. phosphates (PO_4^{3-}), pyrophosphates ($P_2O_7^{4-}$), silicates (SiO_4^{4-}), sulfates (SO_4^{2-}), borates (BO_3^{3-}), etc. The strongly covalent bonding within the polyanion results in a weaker bonding between oxygen and iron, which lowers the Fe^{3+}/Fe^{2+} redox energy and increases the resulting potential against Li^+/Li. This is referred to as the inductive effect.[40] The magnitude of the shift depends not only on the strength of the polyanionic covalent bond, but also on the crystalline structure of the material, as evidenced by the different potentials measured for (lithium) iron phosphates with different structures. Of these phosphates, the olivine-structured $LiFePO_4$ has the largest voltage at 3.45 V vs. Li^+/Li, which is the reason why it is the preferred phosphate for commercial batteries.

1.3.4 *Microstructured thin-film batteries*

Traditionally, lithium-ion battery electrodes incorporate active electrode materials in the form of powder. This powder is mixed with binders and conductive additives into a slurry, which is then applied as a thin layer on a metal foil current collector (typically aluminum foil for the cathode, and copper foil for the anode).[41] Such an electrode is schematically shown in figure 1.9a. The final cell is assembled by placing an electrolyte-soaked separator membrane between the foils and rolling up the resulting sandwich structure inside the cell casing.

Although this is a very cost-effective method to make electrodes on a large scale (bulk powders can be industrially processed in massive quantities), it also has certain drawbacks. In order for the active material to work, it needs to be reached both by Li^+ ions (from the electrolyte) and by electrons (from the current collector). The first criterion is mostly satisfied by making the electrode semi-porous and allowing the liquid electrolyte to penetrate inside the pores. The electronic conduction, however, requires the presence of electronically conductive particles (usually carbon) in order to create electrically conductive paths from the current collector to each active electrode particle. The exact formulation is critical: too little conductive additive will result in a lower electrode capacity because some

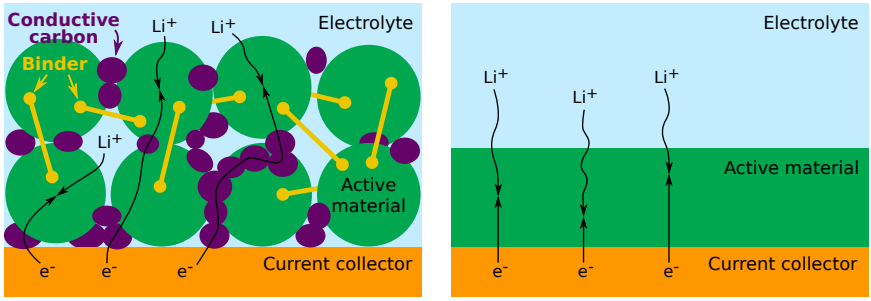

(a) Powder electrode (b) Thin-film electrode

Figure 1.9: Schematic cross sections of (a) a powder-based electrode and (b) a thin-film electrode.

active particles cannot be reached by electrons, while too much will take up valuable space and weight without contributing any capacity.

Powder-based lithium-ion batteries also face kinetic restrictions, limiting the maximum attainable C-rate. This is partly due to the active material itself; some time is required for lithium ions to diffuse from the edge of a particle towards its center, or *vice versa*. Although this could theoretically be improved by decreasing the particle size (i.e. making a finer powder), thus minimizing the diffusion time, this also introduces side effects (e.g. clustering of active material, binder difficulties, and more side reactions due to the increased surface area) which places a lower limit on the practically realizable particle size.

Another limitation stems from the conductive additive which has a non-zero resistance. As the charge/discharge rate increases, so does the current I. Over a fixed resistance R, a voltage $U = IR$ is lost (hence the term IR-drop). A large potential drop can be detrimental to an electrode because of local over- or undercharging. Additionally, it results in heating and a loss of efficiency, both of which are clearly undesirable effects.

Some of these issues can be resolved by using an alternative strategy to produce the electrode. By coating the active material directly onto the current collector substrate using a thin-film deposition method, as shown in figure 1.9b, no additives are needed and the electrode consists purely of active material. The paths for electronic and ionic transport are simple and direct: electrons are transferred where the active material contacts the current collector, and Li^+ ions where it faces the electrolyte. In fact,

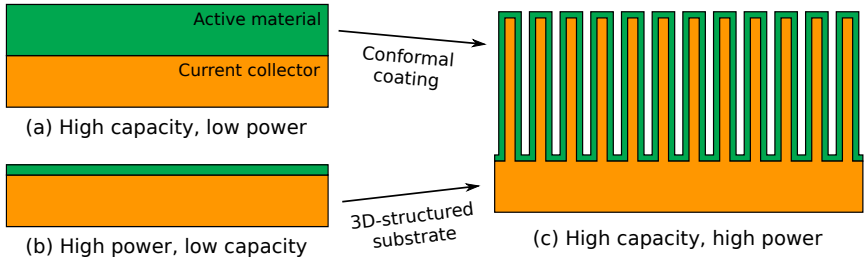

Figure 1.10: Thin-film electrode concepts: (a) thick planar film, yielding a high capacity but slow kinetics; (b) thin planar film, yielding fast kinetics but a low capacity; (c) thin 3D-structured film, yielding a combination of a high capacity and fast kinetics.

the electrolyte can also be a thin film[5]; by stacking another electrode and current collector thin film on top of it, a complete thin-film battery can be fabricated, as has been demonstrated by J. B. Bates et al. in the year 2000.[42]

In a planar thin-film battery, as shown in figure 1.10 (a,b), choosing the thickness of the electrode films requires a careful compromise between capacity and power handling. As the capacity scales with the amount of electrode material and the surface area is limited by the dimensions of the battery, high film thicknesses are necessary in order to have good capacities. However, similar to the particle size considerations in the case of electrode powders, thick films are unfavorable for fast (i.e. high-rate, high-current) charging and discharging due to the long diffusion lengths for Li^+ ions. Reducing the film thickness makes everything faster, but decreases the capacity.

An interesting way to get around this limitation is to abandon the idea of planar films, and switch to a three-dimensionally (3D) structured substrate instead, as shown in figure 1.10c. This drastically increases the surface area compared to a planar film of the same size (i.e. having the same projected area). By conformally depositing an electrode material on this substrate, the amount of material and thus the capacity of the electrode can be made much higher compared to a planar electrode with the same film thickness, without the penalty of slower kinetics. In the same way as the planar thin-film battery, a full battery could be fabricated as a thin-

5 An often-used solid electrolyte in this context is LiPON, an amorphous material consisting of lithium phosphate doped with nitrogen.

film stack on the 3D structure. Several variants of this concept have been proposed in literature.[43–48]

The challenge of the 3D approach is that the electrode material (and, by extension, the rest of the thin-film stack in order to make a complete battery) needs to be deposited conformally. This eliminates physical vapor deposition (PVD) techniques, e.g. evaporation and sputtering, which are usually used for planar thin-film batteries, and leaves e.g. electrodeposition, CVD and ALD as suitable candidates. Coupled with other applications of ALD for lithium-ion batteries (e.g. protective electrode coatings) over the last years, this has led to the development of many new ALD processes for anode materials, cathode materials, and solid-state electrolytes, as summarized in a recent review article.[49] Notable recent advances towards a full ALD-grown battery include the Ru/V_2O_5 nanopore battery by Liu et al.[50] and the "two-thirds" of a silicon micropillar-based battery including TiO_2 electrode and Li_3PO_4 solid electrolyte films by Létiche et al.[51]

1.4 GOALS AND OUTLINE OF THIS THESIS

This thesis explores the development of new plasma-enhanced ALD processes for transition metal phosphates and the evaluation of their potential use as lithium-ion battery electrode materials. The work has led to five original research papers, which are contained in Chapters 3-7; as such, the thesis is paper-based. The following list summarizes the significance of each paper and the advancements made therein:

- Paper I: "Atomic layer deposition of aluminum phosphate based on the plasma polymerization of trimethyl phosphate"[30]

  This is the original paper about the use of TMP plasma as part of an ALD process. It contains a detailed study of the properties of the plasma, and its tendency to polymerize at low temperatures. The nature of the polymerization product and the effect of O_2 plasma on it are studied. Its reactions with TMA vapor are investigated, and a PEALD regime is discovered at sufficiently high temperatures. The produced aluminum phosphate films are characterized and a reaction mechanism is proposed.

- Paper II: "Plasma-enhanced atomic layer deposition of zinc phosphate"[31]

  The findings in Paper I strongly hinted towards a "universal" PEALD phosphate deposition method. By swapping TMA with diethylzinc, zinc phosphate films were produced. Paper II contains

a full characterization of the zinc phosphate process and the properties of the produced films. However, the hygroscopic nature of the films limited their practical application.

- Paper III: "Plasma-enhanced atomic layer deposition of iron phosphate as a positive electrode for 3D lithium-ion microbatteries"[32]

  Iron phosphate was the first material to be developed through a TMP plasma / O_2 plasma process which could accommodate lithium ions and thus could be used as a lithium-ion battery electrode. This paper contains a process characterization, material analysis, and an investigation of the electrochemical lithiation behavior of the deposited iron phosphate. The material is also tested on a 3D (micropillar) substrate with a focus on the attainable conformality and capacity increase.

- Paper IV: "Plasma-enhanced atomic layer deposition of titanium phosphate as an electrode for lithium-ion batteries"[33]

  This paper reports on the deposition process, film properties, and electrochemical lithiation behavior of titanium phosphate. It follows a similar structure as Paper III.

- Paper V: "Plasma-enhanced atomic layer deposition of vanadium phosphate as a lithium-ion battery electrode material"[34]

  This work exploits a remarkable effect that was found for the TEMAV vanadium precursor when used above its reported decomposition temperature within the TMP plasma / O_2 plasma process. Under these conditions, its decomposition is suppressed, allowing a PEALD process for vanadium phosphate to be developed. As in the previous papers, growth and material characteristics are reported, and the vanadium phosphate is electrochemically lithiated and cycled.

The research results are based on a wide array of experimental characterization methods, some of which might be unfamiliar to the reader; for this purpose, Chapter 2 provides short introductions to the theory behind (and the practical use of) each technique. Chapter 8 contains explorative work towards the deposition of cobalt and nickel phosphate and the reduction of phosphates to phosphides for applications in electrocatalysis, which may open up new research pathways. Finally, Chapter 9 provides general conclusions that can be drawn from this work and a perspective on future possibilities.

2

EXPERIMENTAL TECHNIQUES

The experimental nature of the work in this PhD thesis necessitates a wide array of physical characterization techniques. This chapter provides a brief summary of each technique in order to provide some context to the experimental results which will be shown in the following chapters. The first section describes some techniques which are particularly powerful because they can be used *in situ*, i.e. during the deposition process. The second section lists the ones that are used on the sample after deposition, i.e. *ex situ*. The final section focuses specifically on the electrochemical characterization.

2.1 IN-SITU CHARACTERIZATION

2.1.1 *Spectroscopic ellipsometry*

Ellipsometry is an optical measurement technique that allows for fast and non-destructive characterisation of thin films. It is based on the analysis of the change of polarization of light reflecting on the sample surface. Although many material properties can be determined through ellipsometry, it is especially useful in the investigation of dielectric properties (wavelength-dependent complex refractive index) and film thickness.[52]

Figure 2.1 illustrates the experimental geometry. The set-up consists of a light source and a detector, mounted under equal angles θ with regard to the sample's surface normal to enable specular reflection of the light beam. In the spectroscopic ellipsometry system implemented by J.A. Woollam, the light source contains a Xenon arc lamp which emits light in a broad wavelength range, from UV to near infrared. The light is collimated and passed through a fixed polariser plate to create a linearly polarised light beam with a known polarisation direction.

Reflection on the sample surface changes the polarisation state of the light beam. In general, the reflected beam has an elliptical polarisation, hence the name ellipsometry. The detector uses a rotating compensator (quarter-wavelength retardation plate) together with another fixed polariser plate (now called the analyser) and a CCD detector to measure the polarisation

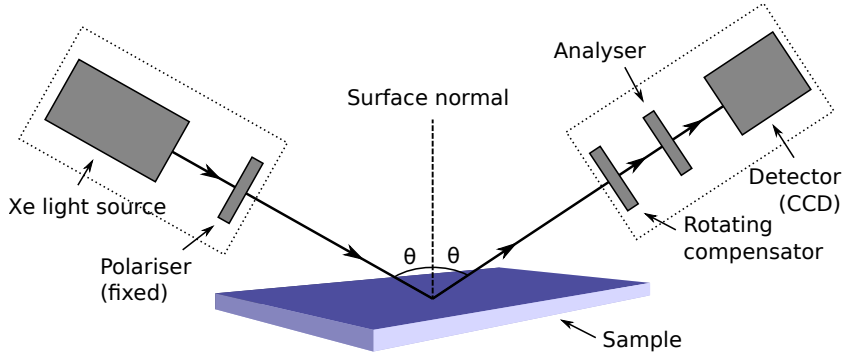

Figure 2.1: Simplified view of the J.A. Woollam spectroscopic ellipsometry set-up.

state of all wavelengths simultaneously, hence the name *spectroscopic* ellipsometry.

The polarisation change upon reflection is described by the Fresnel coefficients, which are complex numbers denoted by r_p and r_s. They determine the reflected amplitudes for light with a polarisation vector resp. parallel to (p-polarised) and perpendicular to (s-polarised, from the German word *senkrecht*) the plane defined by the incident and reflected beam. The detector measures the *ratio* of r_p and r_s, which is again a complex number:

$$\rho = \frac{r_p}{r_s} = \tan(\Psi)e^{i\Delta}$$

This complex reflectance ratio is commonly parametrised by the amplitude ratio $\tan(\Psi)$ and the phase shift Δ. For a given multilayer thin-film stack, Ψ and Δ can be uniquely calculated for each wavelength by the Fresnel equations. However, the inverse operation is not possible: the measured wavelength-dependent Ψ and Δ values do not define a unique layer system.

In practice, the thin-film system is modelled by one or more homogeneous layers on a substrate and the optical constants and layer thickness are included as free parameters. The values of these parameters are then determined by a least-squares fitting procedure, aiming to minimize the difference between the calculated and measured Ψ and Δ values. This method is included in ellipsometry analysis software like CompleteEASE and runs very fast on modern-day computer hardware. The only weakness is the model assumption: the parameters can lose their physical meaning if the assumed model does not actually represent the measured thin film.

2.1.2 *Mass spectrometry*

Mass spectrometry, often abbreviated as mass-spec or MS, is an analytical technique that allows the separation and identification of vapor-phase chemical species based on their mass. The general principle is that incoming molecules are first ionized, then filtered based on their mass-to-charge (m/q) ratio, and finally detected. Each of these three steps can be achieved by a multitude of methods; for brevity, the discussion below focuses on the specific methods implemented in the Hiden HPR-30 mass spec system. A schematic overview of this system is shown in figure 2.2.

- Electron impact ionization

  Incoming molecules are bombarded by energetic electrons. These electrons are thermionically emitted by a heated filament and accelerated over a potential difference; using a typical value of 70 V, the electrons receive a kinetic energy of 70 eV. Upon collision with a molecule M, this energy is sufficient to invoke ionization:

  $$M + e^- \longrightarrow M^+ + 2\,e^-$$

  producing a molecular ion M^+. In many cases, secondary reactions result in the fragmentation of the molecule and/or the production of multiply charged ions. For some heavy molecules, the fragmentation may be so extensive that almost all of the ions are fragments, which tends to complicate the interpretation of the resulting mass spectrum.

- Quadrupole mass filtering

  The quadrupole mass filter consists of four conductive rods arranged as shown in the center of figure 2.2. Each pair of opposite rods is con-

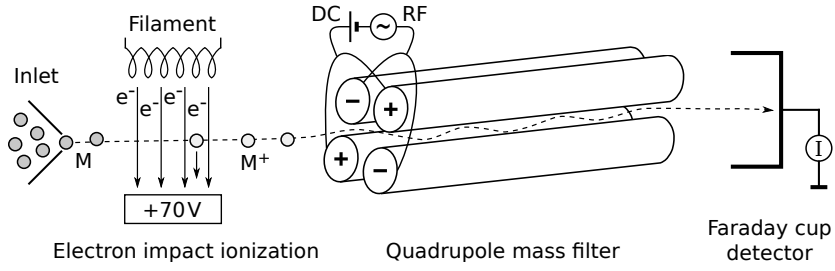

Figure 2.2: Schematic overview of the quadrupole mass spectrometer, showing the path of molecules as they are ionized, filtered, and detected.

nected together, and a potential difference is applied between the pairs; this forms an electric quadrupole moment (the monopole and dipole contributions are cancelled by the arrangement of the rods) in the center of the rods. The applied potential difference is a superposition of a DC offset and an RF oscillating component, resulting in a time-varying electromagnetic field. Ions are sent through the center of these rods and travel in the longitudinal direction by oscillating trajectories governed by differential equations; these equations will not be discussed here, but can be found in literature.[53] The important result is that only ions with a certain mass-to-charge ratio m/q pass through the rods, while the others form unstable trajectories and collide; in this way, the arrangement acts as a m/q filter, and the value of m/q can be selected by tuning the applied voltages and/or RF frequency.

- Faraday cup detection

  The filtered ions are detected by collecting them in a metal cup. Upon collision, they are neutralized, resulting in a transfer of charge to the cup which is grounded through an external current measurement circuit. Conservation of charge demands that the measured current is proportional to the collection rate of the ions.

Aside from the application of mass spectrometry to verify the "quality" of a vacuum (i.e. the presence of residual gases such as H_2O, N_2, or CO_2) or to verify if an ALD precursor reaches the chamber, it can be used to acquire important information on ALD reaction mechanisms by measuring the vapor-phase reaction products. For example, in the case of a TMA/H_2O process, spikes of methane can be detected during each half-reaction.[54] The Hiden HPR-30 instrument has two main modes of operation: in "bar scan" mode, it scans over a range of masses and plots the intensity as a function of m/q; in "multiple ion detection" mode, it measures and plots the time evolution of specific masses.

2.1.3 *Optical emission spectroscopy*

In a plasma-enhanced ALD process, at least one of the reaction steps is based on exposure to a plasma discharge. The plasma can be generated in various ways; for the work in this PhD thesis, an inductively coupled plasma (ICP) setup was used. This system generates plasma by applying RF power to a coil wrapped around a glass tube which flanges out from the deposition system. The RF field within the coil excites and ionizes the low-pressure gas within the tube, a process which is immediately visible

by the emission of light. Aside from being pretty to look at, this light can yield important information about the nature of the plasma and the PEALD process if it is collected and guided into a spectrometer. Electronic transitions within excited atoms, molecules, and ions may give rise to emission of photons at specific wavelengths, resulting in a "fingerprint" consisting of specific spectral lines.[55]

2.1.4 *Fourier-transform infrared spectroscopy*

Fourier-transform infrared spectroscopy (FTIR) is a particular implementation of infrared spectroscopy, an analytical technique which probes a sample with infrared light and yields information on its chemical composition. The technique is based on the characteristic rotational and vibrational energies of interatomic bonds within molecules. Incident photons matching these energies are absorbed, while others pass through without interaction. By scanning the photon energy (or, equivalently, the wavelength of the incident light), an absorption spectrum is produced which contains "fingerprints" that can be related to chemical functional groups.

A conventional wavelength range for mid-infrared spectroscopy spans 2.5 – 25 μm. For historical reasons, wavenumbers are used more commonly than wavelengths in spectroscopy; using the conversion to wavenumber $\tilde{\nu} = 1/\lambda$ (which strictly holds only in vacuum), this range is equivalent to 4000 – 400 cm^{-1} in "inverse centimeter" units. Tables are available in literature to correlate absorptions at certain wavenumbers to the presence of certain functional groups.[56]

The method of acquiring the absorption spectrum differs considerably between conventional infrared spectrometers and FTIR instruments. The former instruments use a monochromator to filter a single wavenumber

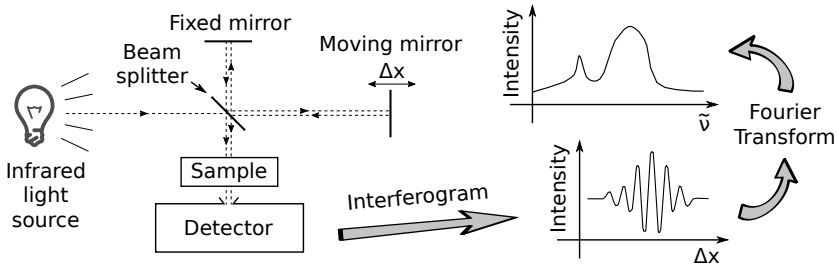

Figure 2.3: Illustration of the FTIR technique, showing the beam paths in the interferometer, the interferogram, and the resulting spectrum.

from a wideband infrared light source, send the monochromated infrared light through the sample, and measure the transmitted intensity. To scan over a range of wavenumbers, this process is repeated while moving the monochromator. FTIR instruments, however, take a radically different approach: the sample is included in the light path of an interferometer, and polychromatic infared light (i.e. containing all wavenumbers at the same time) is passed through it and detected; by sweeping the interferometer path length, an interferogram is created, from which the absorption spectrum of the sample can be calculated by means of a Fourier transform. This process is illustrated in figure 2.3.

2.2 MATERIAL CHARACTERIZATION

2.2.1 *X-ray diffraction*

X-ray diffraction (XRD) is one of the many X-ray based characterization techniques that have been used in the course of this thesis. XRD essentially probes the structure of a material, i.e. it reveals the way in which the atoms that make up a material are ordered. Poorly ordered structures are referred to as amorphous or "glassy", while highly ordered ones are said to be crystalline. XRD can be used either for the measurement and reconstruction of unknown crystalline structures, or for "phase identification" by comparing measured diffraction patterns to reference patterns from a database. The theory behind the technique is elegant, and deserves some discussion.

LAUE CONDITIONS Given a crystalline structure, the location of the XRD peaks can be predicted purely from its geometry. The crystal lattice is essentially a periodically repeating structure of scattering centres.[1] Constructive interference (which corresponds to a maximum in the diffracted intensity) occurs when the scattered rays are in phase, i.e. when the path difference between them is an integer multiple of the wavelength λ.

Because each lattice point is connected to all other ones by a series of translations along the a-, b-, and c-axes, all the scattered rays are in phase if and only if they are in phase for a row along each axis. Therefore, the condition for constructive interference can be derived once for the a-axis and also demanded for the two other axes, yielding the diffraction condition for the whole crystal.

1 In reality, X-rays scatter on the electron clouds which surround the nuclei, but our reasoning is still valid because the electron probability density still forms a periodically repeating structure.

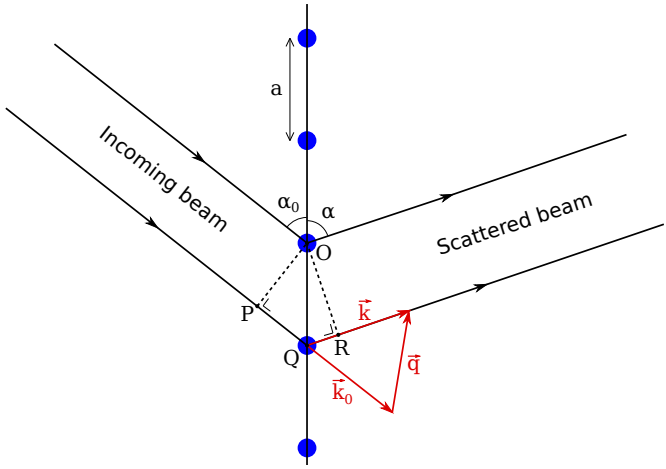

Figure 2.4: Path difference for scattered X-rays along a single row of a crystal, in this case the a-axis.

Figure 2.4 shows the scattering geometry for a single row along the a-axis (i.e. the [100] direction) of the crystal. The incoming X-rays have a wave vector $\vec{k}_0$ and make an angle α_0 with the a-axis, while the outgoing (scattered) X-rays have a wave vector $\vec{k}$ and make an angle α with this axis. The scattering centres are indicated by blue dots; the distance between them (i.e. the lattice parameter) is a.

For constructive interference, the difference in path length as measured between the wave fronts of the scattered waves should be an integer h times the wavelength λ:

$$|PQ| + |QR| = h\lambda \tag{2.1}$$

Because $|PQ|$ is the projection of $\vec{a}$ in the direction of $-\vec{k}_0$ and $|QR|$ is the projection of $\vec{a}$ in the direction of $\vec{k}$, we have

$$|PQ| = -\vec{a} \cdot \frac{\vec{k}_0}{\|\vec{k}_0\|} \quad \text{and} \quad |QR| = \vec{a} \cdot \frac{\vec{k}}{\|\vec{k}\|}. \tag{2.2}$$

Additionally,

$$\|\vec{k}\| = \|\vec{k}_0\| = \frac{2\pi}{\lambda} \tag{2.3}$$

because we only consider elastic scattering. We define the scattering vector $\vec{q}$ as

$$\vec{q} = \vec{k} - \vec{k}_0 \tag{2.4}$$

This enables us to rewrite (2.1) as:

$$\vec{a} \cdot \vec{q} = 2\pi h \tag{2.5}$$

By doing the same thing for the b-axis ([010] direction) and c-axis ([001] direction), we arrive at a set of three equations called the *Laue conditions*:

$$\begin{cases} \vec{a} \cdot \vec{q} &= 2\pi h \\ \vec{b} \cdot \vec{q} &= 2\pi k \\ \vec{c} \cdot \vec{q} &= 2\pi l \end{cases} \tag{2.6}$$

where h, k, and l are integers; in fact, they are the reciprocal lattice indices. The reciprocal lattice can be constructed from the reciprocal primitive vectors $\vec{a}^*$, $\vec{b}^*$ and $\vec{c}^*$, defined by:

$$\begin{cases} \vec{a}^* \cdot \vec{a} &= 2\pi \\ \vec{a}^* \cdot \vec{b} &= 0 \\ \vec{a}^* \cdot \vec{c} &= 0 \end{cases} \quad \begin{cases} \vec{b}^* \cdot \vec{a} &= 0 \\ \vec{b}^* \cdot \vec{b} &= 2\pi \\ \vec{b}^* \cdot \vec{c} &= 0 \end{cases} \quad \begin{cases} \vec{c}^* \cdot \vec{a} &= 0 \\ \vec{c}^* \cdot \vec{b} &= 0 \\ \vec{c}^* \cdot \vec{c} &= 2\pi \end{cases} \tag{2.7}$$

The reciprocal lattice vector $\vec{r}^*_{hkl}$ can then be written as

$$\vec{r}^*_{hkl} = h\vec{a}^* + k\vec{b}^* + l\vec{c}^* \tag{2.8}$$

By substituting this vector for $\vec{q}$ in 2.6 and making use of 2.7, we find that the Laue conditions are satisfied. In other words, *the scattering vector must be a lattice vector of the reciprocal lattice.*

BRAGG'S LAW The Laue conditions can be reformulated in terms of reflections on crystal planes, yielding a more intuitive and practical way to understand X-ray diffraction. The geometric derivation is illustrated in figure 2.5. The basic idea is unchanged: diffraction peaks occur when rays are scattered in phase from all scattering centres.

First consider two rays scattering on P_1 and P_2 of the upper (hkl) plane. The path difference between the incoming wave front Π and the outgoing wave front Π'' is indicated by δ_1 for P_1 and δ_2 for P_2. The waves are scattered in phase when $\delta_1 = \delta_2$, which implies that the angle between the incoming wave and the crystal plane should be the same as the angle between the outgoing wave and the crystal plane. In other words: *X-rays must undergo mirror reflection on crystal planes.*

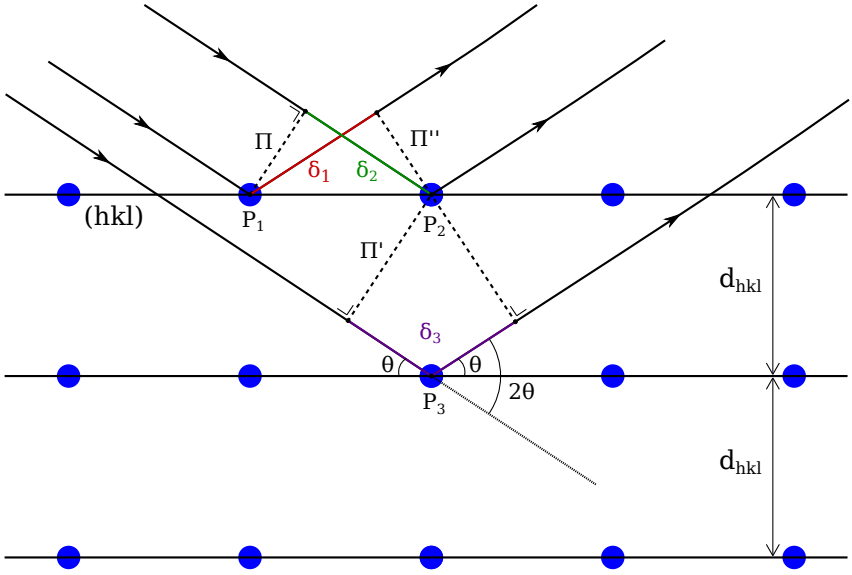

Figure 2.5: Geometrical derivation of Bragg's law.

Now consider two rays scattering on P_2 and P_3, separated by a distance d_{hkl}. By our previous argument, the incoming and outgoing rays must be symmetric with regard to the surface normal, and make an angle θ with the (hkl) plane. Using some trigonometry, the path difference δ_3 between the incoming wave front Π' and the outgoing wave front Π'' is given by:

$$\delta_3 = 2d_{hkl} \sin\theta \tag{2.9}$$

And because, for constructive interference, this difference has to be an integer n times the wavelength:

$$2d_{hkl} \sin\theta = n\lambda \tag{2.10}$$

Equation 2.10 is commonly known as Bragg's law. It states that each crystal plane diffracts X-rays in a mirror-like fashion, but only under a specific angle θ which is related to the interplanar distance d_{hkl}.

POWDER DIFFRACTION Powders consist of a huge number of tiny crystallites in random orientations. In an X-ray diffractometer, the source irradiates the sample surface under an angle θ and the detector makes an angle 2θ with the incoming beam. By simultaneously scanning over θ and 2θ, all possible (hkl) reflections can be recorded, provided that for each

(hkl) plane there are enough crystallites which happen to have this plane parallel to the sample surface. This results in a fingerprint pattern of the diffracted intensity as a function of the 2θ angle, from which crystalline phases can be identified.

HIGH-TEMPERATURE XRD The crystalline structure of some materials can be rearranged by a heat treatment process known as thermal annealing. The thermal energy provided by this process allows atoms to become more mobile and overcome activation barriers so that they may reconfigure into a thermodynamically more favorable configuration. The ALD-deposited phosphates in this thesis are an example of this; all of them are amorphous as deposited, but they will crystallize upon annealing.

The CoCooN lab possesses home-built setups which combine an XRD diffractometer with a high-temperature annealing stage within a controlled atmosphere, facilitating this kind of measurement by acquiring XRD patterns while a sample is being annealed. This technique is known as (high-temperature) *in-situ* XRD, where the *in-situ* aspect now refers to the annealing process rather than the deposition process. More information on this setup can be found in the PhD thesis of a former group member who originally constructed it.[57]

2.2.2 *X-ray reflectometry*

X-ray reflectometry (XRR) is a thin-film measurement technique based on the specular reflection of grazing incidence X-rays to determine parameters such as thickness, density, and surface or interface roughness.[58] The method provides direct and accurate thickness measurements of single-layer and multilayer films without having to rely on complex optical model assumptions (as is often the case for ellipsometry).

The XRR setup (figure 2.6a) consists of a monochromatic X-ray source which irradiates the sample at a grazing angle θ, and a detector which measures the reflected X-ray intensity in a mirror reflection geometry. As the refractive index of materials in the X-ray region is slightly less than unity, there will be total reflection on the sample surface if the angle is lower than the critical angle θ_c (typically, $\theta_c < 0.3°$). For $\theta > \theta_c$, some incident X-rays will reflect on the surface while others will penetrate into the thin film and reflect on the interface layer, yielding an interference pattern. The measured intensity is usually plotted on a log scale (due to the high dynamic range) as a function of 2θ.

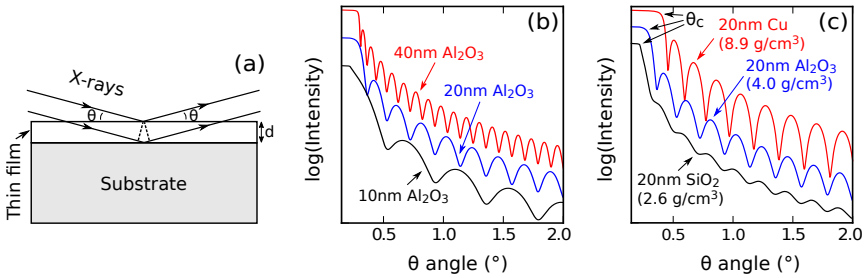

Figure 2.6: Illustration of the XRR technique: (a) X-ray beam reflection and interference; (b) simulated patterns showing the influence of film thickness; (c) simulated patterns showing the influence of film density (the curves are vertically offset for clarity).

The complex refractive index can be expressed as $\tilde{n} = 1 - \delta + i\beta$. The parameter β represents absorption and relates to the linear absorption coefficient μ of the material as $\beta = \lambda\mu/4\pi$, where λ is the X-ray wavelength. The parameter δ represents dispersion and is proportional to the density of the material. In a small-angle approximation, it relates to the critical angle θ_c as

$$\theta_c = \sqrt{2\delta}$$

Therefore, the density of the material can be calculated from the critical angle.

For single-layer thin films, a simple periodic oscillation of the intensity as a function of the reflection angle is observed, characterized by a series of intensity modulations known as Kiessig fringes. The location of the m-th interference fringe maximum θ_m satisfies the equation

$$m\lambda \approx 2d\sqrt{\theta_m^2 - 2\delta}$$

where d is the layer thickness and λ, δ are as previously defined. For $\theta \gg \theta_c$ (but still in the small-angle approximation), the spacing $\Delta\theta$ between the fringes is given by

$$\Delta\theta \approx \frac{\lambda}{2d}$$

In other words, the periodicity of the interference pattern is directly determined by the layer thickness and the fringes get closer together when the layer thickness increases.

Figure 2.6 shows simulated XRR patterns which demonstrate the effects of film thickness (fig. 2.6b) and density (fig. 2.6c) on the interference pat-

tern. As stated earlier, the spacing of the fringes is inversely proportional to the film thickness. The critical angle increases with the film density, but also the amplitude of the fringes is proportional to the "density contrast" between the film and the substrate. The simulated patterns assume zero roughness for the substrate and the thin film; increasing levels of roughness will result in XRR patterns which decay quicker and have lower fringe amplitudes at higher θ angles.

2.2.3 *X-ray photoelectron spectroscopy*

X-ray photoelectron spectroscopy (XPS) is an X-ray based analytical technique which yields surface-sensitive chemical information. In an XPS measurement, the sample is placed in a UHV chamber and bombarded with soft X-rays, typically from a monochromatic Al K_α source (E_γ = 1486.7 eV). Impinging photons knock out electrons from atomic shells through a process known as photo-ionization. The kinetic energy of these electrons is then measured with an electron energy analyzer. Because the photon energy E_γ is fixed and conservation of energy applies, electrons from deeper levels (higher binding energy) will have less kinetic energy available when leaving the sample. The binding energy of the electron (relative to the Fermi level of the sample) can be calculated as:

$$E_B^F = E_\gamma - E_{kin}(\mathrm{sp}) - \phi_{spec},$$

where $E_{kin}(\mathrm{sp})$ is the measured kinetic energy of the electron in the spectrometer and ϕ_{spec} is the spectrometer work function (a calibration constant).[59]

As each element has characteristic binding energies, XPS can be used for element identification and quasi-quantification by counting the number of detected electrons for each energy. It also gives information about the chemical environment of each element because binding energies are slightly influenced by chemical bonds.

XPS is very surface sensitive due to the limited escape depth of the electrons, typically around 1–2 nm. The information from the surface might not be representative for the whole layer, and the surface can easily be contaminated by exposure to the atmosphere. Some carbon can be observed on most exposed surfaces. To avoid this problem, the sample surface may be simultaneously sputtered by heavy ions (e.g. argon) to make the measurement of concentration depth profiles possible. However, the sputtering process itself can change the composition ratio of the surface due to preferential sputtering, severely complicating a quantitative analysis.

2.2.4 *Elastic recoil detection*

Elastic recoil detection (here abbreviated as ERD, also known as ERDA) is an ion beam analysis technique that can be used to measure quantitative atomic compositions and depth profiles of thin films. It is related to the technique of rutherford backscattering spectrometry (RBS), as they are both based on elastic collisions between an incident high-energy ion beam and the atoms in the sample surface. However, unlike RBS, ERD does not detect the backscattered beam particles, but instead it analyses the energy of the target nuclei recoiled in the forward direction.[60]

IDENTIFICATION The sample's atoms are identified by measuring their energy. The kinematics can be derived through conservation of energy and momentum; the energy E_2 of a target atom with mass M_2 scattered with a recoil angle ϕ (measured between the direction of the recoiled target atom and direction of the incident ion beam) is given by

$$\frac{E_2}{E_0} = \frac{4M_1M_2}{(M_1+M_2)^2}\cos^2\phi$$

where the incident ions have a mass M_1 and an energy E_0. In other words, if the experimental parameters M_1, E_0 and ϕ are fixed and known, the target atom's mass can be identified by measuring E_2 using a solid-state nuclear particle detector or by other means. This arrangement is illustrated in figure 2.7.

QUANTIFICATION The amount of recoiled nuclei with a particular mass is proportional to the atomic concentration in the thin film and to the

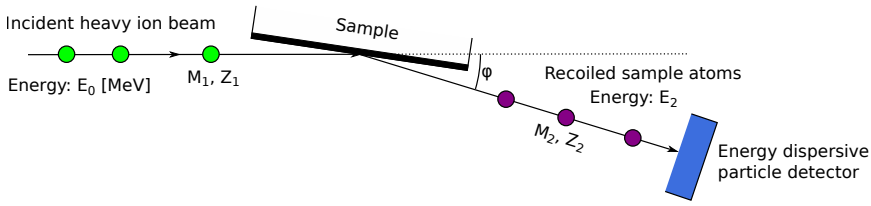

Figure 2.7: Experimental geometry of an ERD measurement.

differential cross section of recoils $d\sigma_R/d\Omega$, which can be derived from the Coulomb repulsion force and is given by

$$\frac{d\sigma_R}{d\Omega} = \left(\frac{e^2}{8\pi\epsilon_0}\frac{Z_1 Z_2}{E_0}\right)^2 \frac{(1 + M_1/M_2)^2}{\cos^3\phi}$$

where Z_1 and Z_2 denote the atomic numbers of resp. the beam and target nuclei.[61] By counting the number of detected particles and taking the cross section into account, the atomic concentration in the thin film can be accurately determined.

DEPTH PROFILING Both the incident beam ions and the recoiled target nuclei lose some energy while traversing the thin film, resp. before and after the collision. This energy loss is proportional to the stopping power (dE/dx, expressed in eV/Å) of the host material and to the path length traversed through the solid, which is in itself proportional to the collision depth in the material. By measuring the energy loss, depth profiling becomes possible. The tabulated or calculated stopping power of the material is used to convert the energy scale into a depth scale.

2.2.5 *Scanning electron microscopy / energy-dispersive X-ray spectroscopy*

Abbreviated as resp. SEM and EDX, these two techniques are usually simultaneously implemented on the same instrument. SEM provides morphological information (comparable to an optical microscope but with a much higher resolution), while EDX provides chemical information (elemental identification and quantification).

A simplified diagram of the instrument is shown in figure 2.8a. It consists of a vacuum chamber containing an electron column, a sample stage, and various detectors. The column produces an electron beam which is finely focused on the specimen surface trough magnetic lenses. Additional magnetics deflect the electron beam and scan it in a raster-like fashion over the specimen. Meanwhile, the intensities of various signals created by the interaction of the electrons with the sample surface (figure 2.8b) are detected and recorded by a computer. By representing the detected signal intensity as pixel brightness, an image display is created. The information in the image depends on the type of signal being collected.

The secondary electron image (SEI) is most comparable in appearance to an optical microscope image. It shows a high-resolution topographic view of the specimen with a large depth of field. Secondary electrons are produced by inelastic collisions occurring when an incoming electron ejects

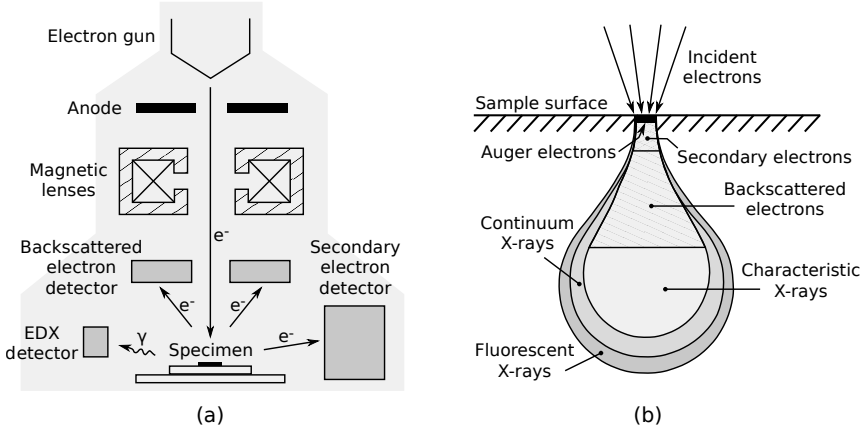

Figure 2.8: Illustrations of scanning electron microscopy, showing (a) a simplified diagram of an SEM instrument and (b) the interaction of the electron beam with the specimen.

a loosely bound electron from a specimen atom. Due to their low energy ($10 - 50$ eV), the mean free path length of secondary electrons traversing the material is very short, typically $\sim 1\,\text{nm}$.[62] This implies that they can only escape from very close to the surface, yielding topographic contrast. Secondary electrons are usually detected by an Everhart-Thornley detector (ETD), which attracts the electrons to a positively biased cage containing a scintillator and detects the emitted light with a photomultiplier outside the specimen chamber.

Backscattered electrons (BSE) are beam electrons which have scattered in a backward direction by elastic collisions on the specimen atoms. Compared to secondary electrons, they have much higher energies (up to the beam energy) and can originate from a larger volume due to the increased path length, resulting in a poorer image resolution. However, as backscattering efficiency increases with the atomic number of the scattering atom, the BSE image provides contrast based on chemical composition.

The energy-dispersive X-ray (EDX) signal stems from X-rays emitted by the specimen when core-level electrons fall back to their ground states after excitation by the high-energy electron beam, releasing the energy difference in the form of a photon. The photon energy depends on the atomic number of the excited atom. By collecting the X-ray photons and analyzing their energy, which is typically achieved with a solid-state detector, a spectrum is produced which shows characteristic X-ray lines and reveals the elements present in the specimen. The peak areas may be used for (ap-

proximate) quantification by comparison against a calibration specimen or by making use of a standardless quantification scheme. By analyzing the EDX spectra as a function of the scanning position, an image showing the local distribution of elements can be acquired. This is known as elemental mapping.

2.2.6 *Atomic force microscopy*

Atomic force microscopy (AFM) is a type of scanning probe microscopy that is based on the interaction between a microscopic tip and the surface of a sample through interatomic forces. The tip is mounted on a cantilever, of which the deflection is measured by reflecting a laser beam on it and detecting the beam position by a photodiode. The sample is placed on a highly accurate piezoelectric xyz positioning stage. By scanning the sample in the xy direction and adjusting the z direction using a feedback loop monitoring the cantilever deflection and acting to keep the distance between the (stationary) tip and the sample surface constant, the z signal will follow the height variations of the sample surface. This results in a topological image with Å-level resolution. The feedback can be acquired in different modes (contact mode, tapping mode, and non-nontact mode) of which detailed discussions are outside the scope of this thesis and can be found in existing literature.[63]

2.3 ELECTROCHEMICAL CHARACTERIZATION

2.3.1 *Test cell construction*

The electrochemical properties of the deposited films were measured by using them as working electrodes in lithium-ion test cells. The setup is shown schematically in figure 2.9. The test cells are made of PTFE and contain two vertical bores. The largest bore is open on the bottom and accommodates an O-ring which presses against the thin film to be measured as the working electrode (WE).[2] This makes a tight seal, allowing the cell to be filled with an electrolyte (1M $LiClO_4$ in propylene carbonate (PC)). Strips of lithium metal are submerged in both openings; the one facing the sample acts as the counter electrode (CE), while the other (which "sees" the working electrode by means of a Luggin cappilary) acts as the

2 The accessible surface area of the electrode is determined by the area enclosed within the O-ring. In Papers III and IV, this was calculated as 0.95 cm^2 based on the specified inner diameter of the O-ring. Later measurements revealed 1.05 cm^2 as a better estimate of the actual area, which is the value used from Paper V onwards. Although this discrepancy of approx. 10% propagates through to the calculated capacities, it is comparable in magnitude to the assumed experimental error and so does not change any conclusions.

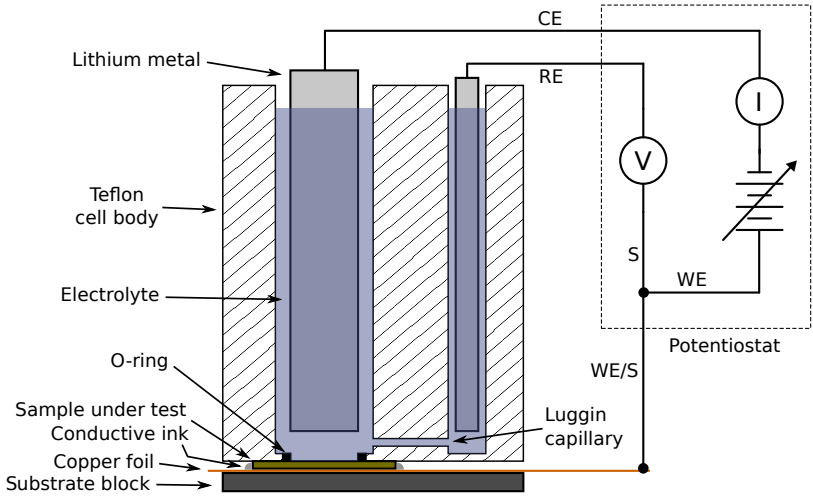

Figure 2.9: Schematic diagram of the li-ion test setup, showing a cross section of the test cell and the connections to the potentiostat.

reference electrode (RE). Potentials at the working electrode are therefore measured against the Li^+/Li redox couple. The working electrode is contacted by silver ink applied around the edges of the sample, forming an electrically conductive connection between the thin-film current collector layer and a piece of copper foil underneath.

Because lithium spontaneously reacts with oxygen, nitrogen, or moisture, the cell must be constructed and used within an inert atmosphere. For this purpose, an argon glovebox with O_2 and H_2O levels below 1 ppm was used.

A potentiostat is connected to the test cell using a three-electrode connection scheme, which entails that voltage is sensed between RE and WE and current is applied between CE and WE. This ensures that the reference couple (Li^+/Li) is undisturbed by any current draw and provides an accurate reference voltage. Measurements were performed with both commercial (Metrohm Autolab) and home-made potentiostats. Details on the home-made potentiostat design (including more technical information on potentiostats in general) can be found in the appendix of this thesis.

2.3.2 *Constant-current charge/discharge*

The most straightforward method to characterize an electrode material is to apply a constant current I and to measure the potential of the electrode

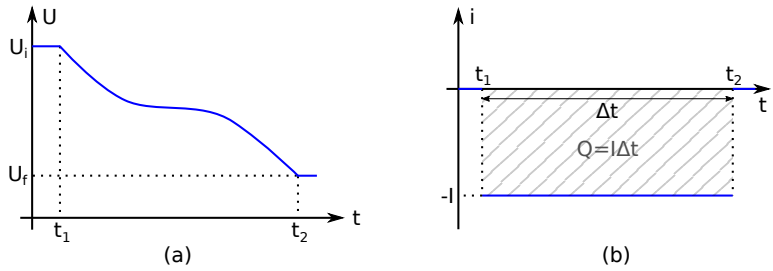

Figure 2.10: Illustration of a constant-current charge/discharge measurement, showing (a) the potential as a function of the elapsed time and (b) the current as a function of the elapsed time, together with the charge (striped area).

$U(t)$ as a function of time. Depending on the direction of the current, the electrode material is said to be charged or discharged.[3] The way in which the potential changes over time gives information on the electrochemical processes (e.g. coexistence of two phases showing a plateau in the discharge curve)[64] and the electrode capacity can be calculated by multiplying the current I by the amount of elapsed time Δt:

$$Q = \int_{t_1}^{t_2} i(t)\, dt = I \times \Delta t$$

The potential and current as a function of the elapsed time are sketched in figure 2.10 for a discharge measurement on a hypothetical electrode material with a single potential plateau between the limits of U_i (initial potential) and U_f (final potential).

2.3.3 *Cyclic voltammetry*

The cyclic voltammetry (CV) method is based on the application of repeated linear potential sweeps between upper and lower bounds, describing a triangle wave as a function of time (as shown in figure 2.11a). The resulting cell current is measured and plotted as a function of the applied potential. As the cell current is proportional to the reaction rate, this tech-

3 It must be noted that the meaning of charge and discharge is ambiguous for an electrode in a half cell. In a complete lithium-ion battery, the positive electrode material is delithiated (removal of lithium ions, corresponding to oxidation) during charge and lithiated (insertion of lithium ions, corresponding to reduction) during discharge, but the exact opposite happens for the negative electrode material. By convention, the point of view of a positive electrode material will be assumed.

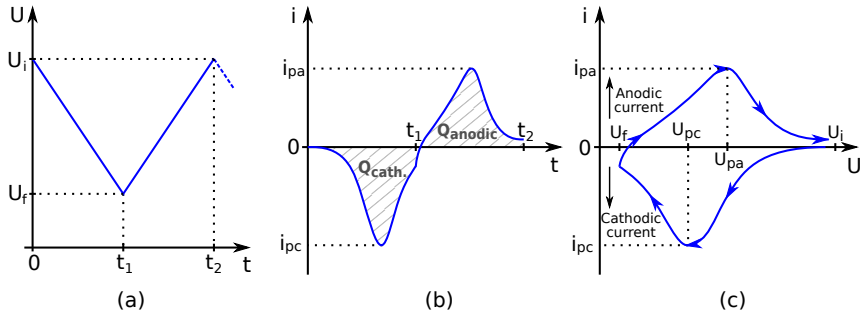

Figure 2.11: Illustration of a cyclic voltammetry measurement, showing (a) the potential as a function of the elapsed time; (b) the current as a function of the elapsed time; (c) the current as a function of the potential.

nique essentially reveals the reduction or oxidation reactions that occur in a chosen potential window.

Suppose we first let the potential decrease linearly from its initial value U_i with a scan rate v (usually expressed in mV/s), then $U(t)$ is given by:

$$U(t) = U_i - vt$$

At some point, the potential will be sufficiently low for a reduction reaction (e.g. intercalation of lithium into the working electrode, lithiation) to start happening, evidenced by an onset of current in the cathodic direction. As the potential keeps decreasing, the "driving force" for reduction gets stronger, and the current increases. Eventually, the reaction nears completion or the oxidant gets depleted, and the current decreases again. This explains the appearance of the cathodic current peak, characterized by a peak potential U_{pc} and a peak current i_{pc}, as shown in figure 2.11b.

Upon reaching the minimum potential, U_f, the scan direction is reversed. The potential now rises linearly as a function of time, still with the same scan rate:

$$U(t) = U_f + vt$$

The species that have been previously reduced, will now be driven to oxidation (e.g. delithiation) by the rising potential. Again, the current increases, but now in the anodic direction. At a certain point, the oxidation reaction completes, resulting in a decreasing anodic current. An anodic current peak is observed with a peak potential U_{pa} and a peak current i_{pa}.

When the potential reaches its initial value U_i, the measurement can either be stopped, or the scan direction can be reversed again to repeat this

whole reduction–oxidation process for an arbitrary number of cycles. The cyclic voltammogram (figure 2.11c) yields information on the redox potential and the kinetics of the reaction. The storage capacity of the electrode (i.e. the total charge) can be calculated by integrating the current as a function of time. It is also proportional to the area under the cathodic or anodic peaks in the cyclic voltammogram because of the linear relationship between potential and time.

3

PAPER I: ALUMINIUM PHOSPHATE

The following chapter has been published as an original research paper in Chemistry of Materials, titled *"Atomic Layer Deposition of Aluminum Phosphate Based on the Plasma Polymerization of Trimethyl Phosphate"*.[30] The content below has been reformatted to fit the layout of this PhD thesis, but is otherwise identical to the published version.

3.1 ABSTRACT

Aluminium phosphate thin films were deposited by plasma-assisted atomic layer deposition (ALD) using a sequence of trimethyl phosphate (TMP, Me_3PO_4) plasma, O_2 plasma and trimethylaluminium (TMA, Me_3Al) exposures. In-situ characterization was performed, including spectroscopic ellipsometry, optical emission spectroscopy, mass spectrometry and FTIR. In the investigated temperature region between 50 °C and 320 °C, nucleation delays were absent and linear growth was observed, with the growth per cycle (GPC) being strongly dependent on temperature. The plasma polymerization of TMP was found to play an important role in this process, resulting in CVD-like behavior at low temperatures and ALD-like behavior at high temperatures. Films grown at 320 °C had a GPC of 0.37 nm/cycle and consisted of amorphous aluminium pyrophosphate ($Al_4P_6O_{21}$). They could be crystallized to triclinic $AlPO_4$ tridymite by annealing to 900 °C, as evidenced by high temperature XRD

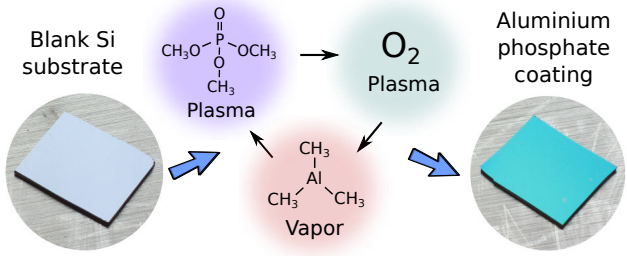

Figure 3.1: Abstract graphic for Paper I.

measurements. The use of a TMP plasma might open up the possibility of depositing many other metal phosphates by combining it with appropriate organometallic precursors.

3.2 INTRODUCTION

Atomic layer deposition (ALD) is a thin-film deposition technique in which layer-by-layer growth is achieved through alternating exposures to chemical vapors. It can be seen as a special form of chemical vapor deposition (CVD) where the precursor exposures are separated in sequential, self-limiting half reactions. Many classes of materials have been deposited by ALD processes, including various oxides, II-VI and III-V semiconductors, metal nitrides, metals, metal sulfides, and fluorides.[65] Reports on the atomic layer deposition of phosphates are still scarce, but seem to be gaining popularity over the last years. Table 3.1 presents a summary of the existing literature on this subject.

Phosphate ALD processes have been developed targeting a wide range of applications: aluminium phosphate as a catalyst support,[12] as an ion barrier in electroluminescent displays,[13] to improve lithium-ion battery cathodes,[66] as a transistor gate dielectric,[67] and to improve the oxidation resistance of carbon fibers;[26] calcium phosphate (hydroxyapatite) for biomedical applications;[17] titanium phosphate for its ion-exchange properties[68] and for its catalytic activity;[69] iron phosphate as a cathode material[22] and lithium phosphate as a solid-state electrolyte[70] for lithium-ion batteries.

These processes are typically based on the inclusion of a phosphorus source in an existing metal oxide ALD process. In theory, phosphoric acid (H_3PO_4) would be an ideal candidate for this, but its use in vapor deposition is prohibited by its low vapor pressure at room temperature and its tendency to decompose rather than evaporate upon heating. Phosphorus pentoxide (P_2O_5) can be used, but needs to be heated to 170 °C or higher[12, 13]; this presents challenges to the reactor design. Trimethyl phosphate (TMP, Me_3PO_4) is an attractive alternative: this organophosphate compound reaches a vapor pressure of 15 mbar at 70 °C.[71]

Thermal ALD processes using TMP have been demonstrated for a variety of metal sources. Especially where chloride precursors were avoided,[15, 17, 19, 22, 26] it has proven difficult to incorporate a sufficiently high atomic percentage of phosphorus in the growing film (presumably due to the low reactivity of TMP with organometallic compounds), unless one introduces a large number of phosphate subcycles for each metal pulse.

Table 3.1: Overview of earlier work on the atomic layer deposition of phosphates.

Authors (Year)	Metal (source)	Phosphorus source	Temperature (°C)	GPC (nm)	GPSS (nm) [a]
Nieminen et al. (1995) [12]	Aluminium (trichloride)	P_2O_5, TMP	500	N.A.	N.A.
Tiitta et al. (1998) [13]	Aluminium (trichloride, n - propoxide)	P_2O_5	450 - 500	0.05 - 0.13	0.03 - 0.06
Putkonen et al. (2009) [17]	Calcium ($(thd)_2$)	TMP	300	0.04	0.01
Hämäläinen et al. (2012) [19]	Lithium (hexamethyldisilazide)	TMP	225 - 300	0.07 - 0.10	0.03 - 0.05
Hämäläinen et al. (2012) [19]	Lithium (tert - butoxide)	TMP	275 - 350	0.04 - 0.13	0.02 - 0.07
Wiedmann et al. (2012) [16]	Titanium (tetrachloride)	TMP	150 - 300	0.12	0.03
Hämäläinen et al. (2012) [14]	Aluminium (trichloride)	TMP	150 - 400	0.14 - 0.24	0.07 - 0.12
Hämäläinen et al. (2012) [14]	Titanium (tetrachloride)	TMP	275 - 450	0.04 - 0.14	0.02 - 0.07
Liu et al. (2013) [15]	Aluminium (trimethyl-)	TMP	150	0.17	0.008
Knohl et al. (2013) [26]	Aluminium (trimethyl-)	TEP	250	0.08 - 0.13	0.04 - 0.07
Gandrud et al. (2013) [22]	Iron ($(thd)_3$)	TMP	200 - 380	0.10	0.005
Sønsteby et al. (2014) [21]	Lanthanum ($(thd)_3$)	TMP	250 - 300	0.08	0.02
This work	Aluminium (trimethyl-)	TMP plasma	320	0.37	0.12

[a] Growth per substep = (growth per cycle) / (number of substeps in one cycle)

This considerably slows down the growth; for this reason, table 3.1 not only lists the reported growth per cycle (GPC) but also the average growth per substep (calculated by dividing the GPC by the number of substeps in one cycle) in order to make a fair comparison between the expected deposition rates of different ALD chemistries.

In this work, the TMP precursor is used in a novel way: the vapor is brought into an inductively coupled plasma (ICP) discharge, and a TMP plasma is created. To the best of our knowledge, the use and/or properties of an inductively coupled plasma of low-pressure TMP vapor have not previously been reported in literature. Perhaps most closely related to this topic is the work by Hilt et al.[72] wherein organophosphate coatings were deposited by an atmospheric-pressure plasma of triethyl phosphate (TEP), and a patent application by Zhang et al.[73] which describes the deposition of lithium-containing solid electrolyte films by mixing a volatile lithium precursor and a volatile phosphate precursor (TMP or TEP) into a low-pressure nitrogen/hydrogen plasma. The use of plasma greatly increases the reactivity of TMP and its tendency to introduce phosphorus into the deposited film. By alternating TMP plasma pulses with O_2 plasma and TMA exposures in an ALD-type process, we are able to grow thin films of aluminium phosphate with a high growth rate and with precise thickness control.

3.3 EXPERIMENTAL

Depositions were carried out in a home-built pump-type ALD reactor, shown schematically in figure 3.2. The stainless steel deposition chamber was continuously evacuated by a turbomolecular pump to a base pressure in the 10^{-6} mbar range. Precursor vapors and gases were admitted through computer-controlled pneumatic valves and manually adjustable needle valves. The TMP precursor was heated in a stainless steel container to 68 °C, while the tube leading to the reactor was kept at 70 °C. The TMA precursor was used at room temperature. The temperature of the chamber walls was set to 95 °C. On top of the chamber, a gate valve leads to a fused quartz column wrapped by a copper coil. The coil is connected to a 13.56 MHz RF generator (Advanced Energy CESAR 136) and a matching network in order to generate an inductively coupled plasma in the column. By opening the gate valve and pulsing the RF generator, substrates could be exposed to remote plasma. The TMP plasma was created by feeding TMP vapor from the chamber through the gate valve, while for the oxygen plasma the O_2 gas was injected directly into the column. The plasma power was set to 100 W and the impedance matching parameters

were tuned to minimize the reflected power. All gas flows (TMP, TMA and oxygen) were adjusted to reach a partial pressure of 6×10^{-3} mbar in the deposition chamber. All substrates were pieces of standard p-type silicon (100) wafer cut to size; for in-situ FTIR measurements in transmission mode, the double polished variety was used. They were mounted to a molybdenum sample holder which rested on a heated copper block. The temperature of the copper block was PID controlled, and sample temperatures were calculated from copper block temperatures by calibration.

In-situ spectroscopic ellipsometry measurements were performed with a J.A. Woollam M-2000 ellipsometer working in the ultraviolet-visible region and using the CompleteEASE software for fitting and data analysis. The optical model always consisted of a silicon substrate covered by a single layer which satisfied a Cauchy dispersion relation; coefficients were determined from layers with a known thickness (aided by XRR) and were held fixed, while the thickness (as the only free parameter) was fitted in situ. Optical emission spectra were recorded with an Ocean Optics QE Pro spectrometer coupled to the plasma column by an optical fiber. Mass spectrometry was carried out with a Hiden HPR-30 mass spectrometer using 70 eV electron impact ionization and a quadrupole mass filter combined with a Faraday detector. Infrared spectroscopy was performed on a Bruker VERTEX 70V FTIR spectrometer with KBr beamsplitter and an LN_2-cooled MCT detector (mid-infrared). XRR and XRD patterns were acquired on a Bruker D8 diffractometer using Cu Kα radiation; in-situ annealing was performed in a home-built chamber under a helium atmosphere using a position sensitive detector. Energy-dispersive X-ray spec-

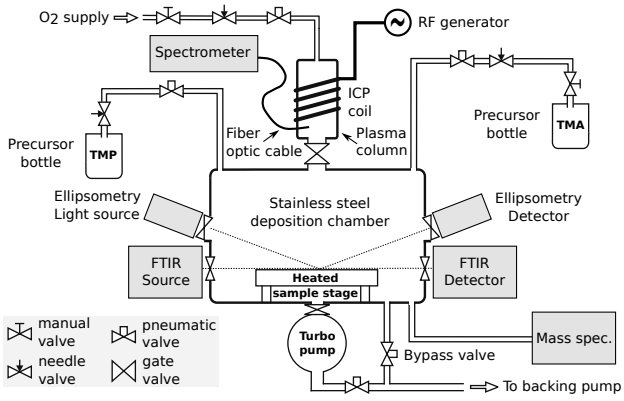

Figure 3.2: Schematic drawing of the deposition system used in this work, along with the in-situ characterization options.

troscopy (EDX) was carried out in an FEI Quanta 200 F scanning electron microscope using a 10 keV electron beam and an EDAX silicon-drift detector. X-ray Photoelectron Spectroscopy (XPS) analysis was performed on a Thermo Scientific Theta Probe XPS instrument using Al Kα X-rays generated at 15 kV and 70 W and focused to a spot size of 0.3 mm by an MXR1 monochromator gun. The sample surface was etched by Ar^+ ions at an acceleration voltage of 3 keV and a current of 2 μA. The elastic recoil detection (ERD) measurements were carried out using a 10 MeV $^{63}Cu^{5+}$ beam, with a scattering angle of 40° and a sample tilt of 20°.

3.4 RESULTS AND DISCUSSION

3.4.1 *TMP plasma properties*

To start, we will focus on the TMP plasma, which is the first step in the proposed ALD process. Figure 3.3 shows the optical emission spectrum of this plasma in the visible range. To the naked eye, its color appears bluish white. The spectrum contains atomic emission lines of hydrogen (Balmer series: H_α at 656.3 nm, H_β at 486.1 nm and H_γ at 434.0 nm) and oxygen (O I triplet around 777.4 nm) in addition to a molecular band structure which could not be identified from literature but which is thought to arise from transitions between molecular energy levels in the (charged) TMP molecule and/or fragments of it.

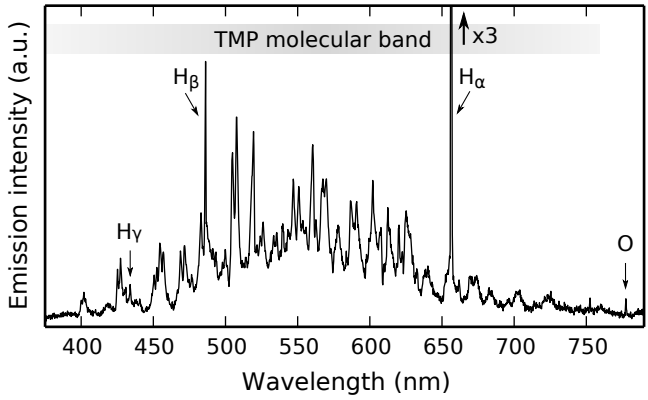

Figure 3.3: The optical emission spectrum of a 100W inductively coupled TMP plasma between 375 nm and 790 nm. Hydrogen and oxygen atomic emission lines are superimposed on the molecular band spectrum.

To further investigate what makes up this plasma, the mass spectra of TMP vapor and TMP plasma were compared. The results are shown in

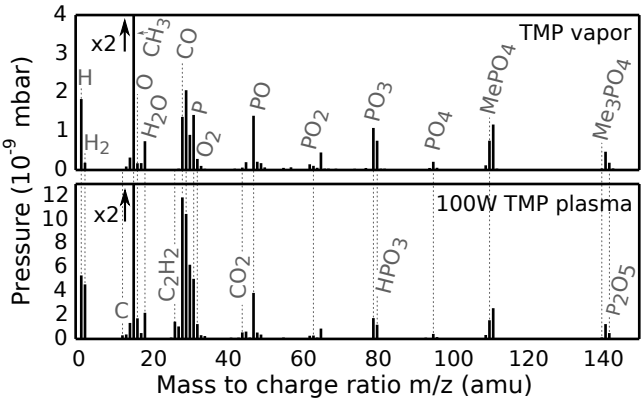

Figure 3.4: Mass spectra of TMP vapor (upper graph) and TMP plasma (lower graph) between 1 and 150 amu. Selected peaks are labeled with their corresponding fragment structures.

figure 3.4. While the spectrometer measured masses between 1 and 300 atomic mass units (amu), figure 3.4 only shows masses up to 150 amu because no heavier species were detected.

The upper and lower graphs are largely identical; even as vapor, TMP is broken up into many fragments by electron impact ionization in the spectrometer. One could expect the plasma to do the same thing, but it is not possible to distinguish this from fragmentation in the instrument. However, upon close inspection, some differences due to the plasma are visible. Most notable is the formation of H_2 (hydrogen gas), witnessed by a significant increase at $m/z = 2$. This is obviously related to the strong hydrogen emission lines in OES. Other appearances include elemental carbon at $m/z = 12$, C_2H_2 (acetylene) at $m/z = 26$, C_2H_3 at $m/z = 27$ and CO_2 at $m/z = 44$. The increase at $m/z = 16$ could be attributed to contributions from either atomic oxygen or CH_4 (methane), but the presence of the atomic oxygen emission line in the optical spectrum makes the former option the most likely one.

3.4.2 *TMP plasma polymerization*

It was observed that material got deposited onto substrates by exposure to this remote TMP plasma. Figure 3.5 shows the result of exposing a substrate to a sequence of TMP plasma pulses at different temperatures while monitoring the growth using in-situ ellipsometry. The Cauchy dispersion relation for these layers was $n(\lambda) = 1.454 + 5.30 \times 10^{-3}\,\mu m^2/\lambda^2 - 7.82 \times 10^{-5}\,\mu m^4/\lambda^4$, yielding a refractive index of 1.47 at a wavelength of 589 nm.

Two pulse lengths had been chosen, namely 3 s and 10 s. At low temperatures, a large amount of material was deposited, and the amount increased with the TMP plasma pulse length. This suggests a continuous, CVD-like deposition process. However, at higher temperatures, the deposition rate dropped spectacularly and the process was almost totally inhibited.

The formation of a solid deposit by a plasma discharge is generally known as plasma polymerization. The growth rates of such processes often show a strong temperature dependency. In particular, the growth rate vs. temperature plot of the plasma polymerization of tetrafluoroethylene[74] looks very similar to the curve in figure 3.5. This can be understood from thermodynamic arguments: whether the polymerization reaction proceeds is determined by the change in Gibbs free energy $\Delta G = \Delta H - T\Delta S$, where ΔH represents the reaction enthalpy and ΔS the change in entropy. The reaction will only proceed if $\Delta G < 0$. As $\Delta H < 0$ (the formation of new chemical bonds in the solid deposit is energetically favorable) but also $\Delta S < 0$ (the gas $\rightarrow$ solid transition results in increased order and thus decreased entropy), $\Delta G < 0$ for sufficiently small T. However, as ΔG increases with temperature, there will be a temperature above which $\Delta G > 0$ and the polymerization reaction no longer takes place. In other words, there is a ceiling temperature above which the polymerization reaction is inhibited. Another piece of evidence to support our argument is the

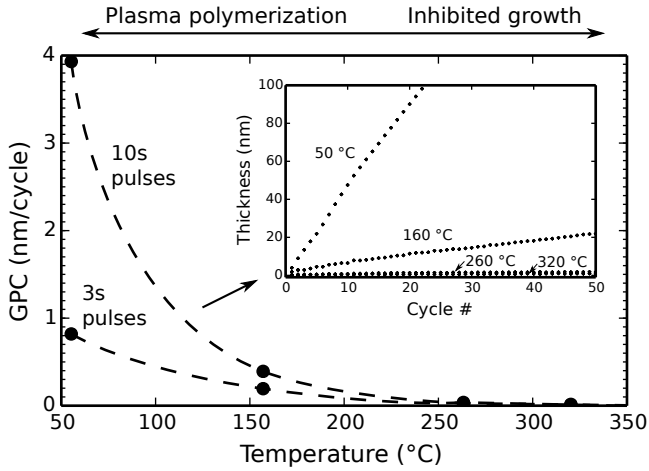

Figure 3.5: The growth per cycle as a function of the deposition temperature for sequences consisting of 3 s and 10 s TMP plasma pulses. Inset: growth curves measured by in-situ ellipsometry for 10 s TMP plasma pulses, showing linear growth.

formation of hydrogen gas in the plasma by the release of hydrogen from C−H bonds, in this case witnessed by mass spectrometry and OES, and as frequently encountered in the plasma polymerization of hydrocarbons.[74] We therefore identify this process step as the plasma polymerization of TMP, with a ceiling temperature in the vicinity of 300 °C.

The chemical nature of the deposited layer was further investigated by in-situ FTIR as shown in figure 3.6. For reference purposes, the absorption spectrum of TMP vapor was separately measured and included in the same figure. In this spectrum, peaks at 2960, 2860 and 2350 cm^{-1} can be attributed to various C−H stretching vibrations of methyl groups in the TMP molecule, while a P=O stretch can be identified around 1300 cm^{-1}, a CH_3 rocking vibration at 1190 cm^{-1}, a (P)−O−C stretch at 1060 cm^{-1}, and a P−O−(C) stretch at 850 cm^{-1}.[75, 76] During deposition, absorption spectra of the deposited material were measured in-situ at a substrate temperature of 150 °C; the sample was exposed to TMP plasma for 120 s between two consecutive measurements. The infrared absorbance grows progressively stronger over time, which is in agreement with the linear growth evidenced earlier by in-situ ellipsometry, confirming the continuous deposition of material at this temperature. Several absorption peaks coincide with the TMP vapor reference spectrum, which suggests that the solid deposit is chemically similar to TMP. However, the peaks are heavily broadened, and in particular a new structure consisting of three very broad bands around 2700 cm^{-1}, 2200 cm^{-1} and 1600 cm^{-1} can be observed. This is a so-called ABC structure, which typically arises from O−H stretching vibrations in strongly hydrogen bonded complexes; in particular, the

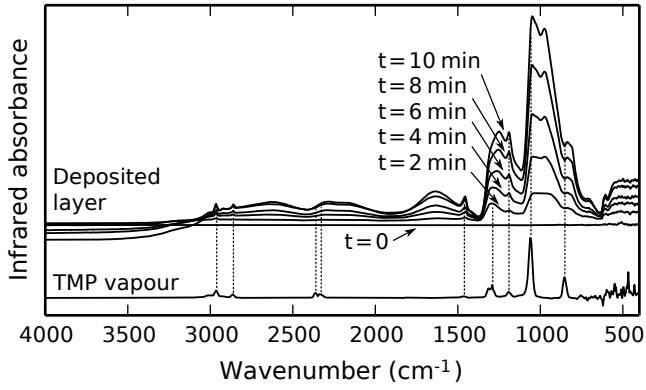

Figure 3.6: In-situ FTIR during TMP plasma polymerization at a substrate temperature of 150 °C, along with the absorption spectrum of TMP vapor.

observed O−H band structure is very similar to the one encountered for dimethylphosphinic acid ($(CH_3)_2POOH$) in the solid state.[77] This implies that some of the $-O-CH_3$ groups in the TMP precursor are being converted to $-OH$ groups during the plasma polymerization process, and the resulting deposited layers are presumably mixtures of phosphate esters.

The layers resulting from TMP plasma polymerization completely covered the surface when inspected immediately after removal from the reactor, but film degradation became visible after a few hours of exposure to an ambient atmosphere. This suggests a reaction of the deposited material with ambient oxygen and/or water vapor. After a few weeks, some samples started to show fractal-like dendritic structures. This reactivity might be related to the high amount of free radicals which are typically embedded in plasma-polymerized films.[74]

3.4.3 *Further oxidation by O_2 plasma*

Freshly deposited samples were brought into a scanning electron microscope for EDX analysis. The results are shown in figure 3.7. Layers deposited by the TMP plasma contained oxygen, phosphorus and carbon, as shown by curve (a); we can thus refer to them as organophosphate coatings. When one wants to grow metal phosphates, however, carbon

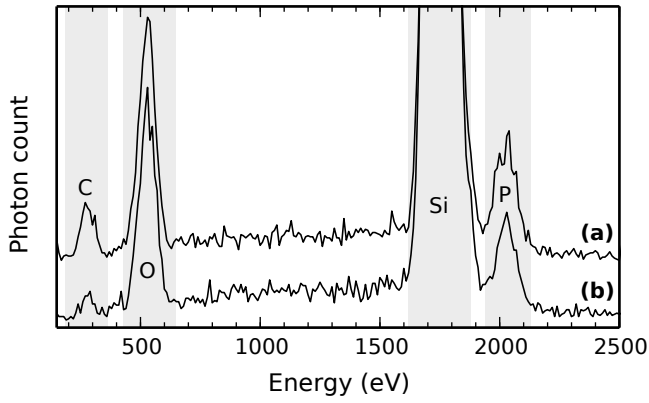

Figure 3.7: Energy-dispersive X-ray spectroscopy of phosphate films grown on silicon substrates by TMP plasma polymerization at 150 °C. Peaks at the characteristic X-ray K-lines of C, O, Si and P are indicated. Curve (a) corresponds to a layer grown by 400 cycles of 3 s TMP plasma, while curve (b) is the result of $400 \times$ [3 s TMP plasma - 3 s O_2 plasma] and contains a significantly lower amount of carbon.

is an undesirable contaminant in the final layer. An additional oxygen plasma exposure was therefore introduced after each TMP plasma step in order to remove carbon by combustion. The effectiveness of this step is illustrated by curve (b) in figure 3.7, which shows that the amounts of phosphorus and oxygen remain the same but the amount of carbon is significantly reduced. The oxygen plasma presumably converts remaining $-O-CH_3$ groups in the phosphate deposit into $-OH$ groups, transforming dimethylphosphinic acid into methylphosphinic acid or possibly phosphoric acid. As many metal precursors (e.g. TMA) need $-OH$ groups to chemisorb on, this not only removes unwanted carbon but also enhances the reaction of the organophosphate layer with a metal precursor to form a metal phosphate. In other words, a phosphorus source is formed "in-situ" on the sample surface, ready to accept a metal source.

3.4.4 *Growth of aluminium phosphate*

In what follows, we will focus on a three-step process to grow aluminium phosphate by combining TMP plasma and O_2 plasma with a third step in the form of a TMA exposure. As opposed to the films deposited by TMP plasma or TMP/O_2 plasma alone, which degraded after removal

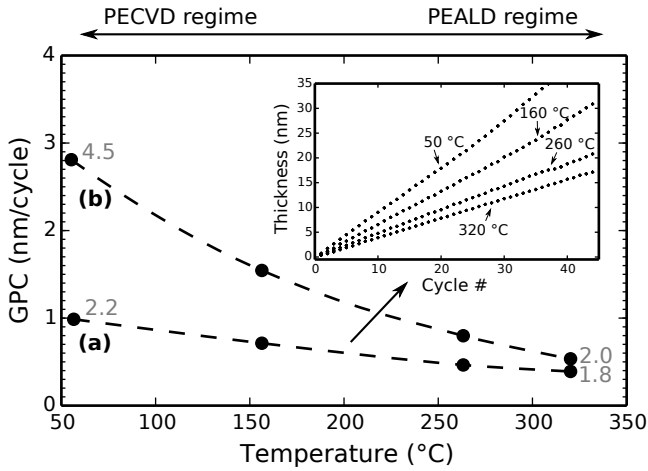

Figure 3.8: The growth per cycle as a function of the deposition temperature for two sequences: (a) [3 s TMP plasma - 3 s O_2 plasma - 3 s TMA] and (b) [10 s TMP plasma - 3 s O_2 plasma - 3 s TMA]. Inset: growth curves measured by in-situ ellipsometry for (a), showing linear growth (similar for (b)). Numbers in gray represent the P/Al ratios of certain samples determined from XPS analysis.

from the reactor, the [TMP plasma - O_2 plasma - TMA] process resulted in the growth of aluminium phosphate films which remained stable in an ambient atmosphere.

Figure 3.8 shows the growth per cycle of this process as a function of the deposition temperature. It can be compared to figure 3.5, the only difference being the inclusion of an O_2 plasma and TMA pulse after each TMP plasma pulse. The TMP plasma pulse durations were set to 3 s for curve (a) and 10 s for curve (b), while the O_2 plasma pulse and TMA pulse durations were fixed to 3 s each in both cases. GPC values were determined from the slopes of in-situ ellipsometry growth curves, as shown in the inset of figure 3.8. All layers satisfied a single Cauchy dispersion relation $n(\lambda) = 1.511 + 3.00 \times 10^{-3}\,\mu m^2/\lambda^2 + 5.50 \times 10^{-5}\,\mu m^4/\lambda^4$, which yields a refractive index of 1.52 at a wavelength of 589 nm. At low temperatures ($< 100\ ^\circ C$), curve (b) shows a significantly higher GPC than curve (a). This should not come as a surprise: at low temperatures, TMP plasma polymerizes at a high rate, and extending the pulse duration significantly increases the total amount of deposited material (i.e. the GPC) and also the P/Al ratio (numbers in gray). At the high-temperature side ($> 300\ ^\circ C$), however, something remarkable happens: material still gets deposited at a rate of 0.4 to 0.5 nm/cycle, even though the polymerization of TMP plasma is inhibited (as seen in figure 3.5). Additionally, the GPC of curve (b) is only slightly higher than for curve (a), despite the three-fold increase in TMP plasma duration, and the P/Al ratios are similar. We are lead to the conclusion that this process must be split up in two regimes: a low-temperature regime characterized by continuous and unsaturated growth (plasma-enhanced CVD), and a high-temperature regime characterized by saturated growth where individual TMP plasma pulses do not result in deposition but sequential exposures with O_2 plasma and TMA vapor do. We therefore regard this high-temperature regime as plasma-enhanced ALD. The fact that TMP polymerization is no longer temperature-inhibited when TMA pulses are included might be caused by an increased tendency to form chemical bonds on the surface, i.e. the reaction enthalpy is more negative by the presence of TMA on the sample surface, which shifts the ceiling temperature upwards.

The influence of the TMA pulse duration on the GPC was investigated for the same process in both low-temperature (PECVD) and high-temperature (PEALD) regimes. The results are shown in figure 3.9. The GPC does not depend on the TMA pulse duration if the duration is 1 s or longer, and this holds for both regimes, although with very different values. In the low-temperature regime, the saturated GPC value (i.e. for $\geq$1 s TMA) is about 2.8 nm/cycle and the one for 0 s TMA (i.e. for the [TMP plasma -

O_2 plasma] process) is even higher than that. This might be because the aluminium-containing layers are denser and thus have a lower thickness for the same amount of material. In the high-temperature regime, the GPC is close to zero in the absence of TMA pulses (as previously discussed) and assumes a value of 0.55 nm/cycle for TMA durations of 1 s or longer. Additionally, P/Al ratios derived from XPS analysis are independent of the TMA pulse duration. These observations suggest saturation during the TMA exposure step.

3.4.5 *Unraveling the reaction mechanism*

In order to better understand how this deposition process works, the reaction products were analyzed by multiple ion detection mass spectrometry. In figure 3.10, two species were monitored: PO at $m/z = 47$ (a fragment of TMP, as can be seen in figure 3.4, chosen to track the TMP pulses) and CH_4/oxygen at $m/z = 16$ (chosen because methane is released when TMA reacts with hydroxyl surface groups). The substrate temperature was set to 150 °C. However, as the reaction products may originate from all over the deposition chamber and the chamber walls comprise most of the inner surface area, we assume that the reaction products mainly originate from deposition on the chamber walls at a temperature of 95 °C. In both cases, the reactions happen in the PECVD temperature regime.

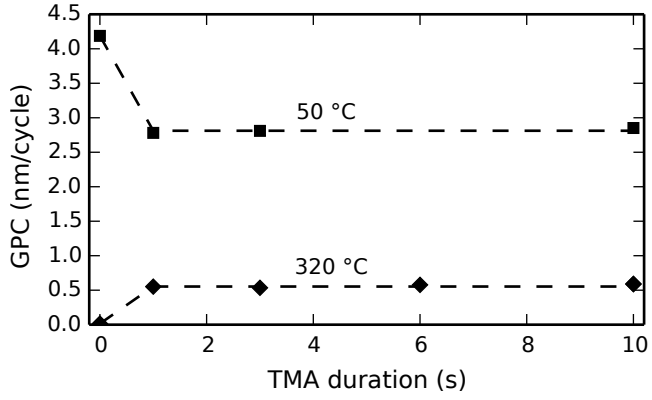

Figure 3.9: Growth per cycle of the [TMP plasma - O_2 plasma - TMA] process as a function of the TMA pulse duration, showing saturated behavior in both the PECVD temperature regime (50 °C, upper curve) and the PEALD regime (320 °C, lower curve). The TMP plasma and O_2 plasma pulse times were fixed to resp. 10 s and 3 s.

In figure 3.10a, the [TMP plasma - O_2 plasma - TMA] process was studied. During the TMP plasma discharge, both PO and oxygen were present, as previously discussed and shown in figure 3.4. During the subsequent oxygen plasma step, only oxygen was visible. When TMA was introduced, a sharp spike in the channel at $m/z = 16$ was observed. This signal is very similar to what is observed in the well-known TMA-water process (figure 3.10f) where Al_2O_3 is grown and CH_4 is produced as a reaction product. This provides experimental evidence that TMA reacts with $-OH$ groups in the organophosphate layer created by the TMP and O_2 plasma exposures and forms CH_4 as a byproduct:

$$-OH + Al(CH_3)_3 \longrightarrow -O-Al(CH_3)_2 + CH_4$$

In figure 3.10b, the oxygen plasma step was skipped, resulting in a [TMP plasma - TMA] process. The CH_4 spike while pulsing TMA is still present,

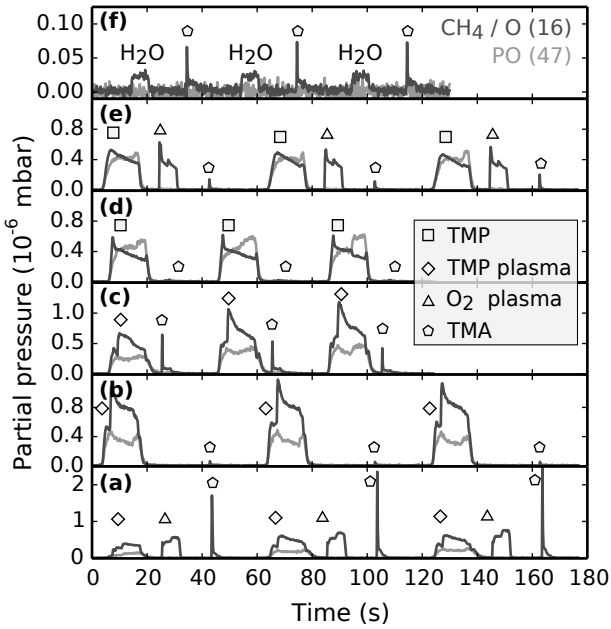

Figure 3.10: Multiple ion detection mass spectrometry during five different variations on the [TMP plasma - O_2 plasma - TMA] process (a–e) and one standard [TMA - H_2O] process for reference purposes (f). Dark gray: CH_4/oxygen signal at $m/z = 16$. Light gray: PO signal (TMP fragment) at $m/z = 47$.

but is much lower in magnitude. However, as can be seen in figure 3.10c, when TMA is pulsed immediately after the TMP plasma, the spike increases in magnitude again. This might indicate dehydration of the organophosphate layer over time. In figure 3.10d, TMP vapor was used instead of TMP plasma; no methane spike was visible, supporting our observation that the [TMP vapor - TMA] process does not grow anything due to lack of a chemical reaction. However, by adding an intermediate oxygen plasma, as was done in figure 3.10e, a (weak) methane spike is again observed; this process resembles the one by Liu et al[15] and grows material very slowly.

Figure 3.11 focuses on the [TMP plasma - O_2 plasma - TMA] process as in figure 3.10a but provides additional channels. Figure 3.11a is identical to figure 3.10a but is repeated for comparison purposes. Figure 3.11b shows CH_3 at $m/z = 15$, which is prominent during the TMP plasma (as can be seen in figure 3.4) and spikes simultaneously with the methane channel. A weak signal can also be observed during the oxygen plasma pulse; this is probably the result of instrumental bleed from the adjacent oxygen channel. Figures 3.11c and 3.11d respectively show CO_2 at $m/z = 44$ and H_2O at $m/z = 18$. Both of them are formed during the TMP plasma (as

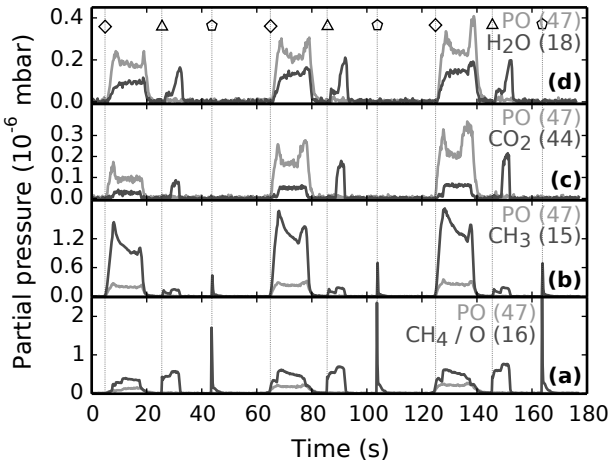

Figure 3.11: Multiple ion detection mass spectrometry of the [TMP plasma - O_2 plasma - TMA] process (designated by resp. diamonds, triangles and pentagons, same as in figure 3.10a), monitoring additional species. The PO signal (TMP fragment) at $m/z = 47$ is shown throughout, in addition to (a) CH_4/oxygen at $m/z = 16$ (same as fig. 3.10a), (b) CH_3 at $m/z = 15$, (c) CO_2 at $m/z = 44$ and (d) H_2O at $m/z = 18$.

previously noted) and during the oxygen plasma, while they are absent during the TMA pulse. Their presence during the oxygen plasma, coupled with the observation that the amount of carbon in the organophosphate layers is reduced, suggests that the O_2 plasma removes methyl ligands in the organophosphate layer by a combustion reaction:

$$-O-CH_3 + 3\,O\cdot \longrightarrow -OH + CO_2 + H_2O$$

The surface chemistry during the [TMP plasma - O_2 plasma - TMA] process was also investigated by in-situ infrared spectroscopy. The substrate temperature was held at 150 °C; spectra were acquired after each substep, and this was repeated during 50 cycles. The results are shown in figure 3.12, wherein the total absorption spectrum of the deposited film is plotted along with difference spectra after each substep. Each difference spectrum was averaged over 50 cycles in order to minimize noise contributions. The absorption spectrum equals the sum of the three difference spectra, as the absorption of the substrate was already subtracted.

The difference spectrum after the TMP plasma shows a C−H stretch at 2960 cm^{-1}, P=O stretching vibrations around 1300 cm^{-1}, P−O stretching vibrations around 1050 cm^{-1} and O−P−O bending vibrations around 600 cm^{-1}.[12, 72, 78, 79] This demonstrates the formation of (poly)phosphate groups by exposure to the TMP plasma. The O_2 plasma difference spec-

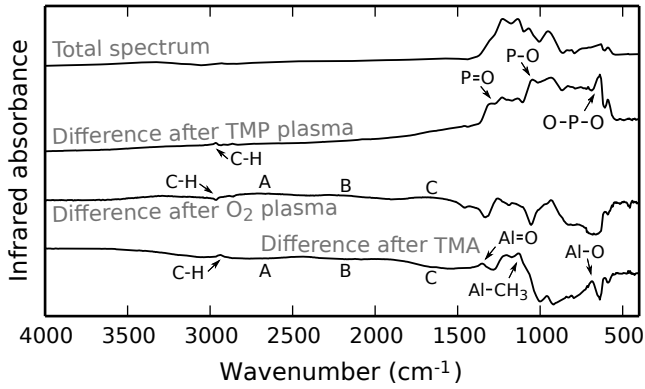

Figure 3.12: In-situ infrared spectroscopy during the [TMP plasma - O_2 plasma - TMA] process at 150 °C. The upper curve shows the infrared absorption spectrum of the aluminium phosphate film after 50 cycles. The three curves below it are difference spectra after each substep, each one averaged over 50 cycles to improve the signal/noise ratio.

trum shows a small valley at the exact location of the TMP plasma C−H stretch, implying the removal of methyl groups. Additionally, the ABC-type band structure characteristic for O−H bonds and previously seen in figure 3.6 (weakly) appears again. This confirms the idea of a combustion-type reaction in which the O_2 plasma removes carbon from the surface by converting methyl groups into hydroxyl groups, releasing CO_2 and H_2O as reaction products. The region between 1500 and 500 cm^{-1} shows a number of valleys; these are supposedly also related to the removal of carbon-containing bonds, although their exact attribution is unclear. The difference spectrum associated with the TMA pulse shows a "mirror image" of the aforementioned ABC structure (valleys instead of bumps), showing the removal of O−H by reaction with TMA, and a C−H stretch at 2940 cm^{-1} due to the methyl ligands which remain around each aluminium atom. Additionally, Al=O and Al−O stretch bands[80] could be identified at resp. 1350 cm^{-1} and 700 cm^{-1}.

To summarize, the information above leads us to the following picture of the deposition process (illustrated graphically in figure 3.13):

1. Through plasma polymerization of the TMP precursor, a surface organophosphate layer is grown, its chemical structure being similar to TMP albeit with some methyl groups getting replaced by hydroxyl groups.
2. By exposure to O_2 plasma, additional methyl groups in the surface layer are replaced by hydroxyl groups. The resulting chemical struc-

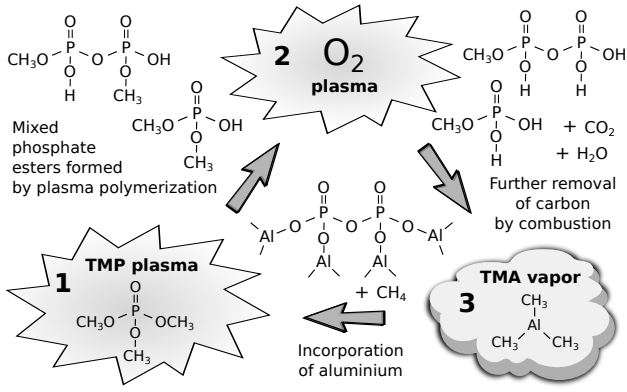

Figure 3.13: Schematic overview of the aluminium phosphate deposition process studied in this work, and the proposed chemical mechanism behind it.

ture is presumably more similar to phosphoric acid than to the original TMP molecule. One could state that the plasma induces the in-situ synthesis of a suitable phosphorus precursor on the substrate surface, thereby circumventing the impossibility of bringing phosphoric acid into the vapor phase.

3. TMA now chemisorbs on the surface because its methyl ligands react with hydroxyl groups, creating Al−O bonds and resulting in the formation of aluminium phosphate.

3.4.6 *PEALD film properties*

Films were deposited at 320 °C using the [TMP plasma - O_2 plasma - TMA] process with 3 s pulse times in order to characterize them by XPS, ERD and in-situ XRD.

The XPS analysis of an 18.5 nm aluminium phosphate film deposited under these conditions is shown in figure 3.14. The figure shows two survey spectra: the lower one (shown in light gray) was directly measured on the sample surface, while the upper one (shown in dark gray) was acquired after slightly sputtering away the surface (20 s at 3 keV and 2 μA). Both spectra show the presence of aluminium, oxygen and phosphorus. Coupled with the lack of a silicon substrate signal, this confirms the realization of an aluminium phosphate layer with complete surface coverage. Carbon could only be detected on the film surface, but not after sputter-

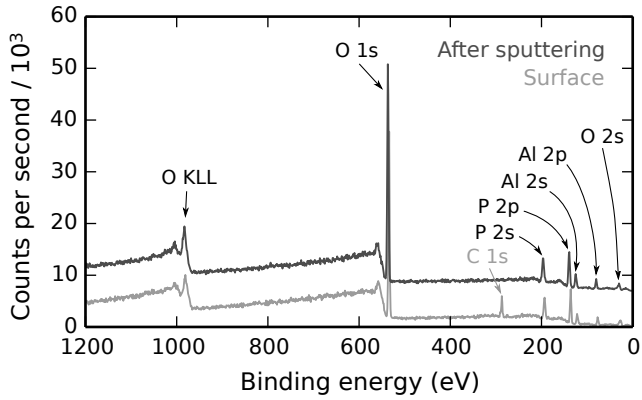

Figure 3.14: XPS survey spectrum of an 18.5 nm aluminium phosphate film grown at 320 °C for 50 cycles, indicating the presence of aluminium, oxygen and phosphorus throughout the film while carbon is only present on the surface.

ing; this suggests that the layer is free from carbon contamination, with the surface carbon originating from exposure of the sample to the ambient atmosphere.

High-resolution measurements of the Al 2p, P 2p, O 1s and C 1s surface regions were additionally made for quantification and chemical identification purposes. For each region, a Shirley-type background was subtracted and a Gaussian/Lorentzian peak shape was fitted. All peak locations were then shifted downwards by 2.7 eV to bring the adventitious carbon peak to its reference energy of 284.8 eV. The resulting peak locations are shown in table 3.2, along with the atomic percentages of Al, P, O and C. These were calculated from the surface areas under each peak, making use of tabulated sensitivity factors. A sample deposited under these conditions was also quantified by elastic recoil detection (ERD) analysis, of which the results are also shown in table 3.2. Finally, the theoretical amounts of aluminium, phosphorus, oxygen are included for two possible types of aluminium phosphate, namely aluminium orthophosphate ($AlPO_4$) and aluminium pyrophosphate ($Al_4P_6O_{21}$). The main difference between them is the P/Al ratio, which is unity in the former case and 1.5 in the latter.

The chemical shifts are in agreement with the ones expected for an aluminophosphate material.[81] The XPS surface measurement shows a considerable amount of carbon; after etching away some surface material, the remaining amount of carbon is below the detection limit of about 1%, the P/Al ratio is 1.8 and the atomic percentage of oxygen is 57%. The ERD analysis (which is more accurate, generally to within $\pm 1\%$) shows a P/Al

Table 3.2: XPS peak positions measured on the deposited aluminium phosphate film, together with theoretical and measured atomic percentages of aluminium, phosphorus, oxygen and carbon determined by XPS and ERD.

Peak position (eV)	Al 2p	P 2p	O 1s	C 1s
	74.4	133.9	531.6	284.8
Material	% Al	% P	% O	% C
$AlPO_4$	16.7	16.7	66.7	0
$Al_4P_6O_{21}$	12.9	19.4	67.7	0
Measurement	% Al	% P	% O	% C
XPS (surface)	11.8	23.0	50.0	15.3
XPS (sputtered)	15.5	27.5	57.0	< 1
ERD	11.3	20.2	67.8	2.2

ratio of 1.8, and 2.2% of carbon impurities. We conclude that this layer mainly consists of aluminium pyrophosphate, although still with some excess phosphorus.

A thick film (400 cycles, resulting in a layer thickness of about 150 nm) was grown to study its crystallinity by in-situ X-ray diffraction (XRD) during annealing in a helium atmosphere. Figure 3.15 shows the diffraction pattern (color mapping: higher intensities are lighter) and the temperature (dashed white line) as a function of time during a linear ramp up to 1050 °C at 12 °C/min. The material starts off amorphous, but three distinct diffraction peaks appear when the temperature approaches 900 °C. These are more easily visible in figure 3.16, where the XRD patterns before and after annealing have been plotted in a more conventional way. The observed diffraction pattern after crystallization corresponds to triclinic $AlPO_4$ tridymite.[82]

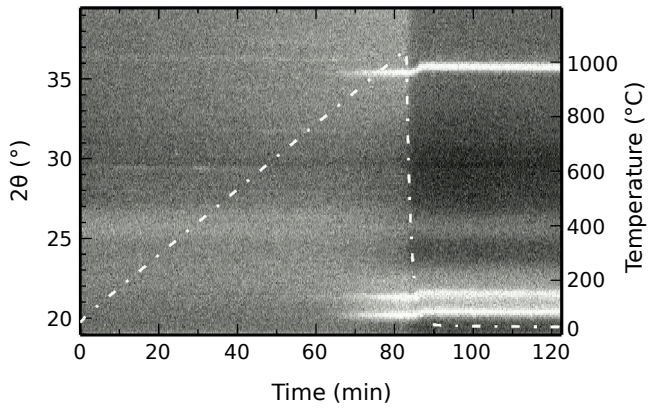

Figure 3.15: In-situ XRD measurement of the aluminium phosphate film while applying a linear temperature ramp from room temperature to 1050 °C at 12 °C/min in a He atmosphere. The as-deposited material is amorphous, but becomes crystalline upon heating to around 900 °C.

3.5 CONCLUSIONS

We demonstrated the layer-by-layer growth of aluminium phosphate by exploiting the polymerization properties of an inductively coupled trimethyl phosphate plasma. The plasma was shown to contain excited hydrogen and oxygen atoms and produced hydrogen gas in addition to hydrocarbons, oxygen and CO_2, indicating that chemical bonds in the TMP molecule were being broken and reconfigured. At low temperatures,

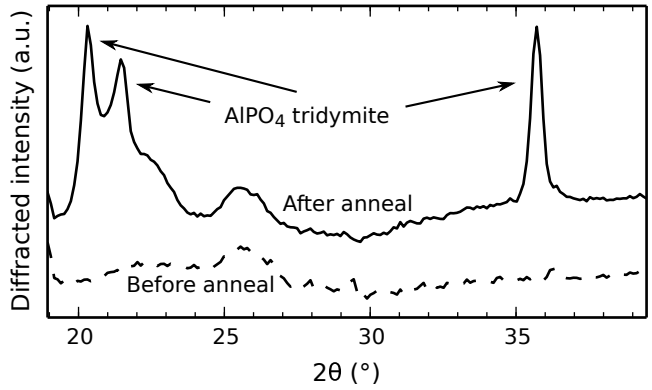

Figure 3.16: XRD patterns measured at room temperature before and after annealing for the same aluminium phosphate film as in figure 3.15. The pattern before annealing only shows an amorphous background, while the one after annealing shows clear diffraction peaks corresponding to triclinic $AlPO_4$ tridymite.

the TMP plasma polymerized at a high rate and continuously grew an organophosphate layer; at temperatures above 300 °C, this process was inhibited. The addition of subsequent O_2 plasma and TMA pulses resulted in the growth of aluminium phosphate, likewise showing a strong temperature dependency. We distinguished a low-temperature PECVD regime, where the growth per cycle and the P/Al ratio increased with the TMP plasma duration, and a high-temperature PEALD regime, where they saturated. The TMP plasma and O_2 plasma steps resulted in the formation of a phosphorus-containing surface which contained hydroxyl groups and readily reacted with an organometallic precursor such as TMA to form aluminium-oxygen bonds. Saturation with regard to the TMA exposure was found in both temperature regimes, backed by the observation of short CH_4 spikes when TMA was pulsed. The resulting films consisted of slightly phosphorus-rich aluminium pyrophosphate; crystalline aluminium orthophosphate was formed by annealing above 900 °C.

4

PAPER II: ZINC PHOSPHATE

The following chapter has been published as an original research paper in the Journal of Non-Crystalline Solids, titled *"Plasma-enhanced atomic layer deposition of zinc phosphate"*.[31] The content below has been reformatted to fit the layout of this PhD thesis, but is otherwise identical to the published version.

4.1 ABSTRACT

Zinc phosphate thin films were grown by plasma-enhanced atomic layer deposition (ALD) using a sequence of trimethyl phosphate (TMP, Me_3PO_4) plasma, O_2 plasma, and diethylzinc (DEZn, Et_2Zn) exposures. The film growth was monitored by in-situ spectroscopic ellipsometry. At a substrate temperature of 300 °C, linear and saturated growth was observed with a remarkably high growth rate of 0.92 nm/cycle. As-deposited films were smooth, amorphous and very hygroscopic, suggesting a phosphorus-rich composition resembling zinc phosphate glass. Upon annealing in air, crystalline zinc phosphate and pyrophosphate phases were formed.

4.2 INTRODUCTION

4.2.1 *Atomic layer deposition*

Atomic layer deposition (ALD) is a thin-film deposition method in which material is grown in a layer-by-layer fashion by alternating exposures to chemical vapors. In contrast to chemical vapor deposition (CVD), the precursors are introduced separately, with pumping or purging steps in between. This causes self-limiting reactions to take place on the substrate surface, resulting in slow but precisely controlled film growth. Many ALD processes exist for oxides, II-VI and III-V semiconductors, metal nitrides, metals, metal sulfides, and fluorides.[65] ALD of phosphates has been reported for aluminium phosphate,[12–15, 26, 30] calcium phosphate,[17] titanium phosphate,[14, 16] lanthanum phosphate,[21] lithium phosphate,[19, 20] iron phosphate,[22, 23] and lithium iron phosphate.[24] The phosphorus precursor is almost always trimethyl phosphate (TMP) because it is a

stable liquid with a suitable vapor pressure. Its high stability, however, also limits its use as an ALD reactant, often resulting in very slow growth or difficulty in incorporating sufficient amounts of phosphorus into the film.

We previously reported a novel plasma-enhanced atomic layer deposition (PEALD) process for aluminium phosphate, which was based on the use of a TMP plasma instead of vapor.[30] By studying the reaction mechanism using in-situ techniques, we concluded that the combined action of TMP plasma with O_2 plasma created phosphoric acid-like precursor species on the substrate surface, which subsequently reacted with trimethylaluminium (TMA) to produce aluminium phosphate. We further hypothesized that the same process could be used to grow other phosphates by swapping TMA with a different metal precursor. In this work, diethylzinc (DEZn) was used as the metal precursor, and this resulted in the plasma-enhanced atomic layer deposition of zinc phosphate.

4.2.2 *Zinc phosphate*

ALD growth of zinc oxide is a well-known process that is typically achieved by combining diethylzinc with a reactant such as water vapor,[83, 84] ozone,[85, 86] or oxygen plasma.[87, 88] Phosphorus has been incorporated into ALD-grown ZnO as a p-type dopant [89, 90] in concentrations below 5 at.% and in the crystalline form (wurtzite structure). To the best of our knowledge, ALD of amorphous zinc phosphate has not been previously reported. Amorphous (or "glassy") zinc phosphate is, however, an interesting material with applications in photonics (including femtosecond laser waveguide writing[91] and hosting luminescent ions[92]), in glass-metal sealing, and in glass-polymer composites.[93] Its glass properties can be tuned by adding e.g. aluminium oxide and varying the Al/Zn and/or P/O ratios,[94] for which ALD could be a very suitable technique.

4.3 EXPERIMENTAL

4.3.1 *Deposition system*

Depositions were carried out in a home-built pump-type PEALD reactor, shown schematically in figure 4.1. All parts were stainless steel, unless otherwise specified. The deposition chamber was continuously evacuated by a turbomolecular pump to a base pressure of approx. 4×10^{-6} mbar. Precursor vapors and gases were admitted through computer-controlled pneumatic valves. The TMP precursor (Sigma-Aldrich, 97%) was heated

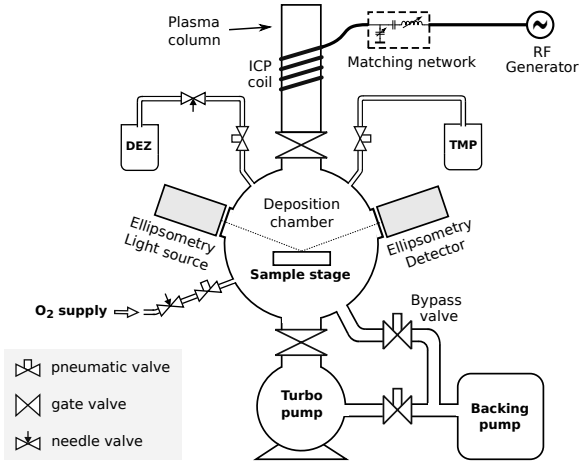

Figure 4.1: Schematic drawing of the deposition system used in this work, showing the vacuum chamber, precursor connections, and the plasma system.

to 45 °C. The DEZn precursor (Sigma-Aldrich) was used at room temperature, and its flow was regulated by a needle valve. The flows of DEZn and O_2 were adjusted to reach a pressure of 5×10^{-3} mbar in the deposition chamber. The temperature of the chamber walls was set to 100 °C, and all precursor tubes leading to the chamber were additionally heated to prevent any precursor condensation. On top of the chamber, a gate valve lead to a fused quartz column wrapped by a copper coil. The coil was connected to a 13.56 MHz RF generator (ENI GHW-12Z) and a matching network in order to generate an inductively coupled plasma in the column. The remote plasma was generated by feeding vapor or gas from the chamber to the plasma column through the gate valve and pulsing the RF generator. The plasma power was set to 200 W for the TMP plasma and 300 W for the O_2 plasma, and the impedance matching was tuned to minimize the reflected power on both. The substrates consisted of p-type silicon (100) wafer pieces and were mounted to a heated copper block with PID temperature control.

4.3.2 *Deposition process*

A single cycle of a typical deposition process consisted of: TMP plasma – pumping – O_2 plasma – pumping – DEZn exposure – pumping. All precursors were introduced into the chamber while it was continuously pumped, reaching a partial pressure of 5×10^{-3} mbar in the deposition

chamber. In between precursor pulses, pumping times of 20 s were found sufficient to bring residual pressures to below 4×10^{-5} mbar, thereby avoiding CVD side reactions.

4.3.3 *Material characterization*

In-situ spectroscopic ellipsometry measurements were performed with a J.A. Woollam M-2000 ellipsometer working in the ultraviolet-visible region and using the CompleteEASE software for fitting and data analysis. The optical model consisted of a silicon substrate covered by a single layer which satisfied a Cauchy dispersion relation. Measurements were acquired after each deposition cycle. Systematic parameters (angle offsets, window corrections) were fitted prior to deposition and then held fixed. The final thickness and the Cauchy parameters were fitted to the measurement acquired after the last cycle (i.e. after deposition). A growth curve was then obtained by fitting the thickness to each measurement, keeping all other parameters fixed.

An FEI Quanta 200 F scanning electron microscope was used for SEM imaging and energy-dispersive X-ray spectroscopy (EDX) analysis, using an electron beam energy of 5 keV. EDX spectra were acquired while scanning over an area of 500×500 µm during an acquisition time of 100 s. In-situ XRD during annealing was performed in a home-built setup.[95–97] The annealing atmosphere was ambient air; the XRD patterns were acquired using a Cu Kα X-ray source and a position sensitive detector. X-ray Photoelectron Spectroscopy (XPS) analysis was performed on a Thermo Scientific Theta Probe XPS instrument using Al Kα X-rays generated at 15 kV and 70 W and focused to a spot size of 0.3 mm by an MXR1 monochromator gun. The sample surface was etched by Ar^+ ions at an acceleration voltage of 3 keV and a current of 2 µA. Atomic Force Microscopy (AFM) was performed using an Omicron VT XA AFM system operating in non-contact mode, with a base pressure of 10^{-10} mbar.

4.4 RESULTS AND DISCUSSION

4.4.1 *Hygroscopicity*

The deposited zinc phosphate layers were very hygroscopic: upon removal from the deposition system and exposure to ambient air, the thin films gradually changed color, and eventually (in the course of a few days) became non-uniform and irregular in appearance. Furthermore, the film color changed immediately by simply exhaling on it, indicating rapid swelling due to the absorption of moisture. This complicated the analysis

of the samples, e.g. making it impossible to measure film thicknesses in a reproducible way by X-ray reflectometry due to uncontrollable humidity exposure which influences the layer thickness and/or density.

As the most common form of zinc phosphate, zinc orthophosphate ($Zn_3(PO_4)_2$), is not hygroscopic,[98] the deposited material must have a different composition. Hygroscopicity typically increases with phosphorus content, as the bridging oxygens between phosphorus atoms are highly susceptible to hydrolysis. In the case of zinc ultraphosphate, where the amount of P_2O_5 is bigger than the amount of ZnO, each phosphate group can bond with three other phosphate groups, and the resulting P−O bonds are particularly reactive with water.[99] We can therefore anticipate that the deposited material must be a phosphorus-rich form of zinc phosphate, likely in the metaphosphate to ultraphosphate category.

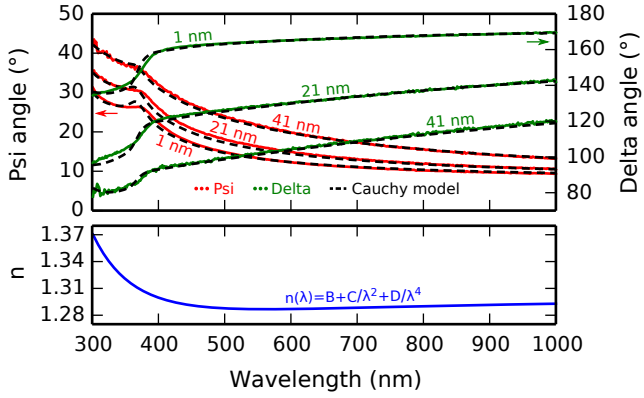

Figure 4.2: Upper part: the Psi and Delta angles measured by spectroscopic ellipsometry as a function of the wavelength between 300 nm and 1000 nm, shown at three different stages during layer growth, each one compared with the model fit. Lower part: plot of the fitted Cauchy dispersion relation, showing the refractive index of the deposited material as a function of the wavelength between 300 nm and 1000 nm.

4.4.2 *Optical model*

Due to the difficulty of accurate ex-situ characterization, the deposition process was completely characterized by in-situ spectroscopic ellipsometry, making it possible to measure the layer growth without breaking the vacuum. A well-fitting model of the optical properties of the deposited layer is a necessary requirement for this, and in this case a Cauchy dispersion relation of the form $n(\lambda) = B + C/\lambda^2 + D/\lambda^4$ was used. The

parameters were determined by least-squares fitting as $B = 1.30 \pm 0.01$; $C = (-0.0085 \pm 0.0014)\ \mu m^2$; and $D = (0.0013 \pm 0.0002)\ \mu m^4$. This dispersion relation is plotted in figure 4.2. The same figure also shows the evolution of the measured Psi and Delta angles during different stages of the layer growth, showing good correspondence with the calculated curves based on the aforementioned Cauchy model where the thickness was the only adjusted parameter. The measured refractive index of 1.29±0.01 (defined at a wavelength of 589 nm) is remarkably low; this might be related to the high phosphorus content of the deposited material, due to the low ionic refractivity of phosphorus.[100]

4.4.3 *Growth linearity*

Using this model, the layer thickness was determined after each cycle during a deposition consisting of 50 × [10 s TMP plasma – 5 s O_2 plasma – 5 s DEZn] at a substrate temperature of 300 °C, and the result is shown in figure 4.3. The growth curve is linear, aside from a small nucleation-type delay in the first five cycles, and its slope yields a growth per cycle (GPC) of 0.92±0.01 nm/cycle. This value is very high for (PE)ALD growth; most ALD processes have a GPC in the order of 0.1 nm/cycle.

4.4.4 *Saturation behavior*

The dependency of the GPC on the precursor exposure times was measured in-situ during three separate experiments, where in each deposition a single pulse time was varied while keeping the two others constant. For each pulse time, 20 cycles were deposited, and the GPC was determined from the slope of the growth curve at that point. For instance, to study the TMP plasma pulse time dependency, we used a sequence of 20 × [x s TMP plasma – 5 s O_2 plasma – 5 s DEZn] which was repeated for $x = 2$ s, 5 s, 10 s and 15 s to result in a total of 80 cycles. The resulting growth curve was split into four parts, and the GPC was given by the slope of each part. Analogous procedures were used for the O_2 plasma and DEZn pulse times. The pulse times that were not varied, were always fixed to 10 s for TMP plasma, 5 s for O_2 plasma, and 5 s for DEZn. The substrate temperature was always 300 °C. The results are shown in figure 4.4.

For all three precursor/plasma steps, saturative behavior is observed, and it can be seen that the pulse times chosen earlier for the linearity experiment were within the saturated region. This strongly suggests that we are dealing with ALD-type growth. The DEZn saturation curve shows that there is no deposition when the DEZn pulse is omitted (corresponding to the 0 s point), as expected for ALD growth. However, the O_2

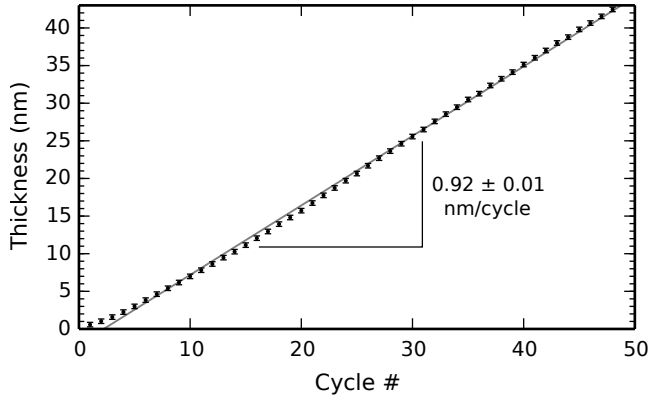

Figure 4.3: Growth curve measured by spectroscopic ellipsometry, showing the layer thickness as a function of the cycle number for a deposition consisting of 50 × [10 s TMP plasma – 5 s O_2 plasma – 5 s DEZn] at 300 °C. The error bars represent the standard errors on each thickness from least-squares fitting. A line was fitted to the data points by linear regression; the GPC is equal to the slope of the line, with its error given by the statistical error on the slope.

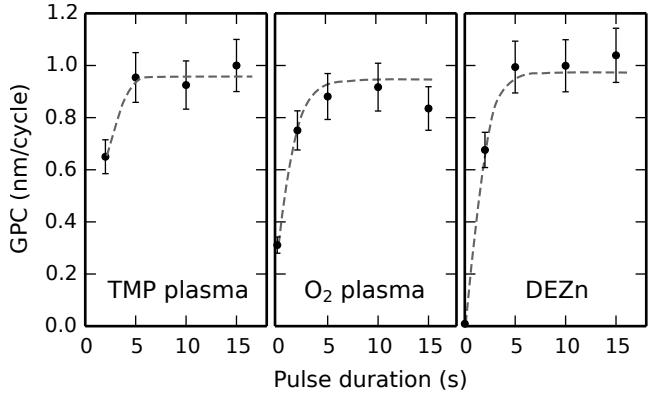

Figure 4.4: Saturation curves showing the GPC as a function of the precursor/plasma pulse durations at a substrate temperature of 300 °C. In each subplot, the indicated precursor/plasma pulse time was varied, and the two others were fixed. Clear saturative behavior can be observed in all three cases. The 10% error bars represent process variations as the main error source; the statistical fitting errors are negligibly small.

plasma saturation curve shows that there is still deposition without the O_2 plasma, i.e. using a [TMP plasma – DEZn] process. Earlier studies[30] have shown that this is possible, because the TMP plasma leaves surface species consisting of mixed $-OH/-CH_3$-terminated phosphoric acid esters; the $-OH$ terminations are reactive with DEZn, but the $-CH_3$ terminations are not. The oxygen plasma's function is to "combust" the $-CH_3$ groups in these surface species and convert them into $-OH$ terminations. This serves two purposes; firstly, it eliminates carbon impurities from the film; secondly, it increases the growth rate, because more DEZn can chemisorb. The O_2 plasma exposure saturates once all $-CH_3$ is converted into $-OH$.

4.4.5 *Temperature dependency*

In the closely related PEALD process for aluminium phosphate, the GPC was found to decrease with temperature.[30] This was caused by the continuous polymerization of TMP plasma at lower temperatures, resulting in fast and unsaturated growth. Only at sufficiently high temperatures (around 300 °C), the TMP plasma did not deposit material by itself, and ALD growth was achieved.

Using pulse times of 10 s TMP plasma, 5 s O_2 plasma, and 5 s DEZn, the temperature dependency of the zinc phosphate process was investigated

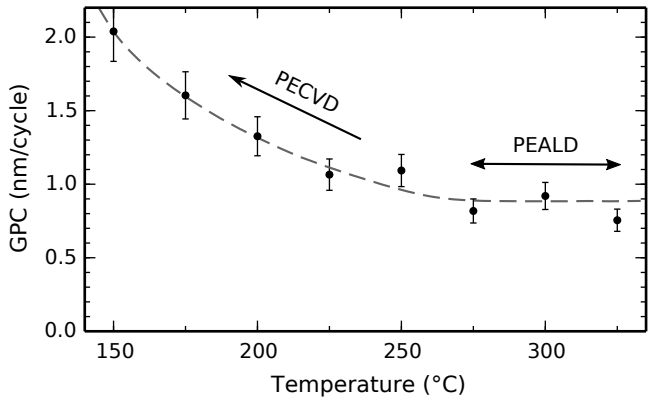

Figure 4.5: The GPC as a function of the substrate temperature between 150 °C and 325 °C, using fixed pulse times of 10 s TMP plasma, 5 s O_2 plasma, and 5 s DEZn. The 10% error bars represent typical process variations; the statistical fitting errors are negligibly small. At high temperature, in the PEALD region, the GPC curve is flat. When decreasing the temperature, the GPC increases due to the TMP plasma's increasing CVD contribution.

between 150 °C and 325 °C. 50-cycle depositions were carried out for each temperature, and the growth per cycle was extracted from ISE in the same way as for the previous experiments. The result is shown in figure 4.5. The GPC first decreases monotonously with temperature, and then levels off above 250 °C. This can be explained by the TMP plasma's CVD contribution (i.e. the plasma polymerization) which decreases with temperature and becomes negligible when reaching 300 °C, leaving only the ALD contribution.

4.4.6 *Elemental composition*

In order to measure the elemental composition of the deposited film, a deposition of 120 × [10 s TMP plasma – 5 s O_2 plasma – 5 s DEZn] at a substrate temperature of 300 °C was ran, and the resulting sample was quickly transferred to a scanning electron microscope. The acquired secondary electron image was entirely featureless, suggesting that the substrate was fully and uniformly covered by a flat coating. The EDX analysis is shown in figure 4.6. Characteristic X-ray lines of the expected elements in the coating (Zn, P, O) and the substrate (Si) are clearly visible, along with a small amount of residual carbon which barely protrudes from the background signal. A ZAF-corrected quantification of the atomic percentages of Zn, P, and O reveals an empirical stoichiometry of $ZnP_{2.3}O_{4.6}$ (with a relative accuracy of about ±10% due to uncertainties in X-ray absorption

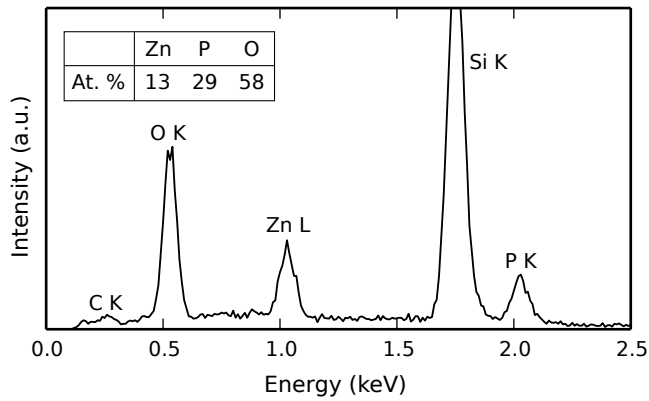

Figure 4.6: EDX analysis of the deposited zinc phosphate film. Elements are identified based on their characteristic X-ray emission energies, and quantified based on the surface area under each peak. The result of the quantification, expressed as atomic percentages, is shown in the upper left corner.

and scattering). The analysis was repeated for multiple spots on the sample surface and yielded the same elemental amounts, indicating a uniform stoichiometry.

The same sample was additionally analyzed by XPS, and the resulting spectra are shown in figure 4.7. In addition to a measurement of the as-deposited film surface, a second measurement was performed after sputtering away some of the surface material (30 s exposure to 3 keV Ar^+ ions at a beam current of 2 μA) in order to access the bulk composition. Zinc, phosphorus, and oxygen are detected in both cases, while carbon is only visible on the surface. The surface carbon originates from environmental contamination; the absence of a carbon signal after sputtering means that the deposition process itself leaves no detectable carbon residue in the film. The absence of a silicon signal in the survey spectra indicates that the substrate is fully covered by a pinhole-free film.

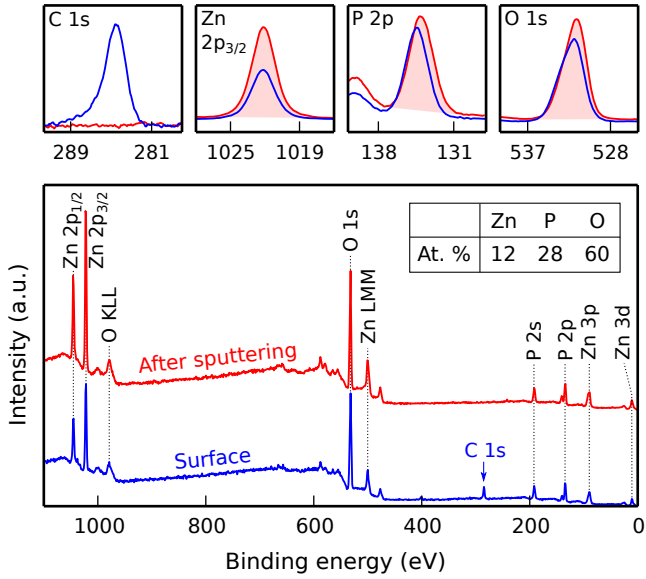

Figure 4.7: XPS analysis of the as-deposited zinc phosphate film, showing complete scans (lower part) and detailed regions (upper parts). Surface scans are shown in blue, while the material underneath (accessed by sputtering away the surface) is shown in red. The atomic percentages of Zn, P and O in the sputtered material are shown in the upper right corner; the quantification was made by integrating the peak areas shown in light red.

Using an energy scale calibration where the C 1s peak of the surface carbon is set to 284.5 eV (which was used for all the spectra shown in fig. 4.7), we get peak positions of 1022.2 eV for Zn $2p_{3/2}$, 134.2 eV for P 2p, and 531.7 eV for O 1s. These values are within ± 0.1 eV to the ones found in literature for zinc metaphosphate glass.[101] The detailed scans were also used for quantification by subtracting Shirley-type backgrounds and making use of tabulated sensitivity factors. This yields an empirical stoichiometry of $ZnP_{2.3}O_{5.0}$, which is (within the experimental error of $\pm 10\%$ due to uncertainties in the sensitivity factors of the elements) in agreement with the EDX analysis. The P/Zn ratio of 2.3 confirms that we have a very phosphorus-rich type of zinc phosphate which is mostly a metaphosphate (P/Zn= 2) with some ultraphosphate contribution.

4.4.7 *Surface topography*

In order to further characterize the film morphology, in addition to SEM, the as-deposited film was measured by AFM. Due to the hygroscopicity of the material, this was performed in a vacuum AFM system; the sample was quickly transferred between systems to minimize exposure to ambient air. A topographic image of the sample surface, scanned over an area of 500×500 nm, is shown in figure 4.8. Calculation of the RMS surface roughness yielded a value of 0.14 nm; together with the lack of any particular features in the image, we can conclude that the as-deposited film is very smooth and has a very low roughness.

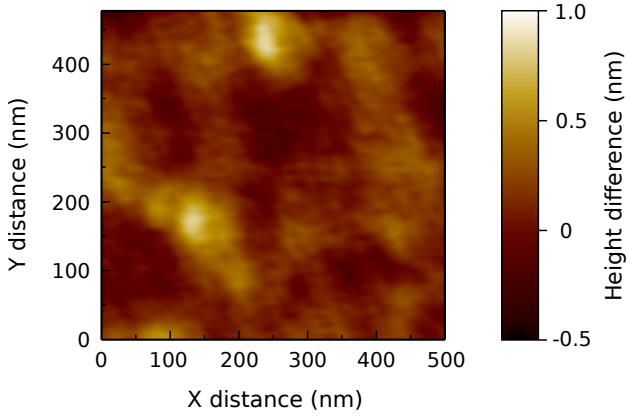

Figure 4.8: AFM topography image of the as-deposited zinc phosphate film, showing differences in height as a function of the position on the surface by means of the indicated color scale.

4.4.8 *Post-deposition annealing*

The crystallinity of the deposited material was investigated by in-situ X-ray diffraction during annealing in air. A deposition of 100 × [10 s TMP plasma – 5 s O_2 plasma – 5 s DEZn] at a substrate temperature of 300 °C was ran, and the resulting thin film was exposed to a temperature ramp from room temperature to 950 °C at a linear heating rate of 10 °C/min. Every 6 s, an XRD pattern was acquired.

The result can be seen in figure 4.9 in the form of a color plot, where diffraction peaks show up as colored horizontal bands. While the as-deposited material shows no diffraction peaks, indicating an amorphous phase, multiple phase transformations into crystalline forms happen at higher temperatures. In order to aid identification, the regions (phases) of interest in figure 4.9 were averaged and plotted in a more conventional way in figure 4.10. The identified crystalline phases are listed in table 4.1. The as-deposited material remains amorphous until a temperature of 670 °C is reached, at which point the Hopeite mineral structure ($Zn_3(PO_4)_2 \cdot 4H_2O$) is formed. Upon further heating, this structure subsequently transforms into several forms of zinc pyrophosphate ($Zn_2P_2O_7$) and upon cooldown after 950 °C has been reached, it remains in the form of β-$Zn_2P_2O_7$. For the α-$Zn_2P_2O_7$ and γ-$Zn_2P_2O_7$ phases, the observed high-temperature peak positions correspond to the room-temperature reference positions,

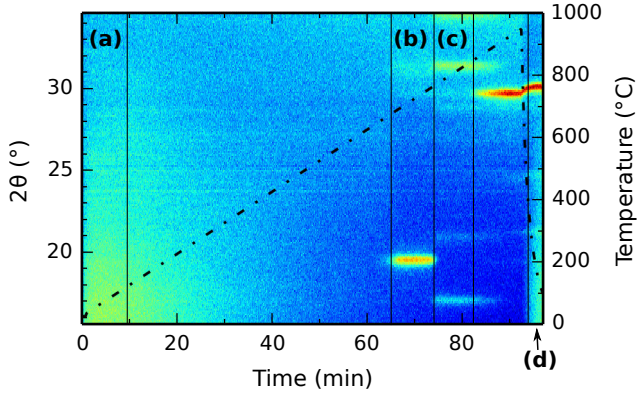

Figure 4.9: XRD pattern of the as-deposited film during annealing in air, from room temperature to 950 °C at a rate of 10 °C/min. The color map represents the diffracted X-ray intensity, while the dashed line shows the current temperature. Selected regions of interest have been indicated by the letters (a) to (d).

indicating that thermal expansion effects in the film are absent and are perhaps compensated by compressive strain from the substrate. For the γ-$Zn_2P_2O_7$ phase, however, a clear shift of the $(20\bar{1})$ reflection from 29.7° (above 870 °C) to 30.1° (after cooldown to room temperature) is observed, indicating thermal contraction.

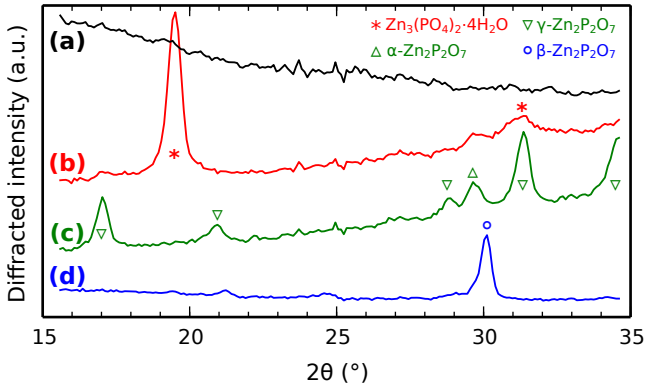

Figure 4.10: Four regions of interest from figure 4.9 averaged and plotted in a conventional way, with peak identifications provided for each pattern.

Table 4.1: Details of the crystalline phases which were observed during annealing of the zinc phosphate film at a rate of 10 °C/min. Listed transition temperatures are ±20 °C due to partial overlap between phases. Observed 2θ angles are ±0.1° due to peak broadening.

Region	Temperature	Phase	JCPDS #	(hkl)	2θ (ref.)	2θ (obs.)
(a)	R.T.→670 °C	Amorphous	–	–	–	
(b)	670→770 °C	$Zn_3(PO_4)_2 \cdot 4H_2O$	37-0465	(220), (040)	19.4°	19.5°
				(241), (151)	31.3°	31.2°
(c)	770→870 °C	α-$Zn_2P_2O_7$	08-0239	$(\bar{2}03)$	29.7°	29.7°
		γ-$Zn_2P_2O_7$	49-1240	(022)	17.0°	17.0°
				(102), (023)	20.9°	20.9°
				(114)	29.0°	28.9°
				(043)	31.4°	31.4°
				(044)	34.6°	34.6°
(d)	270 °C→R.T.	β-$Zn_2P_2O_7$	34-1275	$(20\bar{1})$	30.0°	30.1°

4.5 CONCLUSIONS

A PEALD process for zinc phosphate was successfully developed. The deposition process was fully characterized by in-situ spectroscopic ellipsometry. The results on growth linearity, saturation, and temperature dependency demonstrated the ALD nature of the process at 300 °C. Based on the deposited material's hygroscopicity, we proposed that the deposited film consisted of a phosphorus-rich type of zinc phosphate glass. This hypothesis was confirmed by EDX and XPS analysis, showing a P/Zn ratio of 2.3 which means that the material has a metaphosphate/ultraphosphate composition, and XRD, showing the as-deposited material as amorphous. The film surface was found to be very smooth; an RMS roughness of 0.14 nm was measured. The amorphous phase could be transformed into crystalline β-$Zn_2P_2O_7$ after annealing in air.

5

PAPER III: IRON PHOSPHATE

The following chapter has been published as an original research paper in Chemistry of Materials, titled *"Plasma-Enhanced Atomic Layer Deposition of Iron Phosphate as a Positive Electrode for 3D Lithium-Ion Microbatteries"*.[32] The content below has been reformatted to fit the layout of this PhD thesis, but is otherwise identical to the published version.

5.1 ABSTRACT

A new plasma-enhanced atomic layer deposition process was developed to deposit iron phosphate by using a sequence of trimethyl phosphate (TMP, Me_3PO_4) plasma, O_2 plasma and tert-Butylferrocene (TBF, $Fe(C_5H_5)$-$(C_5H_4C(CH_3)_3)$) exposures. Using in-situ spectroscopic ellipsometry and ex-situ X-ray reflectometry, the growth linearity, growth per cycle (GPC), and density of the resulting thin films was investigated as a function of the pulse times and the substrate temperature. At a substrate temperature of 300 °C and using saturated pulse times, an exceptionally high GPC of 1.1 nm/cycle without nucleation delay was achieved, resulting in amorphous films with an empirical stoichiometry of $FeP_{1.5}O_{4.7}$ with 0.9% hydrogen and no detectable carbon residue. Trigonal $FePO_4$ (Rodolicoite) was formed upon annealing in air. Remarkably, annealing in helium resulted in the formation of elemental phosphorus. The as-deposited, amorphous material became active as a Li-ion cathode after an initial irreversible electrochemical lithiation, showing insertion and extraction of Li^+

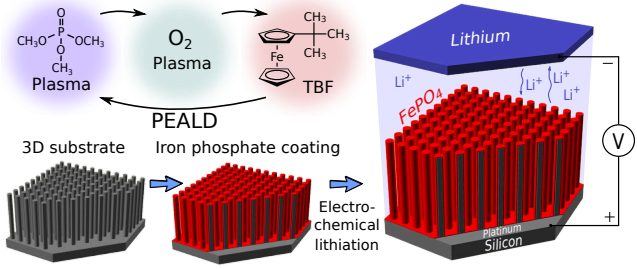

Figure 5.1: Abstract graphic for Paper III.

around a potential of 3.1 V vs. Li^+/Li. By conformally depositing the same material on a 3D-microstructured substrate consisting of Pt-coated Si micropillars, the capacity could be drastically increased without sacrificing rate performance.

5.2 INTRODUCTION

Iron phosphates are widely used as polyanion-based positive electrode materials for lithium-ion batteries. Since the discovery of the interesting electrochemical properties of olivine-type $LiFePO_4$ in 1997,[39] leading to large-scale commercial deployment, a lot of research effort has been devoted to related compounds.[102] The electrochemical activity of iron phosphate is strongly related to its crystalline structure: trigonal $FePO_4$ has a lower voltage and a significantly lower capacity than the aforementioned olivine,[103, 104] while amorphous $FePO_4$ is currently regarded as a promising 3 V lithium-ion battery cathode material which can reach almost 100% of its theoretical capacity.[105–107]

A new advancement in this field, attracting recent scientific and technological interest, is the development of miniaturized lithium-ion microbatteries consisting of thin solid-state electrode and electrolyte layers deposited on 3D-structured silicon substrates.[43–45] This results in fast kinetics caused by low film thicknesses and an increased capacity due to the surface area enhancement of high aspect ratio structures. However, it requires the conformal deposition of very thin and pinhole-free electrode films on complex structures. This can be achieved by atomic layer deposition (ALD).[108]

ALD is a thin-film deposition technique in which layer-by-layer growth of material is invoked by alternating exposures to chemical vapors in a vacuum environment. As opposed to chemical vapor deposition (CVD), the precursor exposures are separated, which results in sequential, self-limiting half reactions taking place on the substrate surface. Because of the self-limiting nature of the half reactions, ALD has the inherent advantage of conformal coatings on complex structures. Many ALD processes exist for various oxides, II-VI and III-V semiconductors, metal nitrides, metals, metal sulfides, and fluorides.[65] ALD of phosphates is less common, but reported processes include aluminium phosphate,[12–15, 26, 30] calcium phosphate,[17] titanium phosphate,[14, 16] lanthanum phosphate,[21] lithium phosphate,[19] iron phosphate,[22, 23] and lithium iron phosphate.[24] An easy-to-use (and thus popular) phosphorus precursor is trimethyl phosphate (TMP); it is a cheap and stable liquid with a suitable vapor pressure. Its high stability, however, also

limits its use as an ALD reactant, often resulting in very slow growth or difficulty in incorporating sufficient amounts of phosphorus into the film.

We previously reported a novel plasma-enhanced atomic layer deposition (PEALD) process for aluminium phosphate, which was based on the use of a TMP plasma instead of vapor.[30] By studying the reaction mechanism using in-situ techniques, we concluded that the combined action of TMP plasma with O_2 plasma created a phosphoric acid-like precursor species on the substrate surface, which subsequently reacted with trimethylaluminium (TMA) to produce aluminium phosphate. We further hypothesized that the same process could be used to grow other phosphates by swapping TMA with a different metal precursor. In this work, an iron precursor was used; the precursor of choice was tert-Butylferrocene (TBF), as it had been previously combined with O_2 plasma for the ALD growth of iron oxide in a broad temperature range and with a high growth rate.[109] We will show that the addition of TMP plasma to this process results in the PEALD growth of iron phosphate with an exceptionally high growth rate (1.1 nm/cycle), and we will demonstrate that the resulting film can be used as a positive electrode material for microstructured thin-film lithium-ion batteries.

5.3 EXPERIMENTAL

5.3.1 *Deposition system*

Depositions were carried out in a home-built pump-type PEALD reactor, shown schematically in figure 5.2.

The stainless steel deposition chamber was continuously evacuated by a turbomolecular pump to a base pressure of approx. 4×10^{-6} mbar. Precursor vapors and gases were admitted through computer-controlled pneumatic valves and manually adjustable needle valves. The TMP precursor (Sigma-Aldrich, 97%) was heated to 45 °C in a stainless steel container. The TBF precursor (Alfa Aesar, 98%) was heated to 75 °C in a fused quartz vial with an argon inlet and a precursor vapor outlet. The temperature of the chamber walls was set to 95 °C, and all precursor tubes leading to the chamber were additionally heated to prevent any condensation. On top of the chamber, a gate valve lead to a fused quartz column wrapped by a copper coil. The coil was connected to a 13.56 MHz RF generator (ENI GHW-12Z) and a matching network in order to generate an inductively coupled plasma in the column. The remote plasma was generated by feeding vapor or gas from the chamber to the plasma column through the gate valve and pulsing the RF generator. The plasma power was set to 200 W for the TMP

plasma and 300 W for the O_2 plasma, and the impedance matching was tuned to minimize the reflected power on both. All vapor and gas flows (TMP, O_2, and Ar carrier gas) were adjusted to reach a partial pressure of 5×10^{-3} mbar in the deposition chamber.

The substrates were mounted to a heated copper block, the temperature of which was PID-controlled. Depositions were performed on pieces of standard p-type silicon (100) wafer (for process characterization), silicon micropillar arrays (for conformality evaluation), silicon wafer coated with platinum, or silicon micropillar arrays coated conformally with platinum (where the platinum coating functions as a lithium ion diffusion barrier and current collector for electrochemical characterization).

5.3.2 *Deposition process*

A single cycle of a typical deposition process consisted of: TMP plasma exposure – pumping – O_2 plasma exposure – pumping – TBF exposure – pumping. TMP and O_2 were introduced into the chamber while it was continuously pumped. TBF was introduced while the gate valve to the turbo pump was closed, i.e. in static pulsing mode. During the pulse, this resulted in a continuous increase in pressure at a rate of approx. 0.1 mbar/s, i.e. for a 30 s static pulse, the final TBF pressure was 3 mbar. The pumping times between pulses were chosen to bring the residual pressure to below

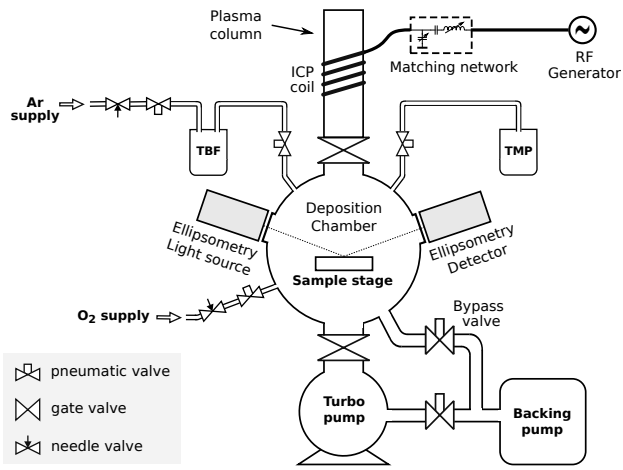

Figure 5.2: Schematic drawing of the deposition system used in this work, showing the vacuum chamber, precursor connections, and the plasma system.

4×10^{-5} mbar; they typically ranged from 15 s after the plasma pulses to 30 s after the static TBF pulse.

5.3.3 *Material characterization*

In-situ spectroscopic ellipsometry measurements were performed with a J.A. Woollam M-2000 ellipsometer working in the ultraviolet-visible region and using the CompleteEASE software for fitting and data analysis. The optical model consisted of a silicon substrate covered by a single layer which satisfied a Tauc-Lorentz dispersion relation; coefficients were determined from layers with a known thickness (aided by XRR) and were held fixed, while the thickness (as the only free parameter) was fitted in situ.

X-ray reflectometry (XRR) and X-ray diffraction (XRD) patterns were acquired on Bruker D8 diffractometers using Cu Kα radiation. Film thickness and density were determined from XRR by fitting simulated patterns to the measured ones. In-situ XRD during annealing was performed in a home-built chamber under either a helium or air atmosphere and using a position sensitive detector.[95–97] An FEI Quanta 200 F scanning electron microscope was used for SEM imaging, with the electron beam energy set to 20 keV and using an EDAX silicon-drift detector for energy-dispersive X-ray spectroscopy (EDX). X-ray Photoelectron Spectroscopy (XPS) analysis was performed on a Thermo Scientific Theta Probe XPS instrument using Al Kα X-rays generated at 15 kV and 70 W and focused to a spot size of 0.3 mm by an MXR1 monochromator gun. The sample surface was etched by Ar^+ ions at an acceleration voltage of 3 keV and a current of 2 μA. The elastic recoil detection (ERD) measurements were carried out using an 8.0 MeV $^{35}Cl^{4+}$ beam, with a scattering angle of 40° and a sample tilt of 15°.

5.3.4 *Electrochemical testing*

Electrochemical test cells were constructed inside an argon-filled glovebox with O_2 and H_2O levels below 1 ppm. The working electrodes consisted of either planar or 3D-structured silicon substrates, coated first with platinum and then with iron phosphate. The cells consisted of a PTFE body filled with electrolyte (1 M $LiClO_4$ in propylene carbonate) clamped against the working electrode, with the coated side facing the liquid, and sealed by a circular O-ring defining an electrode area of 0.95 cm^2. All reported currents and charges were normalized against this footprint area, yielding units of resp. $\mu A/cm^2$ (current) and $\mu Ah/cm^2$ (charge). An electrical contact was made by applying conductive silver ink on the cleaved sides of the substrate in order to connect the current collector layer to

a piece of copper foil. The counter electrode and reference electrode consisted of lithium metal, thereby measuring all working electrode potentials against Li^+/Li. Cyclic voltammetry and constant-current measurements were performed with home-built and commercial (Metrohm Autolab) potentiostat/galvanostat systems.

5.4 RESULTS AND DISCUSSION

5.4.1 *Temperature dependency*

Using 30 cycles of [15 s TMP plasma – 10 s O_2 plasma – 30 s TBF] as described in the experimental section, films were grown on planar Si substrates at temperatures between 150 °C and 350 °C. The films were then analyzed by XRR to determine their thickness and density, and the growth per cycle (GPC) was calculated by dividing the thickness by the number of cycles. For comparison purposes, the same experiment was performed using only TMP plasma pulses (15 s, separated by 15 s pumping) and no other precursors, measuring the GPC with in-situ ellipsometry in the same range of substrate temperatures. The resulting plots (sharing the temperature axis) are shown in figure 5.3.

The deposition process is strongly dependent on temperature. Part of this temperature dependency is due to the TMP plasma step, which has been investigated in detail for the aluminium phosphate process.[30] At low temperature, exposing the substrate to TMP plasma results in a continuous (CVD-like) growth of low-density, phosphorus-rich material. The creation of this solid deposit by the TMP plasma itself is called plasma polymerization.[74] This effect grows stronger with decreasing substrate temperature. This means that we can inhibit it by increasing the substrate temperature, as demonstrated in the upper part of figure 5.3 where almost no growth is observed at $T > 250\,°C$.

Transferring this knowledge to the full process (shown in the lower part of figure 5.3), we can understand why the low-temperature iron phosphate films ($T < 225\,°C$) have a low density and a high GPC: the TMP plasma introduces a PECVD component, resulting in low-density and phosphorus-rich material being added to the films, thereby increasing the GPC. The GPC increases very quickly with decreasing substrate temperature, resulting in an extremely high GPC of 4.1 nm/cycle at 150 °C. The low-temperature films degrade slowly after removal from the deposition system by exposure to ambient air; this is assumed to be a direct consequence of the high phosphorus content, as the P−O−P bonds get easily hydrolyzed, rendering the material hygroscopic.[99]

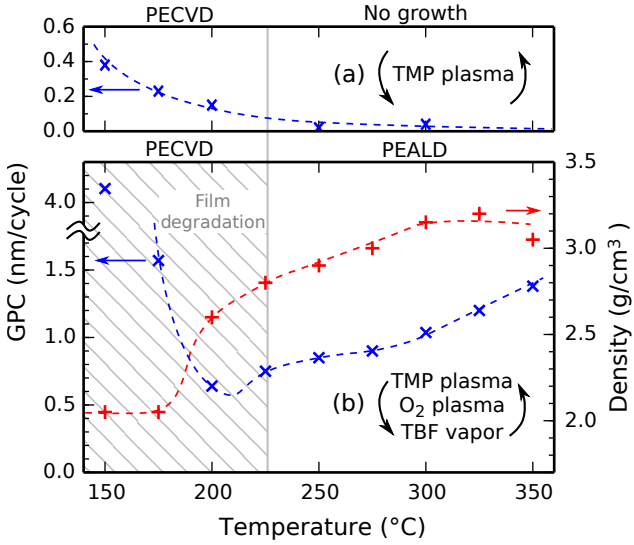

Figure 5.3: The growth per cycle as a function of the substrate temperature, as determined for repeated cycles of (a) only TMP plasma and (b) for the full process (additionally showing the film density on the right y-axis). The region striped in gray is the PECVD regime, where the films were hygroscopic and degraded in air.

At high temperatures, however, the TMP plasma polymerization is inhibited; the TMP plasma grows nothing on its own, but growth is still achieved when combined with the other precursors. This suggests a PEALD growth mechanism. Starting from 250 °C, the film does not degrade in air, and the GPC and density both increase with temperature. This can be attributed to the TBF precursor's chemical reactivity which tends to increase with temperature, as a strongly increasing GPC with temperature was also found earlier for the TBF/O_2 plasma process.[109] The decreasing density and increasing GPC above 325 °C may suggest the onset of TBF precursor decomposition.

We conclude that on the low-temperature side of figure 5.3, we have a PECVD process; on the high-temperature side, we have a PEALD process. Because of the improved thickness control and conformality of ALD compared to CVD, we will focus on the ALD region and choose our substrate temperature accordingly. A substrate temperature of 300 °C was chosen for all subsequent depositions; this results in non-hygroscopic, high-density films, while still avoiding precursor decomposition.

5.4.2 *Pulse time dependency*

In order to investigate the saturation behavior of the process and the degree to which the half-reactions are self-limited, the dependency of the GPC and density on the precursor (plasma) pulse durations was studied in a systematic series of depositions, each consisting of 30 cycles of [TMP plasma – O_2 plasma – TBF] on planar silicon at 300 °C. For each sample, representing a particular combination of pulse times, the GPC and density were measured by XRR. The samples were grouped in three data sets, where in each set one pulse duration was varied, while the two remaining pulse durations were fixed. The fixed pulse durations were always set to 15 s for TMP plasma, 10 s for O_2 plasma, and 30 s for TBF. This results in three saturation curves, shown together in figure 5.4.

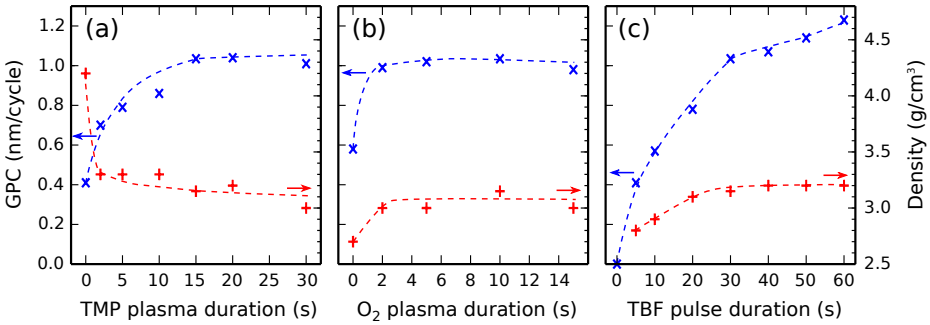

Figure 5.4: The growth per cycle and density of the grown films (determined by XRR) as a function of (a) the TMP plasma duration, (b) the O_2 plasma duration, and (c) the TBF pulse duration. Non-varied pulse durations were fixed to 15 s for TMP plasma, 10 s for O_2 plasma, and 30 s for TBF, and the substrate temperature was set to 300 °C. The three subfigures share their y-axes (left: GPC; right: density).

Figure 5.4a shows that there is still growth without TMP plasma (i.e. the 0 s point), with a low GPC and a high film density, because this is essentially the TBF/O_2 plasma process which grows Fe_2O_3. Increasing the TMP plasma duration results in increasing amounts of phosphorus being incorporated, which increases the GPC and decreases the film density, until saturation is achieved at pulse times of around 15 s. Further increasing the TMP plasma duration does not appreciably change the GPC nor the film density.

Figure 5.4b shows that the O_2 plasma exposure already saturates at 2 s, and that it is not even essential to the process: without O_2 plasma, material is still deposited, albeit at approx. half of the saturated growth rate

and with a lower density. Our earlier work on aluminium phosphate showed that the TMP plasma leaves phosphate surface species having both $-O-CH_3$ and $-OH$ terminations, of which only the $-OH$ will react with the metal precursor.[30] By adding the O_2 plasma, the remaining $-O-CH_3$ gets combusted to $-OH$; this eliminates carbon impurities and increases reactivity, thus increasing the GPC. Upon complete conversion, nothing further happens, resulting in quick saturation.

Figure 5.4c shows that there is no deposition without the TBF precursor pulse, confirming that the TMP plasma polymerization is fully inhibited at 300 °C. Upon increasing the TBF exposure, the GPC and density increase up until a pulse duration of 30 s. For pulse times exceeding 30 s, the film density remains constant, but the GPC keeps increasing slightly (albeit at a much slower rate than below the 30 s mark). This indicates a certain CVD component which is possibly caused by decomposition of the TBF precursor. It should be noted, however, that the x-scale of figure 5.4c is distorted by the static pulsing: in this case, the precursor dose (which is the integral of the pressure over time) is proportional to the square of the duration due to the linearly increasing pressure. This means that doubling the duration from 30 s to 60 s actually corresponds to quadrupling the precursor dosage.

5.4.3 *In-situ monitoring - growth linearity*

Based on the saturation behavior observed in figure 5.4, all subsequent depositions were carried out with pulse times of 15 s TMP plasma, 10 s O_2 plasma, and 30 s TBF, at a substrate temperature of 300 °C, unless mentioned otherwise. This ensures that we are working in a saturated ALD regime. Figure 5.5 shows the evolution of the in-situ spectroscopic ellipsometry data during 50 cycles of this deposition process. A Tauc-Lorentz model was used to represent the optical properties of the deposited film, with the layer thickness as the only free parameter. The psi and delta angles derived from the model (dashed lines) correspond very well with the measured data (red and green lines). The refractive index of the material varies from 1.75 (at 300 nm) to 1.64 (at 1000 nm), and the absorption coefficient becomes non-zero below 400 nm.

During the same deposition, and using the same model, the fitted layer thickness was plotted as a function of the cycle number to produce the growth curve shown in figure 5.6. The graph shows linear growth with practically no nucleation delay. The GPC is given by the slope of the growth curve and amounts to 1.1 nm/cycle. The XRR pattern of the resulting film after removal from the deposition system is shown as an inset

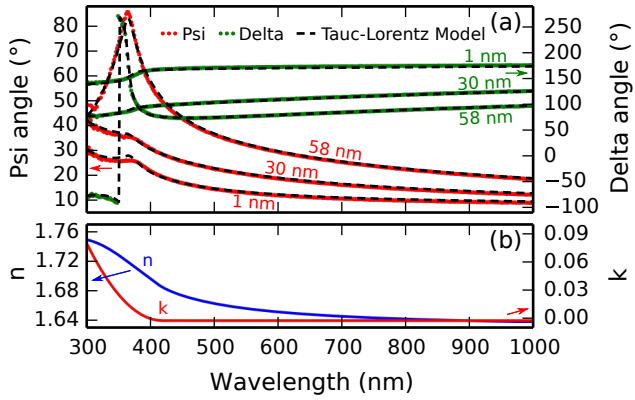

Figure 5.5: (a) The psi and delta angles measured by spectroscopic ellipsometry as a function of the wavelength, along with their Tauc-Lorentz model predictions, at different stages during film growth. (b) The refractive index n and absorption coefficient k plotted on the same wavelength axis as (a).

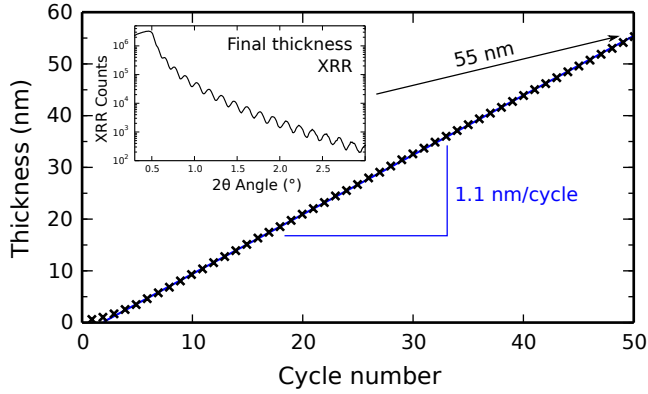

Figure 5.6: Growth curve measured by in-situ spectroscopic ellipsometry, showing the fitted film thickness as a function of the cycle number. Inset: XRR measurement of the resulting film, corresponding to a low-roughness film with a thickness of 55 nm.

in figure 5.6; the layer thickness extracted from it (55 nm) agrees with the last point of the growth curve.

5.4.4 *Proposed reaction mechanism*

A possible reaction mechanism for the process is outlined in figure 5.7. The first part, as depicted in figure 5.7a, was already investigated in our earlier work.[30] In short, the TMP plasma produces surface species that consist of mixed (poly)phosphate esters; starting with the original TMP molecule, some $-O-CH_3$ groups are replaced by $-OH$, and the phosphate groups get polymerized to some degree, indicated by the n repeat units in the structure (e.g. $n = 1$ represents the orthophosphate, $n = 2$ the pyrophosphate, etc.). The subsequent O_2 plasma exposure then combusts any remaining $-O-CH_3$ groups to $-OH$, with CO_2 and H_2O as the exhaust products, resulting in surface species consisting of (poly)phosphoric acids.

In the second part (figure 5.7b), the (poly)phosphoric acid surface species are exposed to the vapor-phase TBF precursor. This invokes a proton-

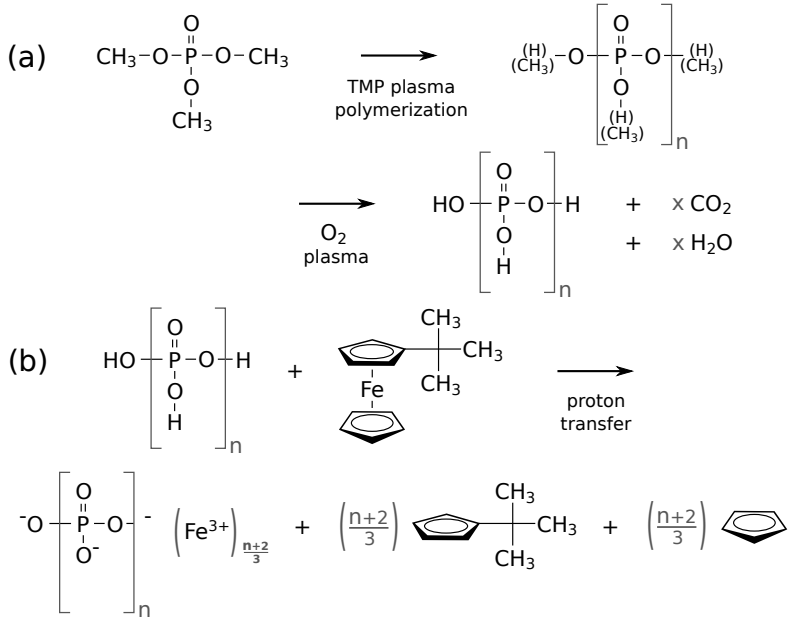

Figure 5.7: Proposed reaction pathway for the process, showing simplified representations of (a) the formation of mixed phosphate esters by TMP plasma polymerization and conversion to (poly)phosphoric acids by O_2 plasma, and (b) the reaction of the polyphosphoric acids with TBF, forming iron phosphate and evolving cyclopentadiene and tert-butylcyclopentadiene as vapor-phase exhaust products.

transfer reaction from the −OH groups to the cyclopentadienyl rings; the iron cation bonds to the (poly)phosphate anion to form iron phosphate, and the ligands of the TBF molecule are liberated in the form of cyclopentadiene and tert-butylcyclopentadiene, which are released in the vapor phase. This reaction is likely promoted by the high substrate temperature and possibly also by the presence of radicals due to the preceding plasma steps. Depending on the degree of polymerization, different types of iron phosphate are formed, with a general formula of $Fe_{(n+2)/3}P_nO_{3n+1}$. For instance, for $n = 1$, we get $FePO_4$ (iron orthophosphate); for $n = 2$, we get $Fe_{4/3}P_2O_7$ (i.e. $Fe_4P_6O_{21}$, iron pyrophosphate), etc.

In light of the unusually high growth per cycle of this process, it is interesting to compare the observed GPC to the thickness of a full monolayer. The latter can be approximately calculated by determining the volume occupied by one molecule ($V = \frac{M}{N_A \rho}$, where M is the molar mass, N_A is Avogadro's constant, and ρ is the measured density, approx. 3.1 g/cm^3) and taking the cube root, thereby approximating these volumes as single-molecule cubes. This results in calculated monolayer thicknesses in the range of 0.43 nm (for $n = 1$) to 0.57 nm (for $n = 3$). Comparing this to the observed GPC of 1.1 nm/cycle, this would imply that we are growing about two monolayers in every cycle; this would further imply that the growth is not surface-controlled, and that another mechanism is responsible for the observed self-limitation and saturation behavior. However, if we instead assume that the molecular volumes are elongated and "standing up" on the surface, and e.g. approximate them by cuboids which are three times as long as they are wide (which is not a far-fetched assumption given the linear structure of polyphosphates), we arrive instead at monolayers ranging from 0.90 nm ($n = 1$) to 1.2 nm ($n = 3$), which would fit the observed GPC and would be consistent with the idea of self-limitation by surface saturation.

5.4.5 *Crystallinity*

In order to study the crystalline structure of the material, a film with a thickness of 190 nm was deposited on a Si substrate and annealed in a controlled atmosphere during in-situ X-ray diffraction. Figure 5.8 compares the results for air and helium atmospheres, showing clearly different behavior. The as-deposited material is amorphous, as evidenced by the lack of any sharp diffraction peaks and the presence of a broad halo around 21° which is typical for amorphous materials and stems from interatomic interference.[110] Upon heating in air at a fixed heating rate of 10 °C/min, crystallization into an unknown phase is observed around

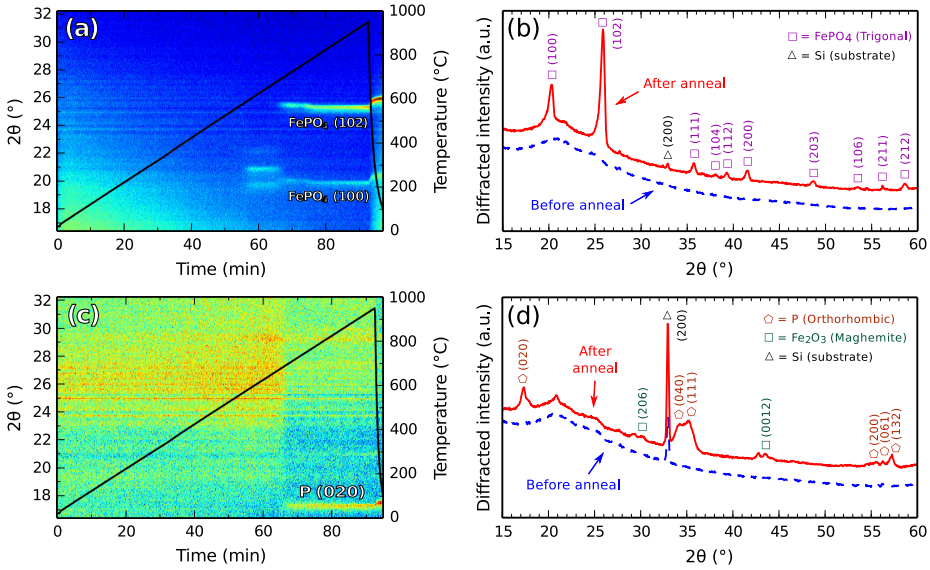

Figure 5.8: In-situ XRD during annealing of the deposited iron phosphate films in air (a, b) and helium atmosphere (c, d) to 950 °C at 10 °C/min. Plots (a) and (c) represent the XRD signal on a color scale as a function of 2θ angle and time, and the temperature as a function of time by a black solid line. Plots (b) and (d) show the as-deposited (before) and annealed (after) XRD patterns, facilitating comparison and analysis of the formed phases.

600 °C, which quickly transforms into trigonal $FePO_4$ indicated by the (100) and (102) reflections showing up around 700 °C (fig. 5.8a). The before/after comparison in fig. 5.8b confirms without any doubt that trigonal $FePO_4$ (Rodolicoite, JCPDS #29–0715) is formed, given that all reflections match. Upon heating in helium at the same rate, no $FePO_4$ is formed, but a different reflection shows up around 700 °C (fig. 5.8c). The wider 2θ window in the before/after comparison of fig. 5.8d reveals that diffraction peaks corresponding to elemental phosphorus (orthorhombic, #47–1626) and Fe_2O_3 (Maghemite, #13–0458) are found after annealing, and that the diffraction peak in fig. 5.8c is the (020) reflection of phosphorus.

These results suggest that, remarkably, the oxidation state of phosphorus can be influenced by the annealing atmosphere: where air annealing resulted in phosphorus in the +V state ($FePO_4$), the helium anneal reduced it to the +0 state (elemental phosphorus). In both cases, however, the amorphous halo is still present as a background in the patterns after annealing;

this suggests that the films only partially crystallize, and that an unknown amorphous component remains present.

5.4.6 *Elemental composition*

As-deposited (amorphous) films were analyzed by XPS and ERD in order to get information on the elemental composition of the deposited material. Figure 5.9 shows an XPS survey spectrum measured directly on the as-deposited film surface, together with a second survey spectrum measured after sputtering away some of the surface material (20 s exposure to 3 keV Ar^+ ions at a beam current of 2 μA). Iron, oxygen, and phosphorus are detected in both cases, while carbon is only visible on the surface. The surface carbon originates from environmental contamination; the absence of a carbon signal after sputtering means that the deposition process itself leaves barely any carbon residue. The absence of a silicon signal implies that the substrate is fully covered by a pinhole-free film.

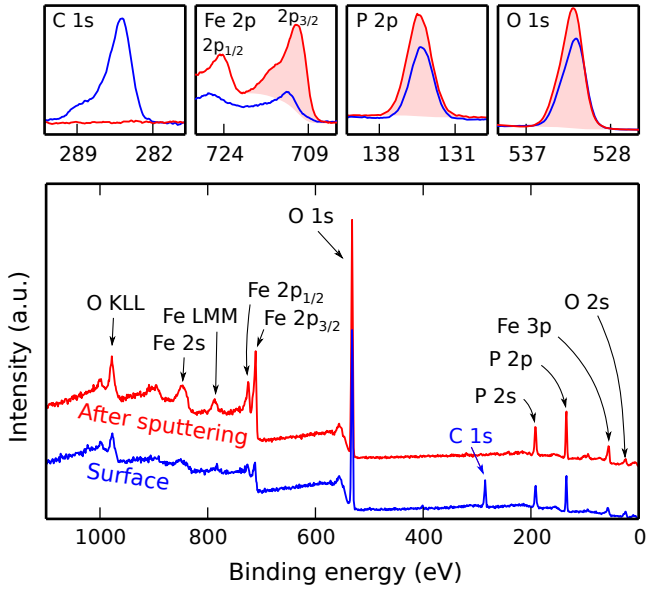

Figure 5.9: XPS analysis of the deposited material. The survey spectra show the presence of iron, phosphorus, and oxygen in the bulk of the film (red spectrum) in addition to some carbon which is only present on the film surface (blue spectrum). The detailed C 1s, Ti 2p, P 2p, and O 1s regions are shown above the survey scans using the same color legend; the quantification areas are filled in light red.

Detailed scans of the Fe 2p, P 2p, O 1s, and C 1s regions were made in order to accurately extract peak positions and intensities. Quantification was performed by subtracting Shirley-type backgrounds and making use of tabulated sensitivity factors. The results are shown in table 5.1. The peak positions of P 2p and O 1s suggest a phosphate compound, but they cannot be used to unambiguously identify the type of phosphate.[111] The peak position of Fe $2p_{3/2}$ (711.0 eV) points to an Fe^{3+} oxidation state.[112] Since there is a large uncertainty on the sensitivity factor of iron (as for all first-row transition metals[113]), we found significant variations in the calculated amounts of iron between several measurements on the same sample, so the tabulated amounts should only be regarded as indicative.

Table 5.1: Peak positions and atomic percentages of Fe, P, O, and C derived from XPS analysis on the as-deposited film, and atomic percentages of Fe, P, O, C, and H derived from ERD analysis on the same film.

Peak position (eV)	Fe $2p_{3/2}$	P 2p	O 1s	C 1s	
	711.0	134.3	531.9	284.8	
Atomic %	% Fe	% P	% O	% C	% H
XPS (surface)	2.6	24.0	50.5	22.9	–
XPS (sputtered)	9.0	30.8	59.2	1.0	–
ERD	13.8	20.7	64.6	0.0	0.9

To get reliable and accurate atomic percentages, the film was also analyzed by elastic recoil detection (ERD). The resulting depth profile is shown in figure 5.10, and the quantification results are given in the last row of table 5.1. Figure 5.10 reveals that iron, phosphorus and oxygen are distributed uniformly throughout the 55 nm layer. A small amount of hydrogen is also present throughout the layer, although most of it is on the film surface, along with a tiny amount of carbon. The surface hydrogen and carbon are most likely the result of environmental contamination. The ERD quantification in table 5.1 is accurate to within $\pm 2\%$ and gives an empirical stoichiometry of $FeP_{1.5}O_{4.7}$ with 0.9% hydrogen and zero carbon. The quantification reveals that the deposited material is more phosphorus-rich than $FePO_4$ (iron orthophosphate), so it is likely a polyphosphate. Its measured stoichiometry is particularly close to iron pyrophosphate, $Fe_4P_6O_{21}$.

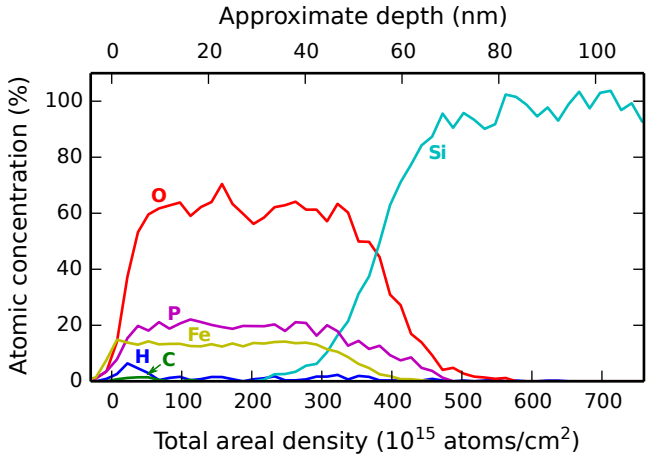

Figure 5.10: ERD depth profile of a 55 nm iron phosphate film on a silicon substrate. The lower x-axis expresses the depth as a total areal density (i.e. the product of the depth and the number density), which determines the measured energy loss of the recoiled atoms; the upper x-axis provides an approximate conversion to a depth in nm (by calibrating against the XRR film thickness). Iron, phosphorus and oxygen are distributed uniformly throughout the layer, while small amounts of hydrogen and carbon are mostly present on the film surface.

5.4.7 *Conformality*

The conformality of the coating was studied by depositing 200 cycles on a high aspect ratio structure consisting of silicon micropillars (2 µm wide, 50 µm high, spaced 4 µm center-to-center on a square lattice) etched into a silicon substrate. The sample was then analyzed with SEM and EDX in order to evaluate the amount of material and the stoichiometry as a function of the penetration depth. The results are shown in figure 5.11. EDX spectra were acquired along horizontal lines at different depths, so that the amounts of the elements of interest could be compared from their corresponding X-ray emission line intensities.

At the top of the pillar array, Fe, P, and O were detected, along with a small amount of C. Halfway along the pillars (25 µm deep), approximately the same amount of Fe was found, while the amounts of P and O had decreased by approx. 50%. At the bottom of the pillars (50 µm deep), the amounts of P and O had further decreased, along with the amount of Fe, although all elements were still clearly present. These results indicate that the process produces a reasonably conformal coating: the pillars are fully

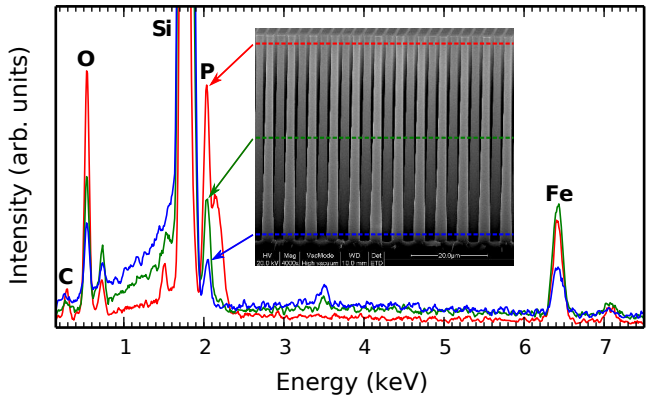

Figure 5.11: EDX spectra acquired by line scans at several depths along a silicon micropillar array coated with 200 cycles of iron phosphate. The line scans are indicated as dashed lines on the SEM image of the pillar array, and arrows point to the corresponding spectra.

coated, although the amount and stoichiometry are not constant along the penetration depth.

5.4.8 *Electrochemical characterization*

Working electrodes for electrochemical characterization were prepared by depositing 39 nm of iron phosphate on Pt-coated planar silicon substrates. Their lithiation behavior was studied by cyclic voltammetry (CV) in the potential range of 2.3–4.0 V, as shown in figure 5.12a. The potential sweep was started at the OCP of 3.3 V in the cathodic direction with a scan rate of 1 mV/s. The measurement reveals a redox reaction characterized by a formal potential of approx. 3.4 V, showing an accessible capacity of 0.14 $\mu Ah/cm^2$, and a significant separation between the cathodic and anodic peaks which increases from 0.7 V (first scan) to 1.0 V (fifth scan).

Upon lowering the potential below 2.3 V, no reaction is observed until the potential reaches 0.8 V, as can be seen in figure 5.12b. This is the onset of a large reduction peak centered at 0.35 V, where a charge of $-14.5\,\mu Ah/cm^2$ is inserted. Upon reversing the sweep direction at 0.2 V and going in the anodic direction, a number of oxidation peaks appear, along with very pronounced oxidation and reduction peaks in the 3 V region which were not originally present. By sweeping the potential back towards 0.2 V in the second scan, a new and sharp reduction peak appears around 1.4 V, and the one at 0.35 V is no longer observed. All subsequent scans are

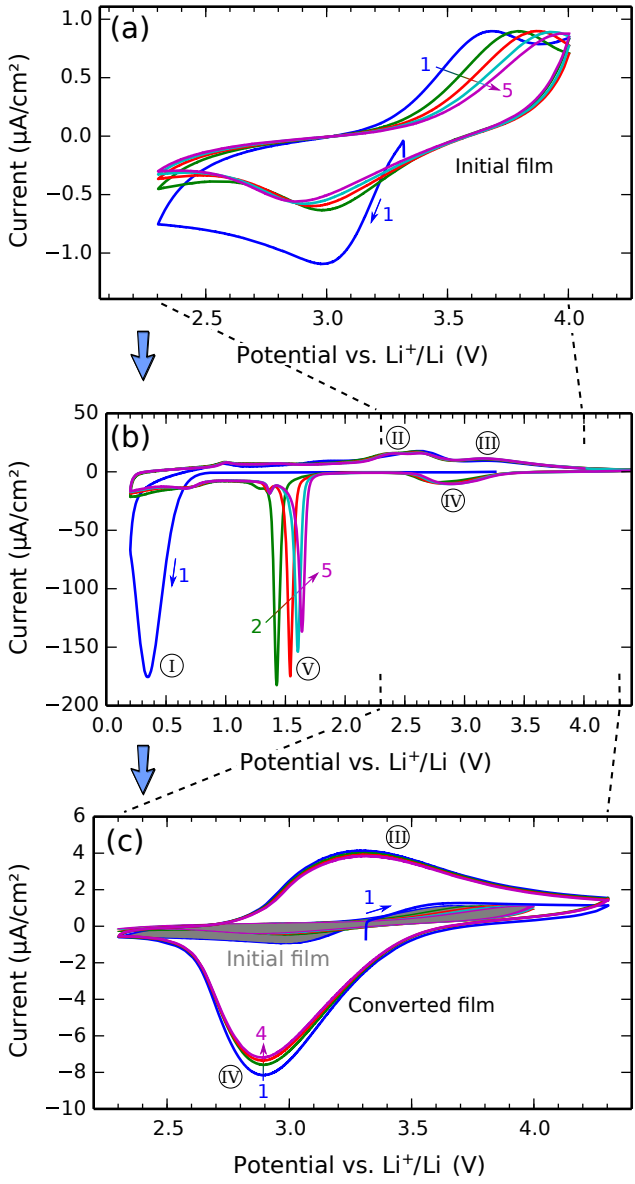

Figure 5.12: Cyclic voltammetry measurements on the as-deposited iron phosphate film at a scan rate of 1 mV/s in three consecutive potential windows: 2.3–4.0 V (fig. 5.12a, first CV after cell assembly), 0.2–4.5 V (fig. 5.12b), and 2.3–4.3 V (fig. 5.12c). The consecutive scans in each CV measurement are color-coded and annotated by numbers and arrows showing their evolution. Peaks of interest are labelled by Roman numerals.

identical, except for the sharp reduction peak which shifts to a slightly higher potential in each scan.

A subsequent CV measurement in the 3 V region (figure 5.12c, between 2.3 and 4.3 V, also showing the original CV scans in gray for comparison) shows that the material has been permanently transformed: the accessible capacity is about 1.1 μAh/cm^2, which is much higher than in the initial scans, and the separation between the cathodic and anodic peaks is about 0.4 V, which is significantly smaller than in the initial scans. The formal potential is 3.1 V, which is the same as reported for amorphous iron orthophosphate ($FePO_4$).[114]

The increase in capacity in the 3 V region by a factor of eight between figures 5.12a and 5.12c is remarkable. The transformation happens in figure 5.12b, where the distinguishable peaks are labelled by Roman numerals (I) to (V). Each of those can be associated with a certain redox reaction. As a means of verification, we will compare the observed charge (calculated by integration of current over time) with the amount of charge expected for each redox reaction. The latter can be calculated from Faraday's law:

$$\frac{Q}{A} = \frac{nd\rho eN_A}{M}$$

where Q/A is the amount of charge per surface area, n is the number of electrons transferred, d is the film thickness, ρ is the film density, e is the elementary charge, N_A is Avogadro's constant, and M is the molar mass. Using the measured values ($d = 39$ nm, $\rho = 3.1$ g/cm^3, and $M = 177$ g/mol for one unit of $FeP_{1.5}O_{4.7}$) and converting units to μAh/cm^2, this yields

$$\frac{Q}{A} = n \times 1.83 \text{ μAh/cm}^2$$

Reaction (I) at 0.35 V suggests a total reduction of Fe^{3+} to Fe^0 (i.e. metallic iron) by means of a conversion reaction. This is a well-known phenomenon in the case of iron oxide (Fe_2O_3), although slightly higher in potential at 0.65 V.[115] Because three electrons are transferred, this reaction results in a charge of $-3 \times 1.83 = -5.5$ μAh/cm^2. The measured charge is, however, -14.5 μAh/cm^2. This large excess of -9 μAh/cm^2 can be attributed to solid electrolyte interphase (SEI) formation; the SEI is a passivating layer grown on the electrode surface by reduction of the electrolyte solvent (in this case, propylene carbonate).[116] We therefore propose the following electrochemical reaction:

(I) $$FePO_4 + 3\,Li^+ + 3e^- \longrightarrow Fe + Li_3PO_4 + \text{SEI}$$

where the remaining 0.5 units of P and 0.7 units of O in the film are assumed to be unreactive (an assumption that will be held for all further reactions).

Upon re-oxidation, we encounter oxidation peaks (II) (which is, in itself, a broad peak consisting of two overlapping contributions) and (III). They are respectively associated with the oxidation of Fe^0 to Fe^{2+} (a conversion reaction) and Fe^{2+} to Fe^{3+} (deintercalation of lithium from $LiFePO_4$):

(II) $$Fe + Li_3PO_4 \longrightarrow LiFePO_4 + 2\,Li^+ + 2e^-$$

(III) $$LiFePO_4 \longrightarrow FePO_4 + Li^+ + e^-$$

The integrated total charge under peaks (II) and (III) is approx. $+5.7\,\mu Ah/cm^2$. This is in agreement with the expected value of $+5.5\,\mu Ah/cm^2$ for a total of three electrons transferred.

Reduction reaction (IV) is the reverse of reaction (III), i.e. Fe^{3+} to Fe^{2+} or the intercalation of lithium in $FePO_4$:

(IV) $$FePO_4 + Li^+ + e^- \longrightarrow LiFePO_4$$

The integrated charge is approx. $-1.5\,\mu Ah/cm^2$, in reasonable agreement with the calculated value of $-1.8\,\mu Ah/cm^2$ using Faraday's law for one electron.

The sharp peaks corresponding to reduction reaction (V) suggest another conversion reaction, bringing Fe^{2+} to Fe^0:

(V) $$LiFePO_4 + 2\,Li^+ + 2e^- \longrightarrow Fe + Li_3PO_4$$

The area under this peak gives a charge of approx. $-3.3\,\mu Ah/cm^2$, which is close to the calculated value of $-3.7\,\mu Ah/cm^2$.

In figure 5.12c, where the potential does not go lower than 2.3 V, only reactions (III) and (IV) occur. These are the typical intercalation and deintercalation reactions encountered in a lithium iron phosphate cathode, making use of the Fe^{2+}/Fe^{3+} redox couple:

$$FePO_4 + Li^+ + e^- \underset{charge}{\overset{discharge}{\rightleftharpoons}} LiFePO_4$$

A charge of $\pm 1.1\,\mu Ah/cm^2$ is inserted/extracted, corresponding to 60% of the theoretical capacity. The same redox reaction already occurs during initial cycling of the as-deposited material in figure 5.12a, yielding however only 8% of the theoretical capacity. This implies that the intermediate step of reducing all Fe^{3+} to metallic Fe and then re-oxidizing back to Fe^{3+} "activates" the film for lithium-ion intercalation.

An ex-situ ERD analysis of lithiated films at two distinct stages is presented in figure 5.13. Figure 5.13a shows direct evidence for the SEI formation proposed in reaction (I). The SEI layer is visible as a region which contains carbon and hydrogen from the organic solvent, as well as an excess of lithium compared to the underlying film. A detailed analysis of the atomic percentages is given in table 5.2. The underlying $Li_xFeP_yO_z$ layer has Li/Fe and P/Fe ratios of resp. 1.8 and 2.0, where we would expect resp. 3.0 from reaction (I) and 1.5 from the as-deposited film. The cause of this discrepancy is unknown. Figure 5.13b shows a film which additionally underwent oxidation reactions (II) and (III). No obvious SEI layer is

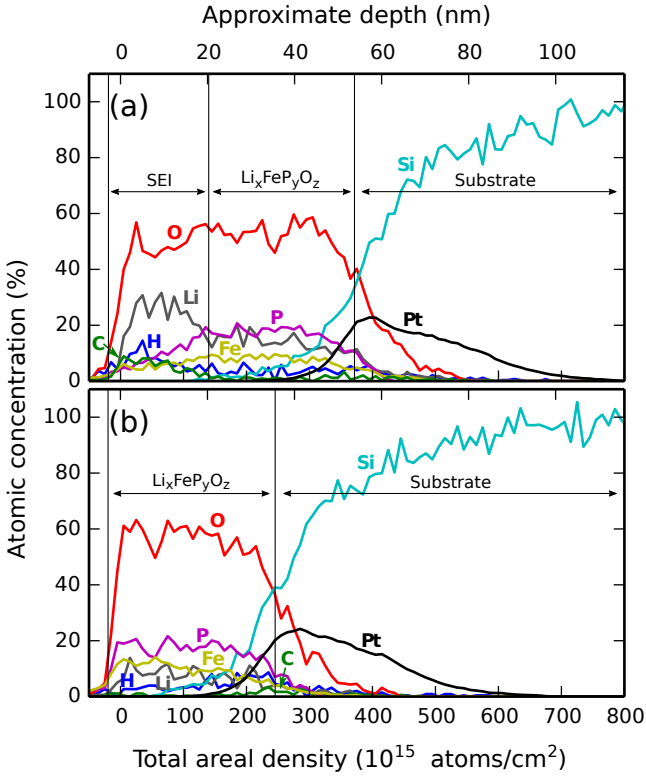

Figure 5.13: ERD depth profiles of iron phosphate films on Pt-coated silicon substrates after (a) initial lithiation (the film underwent reaction (I)) and (b) delithiation (the film underwent reactions (I), (II) and (III)). The lower x-axes express the depth as a total areal density (i.e. the product of the depth and the number density); the upper x-axes provide an approximate conversion to a depth in nm.

visible in the depth profile, suggesting that it perhaps delaminated or dissolved during re-oxidation. Surprisingly, table 5.2 shows that there is still lithium in the "fully delithiated" film, giving a Li/Fe ratio of 0.8. There is also more carbon and hydrogen compared to the as-deposited film. Presumably, the reduction to metallic Fe in reaction (I) induces stress and cracking in the film, causing the voids to be permanently filled up with some of the SEI material.

5.4.9 *Charge/discharge cycling and 3D structuring*

The main challenge of using iron phosphate in a lithium-ion battery cathode is to overcome its low electronic conductivity: one cannot simply enlarge the capacity by increasing the film thickness without suffering from poor kinetics and resistive losses. However, the conformality of the deposition process makes it possible to coat 3D-structured substrates, resulting in a capacity increase proportional to the total surface area. The test structure used for this is the same silicon micropillar substrate as shown earlier in figure 5.11. The effective surface area increase η of the structure can be easily calculated by taking a unit cell of the square lattice and dividing the total (three-dimensional) surface area by the footprint area of the unit cell:

$$\eta = \frac{(4\,\mu\text{m})^2 + 2\,\mu\text{m} \times \pi \times 50\,\mu\text{m}}{(4\,\mu\text{m})^2} \approx 20.6$$

In other words, if the coating is perfectly conformal, the capacity of the 3D-structured electrode will be 20.6 times higher than the capacity of a planar film of the same size. We tested this by conformally coating the micropillar substrate with platinum (10 nm thickness, serving as the current collector) followed by 30 cycles of iron phosphate (33 nm thickness). The precursor pulse times (30 s TMP plasma, 20 s O_2 plasma, and 60 s

Table 5.2: Atomic percentages of Li, Fe, P, O, C, and H derived from ERD analysis on iron phosphate films after (a) initial lithiation (the film underwent reaction (I)) and (b) delithiation (the film underwent reactions (I), (II) and (III)).

		% Li	% Fe	% P	% O	% C	% H
(a): (I)	SEI	21.6	6.9	10.4	47.7	5.3	8.1
	$Li_xFeP_yO_z$	14.4	7.9	16.0	55.2	1.5	5.0
(b): (I),(II),(III)		7.9	10.3	16.9	57.7	1.4	5.9

TBF) were longer than for the planar samples in order to compensate for the decreased exposure in between the pillars. As a reference, the same deposition was made on a planar substrate (Pt-coated Si). In order to "activate" the electrodes as discussed earlier, they were first held at a constant voltage of 0.5 V vs. Li^+/Li in order to invoke the reduction of Fe^{3+} to Fe^0; this was continued until the current decreased to less than 1% of the maximum peak current. They were then re-oxidized to Fe^{3+} by means of a constant current (+1 µA for the planar film, and +15 µA for the micropillars) applied until the potential reached 4.3 V. Both electrodes were then repeatedly cycled between 4.3 V and 2.3 V at ±1 µA for the planar film and ±15 µA for the micropillars, allowing determination of the charge/discharge capacities from the charge/discharge durations. The results are shown in figure 5.14.

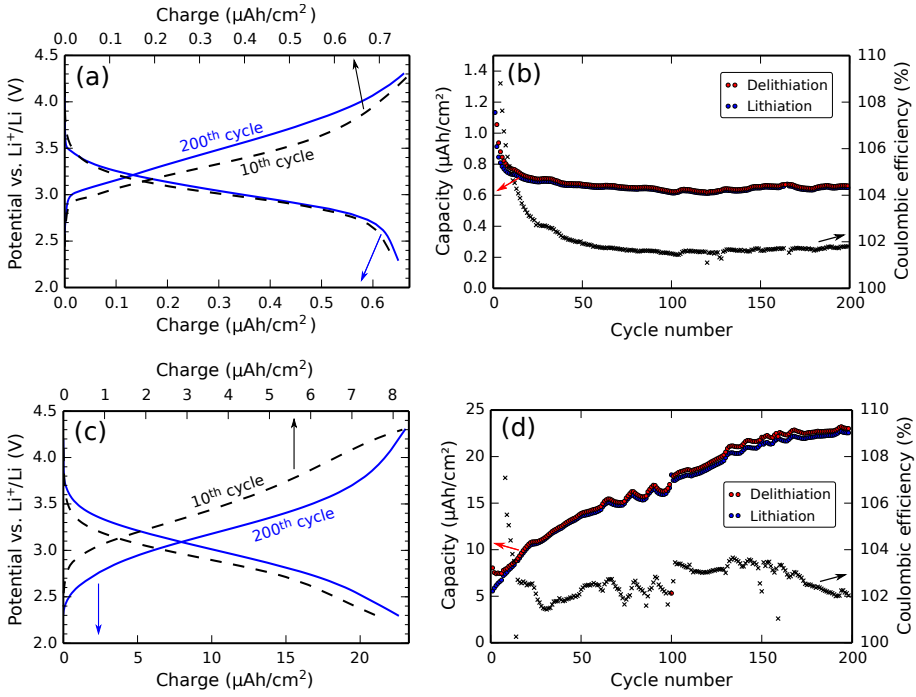

Figure 5.14: Charge/discharge profiles (a, c) and capacity evolution (b, d) over 200 charge/discharge cycles compared between the planar iron phosphate electrode (upper plots (a, b)) and the micropillar electrode (lower plots (c, d)).

For the planar electrode, fig. 5.14b reveals an initial capacity of 1.1 $\mu Ah/cm^2$ which quickly drops during the first 10 cycles and then stabilizes around 0.7 $\mu Ah/cm^2$ for the remaining 190 cycles. The coulombic efficiency (defined as the delithiation capacity divided by the lithiation capacity) is initially far over 100%, likely because of excess lithium that was left in the electrode by the initial lithiation. Afterwards, it stabilizes to a value of 102%, suggesting that minor side reactions occur during delithiation. Figure 5.14a compares the charge/discharge profiles of the 10^{th} (upper x-axis) to the ones of the 200^{th} cycle (lower x-axis). In the 200^{th} cycle, the capacity is about 13% lower, and the overpotential during charging (delithiation) is higher than in the 10^{th} cycle.

For the micropillar electrode, fig. 5.14d shows an initial capacity of approx. 7 $\mu Ah/cm^2$ which steadily increases and then stabilizes around 22 $\mu Ah/cm^2$ after 150 cycles, remaining almost constant for the remaining 50 cycles. The coulombic efficiency behaves similar to the planar electrode, with some periodic artifacts due to ambient temperature fluctuations. Figure 5.14c compares the charge/discharge profiles of the 10^{th} (upper x-axis) to the ones of the 200^{th} cycle (lower x-axis). The 200^{th} cycle shows a capacity which is almost three times higher than in the 10^{th} cycle, along with significanty decreased overpotentials during charging and discharging. The capacity increase might be caused by the non-uniform stoichiometry of the iron phosphate coating on the pillars, which slowly "heals" itself by repeated reduction and oxidation, improving lithium-ion conduction; it has been previously shown that these improvements in kinetics can lead to an increased capacity.[117]

Remarkably, the final capacity of the micropillar electrode (22 $\mu Ah/cm^2$) corresponds to a 31-fold capacity improvement over the final capacity of the planar electrode (0.7 $\mu Ah/cm^2$), which exceeds the theoretical η factor of 20.6 by 50%. This deviation might be caused by a different stoichiometry and/or morphology of the iron phosphate coating on the micropillar substrate compared to the planar iron phosphate film.

The rate performance of both electrodes was tested by measuring the available capacity for constant currents ranging from 1C to 90C, where 1C = 0.7 $\mu A/cm^2$ for the planar film and 1C = 21 $\mu A/cm^2$ for the microstructured one. To ensure steady-state conditions, the electrode was cycled three times for each C-rate and the charge/discharge capacities were determined from the third cycle. The results are shown in figure 5.15. Aside from obvious differences in capacity due to substrate geometry, both electrodes show a similar rate dependency. For the planar substrate between 1C and 50C, the capacity drops almost linearly as a function of the C-rate

on the double-log scale; in good approximation, doubling the rate results in a 15% capacity drop.

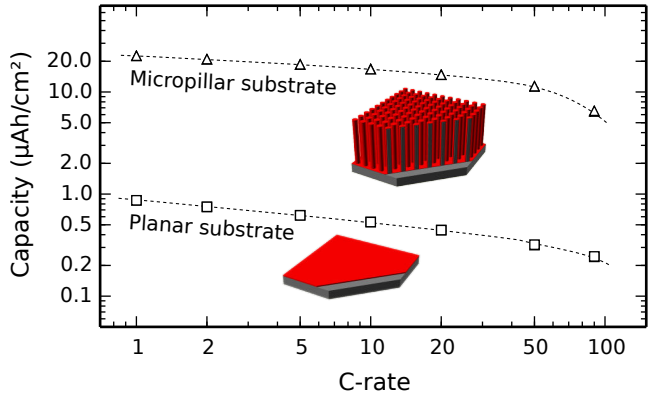

Figure 5.15: Capacity as a function of the C-rate for iron phosphate films on a planar substrate (squares) and on a 3D-structured micropillar substrate (triangles).

5.5 CONCLUSIONS

Repeatedly exposing substrates to a sequence of TMP plasma, O_2 plasma and TBF resulted in the plasma-enhanced atomic layer deposition of iron phosphate. The process was found to be heavily temperature-dependent and proceeded optimally at 300 °C, reaching an exceptionally high GPC of 1.1 nm/cycle and showing linear growth without nucleation delay when using saturated pulse times. The as-deposited films had a density of 3.1 g/cm^3, were amorphous and had an empirical stoichiometry of $FeP_{1.5}O_{4.7}$ with 0.9% hydrogen and no detectable carbon residue. Trigonal $FePO_4$ was formed after annealing to 700 °C in air, while the same anneal in helium resulted in the formation of elemental phosphorus. The conformality of the process was non-ideal, but still sufficient to reach deep into high-aspect-ratio structures. The as-deposited material could be lithiated and delithiated in the 3 V vs. Li^+/Li region, but reached only 8% of the theoretical capacity. However, by reduction below 0.5 V and subsequent oxidation back to 3 V, the capacity increased dramatically to 60% of the theoretical capacity, resulting in a usable 3 V cathode material. Long-term cycling of a 33 nm planar film revealed an initially decreasing capacity which stabilized to 0.7 µAh/cm^2 after 10 cycles. The same film on a micropillar substrate showed a capacity that increased from 7 µAh/cm^2 to 22 µAh/cm^2 over 150 cycles, and then remained constant. The rate

performance of both electrodes was similar, demonstrating the advantage of 3D structuring: the capacity was increased without having the penalty of worse kinetics which would result from increasing the layer thickness.

6

PAPER IV: TITANIUM PHOSPHATE

The following chapter has been published as an original research paper in the Journal of Materials Chemistry A, titled *"Plasma-enhanced atomic layer deposition of titanium phosphate as an electrode for lithium-ion batteries"*.[33] The content below has been reformatted to fit the layout of this PhD thesis, but is otherwise identical to the published version. The last section of this chapter contains supplemental data which was left out of the published version, but is still considered important enough to include here.

6.1 ABSTRACT

Titanium phosphate thin films were deposited by a new plasma-enhanced atomic layer deposition process. The process consisted of sequential exposures to trimethyl phosphate (TMP, Me_3PO_4) plasma, O_2 plasma and titanium isopropoxide (TTIP, $Ti(OCH(CH_3)_2)_4$) vapor, and it was characterized by in-situ spectroscopic ellipsometry and ex-situ X-ray reflectometry. The growth linearity, growth per cycle (GPC), and density of the resulting thin films was investigated as a function of the pulse times and the substrate temperature. The conformality of the process was characterized by deposition on micropillars. At a substrate temperature of 300 °C and using saturated pulse times, linear growth with a GPC of 0.66 nm/cycle and without nucleation delay was achieved. As-deposited films were amorphous, while crystalline TiP_2O_7 was formed upon anneal-

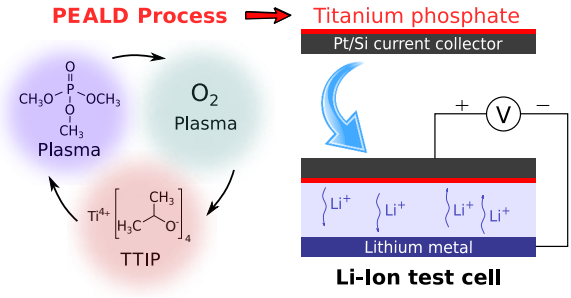

Figure 6.1: Abstract graphic for Paper IV.

ing in air or helium atmospheres. In lithium-ion test cells, the as-deposited films showed insertion and extraction of Li^+ around a potential of 2.7 V vs. Li^+/Li. Charge/discharge measurements revealed a volumetric capacity of 330 mAh/cm^3, together with a good rate capability and minimal capacity fading.

6.2 INTRODUCTION

Atomic layer deposition (ALD) is a thin-film deposition technique wherein material is deposited onto a surface by alternating exposures to chemical precursor vapors. In contrast to chemical vapor deposition (CVD), the precursors are introduced separately, with pumping or purging steps in between them. This causes self-limiting reactions to take place on the substrate surface, resulting in layer-by-layer film growth. Advantages of ALD over CVD include better step coverage (enabling the conformal coating of 3D structures), lower temperature deposition (enabling deposition on temperature-sensitive substrates), and insensitivity to process variations (in a saturated regime, the growth rate is inherently constant, even when the precursor exposure varies).[3] Many ALD processes exist for oxides, II-VI and III-V semiconductors, metal nitrides, metals, metal sulfides, and fluorides.[65] A limited number of ALD processes for phosphates has been reported.[12–17, 19–24, 26, 27, 30] ALD of titanium phosphate has only been reported twice, and in both cases, the metal precursor was titanium tetrachloride.[14, 16] In order to avoid the risk of any chlorine contamination in the deposited films and eliminate corrosive hydrogen chloride as a byproduct, it is favourable to have a chlorine-free ALD process for this material.

One way to achieve this would be to react phosphoric acid with titanium isopropoxide (TTIP). This has been previously demonstrated in a "liquid ALD" process, based on alternate dipping of the substrate in solutions of TTIP and phosphoric acid, which resulted in layer-by-layer growth of titanium phosphate.[118] However, to use the same reaction chemistry for vapor phase ALD, one would need to evaporate both precursors. This is easy enough for TTIP, which reaches a suitable vapor pressure upon moderate heating, but impossible for phosphoric acid, which only evolves water by dehydration when heated. An alternative phosphorus precursor is trimethyl phosphate (TMP), a stable and cheap liquid which easily develops sufficient vapor pressure. However, TMP will not directly react with most metalorganic precursors because of the methyl group termination of its molecular structure.

This problem can be solved by incorporating the TMP vapor in an inductively coupled plasma and using this as the phosphorus precursor. We first explored this idea in a plasma-enhanced atomic layer deposition (PEALD) process for aluminium phosphate, where we investigated the reaction mechanism by in-situ methods to reveal the function of the TMP plasma.[30] In short, we concluded that the combined action of TMP plasma with O_2 plasma created phosphoric acid-like precursor species on the substrate surface, which could subsequently react with a metal precursor. We have since successfully used TMP plasma in new PEALD processes for iron phosphate and zinc phosphate, which yielded exceptionally high growth rates while still showing self-limited behavior.[31, 32] In this work, titanium isopropoxide (TTIP) was used as the metal precursor, and this resulted in the plasma-enhanced atomic layer deposition of titanium phosphate.

Titanium phosphate is useful for its ion-exchange properties and for its catalytic activity.[68, 69] It can also be used as an intercalation-type electrode material for lithium-ion batteries. The crystalline pyrophosphate TiP_2O_7 has a reported redox potential of 2.6 V vs. Li^+/Li, which makes it suitable as a cathode in conventional lithium-ion batteries, or -0.4 V vs. standard hydrogen, which makes it highly interesting as an anode for aqueous lithium-ion batteries.[119–121] We will show that our as-deposited (amorphous) titanium phosphate thin films are similarly active, accommodating the insertion and extraction of lithium ions at a potential of 2.7 V vs. Li^+/Li.

6.3 EXPERIMENTAL

6.3.1 *Deposition system*

Depositions were carried out in a home-built pump-type PEALD reactor, shown schematically in figure 6.2. All parts were stainless steel, unless otherwise specified.

The deposition chamber was continuously evacuated by a turbomolecular pump to a base pressure of approx. 4×10^{-6} mbar. Precursor vapors and gases were admitted through computer-controlled pneumatic valves. The TMP (Sigma-Aldrich, 97%) and TTIP (Sigma-Aldrich, 97%) precursor bottles were heated to resp. 45 °C and 60 °C, so that they both reached pressures of approx. 5×10^{-3} mbar in the deposition chamber. The flow of O_2 was adjusted to reach a pressure of 5×10^{-3} mbar in the deposition chamber. The temperature of the chamber walls was set to 130 °C, and all precursor tubes leading to the chamber were additionally heated

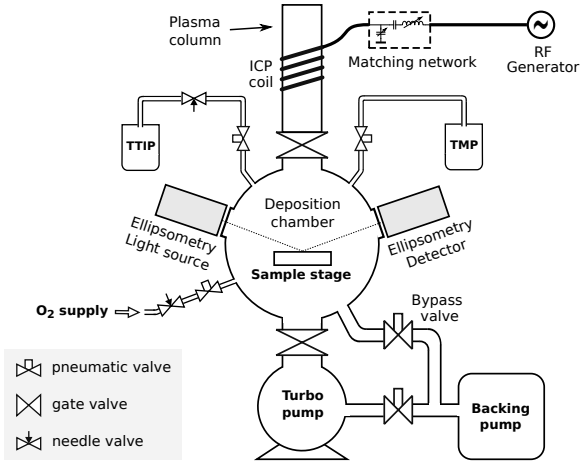

Figure 6.2: Schematic drawing of the deposition system used in this work, showing the vacuum chamber, precursor connections, and the plasma system.

to prevent any precursor condensation. On top of the chamber, a gate valve led to a fused quartz column wrapped by a copper coil. The coil was connected to a 13.56 MHz RF generator (ENI GHW-12Z) and a matching network in order to generate an inductively coupled plasma in the column. The remote plasma was generated by feeding vapor or gas from the chamber to the plasma column through the gate valve and pulsing the RF generator. The plasma power was set to 200 W for the TMP plasma and 300 W for the O_2 plasma, and the impedance matching was tuned to minimize the reflected power on both. The substrates were mounted to a heated copper block, the temperature of which was PID-controlled. Depositions were performed on pieces of standard p-type silicon (100) wafer (for process characterization), silicon micropillar arrays (for conformality evaluation), or silicon wafer coated with platinum (where the platinum coating functioned as a lithium ion diffusion barrier and as a current collector for electrochemical characterization).

6.3.2 *Deposition process*

A single cycle of a typical deposition process consisted of: TMP plasma exposure – pumping – O_2 plasma exposure – pumping – TTIP exposure – pumping. In between precursor pulses, pumping times of 20 s were found sufficient to bring residual pressures to below 4×10^{-5} mbar, thereby avoiding CVD side reactions.

6.3.3 *Material characterization*

In-situ spectroscopic ellipsometry measurements were performed with a J.A. Woollam M-2000 ellipsometer working in the ultraviolet-visible region and using the CompleteEASE software for fitting and data analysis. Measurements were acquired after each deposition cycle. Systematic parameters (angle offsets, window corrections) were fitted prior to deposition and then held fixed. The final thickness and the optical model parameters were fitted to the measurement acquired after the last cycle (i.e. after deposition). A growth curve was then obtained by fitting the thickness to each measurement, keeping all other parameters fixed. An FEI Quanta 200 F scanning electron microscope was used for SEM imaging, with the electron beam energy set to 10 keV and using an EDAX silicon-drift detector for energy-dispersive X-ray spectroscopy (EDX). X-ray reflectometry (XRR) patterns were acquired on Bruker D8 diffractometers using Cu Kα radiation. Film thickness and density were determined from XRR by fitting simulated patterns to the measured ones. In-situ X-ray diffraction (XRD) during annealing was performed in a home-built setup.[95–97] The annealing atmosphere was either helium or ambient air; the XRD patterns were acquired using a Cu Kα X-ray source and a position sensitive detector. X-ray Photoelectron Spectroscopy (XPS) analysis was performed on a Thermo Scientific Theta Probe XPS instrument using Al Kα X-rays generated at 15 kV and 70 W and focused to a spot size of 0.3 mm by an MXR1 monochromator gun. To remove surface contamination, the sample surface was etched by Ar^+ ions at an acceleration voltage of 3 keV and a current of 2 μA. The elastic recoil detection (ERD) measurements were carried out using an 8 MeV $^{35}Cl^{4+}$ beam, with a scattering angle of 40° and a sample tilt of 20°.

6.3.4 *Electrochemical testing*

Electrochemical test cells were constructed inside an argon-filled glovebox with O_2 and H_2O levels below 1 ppm. The working electrodes consisted of silicon substrates coated with PVD platinum (current collector) and then with PEALD titanium phosphate (active material). The cells consisted of a PTFE body filled with electrolyte (1 M $LiClO_4$ in propylene carbonate) clamped against the working electrode, with the coated side facing the liquid, and sealed by a circular O-ring defining an electrode area of 0.95 cm^2. All reported currents and charges were normalized against this footprint area, yielding units of resp. $\mu A/cm^2$ (current) and $\mu Ah/cm^2$ (charge). An electrical contact was made by applying conductive silver ink on the cleaved sides of the substrate in order to connect the platinum

current collector layer to a piece of copper foil. The counter electrode and reference electrode consisted of lithium metal, thereby measuring all working electrode potentials against Li^+/Li. Cyclic voltammetry and constant-current measurements were performed with home-built and commercial (Metrohm Autolab) potentiostat/galvanostat systems.

6.4 RESULTS AND DISCUSSION

6.4.1 *In-situ growth monitoring*

Film growth during the titanium phosphate depositions was monitored by in-situ spectroscopic ellipsometry. In order to extract the film thickness from the optical data, one needs an optical model of the film, and the Tauc-Lorentz oscillator model was found to work best in this case. As shown in figure 6.3a, the measured Psi and Delta angles correspond well to the calculated ones for a range of film thicknesses between 1 and 33 nm, showing that the film thickness can be reliably extracted from the ellipsometry data. The model is also interesting in itself because it reveals the optical properties of the deposited film. The refractive index dispersion and absorption curves are plotted in figure 6.3b. The deposited material has a refractive index of 1.82 (defined at a wavelength of 589 nm), and an optical band gap of 2.96 eV.

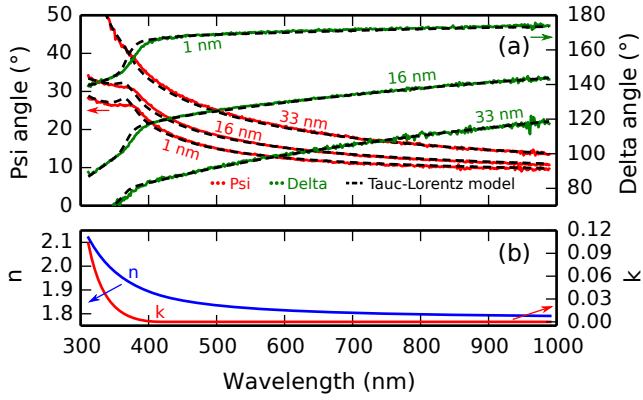

Figure 6.3: In-situ spectroscopic ellipsometry during the titanium phosphate deposition process. (a) Psi and Delta angles measured at three stages during film growth and compared with those calculated from the Tauc-Lorentz model using film thickness as the only variable; (b) refractive index n and absorption coefficient k as a function of the wavelength. Both subfigures share the same wavelength axis.

Figure 6.4 shows the evolution of the film thickness at each cycle during a 50-cycle deposition process consisting of 50×[10 s TMP plasma – 5 s O_2 plasma – 7 s TTIP vapor] at a substrate temperature of 300 °C. Linear growth is observed, without any nucleation delay, with a growth per cycle (i.e. the slope of the growth curve) of 0.66 nm/cycle. This is in perfect agreement with the ex-situ XRR measurement in the inset of figure 6.4, where the interference fringes give a film thickness of 33 nm after 50 cycles. The prominent, non-decaying fringes in the XRR pattern also indicate that a smooth, low-roughness film was deposited.

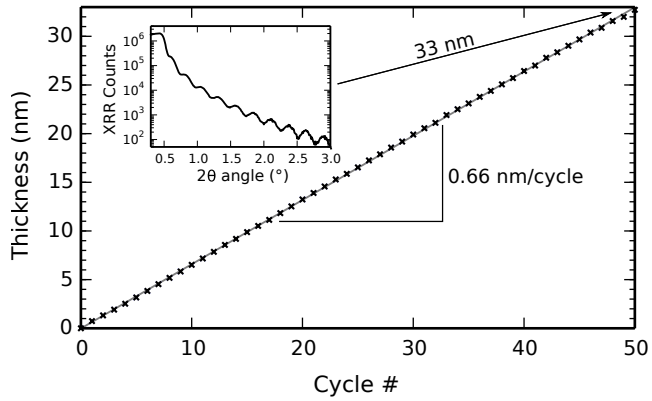

Figure 6.4: Film thickness as a function of the cycle number, fitted from in-situ spectroscopic ellipsometry using the Tauc-Lorentz optical model. One cycle consisted of [10 s TMP plasma – 5 s O_2 plasma – 7 s TTIP vapor] and the substrate temperature was 300 °C. Inset: XRR measurement of the resulting film (i.e. measured after 50 cycles).

6.4.2 *Saturation behavior*

The effect of changing the (plasma) precursor exposures was investigated by varying the pulse times; with constant precursor pressures, the amounts of exposure are indeed proportional to the pulse times. This was done separately for each of the three precursor pulses by systematically performing depositions where one pulse time was varied while the other two were kept constant. The constant pulse times amounted to 10 s for TMP plasma, 5 s for O_2 plasma, and 5 s for TTIP vapor. The substrate temperature was always kept constant at 300 °C. After each deposition, the film thickness and density were determined by XRR. Repeating this procedure for the TMP plasma, O_2 plasma, and TTIP vapor pulses, one arrives at the plots in figure 6.5.

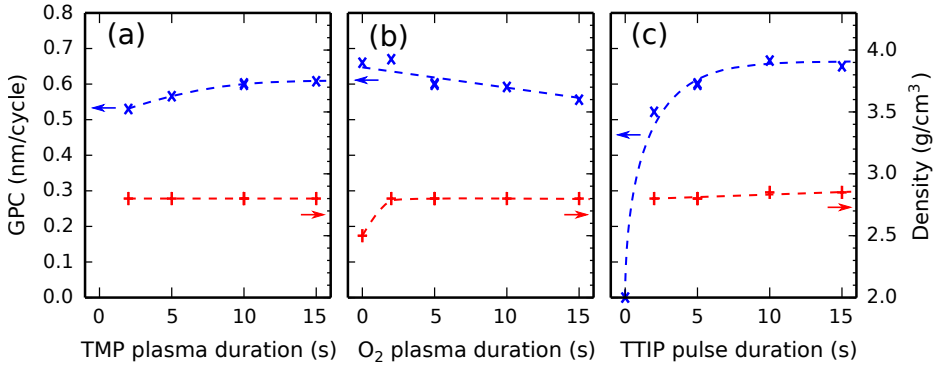

Figure 6.5: The GPC (left y-axes) and film density (right y-axes) as a function of (a) the TMP plasma, (b) the O_2 plasma, and (c) the TTIP pulse durations at a substrate temperature of 300 °C. The three subfigures have identical y-scales.

Figure 6.5a indicates that the GPC increases slightly with the TMP plasma duration between 2 s and 10 s, and levels off after 10 s. The film density is independent of the TMP plasma duration and stays at a constant value of 2.8 g/cm^3 in the investigated range.

Figure 6.5b reveals a weak decrease of the GPC with the O_2 plasma duration which continues over the whole investigated range. The film density is independent of the O_2 plasma duration, unless there is no O_2 plasma (the 0 s point), in which case the film density is significantly lower. As the O_2 plasma's main function is to remove hydrocarbons from the surface species created by the TMP plasma, one may assume that the film density for the [TMP plasma – TTIP vapor] process is lower due to the inclusion of hydrocarbons in the deposited film.

Figure 6.5c shows an initially sharp increase of the GPC with the TTIP pulse duration (there is no deposition in the absence of a TTIP pulse, at the 0 s point), which is followed by a flat region around 10 s. The film density is almost independent of the TTIP pulse duration.

In conclusion, all three exposures show saturating behavior, demonstrating the ALD nature of the process at 300 °C.

6.4.3 *Temperature dependency*

The effect of the substrate temperature on the deposition process was investigated by performing a series of depositions in the temperature range

between 125 °C and 325 °C. The pulse times were kept at constant values of 10 s for TMP plasma, 5 s for O_2 plasma, and 7 s for TTIP vapor, and were all sufficiently long to be in the saturated regions according to figure 6.5. Film thickness and density were determined by XRR, and the GPC was calculated by dividing the thickness by the number of cycles. The results are shown in figure 6.6b. For comparison purposes, the GPC of a process consisting of only TMP plasma pulses (15 s, followed by 15 s pumping) measured by in-situ spectroscopic ellipsometry was plotted on the same temperature axis in figure 6.6a.

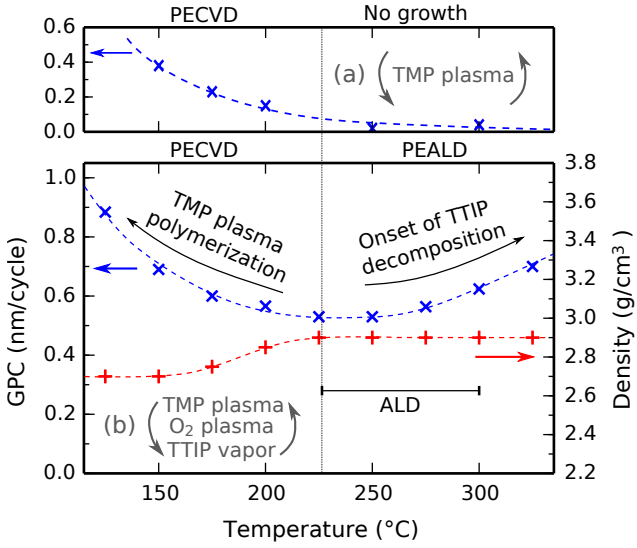

Figure 6.6: Growth per cycle as a function of the substrate temperature, as determined for repeated cycles of (a) only TMP plasma and (b) the full process (additionally showing the film density on the right y-axis). The PECVD and PEALD regions are indicated.

Below 225 °C, lowering the temperature results in an increasing GPC and a decreasing film density. This is caused by the plasma polymerization of TMP, which continuously deposits phosphorus-rich material in a CVD growth mode. This effect gets progressively stronger at lower substrate temperatures, as illustrated by figure 6.6a and investigated in detail in previous studies.[30] The resulting films are phosphorus-rich, which renders them hygroscopic because the P−O−P bonds are easily hydrolyzed. Above 225 °C, the plasma polymerization is almost fully inhibited, as shown on the high-temperature side of figure 6.6a. Because there is no longer a CVD component, we are left with an ALD process. The deposited

films are then no longer hygroscopic, and the film density reaches a constant 2.9 g/cm^3.

Above 275 °C, the GPC starts to increase with temperature. Similar behavior has been observed for TiO_2 deposition from TTIP and H_2O[122, 123] or TTIP and O_2 plasma,[124] and it is typically attributed to the thermal decomposition of the TTIP precursor, as studies show that the decomposition rate of TTIP increases strongly around this temperature.[125, 126] However, given the saturative behavior of the TTIP pulse at 300 °C in figure 6.5c, the contribution from thermal decomposition must still be negligible compared to the ALD contribution in each cycle. We therefore conclude that the process has an ALD window between 225 °C and 300 °C, as indicated by the horizontal bar in figure 6.6b.

6.4.4 *Film composition*

Using saturated pulse times and at a substrate temperature of 300 °C, a titanium phosphate film was deposited on a silicon substrate using 120 cycles of the aforementioned process, resulting in a layer thickness of approx. 80 nm. Material characterization was then carried out on this sample. An XPS analysis of the as-deposited material is shown in figure 6.7. The survey spectra show titanium, phosphorus and oxygen peaks; carbon is only present on the film surface from environmental contamination, and disappears almost completely after etching away some of the top surface and exposing fresh "bulk" film material. No silicon is visible, indicating that the deposited film completely covers the silicon substrate surface. Absence of any other peaks indicates that the film is pure.

Using an energy scale calibration where the C 1s peak is assigned with a binding energy of 284.5 eV, we find peaks of Ti $2p_{3/2}$ at 459.2 eV, Ti $2p_{1/2}$ at 465.0 eV, P 2p at 133.6 eV (deconvoluted as P $2p_{3/2}$ at 133.4 eV and P $2p_{1/2}$ at 134.3 eV), and O 1s at 531.1 eV. The Ti 2p binding energies correspond with a Ti^{4+} oxidation state, similar to TiO_2. The phosporus and oxygen binding energies are typical for a phosphate, but they are insensitive to the exact kind of phosphate, so they cannot be used to discriminate between e.g. orthophosphate and pyrophosphate.[113]

Using the detailed Ti 2p, P 2p, and O 2p spectra acquired after sputtering, a quantification was performed by integration of the peak areas, subtraction of a Tougaard background[127], and correction with empirical atomic sensitivity factors as reported by Ward and Wood.[128] This yielded an empirical stoichiometry of $TiP_{2.0}O_{5.8}$. This quantification is, however, subject to various errors, including stoichiometry deviations caused by preferential sputtering, uncertainties in the background determination, and a poor

knowledge of the electron analyzer transmission function; as such, we estimate the relative error to be ±10%.

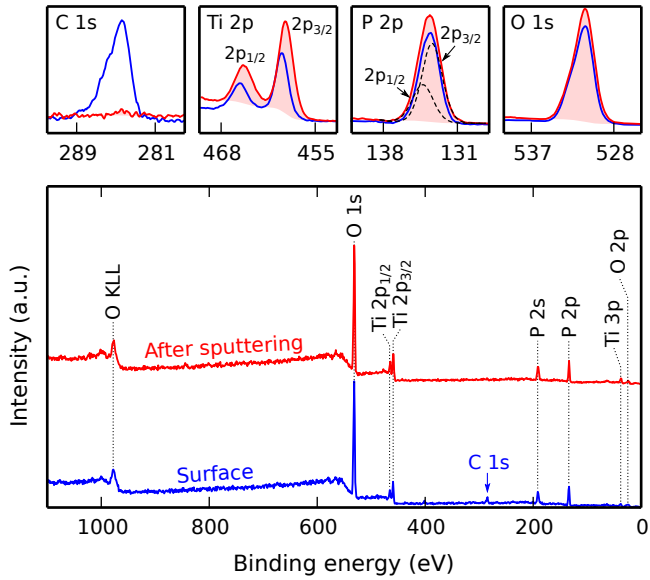

Figure 6.7: XPS analysis of the deposited titanium phosphate film. The survey spectra show the presence of titanium, phosphorus, and oxygen in the bulk of the film (red spectrum) in addition to some carbon which is only present on the film surface (blue spectrum). The detailed C 1s, Ti 2p, P 2p, and O 1s regions are shown above the survey scans using the same color legend; the quantification areas are filled in light red.

To get a more reliable and absolutely quantitative analysis of the stoichiometry, the same film was analyzed by elastic recoil detection (ERD). Figure 6.8 shows the resulting depth profile, along with the quantification results in a table inset. Because the depth information stems from atomic energy loss, which is proportional to the areal density (i.e. the product of the depth and the number density of atoms), the depth profile is primarily given as a function of the areal density. As the number density is unknown and might vary, an exact conversion to a depth in nm is not possible. However, based on linear scaling with the known film thickness, an approximate depth scale in nm is shown on the secondary (upper) x-axis.

The ERD quantification leads to an empirical stoichiometry of $TiP_{1.7}O_{5.6}$, with 4% hydrogen and zero carbon. This should be regarded as the "true" stoichiometry of the as-deposited material, since the errors on the atomic percentages are only ±2% (which is much more accurate than the XPS

quantification). This stoichiometry is somewhere in between titanium pyrophosphate (TiP_2O_7) and titanium orthophosphate ($TiP_{1.3}O_{5.3}$), and as such, the deposited material could be regarded as a mixture of both.

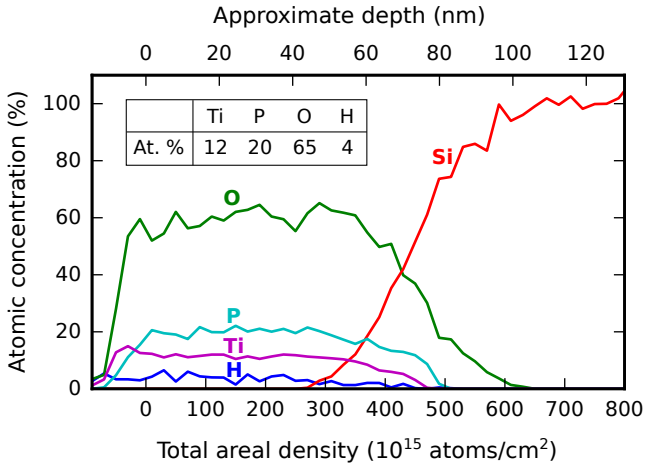

Figure 6.8: ERD depth profile of an 80 nm titanium phosphate film on a silicon substrate. The lower x-axis expresses the depth as a total areal density, while the upper x-axis shows an approximate conversion to a "real" depth (in nm). Titanium, phosphorus, and oxygen are distributed uniformly throughout the layer, along with a small amount of hydrogen; the corresponding atomic percentages are shown in the table inset. No carbon was detected.

6.4.5 *Conformality evaluation*

In order to evaluate the ability of the process to penetrate 3D-structured substrates and coat them conformally, a titanium phosphate film was deposited on a silicon micropillar substrate using 120 cycles of [30 s TMP plasma – 15 s O_2 plasma – 21 s TTIP vapor] (pulse times were chosen three times as long as required for saturation on the planar substrates) at 300 °C. The micropillar substrate consisted of an array of vertical pillars (50 µm long and 2 µm wide, arranged in a square lattice with a lattice spacing of 7 µm) etched into silicon.

A side-view SEM image and EDX analysis of this sample is shown in figure 6.9. The Ti, P, and O intensities overlayed on the SEM image in fig. 6.9a were determined by integration of their corresponding Kα peaks in EDX spectra acquired along horizontal scans at different depths (three of those spectra are visible in fig. 6.9b). In this way, the individual elemen-

tal amounts can be tracked along the penetration depth; this allows us to evaluate not only the total amount of material (i.e. the thickness), but also its composition, which may also vary along the penetration depth. Indeed, while the amount of titanium stays essentially constant along the pillars, the amount of phosphorus decreases by about 20% going from the top to the middle of the pillars. Between the middle and the bottom, it stays rather constant, but near the bottom another 20% decrease is observed. The amount of oxygen remains largely constant along the pillars but decreases by approx. 15% near the bottom. The pronounced differences in behavior between elements are probably related to the fact that oxygen and phosphorus are introduced through plasma exposures, while the titanium comes from a vapor-phase precursor; it is known that plasma exposures do not easily penetrate within trench structures as the radicals get quickly depleted by recombination on the structure walls.[129]

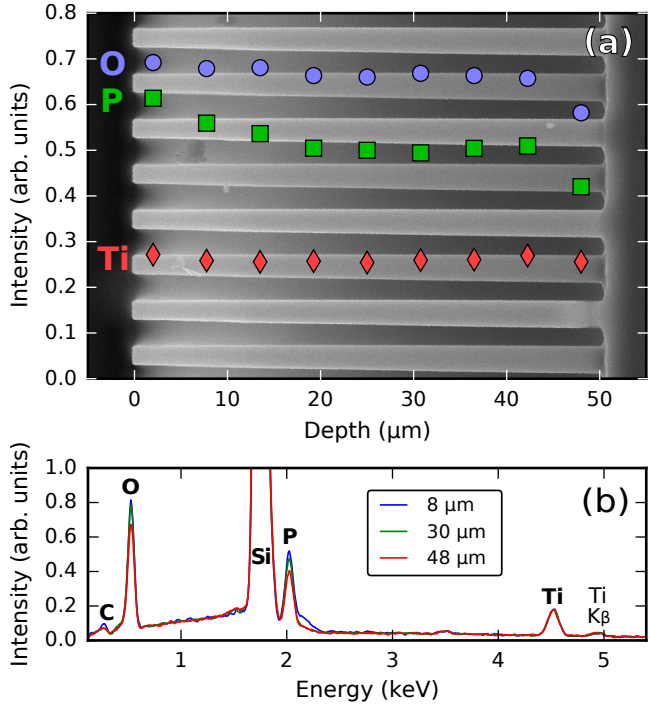

Figure 6.9: SEM/EDX analysis of a silicon micropillar array coated with titanium phosphate, showing (a) the intensities of the Ti, P, and O Kα signals as a function of the penetration depth inside the pillars and (b) the raw EDX spectra at three different depths.

We conclude that, even though the whole structure is coated with titanium phosphate, the amount of deposited material is not entirely constant and there are variations in the stoichiometry along the penetration depth.

6.4.6 *Film crystallinity*

The crystallinity of the deposited titanium phosphate was studied by in-situ XRD during annealing. A 90 nm thick film on a planar silicon substrate was heated from room temperature to 950 °C at a linear heating rate of 10 °C/min in a helium atmosphere, while XRD patterns were continuously acquired in a 2θ range of 19° to 36°. The result is shown in figure 6.10. The as-deposited film is amorphous, and stays amorphous until a temperature of 840 °C is reached. It then tranforms to crystalline titanium pyrophosphate (TiP_2O_7, JCPDS #38–1468),[130] and remains in this phase after cooling down back to room temperature.

The same measurement was also performed in air instead of helium (figure 6.11), with essentially the same result; the same crystallization behavior was observed, albeit with a higher crystallization temperature (890 °C).

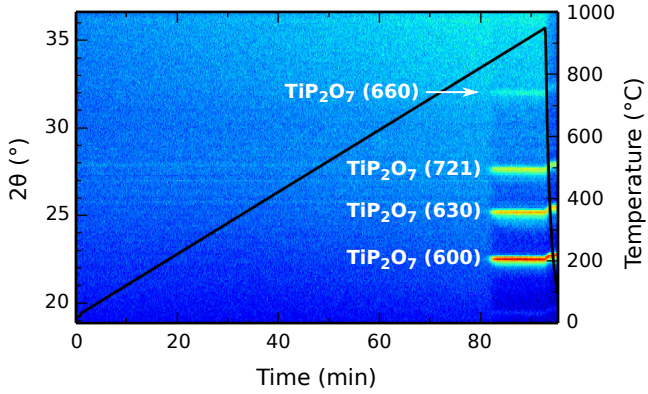

Figure 6.10: In-situ XRD during annealing of a 90 nm thick titanium phosphate film in a helium atmosphere. The diffracted intensity is represented by color intensity as a function of the diffraction angle on the left y-axis and the elapsed time on the x-axis. The temperature profile is drawn by the black solid line, using the temperature scale on the right y-axis.

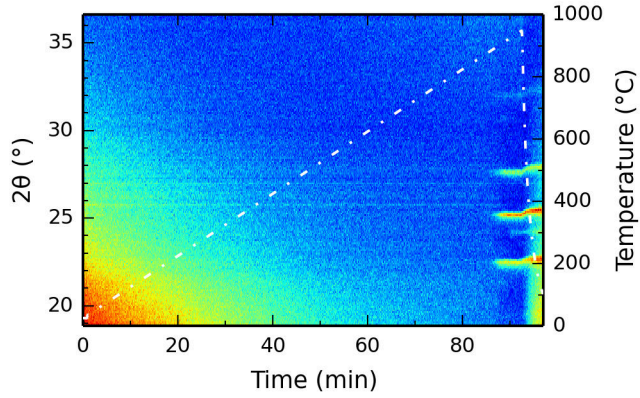

Figure 6.11: In-situ XRD during annealing of a 90 nm titanium phosphate film in an air atmosphere. The diffracted intensity is represented by color intensity as a function of the diffraction angle on the left y-axis and the elapsed time on the x-axis. The temperature profile is drawn by the white dashed line, using the temperature scale on the right y-axis.

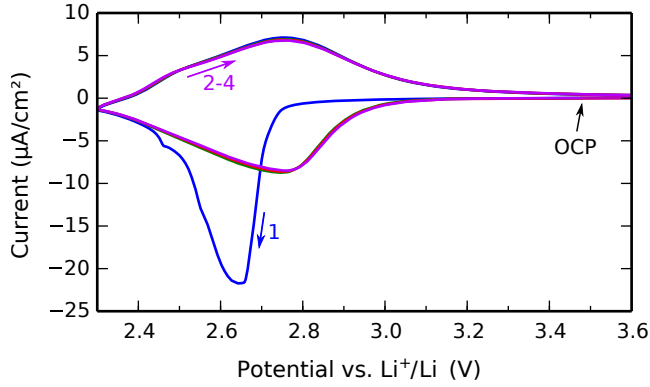

Figure 6.12: Cyclic voltammogram showing the initial lithiation of a 30 nm as-deposited titanium phosphate film. The potential was swept linearly from the open-circuit potential (OCP) to 2.3 V, and then cycled between 2.3 V and 3.6 V at a scan rate of 1 mV/s. Scan numbers are indicated.

6.4.7 *Electrochemical lithiation*

The Li^+ insertion/extraction behavior of the as-deposited, amorphous titanium phosphate was first characterized by cyclic voltammetry.

Right after assembly of the test cell, an open-circuit potential of 3.5 V was measured. During the first scan in the cathodic direction (i.e. decreasing the potential) at 1 mV/s, a lithiation peak was observed around 2.65 V with a total charge insertion of -1.20 μAh/cm^2 (figure 6.12; charges were calculated by integration of the measured current over the elapsed time, which is equivalent to determining the area under the CV peaks and dividing by the scan rate). Subsequent scans at 1 mV/s revealed measured charges of $+1.05$ μAh/cm^2 (oxidation) and -1.02 μAh/cm^2 (reduction). The excess charge measured during the initial lithiation can be attributed to the formation of a solid-electrolyte interphase (SEI), which consumes lithium.[116]

If we approximate the composition of the as-deposited material as TiP_2O_7 with a molar mass of 222 g/mol, and use a thickness of 30 nm and a density of 2.8 g/cm^3 (both measured by XRR), the measured charges correspond with the insertion and extraction of 1.0 moles of lithium per mole of TiP_2O_7. This means we have the following reaction:

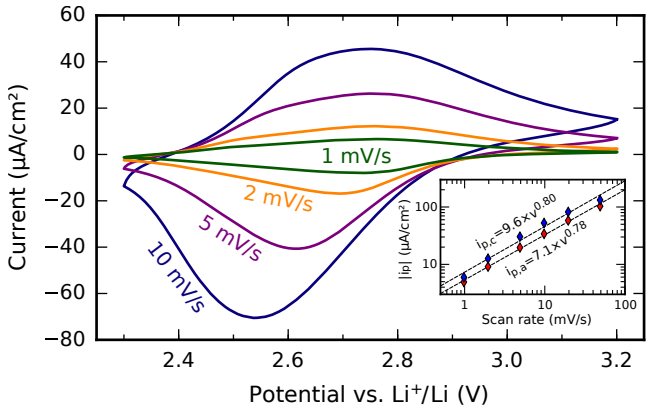

Figure 6.13: Cyclic voltammetry measurements performed between 2.3 V and 3.2 V at scan rates ranging from 1 mV/s to 10 mV/s on a 30 nm as-deposited titanium phosphate film. The figure inset shows the absolute values of the anodic peak current $i_{p,a}$ and the cathodic peak current $i_{p,c}$ as a function of the scan rate v between 1 and 50 mV/s, together with fitted power laws (lines on the double-log scale).

$$TiP_2O_7 + Li^+ + e^- \underset{delithiation}{\overset{lithiation}{\rightleftharpoons}} LiTiP_2O_7$$

where the oxidation state of titanium alternates between +IV (as-deposited, delithiated) and +III (lithiated). Even though the actual (empirical) stoichiometry of the material is slightly different, this reaction should still represent the actual electrochemistry in close approximation.

In order to examine electrode kinetics, additional CV scans were acquired at scan rates of 1, 2, 5, 10, 20, and 50 mV/s between fixed potential limits of 2.3 V to 3.2 V. The resulting cyclic voltammograms (omitting the 20 mV/s and 50 mV/s scans to avoid loss of detail on the 1 mV/s and 2 mV/s scans) are shown in figure 6.13, along with a plot of the anodic and cathodic peak currents ($i_{p,a}$ and $i_{p,c}$) as a function of the scan rate v (figure 6.13, inset). Given that the ratio $i_{p,a}/i_{p,c}$ is significantly less than one, that the peak separation increases with scan rate, and that the peak currents are not proportional to the square root of the scan rate (as predicted by the Randles-Sevcik equation for reversible processes), we can conclude that the Li^+ insertion/extraction reactions at the electrode are electrochemically irreversible.[131] Furthermore, both $i_{p,a}$ and $i_{p,c}$ are in good approximation proportional to $v^{0.8}$; this means that the redox reaction mechanism is neither a diffusion-limited one (where $i_p \sim v^{0.5}$) nor a surface-confined one (where $i_p \sim v$), but is perhaps a combination of both.[35]

6.4.8 *Charge/discharge cycling*

Figure 6.14a shows constant-current charge/discharge curves for the 30 nm titanium phosphate film. Using constant currents of $\pm 1.02\ \mu A/cm^2$ (negative sign for lithiation, and positive sign for delithiation), corresponding to a 1C rate, between potential cut-offs of 2.3 V (lithiation) and 3.2 V (delithiation), lithiation and delithiation capacities of resp. 1.01 $\mu Ah/cm^2$ and 0.99 $\mu Ah/cm^2$ were measured. This yields a coulombic efficiency (defined as the delithiation capacity divided by the lithiation capacity) of 98.6%. Division of the surface-normalized capacity by the film thickness yields a volumetric capacity of 330 mAh/cm^3; an additional division by the density of the material yields a gravimetric capacity of approx. 120 mAh/g.

Figure 6.14b shows the behavior of the material upon repeated cycling, using the same 1C rate and the same potential limits as in the preceding measurement. The measured capacity as a function of the cycle number shows small temperature-related fluctuations together with a systematic decrease due to capacity fading; this decrease only amounts to a loss of

2.2% of the initial capacity after 100 cycles, indicating good cyclability and low capacity fading.

The rate capability of the electrode was investigated by measuring the available capacity for a range of charge/discharge currents between 1C and 100C. For each C-rate, three charge/discharge cycles were ran, and the capacity was determined from the third cycle; in this way, any effect from the preceding C-rates was erased. The same potential limits as previously mentioned were used, so at 1C, the measured capacity was identical to the one shown in fig. 6.14b. The resulting plot of the capacity as a function of the C-rate is shown in figure 6.14c. At higher C-rates, the available capacity decreases; at a rate of 50C, approx. 50% of the 1C capacity remains.

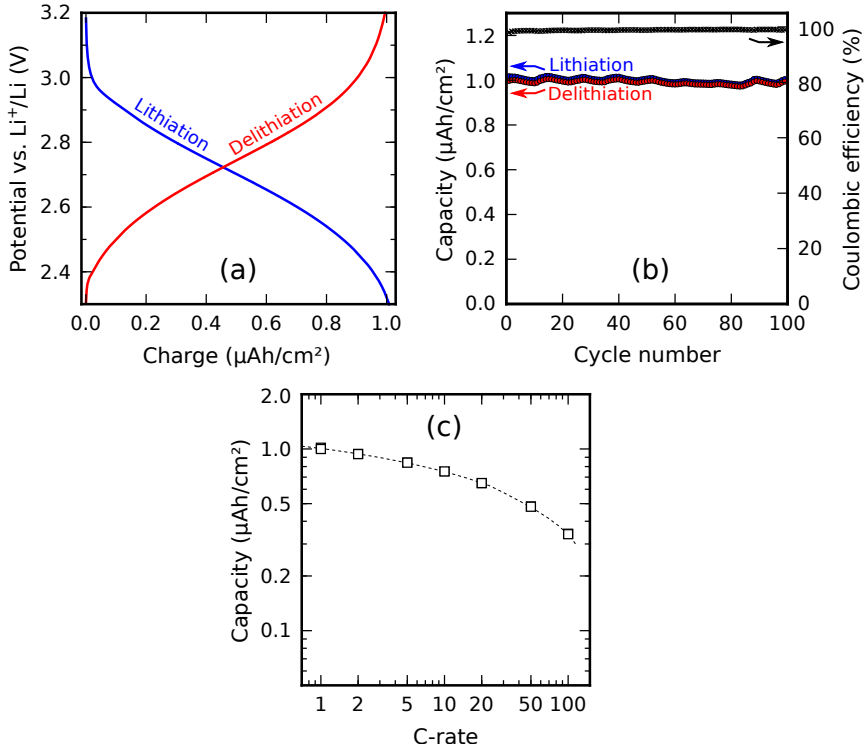

Figure 6.14: Constant-current charge/discharge testing of a 30 nm planar titanium phosphate electrode. (a) Voltage profiles during lithiation and delithiation at 1C; (b) capacity and coulombic efficiency measured over 100 charge/discharge cycles at 1C; (c) capacity as a function of the C-rate.

6.5 CONCLUSIONS

Using pulses of TMP plasma, O_2 plasma and TTIP vapor, a chlorine-free PEALD process for titanium phosphate was developed which worked in a temperature region between 225 °C and 300 °C. At a substrate temperature of 300 °C, precursor saturation and linear growth were observed, demonstrating ALD behavior with a GPC of 0.66 nm/cycle. Outside of this temperature region, the GPC increased; on the low-temperature side due to a CVD contribution from the TMP plasma, and on the high-temperature side due to the decomposition of the TTIP precursor. The films grown at 300 °C had a density of 2.8 g/cm^3 and an empirical stoichiometry of $TiP_{1.7}O_{5.6}$ (measured by ERD); they were amorphous as-deposited, but could be crystallized to TiP_2O_7 by post-deposition annealing in air or helium atmospheres. A silicon micropillar test structure coated with this process showed variations in the amount and composition of the deposited material along the penetration depth, indicating imperfect conformality. The as-deposited material could be electrochemically lithiated and delithiated around 2.7 V vs. Li^+/Li, showing a volumetric capacity of 330 mAh/cm^3 (1.0 μAh/cm^2 for a 30 nm film) and a coulombic efficiency of 98.9%. The material was stable, losing only 2.2% of its initial capacity after 100 cycles. The low film thickness resulted in a good rate capability, still retaining about 50% of the 1C capacity at a rate of 50C.

6.6 SUPPLEMENTAL INFORMATION

6.6.1 *3D electrode testing*

In order to demonstrate the electrochemical capacity enhancement obtainable through 3D structuring of the electrode, a 30 nm titanium phosphate film was deposited on two different platinum-coated 3D micropillar structures. The first one consisted of micropillars with a height of 50 μm and a diameter of 2 μm, arranged in a square lattice with a center-to-center spacing of 7 μm. This geometry yields a surface enhancement factor of:

$$\frac{(7\,\mu\text{m})^2 + 2\,\mu\text{m} \times \pi \times 50\,\mu\text{m}}{(7\,\mu\text{m})^2} \approx 7.4$$

The second structure consisted of micropillars with the same diameter and height but with a smaller center-to-center spacing of 4 μm, resulting in a considerably higher surface enhancement factor:

$$\frac{(4\,\mu\text{m})^2 + 2\,\mu\text{m} \times \pi \times 50\,\mu\text{m}}{(4\,\mu\text{m})^2} \approx 20.6$$

The capacity of each 3D electrode, as well as the one of a planar film for comparison, was evaluated by constant-current charge/discharge cycling. The currents were chosen to approximate 1C rates in each case and amounted to resp. 1 $\mu A/cm^2$ for the planar film, 7 $\mu A/cm^2$ for the $\times 7.4$ micropillar substrate, and 16 $\mu A/cm^2$ for the $\times 20.6$ micropillar substrate. The results are shown in figure 6.15.

Compared to the measured capacity of 1.0 $\mu Ah/cm^2$ in fig. 6.15a, the 3D-structured electrode in fig. 6.15b has a capacity which is 6.0 times higher. This amounts to 81% of the ideal enhancement value of 7.4. The electrode in fig. 6.15c yields a capacity enhancement of a factor of 14.7, while 20.6 would be ideally expected; this corresponds to 71% of the ideal value.

The discrepancy between the geometrical surface enhancement and the measured capacity increase can be attributed to the non-ideal conformality of the deposition process, as has been characterized earlier by SEM/EDX analysis. The increased pillar density on the second 3D substrate presents a higher aspect ratio and lowers the conformality of the coating, resulting in a lower-than-expected capacity enhancement.

Figure 6.16 compares the rate capability of the $\times 20.6$ micropillar electrode to the planar one. The 1C current was determined from the measured capacities, i.e. 1.0 $\mu A/cm^2$ for the planar electrode and 14.7 $\mu A/cm^2$ for the micropillar one. The comparison reveals that the available capacity of both electrodes decreases with the C-rate in the same way; the capacity enhancement factor (visible as the vertical distance between the points because of the log scale in fig. 6.16) remains largely the same up to a rate of 50C. At 100C, the micropillar electrode loses considerably more capacity than the planar electrode. This is attributed to iR-drop over the current collector, as it has to carry a current that is approx. 15 times higher for the micropillar electrode compared to the planar one for the same C-rate.

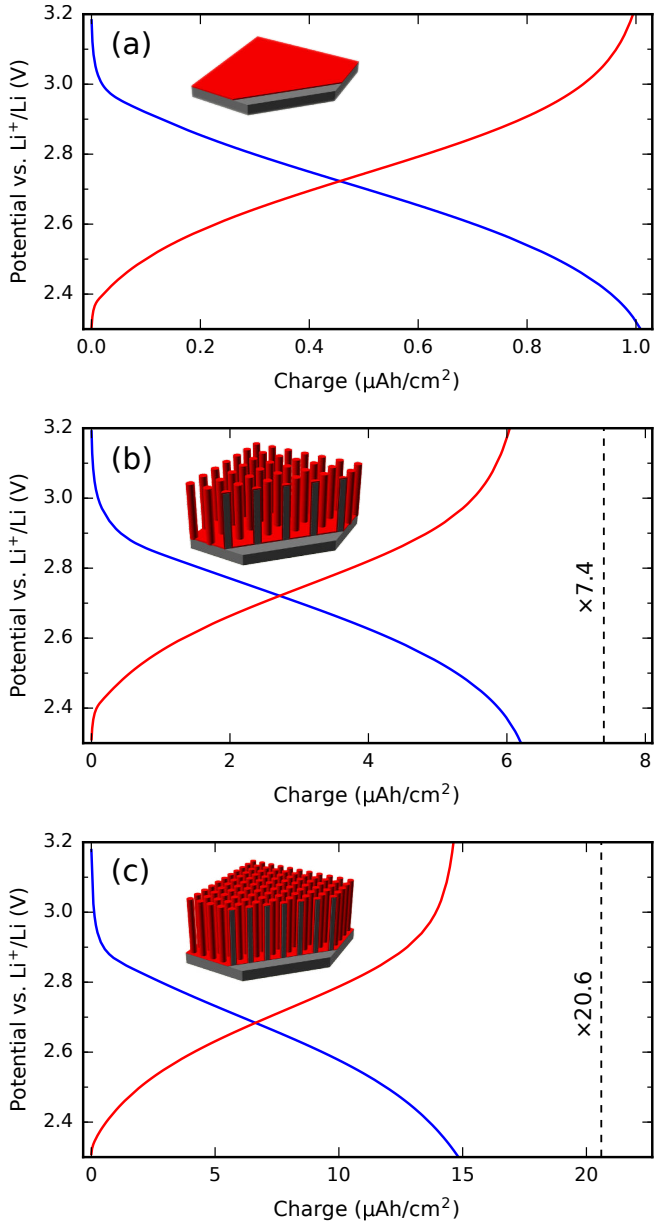

Figure 6.15: Constant-current charge/discharge testing of a 30 nm titanium phosphate film deposited on (a) a planar substrate; (b) a 3D pillar substrate with a surface enhancement factor of 7.4; (c) a 3D pillar substrate with a surface enhancement factor of 20.6.

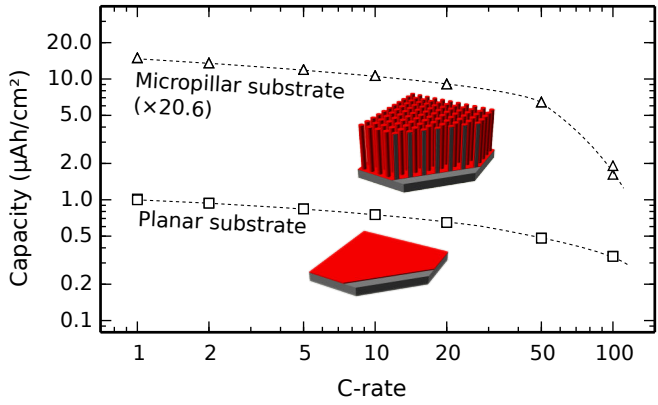

Figure 6.16: Comparison of the rate capabilities of planar and 3D-structured titanium phosphate electrodes.

7

PAPER V: VANADIUM PHOSPHATE

The following chapter has been published as an original research paper in the Journal of Vacuum Science and Technology A, titled *"Plasma-Enhanced Atomic Layer Deposition of Vanadium Phosphate as a Lithium-Ion Battery Electrode Material"*.[34] The content below has been reformatted to fit the layout of this PhD thesis, but is otherwise identical to the submitted version.

7.1 ABSTRACT

Vanadium phosphate films were deposited by a new process consisting of sequential exposures to TMP plasma, O_2 plasma, and either vanadium isopropoxide (VTIP, $OV(O\text{-}i\text{-}Pr)_3$) or tetrakisethylmethylamido vanadium (TEMAV, $V(NEtMe)_4$) as the vanadium precursor. At a substrate temperature of 300 °C, the decomposition behavior of these precursors could not be neglected; while VTIP decomposed and thus yielded a plasma-enhanced chemical vapor deposition (PECVD) process, we found that the decomposition of the TEMAV precursor was inhibited by the preceding TMP plasma/O_2 plasma exposures. The TEMAV process showed linear growth, saturating behavior, and yielded uniform and smooth films; as such, it was regarded as a plasma-enhanced atomic layer deposition (PEALD) process. The resulting films had an ERD-measured stoichiometry of $V_{1.1}PO_{4.3}$ with 3% hydrogen and no detectable carbon contamination. They could be electrochemically lithiated and showed desirable properties as lithium-ion battery electrodes in the potential region between

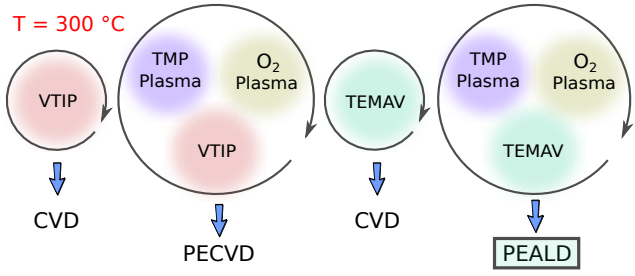

Figure 7.1: Abstract graphic for Paper V.

1.4 V and 3.6 V vs. Li^+/Li, including low capacity fading and an excellent rate capability. In a wider potential region, they showed a remarkably high capacity (equivalent to three lithium ions per vanadium atom), at the expense of reduced cyclability.

7.2 INTRODUCTION

Atomic layer deposition (ALD) is a thin-film deposition method which grows material on a surface by exposing it to alternating chemical precursor vapors. In contrast to chemical vapor deposition (CVD), the precursors are introduced separately, with pumping or purging steps in between them. This causes self-limiting reactions to take place on the substrate surface, resulting in layer-by-layer film growth. Advantages of ALD over CVD include better step coverage (enabling the conformal coating of 3D structures), lower temperature deposition (enabling deposition on temperature-sensitive substrates), and insensitivity to process variations (in a saturated regime, the growth rate is inherently constant, even when the precursor exposure varies).[3] This comes at the expense of very slow growth (typically in the order of 1 Å/cycle), making ALD most suitable for very thin films. Although many different ALD processes have been developed for various classes of materials such as oxides, II-VI and III-V semiconductors, metal nitrides, metals, metal sulfides, and fluorides [65], the existing reports on ALD of phosphates are still limited [12–18, 21, 26, 30, 31] but have recently been increasing in number because of their relevance as electrode [22–24, 32, 33] or electrolyte [19, 20, 27, 29] films in lithium-ion batteries.

Various forms of vanadium oxide (VO_x) can be grown using existing, well-characterized ALD processes based on e.g. vanadium triisopropoxide (VTIP, $OV(O\text{-}i\text{-}Pr)_3$)[132] or tetrakisethylmethylamido vanadium (TEMAV, $V(NEtMe)_4$)[97, 133] as the vanadium precursor. To our knowledge, ALD of vanadium phosphate has not been attempted before. The most closely related work is perhaps a recent report by Strempel et al., wherein a submonolayer of phosphorus was deposited on the surface of V_2O_5 powder in order to modify its catalytic properties.[134] However, no "bulk" vanadium phosphate was synthesised.

In addition to its applications in catalysis, vanadium phosphate finds use as a lithium-ion battery electrode material. In its lithiated, monoclinic crystalline form, $Li_3V_2(PO_4)_3$ (LVP) is known as a high-energy, high-power (i.e. high rate performance) cathode material.[135, 136] Other forms are similarly active; in the amorphous state, it can be regarded as a V_2O_5-P_2O_5 (phosphovanadate) glass, which has been well studied already in

the 1980's as a candidate electrode for lithium cells. [137–139] Some authors have also explored the use of (Li)V(O)PO_4 as a conversion-type anode material. [140–142]

In this study, we present a plasma-enhanced atomic layer deposition (PEALD) process for vanadium phosphate. We incorporate phosphorus by means of a trimethyl phosphate (TMP) plasma; we have previously used this method successfully for PEALD of aluminium phosphate[30], zinc phosphate[31], iron phosphate[32] and titanium phosphate[33]. Our plasma-enhanced method has the advantage of forming highly reactive phosphate species on the surface which easily react with a metalorganic precursor, typically resulting in high growth rates. The drawback is that the substrate temperature must be sufficiently high in order to inhibit any spontaneous polymerization of the TMP plasma, which results in an undesirable CVD contribution.[30] This makes it more challenging to find a suitable metalorganic precursor; an insufficiently high decomposition temperature will result in thermal precursor decomposition and also yield an undesirable CVD contribution.

With this in mind, we start our experiments by investigating the decomposition behavior of two vanadium precursors, VTIP and TEMAV, in the phosphate process using in-situ ellipsometry. Based on these results, we then develop and characterize a PEALD vanadium phosphate process and test the resulting material as a lithium-ion battery electrode.

7.3 EXPERIMENTAL

7.3.1 *Deposition system*

Depositions were carried out in a home-built pump-type PEALD reactor, shown schematically in figure 7.2. All parts were stainless steel, unless otherwise specified.

The deposition chamber was continuously evacuated by a turbomolecular pump to a base pressure of approx. 4×10^{-6} mbar. Precursor vapors and gases were admitted through computer-controlled pneumatic valves. The TMP (Sigma-Aldrich, 97%), VTIP (Sigma-Aldrich), and TEMAV (Air Liquide) precursor bottles were heated to resp. 45 °C, 90 °C, and 75 °C. TMP and VTIP were transported by their own vapor pressure (reaching approx. 5×10^{-3} mbar in the deposition chamber), while TEMAV was carried by an argon flow. The argon and O_2 gas supplies were adjusted to reach a pressure of 5×10^{-3} mbar in the chamber. To avoid CVD side reactions, pumping times in between precursor exposures were chosen

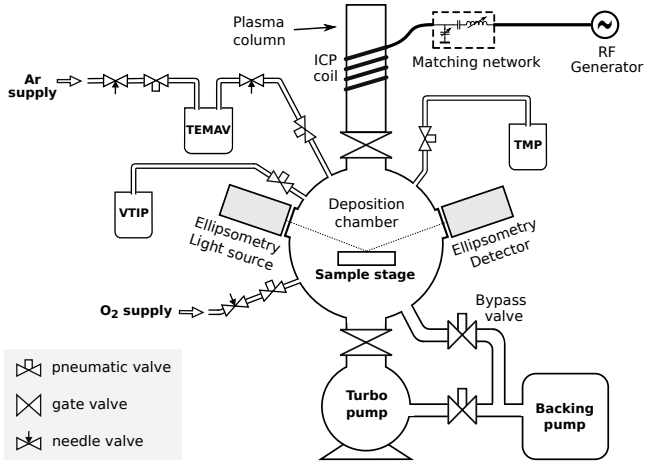

Figure 7.2: Schematic drawing showing the essential components of the home-built PEALD setup used for all the depositions in this study, including the vacuum chamber along with its pumping system, the precursor connections, the inductively coupled plasma setup, and the in-situ ellipsometry light source and detector.

sufficiently long (approx. 20 s) to bring residual pressures down to below 4×10^{-5} mbar. The temperature of the chamber walls was set to 130 °C, and all precursor tubes leading to the chamber were additionally heated to prevent any precursor condensation.

On top of the chamber, a gate valve led to a fused quartz column wrapped by a copper coil. The coil was connected to a 13.56 MHz RF generator (ENI GHW-12Z) and a matching network in order to generate an inductively coupled plasma in the column. The remote plasma was generated by feeding vapor or gas from the chamber to the plasma column through the gate valve and pulsing the RF generator. The plasma power was set to 200 W for the TMP plasma and 300 W for the O_2 plasma, and the impedance matching was tuned to minimize the reflected power on both. The substrates were mounted to a heated copper block, the temperature of which was PID-controlled. Depositions were performed on pieces of standard p-type silicon (100) wafer (for process characterization), or silicon wafer coated with platinum (for electrochemical characterization; the platinum coating functioned as a lithium ion diffusion barrier and as a current collector).

7.3.2 *Material characterization*

In-situ spectroscopic ellipsometry measurements were performed with a J.A. Woollam M-2000 ellipsometer working in the ultraviolet-visible region and using the CompleteEASE software for fitting and data analysis. Measurements were acquired after each deposition cycle. Systematic parameters (angle offsets, window corrections) were fitted prior to deposition and then held fixed. The final thickness and the optical model parameters were fitted to the measurement acquired after the last cycle (i.e. after deposition). A growth curve was then obtained by fitting the thickness to each measurement, keeping all other parameters fixed. The final thicknesses were verified by X-ray reflectometry (XRR) measurements acquired on a Bruker D8 diffractometer using Cu Kα radiation. The XRR patterns were analyzed by fitting simulated patterns to the measured ones, yielding not only the film thickness but also the density. In-situ X-ray diffraction (XRD) during annealing was performed in a home-built setup.[95–97] The annealing atmosphere was either helium or ambient air; the XRD patterns were acquired using a Cu Kα X-ray source and a position sensitive detector. X-ray Photoelectron Spectroscopy (XPS) analysis was performed on a Thermo Scientific Theta Probe XPS instrument using Al Kα X-rays generated at 15 kV and 70 W and focused to a spot size of 0.3 mm by an MXR1 monochromator gun. To remove surface contamination, the sample surface was etched by Ar^+ ions at an acceleration voltage of 3 keV and a current of 2 µA. Elastic recoil detection (ERD) measurements were carried out using an 8 MeV $^{35}Cl^{4+}$ beam, with a scattering angle of 40° and a sample tilt of 20°.

7.3.3 *Electrochemical testing*

Electrochemical test cells were constructed inside an argon-filled glovebox with O_2 and H_2O levels below 1 ppm. The working electrodes consisted of silicon substrates coated with PVD platinum (current collector) and then with PEALD vanadium phosphate (active material). The cells consisted of a PTFE body filled with electrolyte (1 M $LiClO_4$ in propylene carbonate) clamped against the working electrode, with the coated side facing the liquid, and sealed by a circular O-ring defining an electrode area of 1.05 cm^2. All reported currents and charges were normalized against this footprint area, yielding units of resp. µA/cm^2 (current) and µAh/cm^2 (charge). An electrical contact was made by applying conductive silver ink on the cleaved sides of the substrate in order to connect the platinum current collector layer to a piece of copper foil. The counter electrode and reference electrode consisted of lithium metal, thereby measuring all work-

ing electrode potentials against Li^+/Li. Cyclic voltammetry and constant-current measurements were performed with home-built and commercial (Metrohm Autolab) potentiostat/galvanostat systems.

7.4 RESULTS AND DISCUSSION

7.4.1 *Decomposition experiments*

As mentioned in the introductory section, when using TMP plasma, a sufficiently high substrate temperature is required in order to inhibit the spontaneous plasma polymerization of TMP, which would result in PECVD instead of PEALD. Our previous studies using TMP plasma have established this temperature to be 300 °C.[30–33] At this temperature, however, some metalorganic precursors will thermally decompose; this is also the case for our vanadium precursor candidates. From literature, the decomposition temperatures of VTIP and TEMAV are respectively 200 °C and 175 °C, so one would expect strong thermal decomposition of both precursors at 300 °C.[97, 132, 133]

To test their decomposition behavior, we ran experiments where we pulsed the precursors into the chamber onto a silicon substrate heated to 300 °C, while using in-situ ellipsometry to monitor film growth. When only the precursor is pulsed, any film growth is solely due to thermal decompo-

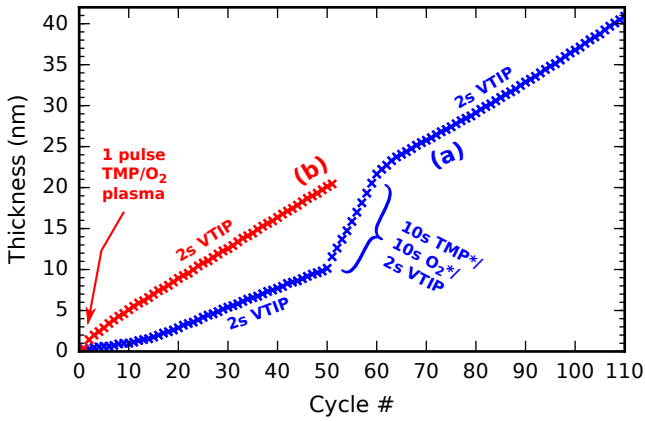

Figure 7.3: Decomposition tests with VTIP at a substrate temperature of 300 °C, showing the evolution of the deposited film thickness as a function of the cycle number for processes consisting of (a) 50 × [2 s VTIP] – 10 × [10 s TMP plasma – 10 s O_2 plasma – 2 s VTIP] – 50 × [2 s VTIP] and (b) 1 × [10 s TMP plasma – 10 s O_2 plasma] – 50 × [2 s VTIP].

sition. The result of doing this experiment with the VTIP precursor is shown in figure 7.3. Curve (a) initially consists of 2 s VTIP pulses, repeated for 50 cycles. Film growth is clearly observed, confirming that the precursor decomposes thermally; neglecting some initial nucleation delay, the growth is linear with a slope of 0.25 nm/cycle (it should be noted that this value is, of course, very dependent on the particular dosing conditions). When included in a vanadium phosphate process (consisting of TMP plasma, O_2 plasma, and VTIP exposures, repeated for 10 cycles, using the same 2 s pulse duration of VTIP), linear growth is again observed, but at a significantly higher growth rate of 1.2 nm/cycle. This can be considered as PECVD of vanadium phosphate, with the CVD contribution originating from the thermal decomposition of VTIP. When the first pulse sequence (50 pulses of 2 s VTIP) is repeated after the 10-cycle phosphate process, thermal decomposition proceeds at a rate of 0.35 nm/cycle, which is higher than before the phosphate process. It appears that the presence of phosphate on the substrate surface enhances the thermal decomposition rate. Indeed, when this experiment is repeated with just a single phosphate exposure pulse (10 s TMP plasma, followed by 10 s O_2 plasma), again followed by 50 VTIP pulses, as in curve (b), no initial nucleation delay is observed, and the VTIP immediately starts decomposing at a rate of 0.35 nm/cycle.

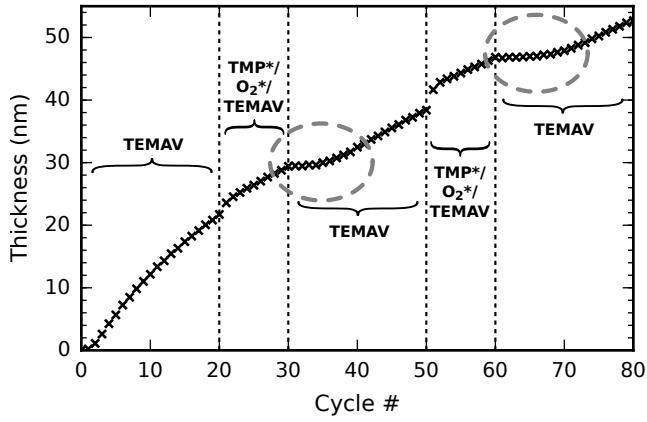

Figure 7.4: Decomposition test with TEMAV at a substrate temperature of 300 °C, showing the evolution of the deposited film thickness as a function of the cycle number for a process consisting of 20 × [20 s TEMAV] – 10 × [15 s TMP plasma – 10 s O_2 plasma – 20 s TEMAV] – 20 × [20 s TEMAV] – 10 × [15 s TMP plasma – 10 s O_2 plasma – 20 s TEMAV] – 20 × [20 s TEMAV].

When a similar experiment is done with TEMAV instead of VTIP, the results are remarkably different, as illustrated in figure 7.4. When pulsing TEMAV onto a blank silicon substrate at 300 °C, thermal decomposition occurs at a rate of approx. 1.0 nm/cycle over 20 pulses of 20 s TEMAV. When included in a vanadium phosphate process (consisting of TMP plasma, O_2 plasma, and TEMAV exposures, repeated for 10 cycles), the growth rate is, surprisingly, slightly lower than when only pulsing TEMAV. This is incompatible with the naive idea of a CVD contribution adding to the growth rate of the total process. Moreover, when pulsing only TEMAV after having deposited vanadium phosphate, growth ceases for about five cycles before resuming (as circled by the dashed gray line in figure 7.4). This effect is repeatable: after decomposition has resumed, running 10 cycles of vanadium phosphate is again sufficient to temporarily inhibit the growth caused by the subsequent TEMAV exposures.

In conclusion, on a blank silicon substrate, at 300 °C, both VTIP and TEMAV decompose thermally. In the presence of phosphate covering the substrate surface, VTIP decomposes at an even higher rate, making a PEALD process impossible due to the CVD contribution. The decomposition of VTIP leads to a poorly-controlled PECVD process and yields non-uniform films. However, TEMAV exhibits strikingly different behavior: in the presence of phosphate, its thermal decomposition ceases. This effect enables us to develop a PEALD process for vanadium phosphate using TEMAV at a substrate temperature of 300 °C, even though this temperature is significantly above the traditionally reported decomposition temperature of the precursor. Our empirical tests reveal that, as long as the phosphate step is included, no thermal decomposition takes place, resulting in a well-controlled PEALD process yielding high-quality films.

7.4.2 *Growth of vanadium phosphate*

From this point on, all depositions have been done using the [TMP plasma – O_2 plasma – TEMAV] process sequence at a substrate temperature of 300 °C, unless otherwise specified. In figures 7.5 and 7.6, pulse times of resp. 15 s, 10 s, and 20 s were chosen, which will later be shown to be in a saturated region.

Figure 7.5 shows a growth curve measured by in-situ ellipsometry during a 50-cycle deposition, revealing linear film growth at a growth rate of 0.78 nm/cycle with no nucleation delay. An ex-situ XRR measurement of the same film after deposition is shown as an inset; the strong and non-decaying fringes indicate a high-quality, smooth film, and the associated film thickness of 39 nm agrees with the in-situ ellipsometry measurement.

Figure 7.6a illustrates the excellent correspondence between the measured Ψ and Δ angles during in-situ ellipsometry and the calculated curves based on a Tauc-Lorentz optical model. By varying only the film thickness as a parameter, the measured curves are reproduced almost perfectly by the calculation, giving confidence in the optical model and in

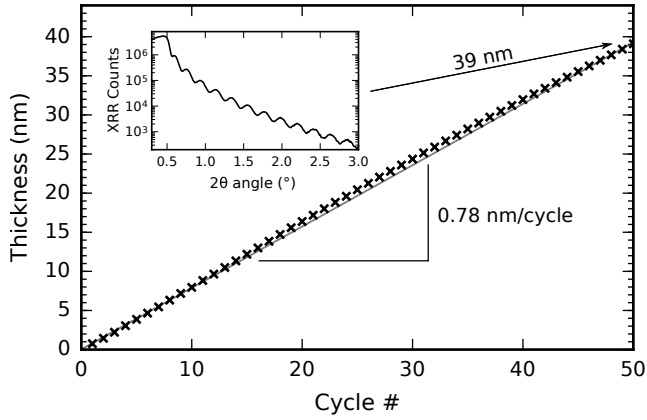

Figure 7.5: Growth curve acquired by in-situ ellipsometry during deposition of vanadium phosphate. The inset shows the corresponding XRR pattern after deposition, yielding a layer thickness of 39 nm.

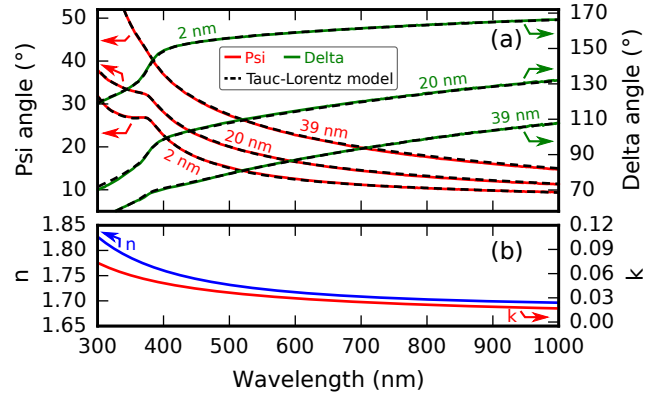

Figure 7.6: Composite plot containing (a) the evolution of the ellipsometric Ψ and Δ angles during film growth, showing excellent correspondence between the measured and the calculated curves, and (b) the optical model of the as-deposited material, showing the refractive index n and the absorption coefficient k as a function of the wavelength (shared x-axis).

the accuracy of the film thickness determination. The dispersion curve (i.e. the wavelength-dependent value of the refractive index) is shown in figure 7.6b. It reveals that the deposited vanadium phosphate has a refractive index of 1.72 at a standard wavelength of 589 nm.

7.4.3 *Pulse time dependency*

The saturation behavior of the process was investigated by running a series of depositions where only one of the pulse times was systematically varied, while keeping the two others constant. For each combination, a 50-cycle deposition was carried out, and the resulting sample was measured by XRR in order to determine the film thickness and density. The average growth per cycle (GPC) was calculated by dividing the film thickness by the number of cycles. The results are shown in figure 7.7. The three subplots show both the GPC and the density as a function of the TMP plasma (fig. 7.7a), O_2 plasma (fig. 7.7b), and TEMAV (fig. 7.7c) exposure durations.

Figure 7.7a reveals a decreasing GPC with increasing TMP plasma duration. Although this is very unexpected for an ALD process (conventionally, increasing the precursor exposure results in an increased GPC, until saturation occurs), it is not surprising when taking into account the results of the decomposition experiments. Without TMP plasma, no phosphate is present on the substrate surface, and TEMAV thermally decomposes,

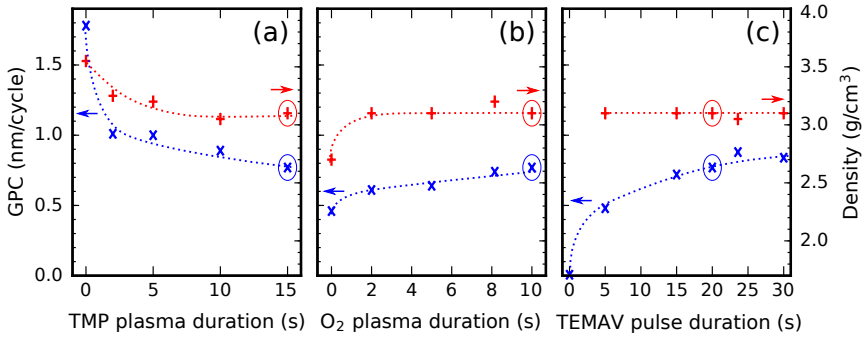

Figure 7.7: The growth per cycle (left y-axis, blue crosses) and the film density (right y-axis, red plus signs) as a function of (a) the TMP plasma duration, (b) the O_2 plasma duration, and (c) the TEMAV pulse duration. The y-axes are shared. The circled points indicate the "standard" durations which were used for the non-varied pulse times. Dashed lines are guides to the eye.

resulting in a high GPC and an increased film density (the decomposition product mainly consists of vanadium oxide, which is denser than vanadium phosphate).

Figure 7.7b demonstrates that the O_2 plasma duration has only a small influence on the GPC (causing it to increase slightly between 2 s and 10 s exposure) and no measurable influence on the film density (it remains constant in the same interval). Without O_2 plasma (the 0 s point, i.e. a [TMP plasma - TEMAV] process), the process also works, albeit with a lower GPC and a significantly lower film density. It is likely that this is caused by (low-density) carbon contamination, which is removed by combustion when including the O_2 plasma.

Figure 7.7c resembles a typical "slow saturation" ALD curve. It confirms that we have a PEALD type process, and that the TEMAV precursor does not exhibit significant thermal decomposition; otherwise, the GPC would be proportional to the TEMAV pulse duration. The film density remains constant at 3.1 g/cm^3 and is independent of the TEMAV exposure.

7.4.4 *Temperature dependency*

The influence of the substrate temperature on the deposition process was investigated by carrying out 50-cycle depositions between 150 °C and 350 °C. The pulse durations were fixed to the saturated values as shown by the circled points in figure 7.7. As in the previous section, the result-

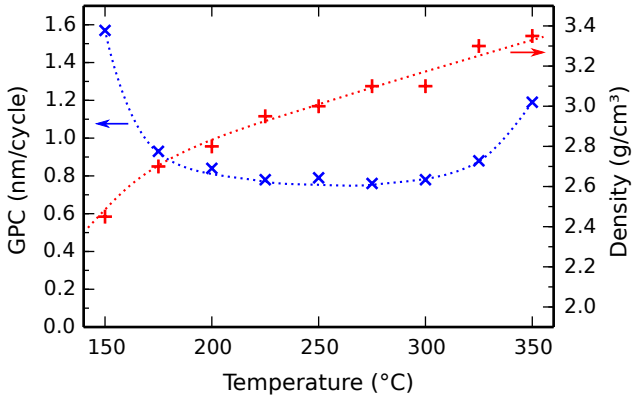

Figure 7.8: The growth per cycle (left y-axis, blue crosses) and the film density (right y-axis, red plus signs) of the vanadium phosphate films as a function of the substrate temperature between 150 °C and 350 °C. Dashed lines are guides to the eye.

ing samples were measured by XRR in order to extract the GPC and film density. The results are shown in figure 7.8.

On the low-temperature side, when the temperature decreases below approx. 200 °C, the GPC increases and the film density decreases. This can be attributed to a CVD component caused by the continuous polymerization of the TMP plasma, as was also observed in other processes using TMP plasma.[30–33] The resulting films are then phosphorus-rich, resulting in a decreased density.

On the high-temperature side (above 300 °C), the GPC and density increase with temperature. We attribute this to the thermal decomposition of TEMAV, resulting in an extra contribution of a (higher-density) vanadium oxide decomposition product.

In the temperature region between 200 °C and 300 °C, the GPC is observed to remain constant. Alhough this is commonly referred to as the "ALD temperature window", this does not explain why the film density increases with temperature; in a classical temperature window, the density should remain constant. We suppose that it is rather a combination of two effects: on the one hand, the GPC may decrease with temperature due to diminishing CVD contributions from the TMP plasma, while on the other hand, it may increase with temperature due to the increased reactivity of the TEMAV precursor. These effects cancel each other out when it comes to the GPC. For the film density, however, this is not necessarily the case; decreasing contributions of the TMP plasma polymerization result in an increasing density, and increasing amounts of vanadium being incorporated may also result in an increasing density, the combined effect being an increasing density with temperature.

7.4.5 *Film composition*

As-deposited films were analyzed by XPS and ERD in order to investigate their chemical composition. They were grown at a substrate temperature of 300 °C, using the same pulse durations as in the previous section. The XPS analysis is shown in figure 7.9. The survey spectra reveal the presence of vanadium, phosphorus, and oxygen. The surface spectrum additionally shows the presence of carbon and nitrogen, which most likely originate from environmental contamination; after sputter erosion, their signals disappear, which implies that they do not occur in the "bulk" of the film. No silicon signal is observed, proving that the silicon substrate is fully covered by the vanadium phosphate film.

After calibrating the energy spectrum so that the peak position of C 1s (surface carbon) occurs at a binding energy of 284.8 eV, the detailed spectra in figure 7.9 reveal P $2p_{1/2}$, P $2p_{3/2}$, V $2p_{1/2}$, V $2p_{3/2}$, and O 1s peak positions of resp. 134.3 eV, 133.4 eV, 524.8 eV, 517.5 eV, and 531.3 eV. After sputter erosion, the peak positions of V $2p_{1/2}$ and V $2p_{3/2}$ shift to resp. 523.9 eV and 516.4 eV, while the phosphorus and oxygen line positions remain unchanged. The phosphorus and oxygen core levels are compatible with a phosphate material, but provide little information on the exact kind of phosphate.[111, 143] The vanadium core levels do yield important information: as the distance between O 1s and V $2p_{3/2}$ is tightly correlated with the oxidation state of vanadium,[144] the observed V $2p_{3/2}$ peak positions reveal a mixture of V^{5+} and V^{4+} on the film surface, and mainly V^{3+} in the bulk of the film. The vanadium peak positions in the bulk of the film did not significantly shift upon further sputter erosion, suggesting that the measured oxidation states were not significantly influenced by the argon sputtering process itself.

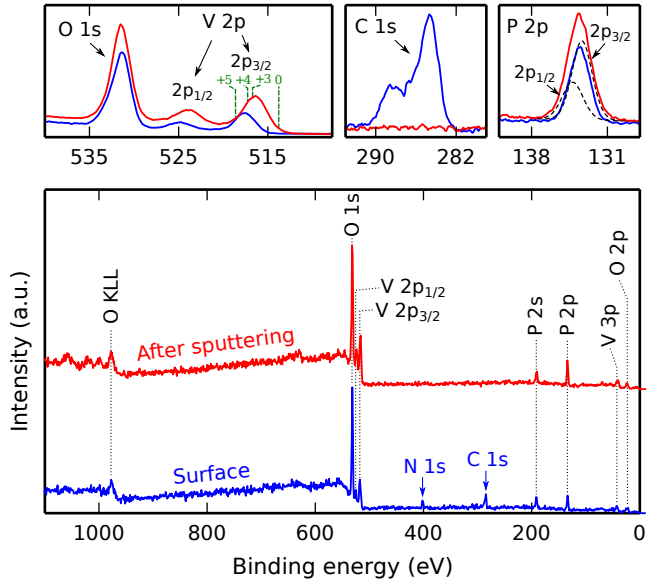

Figure 7.9: XPS analysis of the as-deposited vanadium phosphate. Survey scans and detailed scans were acquired on the film surface (blue) and after argon sputtering (red). Possible vanadium $2p_{3/2}$ oxidation states are labelled by the dashed green lines.

Although XPS can be used for quantification, uncertainties are typically quite large; therefore, we opted to use ERD as a more accurate technique to measure the film stoichiometry, with the added advantage that hydrogen can be detected as a possible impurity element. The ERD depth profile of a 36 nm film is shown in figure 7.10. It should be noted that the depth scale on the upper x-axis of the figure is only approximate, as the true depth scale (lower x-axis) stems from atomic energy loss which is proportional to the total areal density; a rough conversion was provided by comparison with the XRR-measured film thickness in order to aid interpretation. By integrating the amounts of V, P, O, and H over the film thickness, an average stoichiometry of $V_{1.1}PO_{4.3}$ is found with a 3% hydrogen impurity and zero carbon (within the detection limit of 0.1%). This makes it likely that the vanadium is indeed mainly in a 3+ oxidation state, given the triple negative charge of the PO_4^{3-} anion.

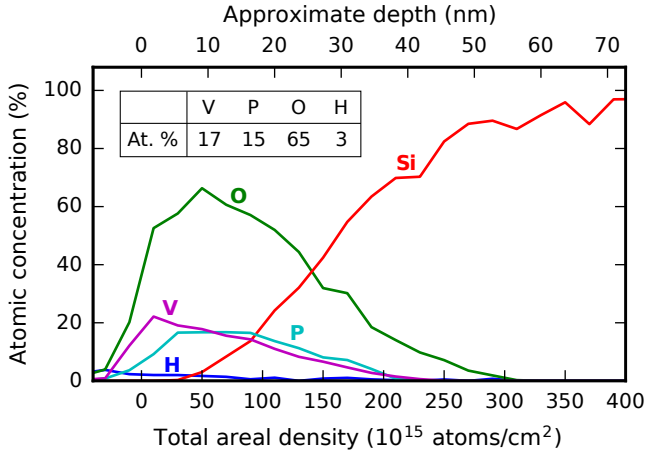

Figure 7.10: ERD depth profile measured on a 36 nm as-deposited vanadium phosphate film, showing the atomic concentrations of elements as a function of the areal density. An approximate depth scale is provided on the secondary x-axis. The table inset shows integrated atomic percentages representing the average film composition.

7.4.6 *Crystallinity*

The crystalline structure of the deposited film was investigated by XRD. Full XRD scans (between 15° and 55° in 2θ angle) were acquired before and after annealing, and are shown in figure 7.11b. The annealing process took place in a helium atmosphere by applying a linear temperature

ramp, starting at room temperature and ramping to 950 °C at a rate of 10 °C/min. During annealing, XRD patterns were acquired using a fixed position sensitive detector with a 2θ window of 16° to 34°, allowing in-situ observation of phase transitions. The resulting plot, showing both the XRD intensity and the temperature as a function of the elapsed time, is given in figure 7.11a.

The as-deposited film does not show any diffraction peaks and is thus amorphous. The film stays amorphous until heated to a fairly high temperature of 900 °C, where the sudden formation of crystalline VPO_4 (orthorhombic; JCPDS #76-2023) appears by its (110) reflection at 20.4°. In the full XRD scan, the (200), (112), (220), and (202) reflections are additionally visible at resp. 34.3°, 35.2°, 41.6°, and 45.1°. Given that the intensity ratios differ from the powder diffraction data and that many additional calculated reflections are not observed, it is likely that there is a high degree of preferential orientation.

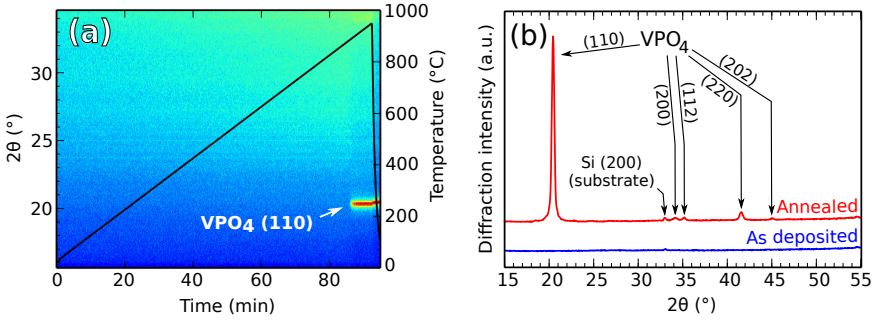

Figure 7.11: In-situ X-ray diffraction during annealing of the as-deposited vanadium phosphate in a helium atmosphere. (a) Color plot showing the evolution of the XRD pattern (in color intensity, left x-axis) and temperature (black solid line, right y-axis) as a function of time; (b) Conventional XRD patterns acquired at room temperature, before and after annealing.

7.4.7 *Electrochemical characterization*

7.4.7.1 *Cyclic voltammetry*

The as-deposited material was tested as a lithium-ion battery electrode. A test cell was assembled using, as the working electrode, a 35 nm vanadium phosphate film deposited on a planar Pt-coated silicon substrate. An open-circuit potential (OCP) of 3.12 V was measured. It was then lithiated by

cyclic voltammetry: starting from the OCP, the potential was decreased at a scan rate of –1 mV/s, until a potential of 0.5 V was reached. This was followed by delithiation through a reversal of the scanning direction up to 4.3 V. The resulting CV pattern is shown in figure 7.12a. Between the OCP and approx. 1 V, almost no current flow is observed, implying that almost no lithium ions are inserted. Between 1 V and 0.5 V, however, a large and sharply peaked reduction reaction is observed, consisting of a doublet with the first peak (at 0.75 V) corresponding to a charge insertion of –3.6 μAh/cm^2, and the second one (at 0.65 V) to a charge insertion of –4.6 μAh/cm^2, with a total inserted charge of –8.2 μAh/cm^2. Assuming

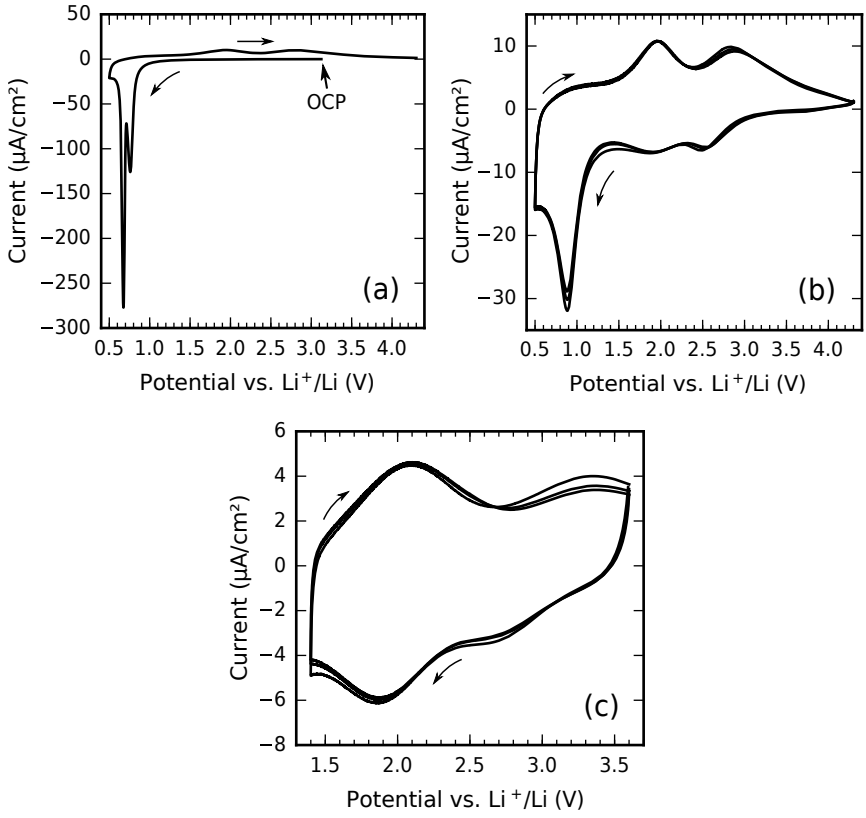

Figure 7.12: Cyclic voltammetry experiments showing (a) the initial lithiation of a 35 nm as-deposited vanadium phosphate film; (b) subsequent cycling between 0.5 V and 4.3 V; and (c) subsequent cycling between 1.4 V and 3.6 V. All patterns were acquired at a scan rate of 1 mV/s. The scanning directions are indicated by arrows.

that the film consists of VPO_4 (which is close to the stoichiometry measured by ERD), with a molar mass of 146 g/mol, a density of 3.1 g/cm^3, and a thickness of 35 nm, it requires a charge of 2.0 μAh/cm^2 to insert one lithium ion. The first peak can likely be attributed to the intercalation of Li^+ in VPO_4, reducing V(+III) to V(+II):

$$VPO_4 + Li^+ + e^- \longrightarrow LiVPO_4$$

This reaction consumes a charge of 2.0 μAh/cm^2, while 3.6 μAh/cm^2 was measured. We thus hypothesize that, in addition to the conversion of V^{3+} to V^{2+}, an additional charge of 1.6 μAh/cm^2 was consumed in the build-up of a solid-electrolyte interphase (SEI).[116] The second peak is attributed to a conversion reaction where vanadium is reduced from V(+II) to V(0) (i.e. vanadium metal):

$$LiVPO_4 + 2\,Li^+ + 2\,e^- \longrightarrow Li_3PO_4 + V$$

The above reaction consumes a charge of 4.0 μAh/cm^2, while 4.6 μAh/cm^2 was measured; the small difference can either be attributed to measurement inaccuracies or to an extra SEI contribution.

Upon re-oxidation to 4.3 V, a total charge of +5.7 μAh/cm^2 is extracted. This is close to the expected charge (+6.0 μAh/cm^2) associated with a full re-oxidation of V(0) to V(+III):[140]

$$Li_3PO_4 + V \longrightarrow VPO_4 + 3\,Li^+ + 3\,e^-$$

Repeated cycling between 0.5 V and 4.3 V, as shown in fig. 7.12b, yields charges of resp. –6.8, +5.9, –6.6, +5.8, –6.4, and +5.7 μAh/cm^2. Perhaps due to incomplete SEI build-up, or due to some other electron-consuming side reaction, the cathodic capacity remains systematically larger than the anodic capacity. Figure 7.12c shows subsequent CV cycling on the same electrode within a narrower potential range between 1.4 V and 3.6 V. This results in charges of resp. –2.0, +2.0, –2.0, +2.0, –2.0, and +1.9 μAh/cm^2; while the capacity is lower (approx. one Li^+ per unit of VPO_4 is inserted or extracted, compared to three in the extended potential range), the difference between the cathodic and anodic capacities is now much smaller. Rather than having full conversion reactions between V(+III) and V(0), we hypothesize that the cycling is now restricted between the V(+III) and V(+II) oxidation states in an intercalation-type reaction:

$$VPO_4 + Li^+ + e^- \longleftrightarrow LiVPO_4$$

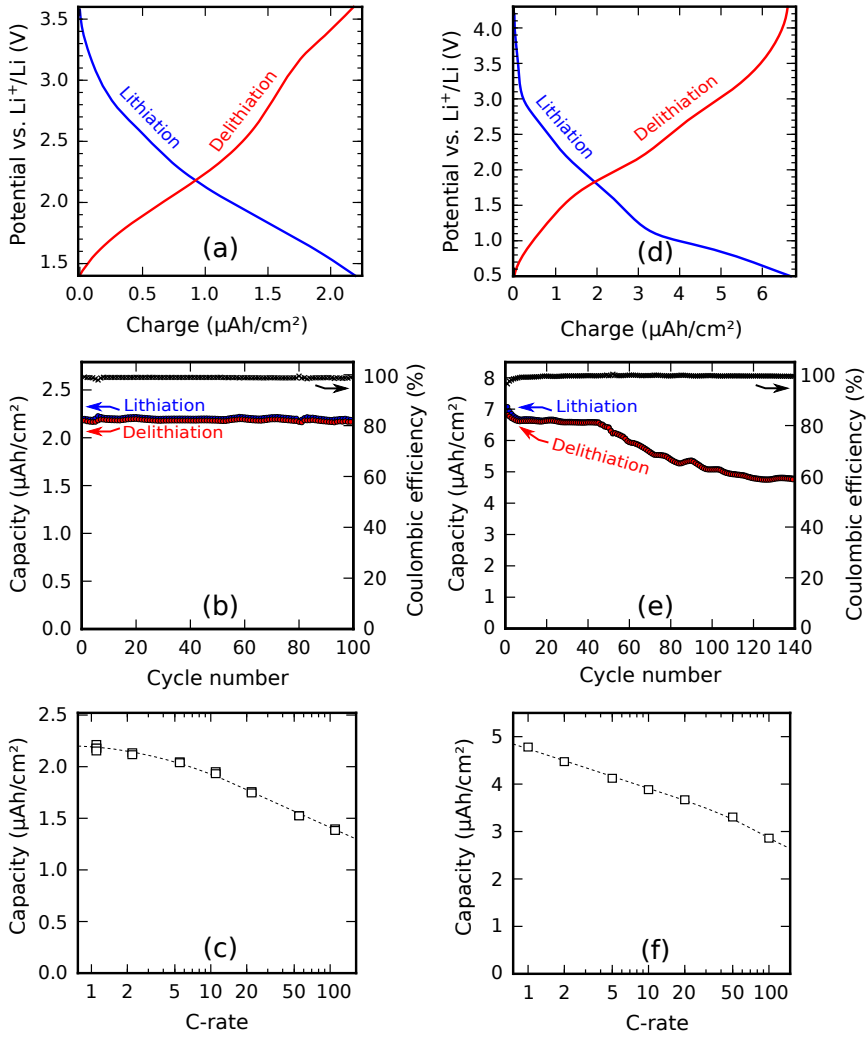

Figure 7.13: Constant-current charge/discharge cycling of a 35 nm vanadium phosphate film between 1.4 V and 3.6 V (a, b, c) and between 0.5 V and 4.3 V (d, e, f), showing (a, d) the potential as a function of the inserted/extracted charge; (b, e) the evolution of the measured capacity (left y-axis) and coulombic efficiency (right y-axis) over multiple charge/discharge cycles at approx. 1C; and (c, f) the available capacity as a function of the C-rate.

7.4.7.2 *Charge/discharge cycling*

After initial lithiation (i.e. the reaction shown in fig. 7.12a), the electrodes were subjected to repeated constant-current charge/discharge cycling, as shown in figure 7.13. These tests were performed in two potential regions: the restricted range between 1.4 V and 3.6 V, used for figures 7.13a, 7.13b,and 7.13c, and the extended range between 0.5 V and 4.3 V, used for figures 7.13d, 7.13e, and 7.13f.

In the restricted potential range, the charge/discharge curves (fig. 7.13a) and the capacity evolution plot (fig. 7.13b) were acquired at constant charge/discharge currents of ± 2.4 $\mu A/cm^2$ (positive for charge, negative for discharge). This yielded an accessible capacity of 2.2 $\mu Ah/cm^2$. Normalized to the film thickness, this corresponds to a volumetric capacity of 630 mAh/cm^3, or taking into account the density of the material, to a specific capacity of 200 mAh/g. Figure 7.13b reveals an average coulombic efficiency of 98.9% and a capacity degradation of only 0.7% over 100 cycles. Assuming a 1C current of 2.2 $\mu A/cm^2$ (corresponding to the current necessary to reach the measured capacity in one hour), fig. 7.13c shows the accessible capacity measured by charge/discharge cycling at multiples of the 1C current up to 100C. The electrode shows an excellent rate capability, still retaining over 60% of its original capacity at a rate of 100C.

In the extended potential range, the charge/discharge curves (fig. 7.13d) and the capacity evolution plot (fig. 7.13e) were acquired at a charge/discharge current of ± 5.7 $\mu A/cm^2$. This resulted in a measured capacity of 6.7 $\mu Ah/cm^2$, i.e. a volumetric capacity of 1.9 Ah/cm^3 or a gravimetric capacity of 620 mAh/g. Although impressively high, this capacity is only retained for 40 cycles, as demonstrated in fig. 7.13e. Upon further cycling, the capacity starts degrading steadily and reaches 4.8 $\mu Ah/cm^2$ after 120 cycles (i.e. a 28% loss compared to the original capacity), whereafter it seems to stabilize again. This rather poor cyclability is typical for conversion-type reactions, and similar behavior has been reported in literature for $VOPO_4$ nanosheet anodes.[141] The coulombic efficiency, however, remains close to 100% (with an average value of 99.6%) throughout the entire cycling experiment. The rate testing results, based on a 1C current of 4.8 $\mu A/cm^2$ (corresponding to the final measured capacity), are shown in fig. 7.13f. Similar to the restricted potential range, the rate capability is excellent, with 60% of the 1C capacity still being available at a rate of 100C.

Although a quantitative comparison with earlier reports on amorphous vanadium phosphate electrodes by Sakurai et al.[138, 139] is not possible

– they focused on V_2O_5–P_2O_5 mixtures with molar ratios between 60% and 95% V_2O_5, while our as-deposited material has only about 52% V_2O_5 based on its measured stoichiometry; furthermore, they cycled in a different potential region of 2.0–3.5 V and used a different electrolyte – some interesting similarities can be noted. The good capacity retention upon repeated cycling (which has been attributed to the presence of phosphorus) is also confirmed here, at least when cycling in the restricted potential range. Compared to the reversible uptake of 0.27 Li/V measured by Sakurai et al.[138] for 60% V_2O_5, we find a much higher value of 1.1 Li/V; this may be due to our lower potential cut-off (1.4 V, versus 2.0 V as chosen by Sakurai et al.) or due to the benefical effect of using a nanoscale thin film rather than a powder mixture.

In the extended potential region (i.e. making use of the full conversion reaction), our results can be compared to the ones of Zhang et al.[141] who started from $VOPO_4$ which was converted to VPO_4 in an initial reduction reaction, making the resulting electrode composition similar to ours. They measured high initial capacities equivalent to approx. 3 Li/V, which however degraded by more than 50% after about 40 charge/discharge cycles. This is very similar to our results. While cycling to low potentials induces full conversion reactions and thus yields a high capacity, it also induces electrode degradation. To prevent this, the potential needs to be restricted to remain above 1.4 V.

7.5 CONCLUSIONS

Using pulses of TMP plasma, O_2 plasma and TEMAV vapor, a PEALD process for vanadium phosphate was developed which worked optimally at a substrate temperature of 300 °C. Given the need for a high substrate temperature to avoid CVD contributions by the TMP plasma, the thermal decomposition of VTIP and TEMAV was investigated. Although both VTIP and TEMAV showed thermal decomposition, TEMAV had the unique property of not decomposing on a substrate surface when phosphate was present. This made a PEALD phosphate process possible. The process showed linear growth at a rate of 0.78 nm/cycle, and slow saturation was observed for the TEMAV pulse. The deposited film density continuously increased with substrate temperature, having a value of 3.1 g/cm^3 at 300 °C, while the GPC strongly increased below 200 °C and above 300 °C due to resp. TMP plasma polymerization and thermal decomposition of TEMAV. The deposited material consisted of $V_{1.1}PO_{4.3}$ with 3% hydrogen and zero carbon, as measured by ERD, and XPS revealed that the vanadium was mainly in a 3+ oxidation state. The material

was amorphous as-deposited, but could be crystallized to VPO_4 by post-deposition annealing to 900 °C in a helium atmosphere. The as-deposited material could be electrochemically lithiated and delithiated, showing a volumetric capacity of 630 mAh/cm^3 between 1.4 V and 3.6 V, and a remarkably high 1.9 Ah/cm^3 between 0.5 V and 4.3 V vs. Li^+/Li. However, while long-term cycling in the former potential region was possible with almost no capacity degradation (0.7% over 100 cycles), in the latter region, the capacity started degrading after 40 charge/discharge cycles, resulting in a 28% capacity loss after 140 cycles. In both regions, the electrode had a high coulombic efficiency and an excellent rate capability, still maintaining over 60% of its 1C capacity at a rate of 100C.

8

CO/NI PHOSPHATE AND CO/NI/FE PHOSPHIDE

8.1 PLASMA-ENHANCED ALD OF COBALT PHOSPHATE

In similarity to the processes described in the previous chapters, a PEALD process for cobalt phosphate was developed by using TMP plasma and O_2 plasma as the phosphate delivery mechanisms and $Co(Cp)_2$ (cobaltocene) as the cobalt precursor. This results in the following three-step process sequence:

1. TMP plasma exposure
2. O_2 plasma exposure
3. $Co(Cp)_2$ vapor exposure

The use of $Co(Cp)_2$ as an ALD precursor had already been demonstrated by e.g. Donders et al., who combined it with O_2 plasma to yield thin films of Co_3O_4.[145] The process described here can be seen as a modification of this process, i.e. by adding TMP plasma, which results in the incorporation of phosphorus and significantly changes the growth characteristics.

8.1.1 *Growth characterization*

The deposition process was characterized by in-situ ellipsometry. Measurements were acquired after each cycle and fitted with a generalized oscillator model, allowing calculation of the film thickness after each cycle. The optical model yielded a refractive index of 1.72 at a wavelength of 589 nm. Depositions were performed within a range of substrate temperatures (at constant pulse durations) and with varying pulse durations (at a constant substrate temperature) in order to investigate the influence of these parameters on the growth process.

TEMPERATURE DEPENDENCY The influence of the substrate temperature on the growth process is depicted in figure 8.1. Pulse times were fixed to 10 s, 20 s, and 7 s for resp. TMP plasma, O_2 plasma, and cobaltocene. Growth curves at temperatures between 150 °C and 325 °C are compared in fig. 8.1a. Below 275 °C (solid lines), the growth curves are

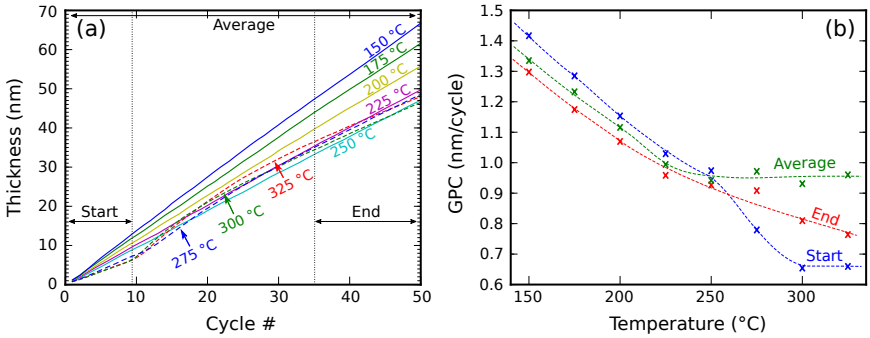

Figure 8.1: (a) Growth curves acquired by in-situ ellipsometry during cobalt phosphate deposition at different substrate temperatures. (b) GPC as a function of substrate temperature determined at the start of growth, end of growth, and averaged over 50 cycles.

linear and their slope (i.e. the GPC) decreases with temperature. At temperatures of 275 ° or higher (dashed lines), there are clear deviations from growth linearity between approx. the 10th and 30th cycle. Before and after this "transition region", the growth is however still linear; therefore, the GPC was separately calculated for the starting section (first 9 cycles), ending section (final 15 cycles) and as an average (final thickness divided by the total number of cycles). Figure 8.1b contains the results of this calculation. The non-linearity at 275 °C and above manifests itself as an increasing difference between the average GPC and the starting/ending GPC.

PULSE TIME DEPENDENCY To avoid CVD contributions by the TMP plasma (as explained in Paper I), the substrate temperature was fixed at 300 °C. At this temperature, the TMP plasma, O_2 plasma, and cobaltocene pulse durations were varied in order to study the saturation behavior of the process. Because the non-linear growth at this temperature makes it difficult to unambiguously define a GPC, the results were plotted in the same way as figure 8.1, yielding figures 8.2, 8.3, and 8.4 (for resp. TMP plasma, O_2 plasma, and cobaltocene), showing both the raw growth curves and the extracted GPC values at different growth stages.

Figure 8.2 shows clear saturative behavior with regard to the TMP plasma duration, yielding growth curves which are almost independent of the pulse durations between 5 s and 15 s. The oxygen plasma dependency (fig. 8.3) is more complicated; the growth increases with increasing O_2 plasma duration, seemingly slowly approaching saturation near the 20 s

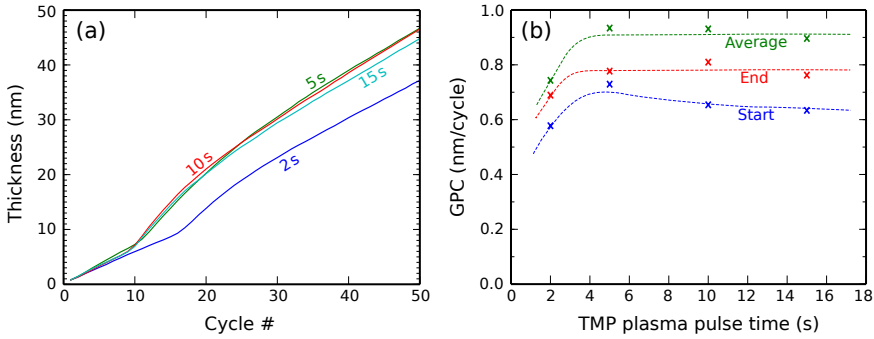

Figure 8.2: (a) Cobalt phosphate growth curves using different TMP plasma durations. (b) GPC as a function of TMP plasma duration determined at the start of growth, end of growth, and averaged over 50 cycles.

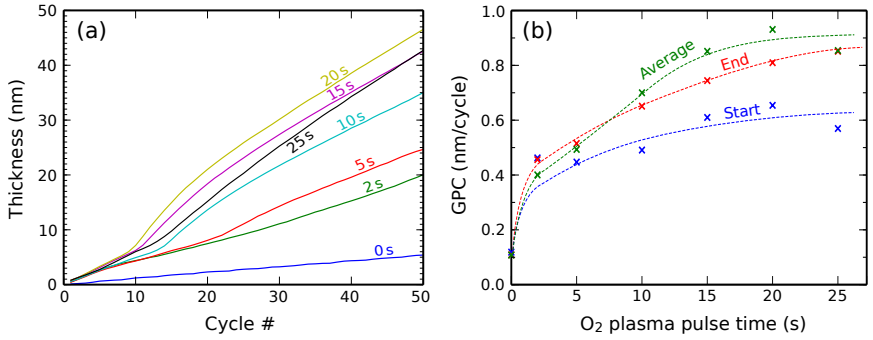

Figure 8.3: (a) Cobalt phosphate growth curves using different O_2 plasma durations. (b) GPC as a function of O_2 plasma duration determined at the start of growth, end of growth, and averaged over 50 cycles.

exposure point. As for many other phosphate processes, there is also growth without O_2 plasma (the 0 s point), although the growth proceeds much slower. Interestingly, the growth is linear in this case (and deviations from linearity are only minor in case of the 2 s curve); the reason for this is unclear. Varying the duration of the cobaltocene pulse, as is done in fig. 8.4, yields mostly identical curves and demonstrates that the process clearly saturates with regard to the cobaltocene pulse duration.

8.1.2 *Film properties*

For all subsequent characterization of the deposited material, the substrate temperature was set to 300 °C and pulse durations were fixed to resp.

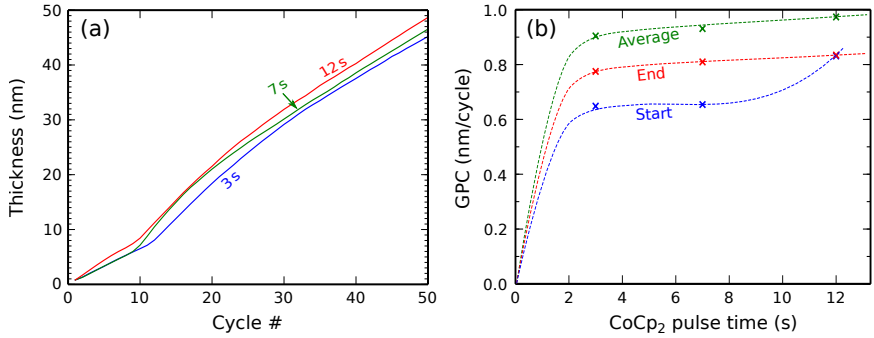

Figure 8.4: (a) Cobalt phosphate growth curves using different cobaltocene exposure durations. (b) GPC as a function of cobaltocene exposure duration determined at the start of growth, end of growth, and averaged over 50 cycles.

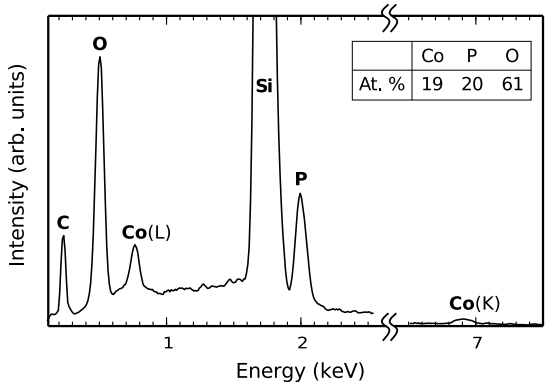

Figure 8.5: EDX analysis of as-deposited cobalt phosphate, with an estimation of atomic percentages as a table inset.

10 s, 20 s, and 7 s for TMP plasma, O_2 plasma, and cobaltocene. An EDX analysis of the as-deposited cobalt phosphate is shown in figure 8.5. The measurement was performed on a (100-cycle) sample with a film thickness of 81 nm and the electron energy was set to 10 keV. Aside from a strong peak of the silicon substrate, the characteristic lines of cobalt, phosphorus, and oxygen are clearly visible, along with some carbon impurity (which might be in part surface carbon). A ZAF-corrected quantification yields a stoichiometry of approx. $CoPO_3$; it should however be noted that the error bars on this estimation are quite large.

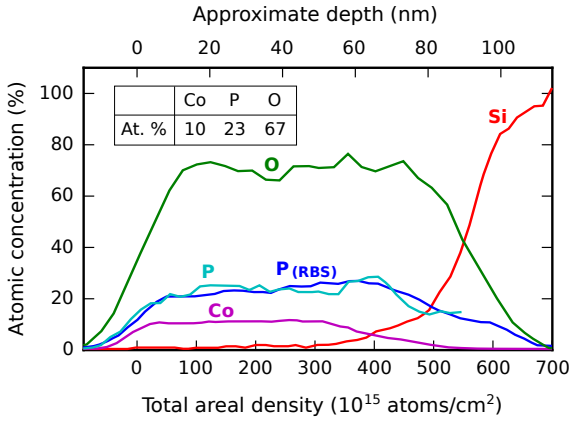

Figure 8.6: Depth profile of an as-deposited cobalt phosphate sample measured by ERD, with atomic percentages shown as a table inset.

In order to have accurate information on the composition, the same sample was measured by ERD. The measurement was performed using a 43 MeV Cl^{7+} ion beam under a 10° incidence angle with the sample surface, and recoiled atoms were collected under a 31° scattering angle. Both ERD and RBS signals were simultaneously acquired and fitted with the program NDF v9.3g.[146] The results are shown in figure 8.6. The depth profile reveals a uniform film composition with an empirical stoichiometry of $CoP_{2.3}O_{6.7}$. For phosphorus, the RBS trace provides a better (lower-noise) signal than the ERD trace, although both are still in agreement. As mentioned already for the ERD depth profile plots in previous chapters, the upper depth scale (in nm) provides only an approximate indication; the lower depth scale is the true measurement, expressing the traversed depth as an areal density of atoms.

Despite the fact that a carbon signal was clearly visible in EDX, no carbon was detected by ERD. Only a small amount of hydrogen (0.3%) was detected as an impurity (it was omitted from figure 8.6 because it is negligibly small). The ERD-measured stoichiometry differs considerably from the stoichiometry measured by EDX; however, due to the large errors on the latter, the ERD measurement should be regarded as the most reliable one. As is the case for many other phosphates produced via this process, the film is relatively phosphorus-rich. Its composition is close to cobalt(IV) pyrophosphate, CoP_2O_7.

An XPS measurement on the same material (figure 8.7) provides complementary chemical information. The experimental conditions were identi-

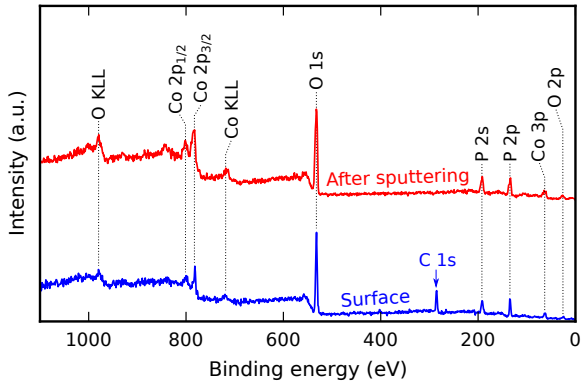

Figure 8.7: XPS survey scans on an as-deposited cobalt phosphate sample, before (blue trace) and after (red trace) sputter erosion.

cal to the ones described in previous chapters. The survey spectra reveal only the expected elements (Co, P, and O) with no detectable impurities aside from surface carbon, which is in agreement with the ERD analysis. In particular, the absence of a silicon substrate signal demonstrates a complete surface coverage. After a calibration placing the C 1s binding energy at 284.8 eV, the P 2p and O 1s peaks occur at their expected positions of resp. 134.3 eV and 532.0 eV. These peaks are insensitive to chemical shifts and so provide little information. The binding energy of Co $2p_{3/2}$, on the other hand, is influenced by the oxidation state of cobalt. A relatively large shift was observed as a result of the argon sputter erosion, from a value of 781.2 eV (before) to 784.9 eV (after). This could either mean that the surface chemistry differs from the "bulk" chemistry in the thin film, or that the oxidation state of cobalt is modified by the argon ion bombardment. The surface value corresponds to the +IV oxidation state of cobalt, which has been placed at 781.4 eV in literature.[147] The "bulk" value, however, exceeds the highest reported binding energy for Co $2p_{3/2}$ in literature (CoF_2 at 783 eV);[113] the origin of this discrepancy is unknown.

Contrary to the phosphate films described in the previous chapters, which were smooth and gave rise to well-defined XRR patterns, this was not the case for cobalt phosphate. The patterns suggested a higher surface roughness, which was quantified by AFM and shown in figure 8.8. The RMS roughness (R_q) depends on the scale and increases when looking at larger scales, from 0.30 nm in a 1 µm × 1 µm area to 1.69 nm in a 20 µm × 20 µm area.

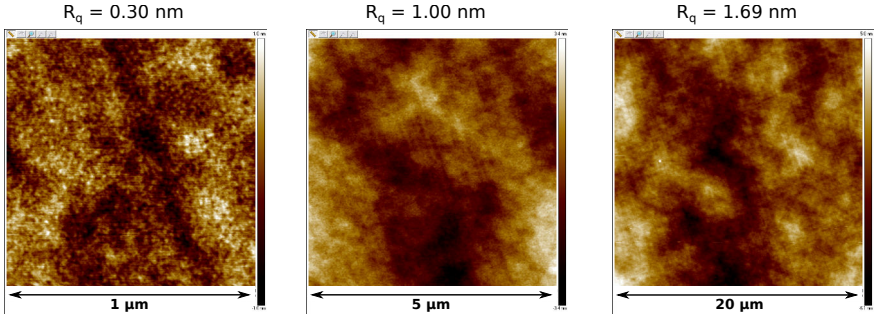

Figure 8.8: AFM topographical images of as-deposited cobalt phosphate, showing the measured RMS roughness at different scales.

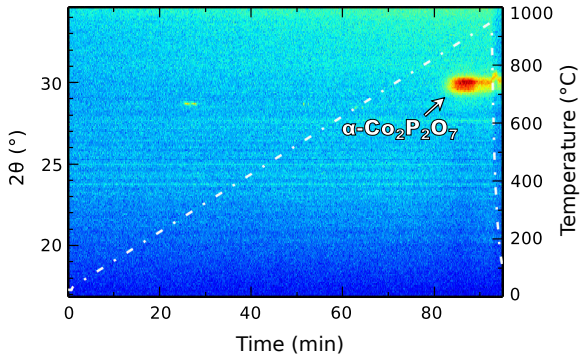

Figure 8.9: In-situ XRD measurement on cobalt phosphate during thermal annealing in a helium atmosphere.

The crystalline structure of the deposited film was investigated by in-situ XRD during thermal annealing. The annealing process took place in a helium atmosphere by applying a linear temperature ramp, starting at room temperature and ramping to 950 °C at a rate of 10 °C/min. During annealing, XRD patterns were acquired using a fixed position sensitive detector with a 2θ window of 16° to 34°, allowing in-situ observation of phase transitions. The resulting plot, showing both the XRD intensity and the temperature as a function of the elapsed time, is given in figure 8.9.

The as-deposited film does not show any diffraction peaks and is thus amorphous. The film stays amorphous until heated to a fairly high temperature of ∼850 °C, where a diffraction peak appears at a 2θ angle of 30.0°, which can likely be attributed to the overlapping (012), $(\bar{1}22)$, and $(\bar{3}02)$ reflections of α-$Co_2P_2O_7$ (JCPDS #49-1091). The other peaks of this

phase might not be observed due to insufficient intensity or preferential orientation.

The same anneal in an air atmosphere did not result in any crystallization.

8.1.3 *Lithium-ion battery electrode tests*

A 38 nm cobalt phosphate film was deposited on a platinum-coated substrate to use as the working electrode for electrochemical characterization in a lithium-ion test cell. A cyclic voltammetry experiment was performed between lower and upper potential bounds of resp. 0.2 V and 4.8 V vs. Li^+/Li at a scan rate of 1 mV/s. The results are shown in figure 8.10. The initial lithiation of the material takes place below 0.8 V. The next scan in the anodic direction shows delithiation at 1.3 V and 2.8 V; the former peak disappears upon repeated cycling, leaving reversible delithiation and lithiation peaks at resp. 2.8 V and 1.7 V. These are shifted to higher potentials compared to literature values for cobalt oxide (resp. 2.1 V and 0.8 V),[148] illustrating the inductive effect of the phosphate anions.

Integration of the peak areas reveals cathodic and anodic capacities of resp. -7.1 $\mu Ah/cm^2$ and +4.3 $\mu Ah/cm^2$. This yields a coulombic efficiency of only 60%. Together with the significant difference between lithiation and delithiation potential (1.1 V), it can be concluded that this material is unsuitable as a practical battery electrode due to its low energy efficiency.

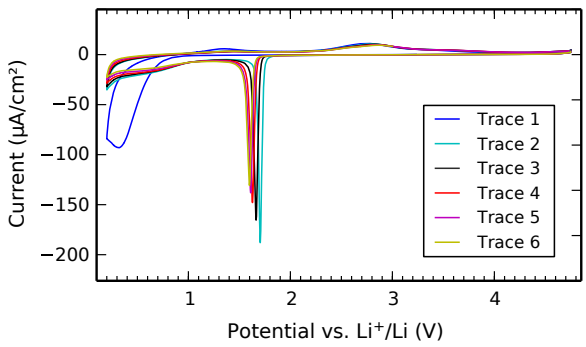

Figure 8.10: Cyclic voltammetry on a 38 nm as-deposited cobalt phosphate film, showing the initial lithiation and five subsequent scans between 0.2 V and 4.8 V at a scan rate of 1 mV/s.

8.2 Plasma-enhanced ALD of nickel phosphate

Continuing down the list of transition metals, it was attempted to deposit nickel phosphate by combining the PEALD phosphate process with a nickel precursor. In similarity to the iron and cobalt phosphate processes, a metallocene-based precursor was chosen, the first option being nickelocene (i.e. bis(cyclopentadienyl)nickel(II), $Ni(C_5H_5)_2$, or $Ni(Cp)_2$; see fig. 8.11a). Literature reports indicated that this precursor had been successfully used in ALD processes for nickel oxide (when combined with either water or ozone as the oxidant) and elemental nickel (when including a hydrogen plasma step).[149, 150]

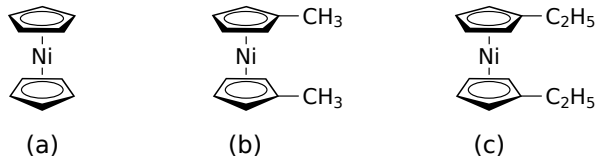

Figure 8.11: Candidate precursors for ALD of nickel compounds: (a) nickelocene; (b) dimethylnickelocene; (c) diethylnickelocene.

Test depositions were performed at a substrate temperature of 300 °C, using 10 s TMP plasma, 5 s O_2 plasma, and x s nickelocene, where x = 2, 5, and 10 s. Despite some roughness, the process yielded thin films of which the thickness and density could be determined by XRR. Figure 8.12 shows the GPC and density of these films as a function of the nickelocene pulse duration, revealing a GPC which saturates at a value close to 0.5 nm/cycle and a constant film density of approx. 3.1 g/cm^3.

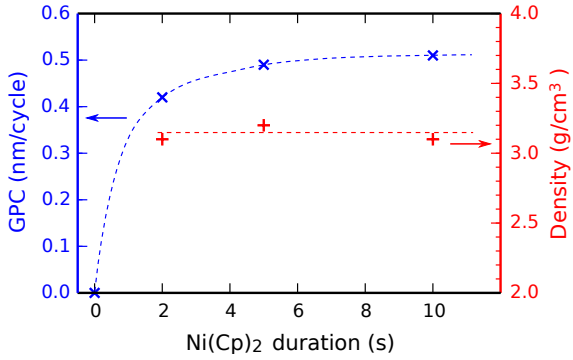

Figure 8.12: GPC and film density as a function of the nickelocene pulse duration, showing saturating behavior.

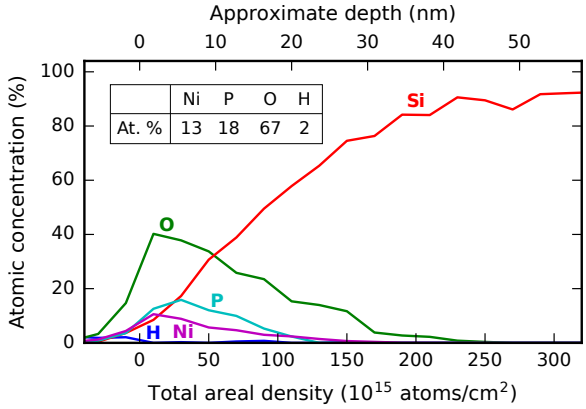

Figure 8.13: Depth profile of an as-deposited nickel phosphate sample measured by ERD, with atomic percentages shown as a table inset.

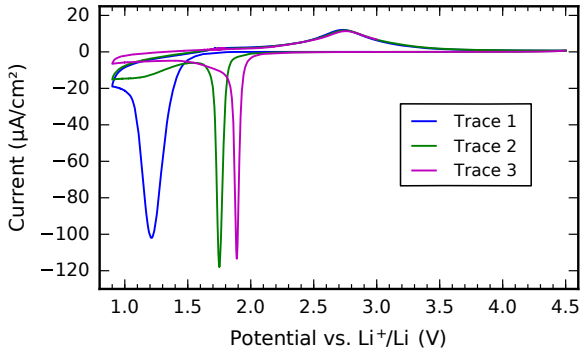

Figure 8.14: Cyclic voltammetry on a 32 nm as-deposited nickel phosphate film, showing the initial lithiation and two subsequent scans between 0.9 V and 4.5 V at a scan rate of 1 mV/s.

A 50-cycle (26 nm) nickel phosphate film, deposited on a silicon substrate using saturated pulsing conditions, was analyzed by ERD. The measurement was performed using an 8.0 MeV Cl^{4+} ion beam under a 20° incidence angle with the sample surface, and recoiled atoms were collected under a 39.6° scattering angle. The depth profile derived from the analysis is shown in figure 8.13. Integration of the atomic percentages yields an empirical stoichiometry of $NiP_{1.4}O_{5.3}$. No carbon impurities could be detected, leaving 2.6% of hydrogen as the only impurity.

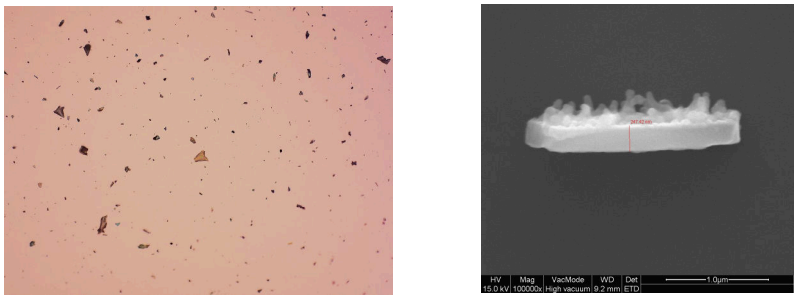

(a) (b)

Figure 8.15: Flakes observed on nickel phosphate films deposited with the nickelocene process, imaged by (a) optical microscopy and (b) SEM.

Using the same saturated pulsing conditions, a 60-cycle (32 nm) nickel phosphate film was deposited on a platinum-coated substrate for electrochemical characterization. Figure 8.14 shows a cyclic voltammetry measurement between lower and upper potential bounds of resp. 0.9 V and 4.5 V vs. Li^+/Li at a scan rate of 1 mV/s. An inital lithiation peak occurs around 1.2 V and disappears upon repeated cycling, suggesting that it is related to SEI formation. Subsequent lithiation and delithiation peaks are observed around resp. 1.8 V (shifting slowly towards more positive potentials upon repeated cycling) and 2.7 V (remaining stable). Integration of charges yields -3.7 $\mu Ah/cm^2$ (lithiation) and +2.9 $\mu Ah/cm^2$ (delithiation). Similar to the case of cobalt phosphate, the distance between the lithiation and delitiation potential, coupled with the unimpressive coulombic efficiency of approx. 78%, makes this material not very attractive as a practical battery electrode material.

Despite the encouraging saturation plot demonstrating the PEALD nature of the process, upon closer inspection, the quality of the samples was found to be rather poor due to the fact that they were covered with micron-sized flakes. This is illustrated in in figure 8.15 by the optical microscope (fig. 8.15a) and scanning electron microscope (fig. 8.15b) images. The SEM image deliberately shows a flake which happens to be oriented upwards, allowing an estimation of its thickness at approx. 250 nm.

The EDX spectra in figure 8.16 reveal that, although the film itself does appear to consist of nickel phosphate (by the presence of Ni, P, and O) as is desired, the flakes contain mostly the same elements, with comparatively less phosphorus and more carbon. The origin of the flakes was ultimately traced to the nickelocene precursor bottle itself; they form as

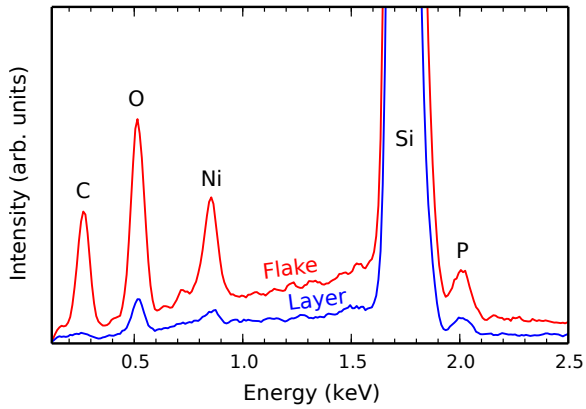

Figure 8.16: EDX spectrum acquired on a flake (red), showing the flake composition, and outside the flake (blue), showing the film composition.

a decomposition product when nickelocene is heated for long periods (which is necessary in order to evaporate it for use in ALD). Coincidentally, the same phenomenon was later reported in a product blog by Strem Chemicals.[151] Because flake-covered films are clearly not desirable and any filtering seemed impossible due to the small size of the particles, it was decided to switch to a different precursor, namely dimethylnickelocene ($Ni(MeCp)_2$; see fig. 8.11b). This compound had also been used before for ALD of nickel oxide when combined with hydrogen peroxide as the oxidant.[152]

Although it was initially possible to deposit clean nickel phosphate films with the $Ni(MeCp)_2$ precursor, there were quality control issues with the product at the supplier's side, which made it impossible to continue using it. An attempt was therefore made to replace it by diethylnickelocene ($Ni(EtCp)_2$; see fig. 8.11c), another cyclopentadienyl-type precursor which has been used for the ALD growth of nickel oxide using ozone as the oxidant.[153] Although a few nickel phosphate films were successfully produced, the precursor degraded quickly and was already unusable after being mounted on the deposition system for approx. two days. Due to the cost of the product, routine replacement was impossible. Therefore, by a lack of reliable precursors, a full characterization of the nickel phosphate process was not possible.

8.3 REDUCTION OF PHOSPHATE TO PHOSPHIDE FILMS

CONTEXT Iron, cobalt, and nickel phosphides are known as electrocatalysts for the hydrogen evolution reaction (HER).[154] This means that they are used to facilitate the production of hydrogen gas (H_2) during the electrolysis of water (a.k.a. water splitting), governed by the following half-reaction at the cathode side:

$$2\,H^+ + 2\,e^- \longrightarrow H_2$$

Modern environmental considerations and the need for sustainable and clean energy sources have made the production of hydrogen through water splitting an important technology which attracts a lot of research attention. The function of the catalyst is to reduce the required overpotential and thus increase the efficiency of the process. Platinum is currently the material of choice due to its high catalytic activity and durability, but it is also scarce and expensive; therefore, an effort is made to investigate alternative materials, including transition metal phosphides.

SYNTHESIS Amongst a variety of synthesis routes, including various solid-state reactions, a straightforward, safe, and practical method to synthesize metal phosphides (MP_x) is to start from the corresponding phosphate (MP_xO_y) and reduce it by high-temperature annealing in a hydrogen-containing atmosphere.[155] Given the ability to produce iron, cobalt, and nickel phosphate films by PEALD and the availability of high-temperature, controlled-atmosphere annealing equipment, it was not a far stretch to devise the following synthesis route:

1. Deposition of a metal phosphate by plasma-enhanced ALD
2. Post-deposition annealing in a reducing atmosphere, transforming the metal phosphate (MP_xO_y) into the corresponding phosphide (MP_x).

During the second step, in-situ XRD was used to observe the phosphide formation process. The results are shown in figure 8.17. Linear temperature ramps were applied from room temperature to 950 °C at a rate of 5 °C/min in an atmosphere consisting of 5% hydrogen in helium. The samples consisted of silicon substrates, each one coated with 100 cycles of iron phosphate (fig. 8.17a,b), cobalt phosphate (fig. 8.17c,d), and nickel phosphate (fig. 8.17e,f) according to the previously described PEALD processes using saturated pulse times and at a substrate temperature of 300 °C. In the case of nickel phosphate, the $Ni(MeCp)_2$ precursor was used.

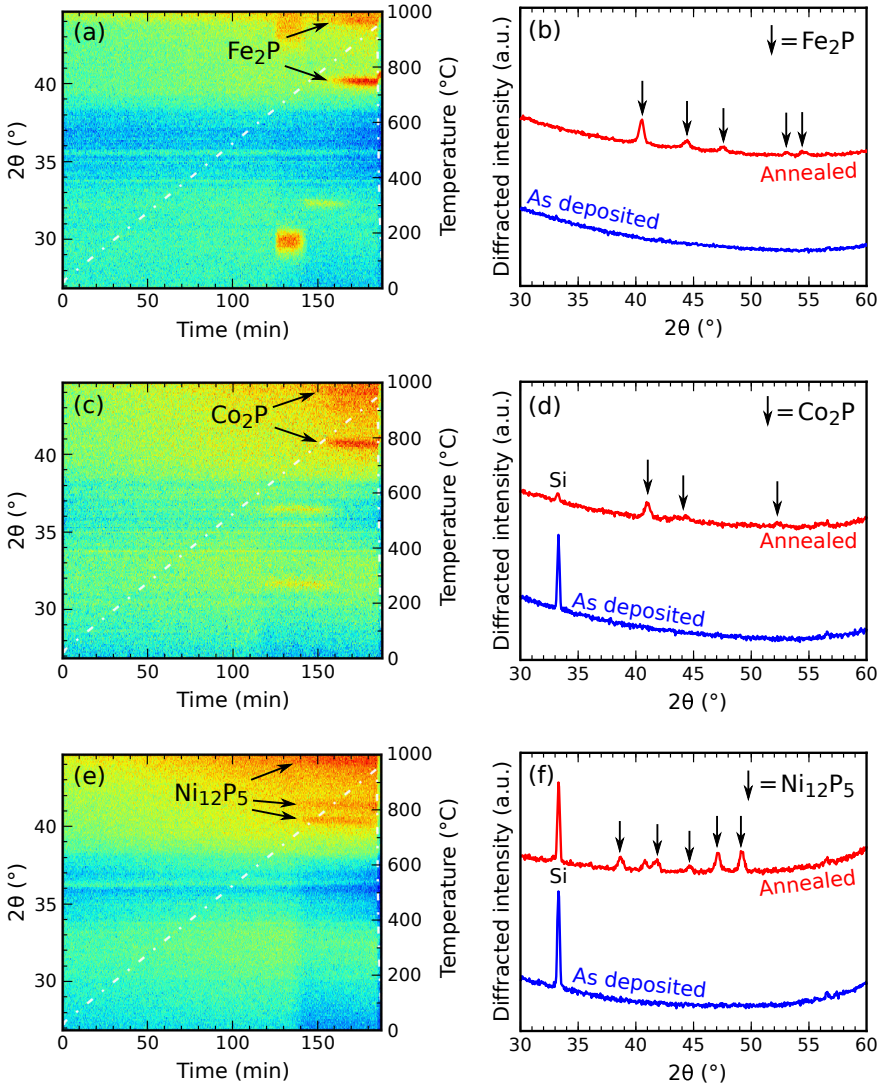

Figure 8.17: Reduction of iron (a,b), cobalt (c,d), and nickel phosphates (e,f) to their respective phosphides by post-deposition annealing in a reducing atmosphere. Plots (a),(c), and (e) show the evolution of the XRD intensity (color scale) together with temperature (white dashed line), while plots (b), (d), and (f) show a comparison of the XRD patterns measured before and after annealing.

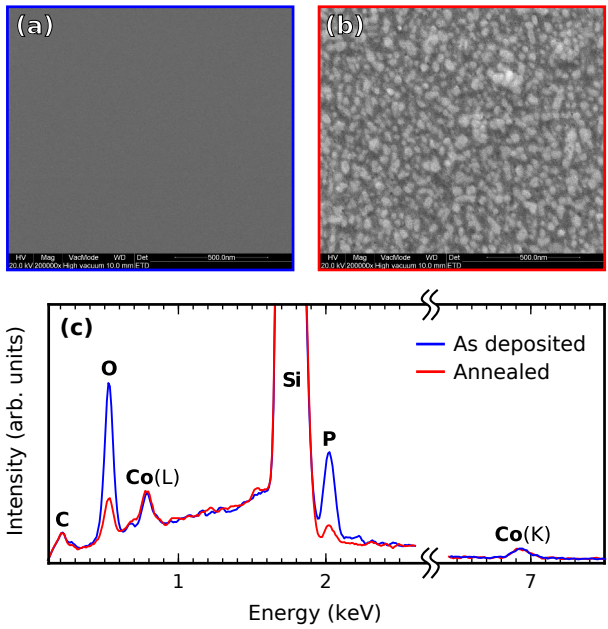

Figure 8.18: SEM images showing the morphology of cobalt phosphate, (a) as-deposited and (b) after annealing in a reducing atmosphere, together with (c) a comparison between the EDX spectra of the same samples.

In all three cases, the formation of crystalline phosphides could be clearly observed. Before annealing, the as-deposited phosphates were amorphous. At temperatures of ~700 °C (nickel phosphate/phosphide) to ~800 °C (iron and cobalt phosphate/phosphide), the diffraction patterns of resp. $Ni_{12}P_5$ (JCPDS #22-1190), Fe_2P (JCPDS #51-0943), and Co_2P (JCPDS #32-0306) emerged.

Aside from the fact that oxygen is removed, as is expected in a reduction reaction, it should be noted that the metal/phosphorus ratio of the produced phosphides differs considerably from the ratio of the starting materials, e.g. 2.0 for Co_2P versus 0.43 for $CoP_{2.3}O_{6.7}$, and similar for iron and nickel (the as-deposited phosphates are generally phosphorus-rich). This means that excess phosphorus is either removed from the film, or remains embedded in an amorphous form (which would be invisible in XRD).

In order to find out which of those two possibilities holds, the cobalt phosphate/phosphide samples were analyzed by SEM/EDX, the results of which are shown in figure 8.18. The SEM images demonstrate the trans-

formation from a smooth and featureless cobalt phosphate film (fig. 8.18a) to a nanocrystalline cobalt phosphide film (fig. 8.18b). The EDX spectra reveal that the amount of cobalt in the film remains unchanged during annealing, but both oxygen and phosphorus decrease dramatically in intensity. This leads to the conclusion that both oxygen and phosphorus are removed from the film during annealing, presumably through the following reduction reaction:

$$\mathrm{MP}_z\mathrm{O}_y + (\tfrac{3}{2}(z-x)+y)\mathrm{H}_2 \longrightarrow \mathrm{MP}_x + (z-x)\mathrm{PH}_3\uparrow + y\mathrm{H}_2\mathrm{O}\uparrow$$

where M is either Fe, Co, or Ni, and $z > x$. In other words, the hydrogen in the reducing atmosphere removes oxygen from the film by converting it to water vapor and removes excess phosphorus by converting it to phosphine gas (PH_3).[1] The result is a stoichiometric and crystalline metal phosphide.

1 The production of phosphine gas, which is notorious for its toxicity and flammability, during this synthesis might lead to safety converns. Luckily, we are working with very thin films and thus very low amounts of material. A back-of-the envelope calculation reveals that, even if all of the phosphorus in a typical thin-film sample would be converted to PH_3, this would only yield about 0.02 mg of gas. Diluted in a typical lab, the concentration would be far below the maximum allowable value of about 1 mg/m^3.

9 CONCLUSIONS AND OUTLOOK

9.1 SUMMARY AND CONCLUSIONS

PROCESS AND MECHANISM The work in this PhD thesis describes a new class of plasma-enhanced atomic layer deposition processes for the deposition of transition metal phosphates. They are all three-step processes following the same basic structure, where a single cycle consists of the following three steps:

1. TMP plasma exposure
2. O_2 plasma exposure
3. Metalorganic precursor vapor exposure

The following reaction mechanism is proposed:

1. Creation of phosphate ester surface species through a plasma polymerization-like process. The created species are believed to be chemically similar to TMP, but with some $-O-CH_3$ groups replaced by $-OH$:

   $$PO(OCH_3)_3 \xrightarrow{plasma} PO(OCH_3)_2(OH)\,(s) + \tfrac{1}{2}\,C_2H_4\,(g)$$

2. Combustion of the remaining methyl ligands by the O_2 plasma, converting the species to (poly)phosphoric acids:

   $$PO(OCH_3)_2(OH) + 6\,O\cdot \longrightarrow PO(OH)_3\,(s) + 2\,CO_2\,(g) + 2\,H_2O\,(g)$$

   During steps 1 or 2, the species may also dehydrate, thereby cross-linking phosphate groups by forming $P-O-P$ bonds:

   $$PO(OH)_3 + PO(OH)_3 \longrightarrow PO(OH)_2-O-PO(OH)_2\,(s) + H_2O\,(g)$$

3. The $-OH$ sites on the (poly)phosphoric acid surface species react with the metalorganic precursor, yielding a metal (poly)phosphate by a proton exchange reaction:

   $$R_1-(OH)_x\,(s) + M-R_2\,(g) \longrightarrow R_1-O_xM\,(s) + H_x-R_2\,(g)$$

   Here, M represents the metal with valency x, R_1 represents the (poly)phosphate, and R_2 represents the ligands of the organometallic precursor.

It is believed that this mechanism is generic, i.e. any metal phosphate can be deposited by choosing a suitable metal precursor. This was explicitly demonstrated for aluminum, zinc, iron, titanium, vanadium, cobalt, and nickel phosphate. Although the reaction proposed in step 3 implies that this metal precursor needs to be reactive towards −OH groups (i.e. it needs to react with water), experiments revealed that this was not necessarily true: while the aluminium, zinc, titanium, and vanadium precursors are indeed hydrolysed to their respective oxides when combined in an ALD process with water,[83, 122, 133, 156] this is generally not the case for the metallocene-type iron, cobalt, and nickel precursors.[157] It is therefore likely that the reaction in step 3 is in reality more complex and may be facilitated by extra reaction pathways which are enabled by the preceding and subsequent plasma exposures, i.e. by the presence of reactive radicals or by the plasma-assisted removal of the metal precursor ligands.

In each case, it was found that the process also worked without the O_2 plasma step, but this resulted in a lower deposition rate and more carbon impurities in the deposited material. The reason for this is easily understood from the proposed reaction mechanism: the presence of (unreactive) methyl groups hinders the attachment of the metal precursor and contributes to the carbon content.

TEMPERATURE The substrate temperature is essential in determining the nature of the process. At low temperatures, the TMP plasma polymerizes, resulting in the continuous deposition of phosphate esters. When combined with a metal precursor, this results in non-saturating (PECVD) growth of a metal phosphate. The polymerization rate decreases drastically as the substrate temperature increases, until it approaches zero at 300 °C. At this temperature, the process enters a PEALD regime, on the condition that the metal precursor does not decompose. Paper V illustrates that precursor decomposition can be influenced by more than just being above or below the traditionally reported "decomposition temperature", with empirical tests showing that the decomposition of TEMAV is suppressed by the presence of phosphate species on the substrate surface.

GROWTH In all cases except for cobalt phosphate, growth proceeds linearly with negligible nucleation effects. This suggests a layer-by-layer growth mode. The non-linearity observed with cobalt phosphate, together with the increased surface roughness, suggests that this process may rather obey island growth.

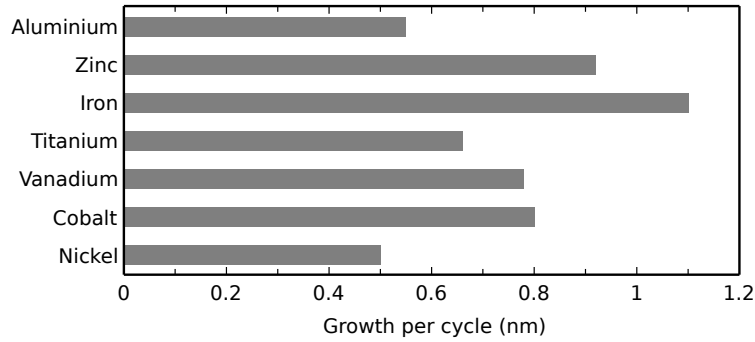

Figure 9.1: Growth per cycle values compared between the different phosphate processes.

A striking feature of these processes is that they have unusually high growth rates. Figure 9.1 shows a graphical comparison of the GPC values for the various phosphate processes, each measured at a temperature of 300 °C and using saturated pulsing conditions. While typical ALD processes have GPC values around or below 0.1 nm/cycle, the GPC of these phosphate processes ranges from 0.5 to 1.1 nm/cycle. This is advantageous because it significantly reduces the number of cycles (and thus the amount of time) to reach a certain desired film thickness; alternatively, one could grow thicker films than would be traditionally attainable by ALD.

The reason why these GPC values are so high, and why there is a considerable variation between them depending on the metal precursor, is unclear. Although theoretical models have been developed to explain the GPC of certain well-understood thermal ALD processes,[158, 159] they assume an exact understanding of the chemistry involved which is obviously still lacking for these phosphate processes. The GPC is often compared to the thickness of a monolayer, which provides an upper limit to the amount of material that can be deposited in a single cycle; however, the concept of a monolayer is poorly defined for an amorphous material, as discussed in Paper II.

COMPOSITION The elemental compositions of the as-deposited phosphates are compared in figure 9.2.[1] All of these films can be seen to be highly pure, with carbon or hydrogen impurity levels below 4%. They gen-

1 Note that all atomic compositions were determined by ERD, except for zinc phosphate, of which only XPS data was available; therefore, the hydrogen content of zinc phosphate could not be determined.

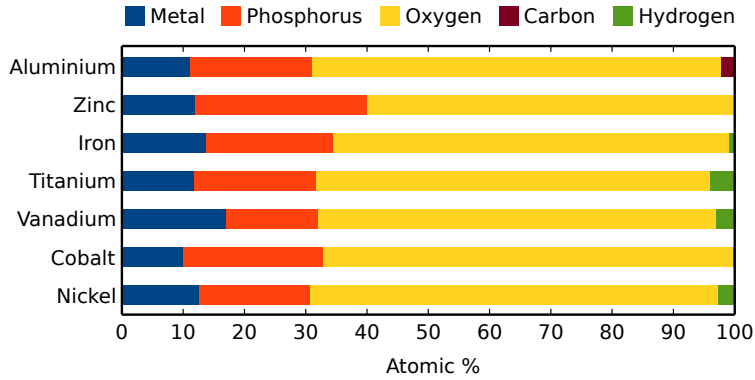

Figure 9.2: Comparison between the elemental compositions of the as-deposited phosphates.

erally contain more phosphorus than metal and are thus phosphorus-rich, suggesting polyphosphate rather than orthophosphate structures. The most phosphorus-rich material is zinc phosphate (with a P/Zn ratio of 2.3), making this material very hygroscopic and prone to degrade by exposure to ambient air. This was not the case for the other phosphates, which remained stable. The least phosporus-rich material is vanadium phosphate, with a P/V ratio of 0.9.

CRYSTALLINITY XRD measurements have revealed that all of the as-deposited phosphates are amorphous. This is strikingly different from the corresponding ALD-deposited oxides produced from the same metal precursors: with the exception of Al_2O_3, which is always amorphous as deposited and requires post-deposition annealing at temperatures exceeding 800 °C in order to crystallize,[160] the oxides of Zn, Fe, Ti, V, Ni and Co are all crystalline as-deposited under similar conditions (i.e. using O_2 plasma as an oxidant and at a substrate temperature of 300 °C).[65] The inhibition of crystallization can be explained by the tendency of phosphorus to act as a glass former.[101]

Crystalline phosphates can be formed by post-deposition annealing. Depending on the ambient atmosphere (oxidizing, inert, or reducing), the same material may form a variety of crystalline products after annealing. For instance, iron phosphate yielded $FePO_4$ when annealed in air, but elemental phosphorus was formed by annealing in helium, and iron phosphide (Fe_2P) was formed after annealing in hydrogen. This clearly

demonstrates that the oxidation state of phosphorus can be modified over a wide range by controlling the ambient atmosphere during annealing.

PHOSPHIDES The formation of nanocrystalline phosphide films consisting of Fe_2P, Co_2P, or Ni_5P_{12} starting from resp. iron, cobalt or nickel phosphate was demonstrated by post-deposition annealing of the amorphous phosphate films in a reducing atmosphere. The hydrogen atmosphere assisted in removing the oxygen as well as the excess phosphorus, yielding phase-pure phosphide films.

CONFORMALITY As the conformality of coatings on complex structures is often touted as one of the unique advantages of ALD, it deserves to be characterized and discussed, even though this is often not done when new processes are reported in literature. To this end, conformality tests were carried out for the iron phosphate and titanium phosphate processes by deposition on silicon micropillar arrays and analysis by EDX. The results revealed that the conformality of the phosphate processes was non-ideal: both the coating thickness and its stoichiometry varied by some degree along the penetration depth. As one might expect, the results were better for widely spaced pillars (50 μm long, 5 μm interpillar distance), with decreases in the order of 20%, than for the more tightly spaced ones (same length, but with 2 μm interpillar distance), with up to an 80% decrease in phosphorus from the top to the bottom of the pillars. Both for iron and titanium phosphate, the amounts of phosphorus and oxygen decreased faster than the amounts of metal; this is consistent with the plasma-based delivery mechanism of the former elements, which has a more limited penetration depth compared to vapor; additionally, the variations in stoichiometry can happen because there is no "preferred" stoichiometry (as would be the case for e.g. a simple metal oxide).

ELECTROCHEMICAL LITHIATION The main application of interest for the produced metal phosphate films was their potential use as lithium-ion battery electrodes. Empirical tests revealed that iron, titanium, vanadium, cobalt, and nickel phosphate could be electrochemically lithiated and cycled. Aluminium phosphate was tested, but appeared to be an ionic insulator. Zinc phosphate was not tested due to its poor stability.

Figure 9.3 shows a comparison of the electrochemical activity of the as-deposited phosphates after initial lithiation. It should be noted that for all of them, the initial lithiation behavior is distinctly different from the reversible cycling, typically requiring activation at a lower potential (i.e. a

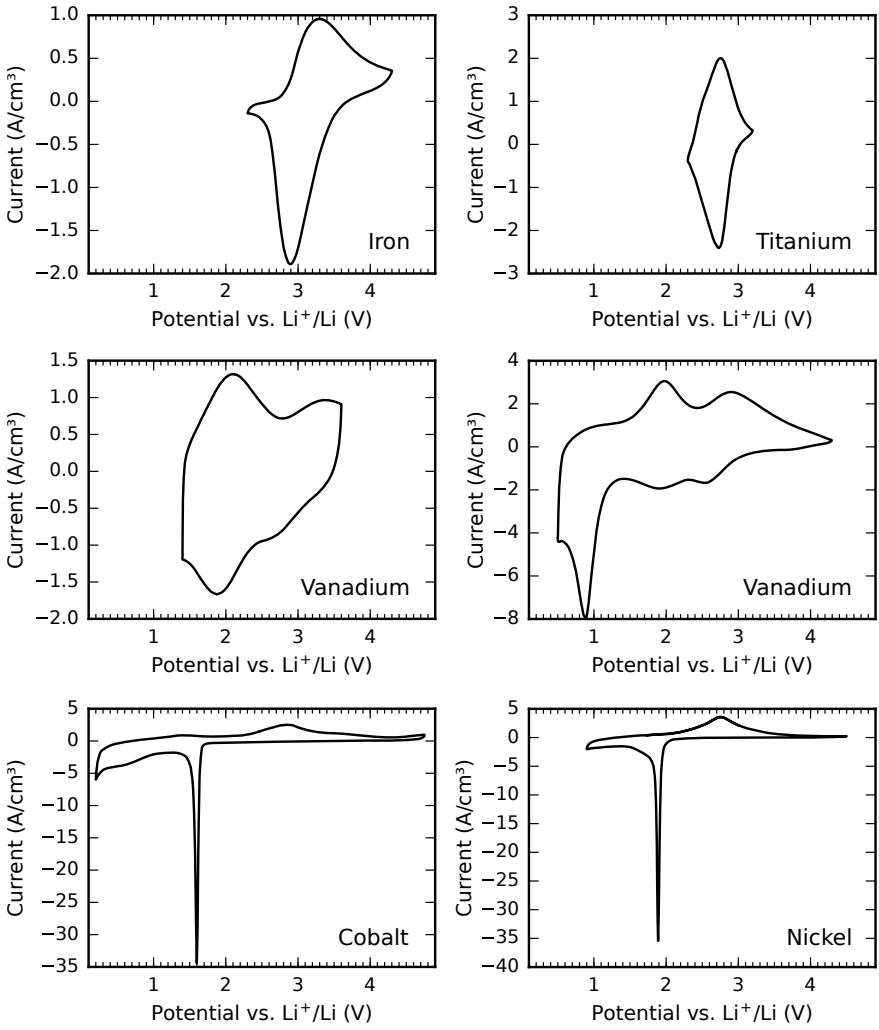

Figure 9.3: Summary of the electrochemical activity windows of the deposited transition metal phosphates, showing "steady-state" cyclic voltammetry patterns for iron, titanium, vanadium (two potential windows), cobalt, and nickel phospate at 1 mV/s. Currents are normalized by volume in order to correct for varying film thicknesses.

Table 9.1: Overview of the potential ranges, volumetric capacities, and coulombic efficiencies measured for the as-deposited phosphate films after initial lithiation.

Metal	Potential (V)	Lithiation capacity (mAh/cm^3)	Coulombic efficiency (%)
Iron	2.3 – 4.3	190	102
Titanium	2.3 – 3.2	300	99
Vanadium	1.4 – 3.6	630	99
Vanadium	0.5 – 4.3	1900	100
Cobalt	0.2 – 4.8	1900	60
Nickel	0.9 – 4.5	1200	78

stronger driving force for reduction) and requiring excess lithium, which is presumably used for SEI formation. The CV patterns in fig. 9.3 only show reversible cycling; details on initial lithiation behavior can be found in the respective chapters.

Table 9.1 provides an overview of the potential ranges, volumetric capacities, and coulombic efficiencies measured for the same as-deposited phosphate films. Iron phosphate can be classified as a cathode material due to its activity around 3 V, but has a comparatively low volumetric capacity. Titanium phosphate has a higher capacity but a lower potential, giving it a rather ambivalent character; depending on the application, it could be used either as an anode or a cathode. Vanadium phosphate is active in a very wide potential range and has a large capacity, although the capacity retention is limited when cycling below 1.4 V. Although cobalt and nickel phosphate also show large capacities, the energetic efficiency of these materials is limited by their low coulombic efficiencies and the considerable potential differences between the anodic and cathodic peaks.

3D ELECTRODES The use of 3D structuring to increase electrode capacities while maintaining fast kinetics was demonstrated for both iron and titanium phosphate electrodes deposited on micropillar substrates. Despite the non-ideal conformality, capacity enhancements of more than a factor of 15 were reached with the same kinetic behavior as for thin planar films. While this sounds promising, a simple exercise reveals that there is still a long way to go to compete with powder-based batteries: applying an enhancement factor of 15 to the 30 nm thick ALD film results in an equivalent thickness of 0.45 µm. Powder-based battery electrodes have

total thicknesses in the order of 100 μm and typically contain about 30% active material, giving them an equivalent thickness of approx. 30 μm. Thus, in order to match the capacity of a "traditional" powder-based electrode with a microstructured ALD film, one would need an additional factor of 67 in surface enhancement. It goes without saying that this would be very challenging.

9.2 SUGGESTIONS FOR FUTURE WORK

Even though a fair number of different transition metals have been explored, the periodic table still presents many other opportunities. It is highly likely that the proposed process allows phosphates of any metal to be synthesized, given that a suitable metalorganic ALD precursor can be found which does not decompose at the substrate temperature required for the TMP plasma. In particular, the nickel phosphate process would benefit from a more stable nickel precursor, and manganese phosphate could be deposited using e.g. $Mn(EtCp)_2$[161] or $Mn(thd)_3$.[162] Lithium phosphate could be deposited by using a lithium precursor such as Li(HMDS) or Li(O^tBu), and could be used as a solid-state electrolyte for lithium-ion batteries.

It would also be possible to explore the synthesis of mixed-metal phosphates, where two (or more) different metal precursors are alternated during the deposition process to form nanolaminates. Although this makes everything even more difficult due to the addition of an extra degree of freedom, it also opens up interesting possibilities, e.g. the synthesis of lithiated transition metal phosphates, which do not need to be electrochemically lithiated after deposition. Post-deposition annealing steps could transform these materials into particular crystalline structures with desirable electrochemical properties.[163]

The variety of phosphorus oxidation states that could be formed during post-deposition annealing also suggests that it might be possible to access an even wider variety of phases by fine-tuning the annealing atmosphere, e.g. by controlling the partial pressures of oxygen and/or hydrogen. This may be a useful route towards optimization for certain applications, e.g. tuning the type of phosphide for the best electrocatalytic effect.[154]

A last observation is that the TMP plasma process represents, to the author's best knowledge, the first occurrence of overlap between the (formerly completely separated) fields of plasma polymerization and (plasma-enhanced) atomic layer deposition. There is no reason to assume that it

stops there, i.e. that this interesting chemistry would only happen with TMP. It is entirely possible that other methyl esters, i.e. those of boric, nitric, or sulfuric acid, could be used in a very similar way to yield PEALD processes for borates, nitrates, or sulfates.

A

APPENDIX

A.1 DESIGN OF A USB-CONTROLLED POTENTIOSTAT/GALVANOSTAT

This appendix describes the design of a low-cost USB-controlled potentiostat/galvanostat which can measure or apply potentials in the range of $\pm$8V, and measure or apply currents ranging from nanoamps to max. $\pm$25 mA. Precision is excellent thanks to the on-board 20-bit D/A-converter and 22-bit A/D-converters. The dual control modes and its wide potential range make it especially suitable for battery characterization. As an example use case, measurements are presented on a lithium-ion test cell using thin-film anatase TiO_2 as the working electrode. A cross-platform Python program may be used to run electrochemical experiments within an easy-to-use graphical user interface. Designed with an open hardware philosophy and using open-source tools, all the details of the project (including the schematic, PCB design, microcontroller firmware, and host computer software) are freely available, making custom modifications of the design straightforward.

A.1.1 *Introduction*

A.1.1.1 *Potentiostat basics*

The potentiostat is an essential tool in electrochemical research. It allows the experimenter to apply a potential to a system (i.e. an electrochemical cell) and measure the resulting current, or *vice versa*. The unique property of the potentiostat – the thing that differentiates it from a simple combination of an adjustable voltage source and an ammeter – is that it can do so while keeping the path where the current flows separate from the path where the potential is measured. This is necessary in electrochemical cells because potentials are usually measured against a "reference electrode" which only provides an accurate and stable potential in equilibrium conditions, i.e. when it is not disturbed by any current flow. Using two terminals for current flow and two others for potential sensing, a total of four electrode connections are needed; they are usually named as follows:

- Working electrode (abbreviation: WE)

- Counter electrode (abbreviation: CE)
- Sense electrode (abbreviation: SE)
- Reference electrode (abbreviation: RE)

In a four-electrode connection scheme, the potential is measured (and no current flows) between SE and RE, and current is applied (regardless of the voltage drop) between WE and CE.[1]

In most electrochemical cells, the SE and WE are tied together (and still referred to as WE), resulting in a three-electrode connection scheme: the potential is measured between WE and RE, and current flows between WE and CE. This is illustrated in figure A.1. Using this scheme, one would naively assume that it is impossible to control the potential; as there is zero current flow, the potential can only be measured and not forced to a certain value. The potentiostat can, however, apply current between WE and CE, which in turn influences the potential between WE and RE; thereby, using a feedback loop, any desired potential between WE and RE can be achieved by applying whatever current is necessary between WE and CE.

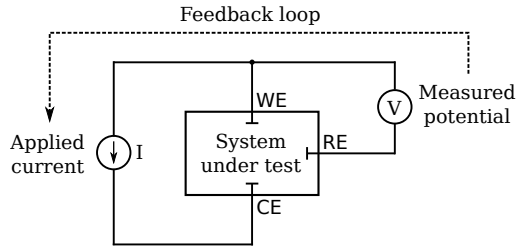

Figure A.1: Schematic diagram showing the three-electrode connection scheme between the electrochemical cell and the potentiostat, resulting in separate paths for the application of current (between WE and CE) and the sensing of potential (between WE and RE).

This control mode is called the "potentiostatic mode": it allows the user to set a desired potential, and the potentiostat will try to reach that potential by adjusting the current. Alternatively, it is often useful to have control over the current instead (i.e. allowing the user to set a desired current, no matter what the resulting potential may be); this is called the "galvanostatic mode". The presented circuit elegantly combines both of these modes

1 It should be noted that the potentiostat is functionally equivalent to a source-measure unit with separate force/sense lines, with the WE/CE pair corresponding to the "force" connections and the SE/RE pair corresponding to the "sense" connections.

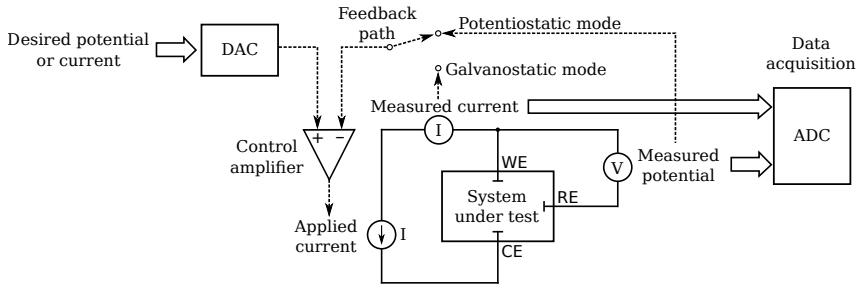

Figure A.2: Block diagram illustrating the working principle of the potentiostat when it is controlling an electrochemical cell. The device is able to switch between potentiostatic (potential control) or galvanostatic (current control) modes by changing the feedback path.

by making it possible to switch the feedback path between the potentiostatic and the galvanostatic modes, as shown in figure A.2. On a basic level, the circuit operates as follows:

- A digital-to-analog converter (DAC) outputs an electrical signal representing either the desired potential (in the potentiostatic mode) or the desired current (in the galvanostatic mode).
- An operational amplifier compares this to the measured potential (in the potentiostatic mode) or the measured current (in the galvanostatic mode), and drives current into the CE until the measured value equals the DAC setpoint.
- Both the measured potential and the measured current are fed into an analog-to-digital converter (ADC) for data acquisition purposes.

A.1.1.2 *Comparison to previously published designs*

Although a number of similar open source, "do-it-yourself" potentiostat designs have recently been published,[164–166] these designs are not suitable for battery characterization. The Friedman et al. design[164] does not allow the working electrode potential to be scanned (it can only be adjusted to a fixed value in hardware), limiting its use to chronoamperometry (i.e. recording the working electrode current as a function of time). The CheapStat[165] supports a number of electrochemical techniques including cyclic voltammetry, but its potential range is limited to ± 1 V. The DStat[166] improves upon the CheapStat in several ways, and has impressive low-current capabilities, but it is still limited to a potential range of

± 1.5 V. Although these potential ranges are wide enough for many aqueous electrochemistry experiments, they are insufficient for e.g. lithium-ion batteries which can reach cell potentials over 4 V. The potential range of the design described in this paper is ± 8 V.

Another highly desirable feature for battery characterization is the inclusion of a galvanostatic mode. The aforementioned designs implement the "adder potentiostat" topology[35] which only provides potentiostatic control. The presented design has a different topology which enables switching between potentiostatic control and galvanostatic control with a single (digitally controlled) switch.

A.1.1.3 *Comparison to commercial instruments*

While there are plenty of commercial instruments which can be bought from manufacturers such as Metrohm Autolab, Bio-Logic, Gamry, Ivium Technologies, CHI, Pine Research, Admiral Instruments, etc. to fulfill the same purpose, including models which provide wider current ranges, higher sample rates, and more measurement techniques (e.g. including impedance spectroscopy), the price of these instruments generally ranges from $2000 up to $20000 and more. To the author's best knowledge, the lowest-cost commercial instrument which could substitute for the presented design is the Squidstat Solo, sold by Admiral Instruments for a retail price of $1900.[167] While it has a higher sample rate (1 ms/sample, versus 90 ms for the presented design), a slightly higher potential range ($\pm$10V versus $\pm$8V) and similar current ranges (± 3 µA to ± 25 mA versus ± 2 µA to ± 20 mA), it has worse potential and current resolution (16-bit versus 22-bit), it is approx. 20 times more expensive, and its hardware and software cannot be freely modified.

A.1.2 *The hardware*

A.1.2.1 *Circuit description*

An annotated schematic diagram of the device is shown in Figure A.3. It consists of several subcircuits, which are discussed below.

POWER SUPPLY In order to be able to apply cell voltages between -8 V and $+8$ V, the analog circuitry needs dual power supply rails which supply at least these voltages (plus some overhead). The required current is fairly low; the cell current will not exceed 25 mA, and the quiescent current of the analog circuitry is in the order of a few mA. To eliminate the inconvenience of needing an external power supply, the supply is generated

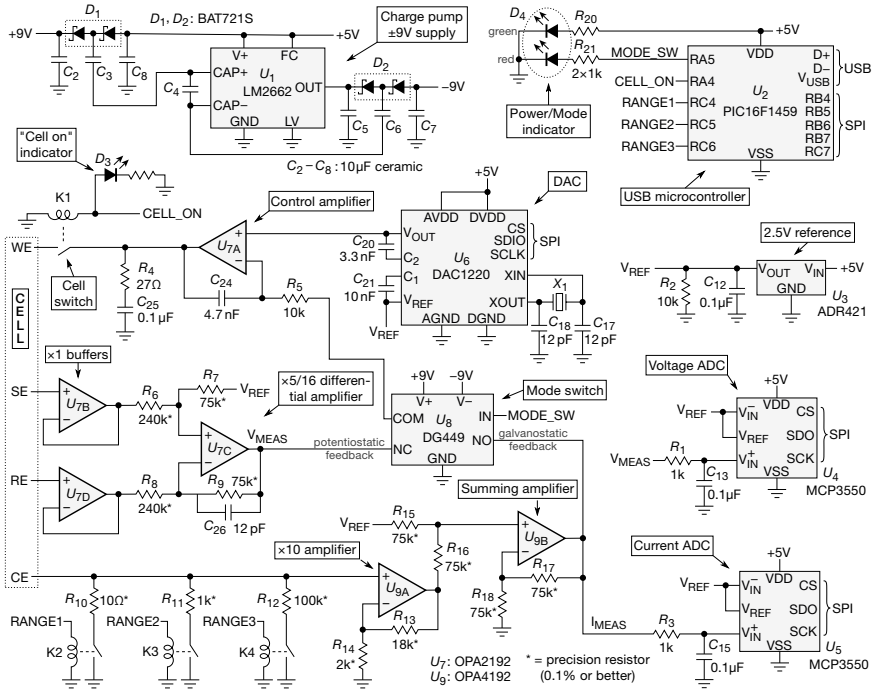

Figure A.3: Annotated schematic diagram of the USB potentiostat/galvanostat circuit. Certain details are omitted for clarity; a complete and fabrication-ready circuit schematic can be found in the github repository.[168]

internally from the +5 V line provided by the USB bus. This is achieved by a charge pump[2] consisting of U1 (an LM2662 switched-capacitor voltage converter) and its associated circuitry. The switching action of U1 drives both a positive voltage doubler network (C2, C3, C4 and D1) and an inverting voltage doubler network (C5, C6, C7 and D2); this results in supply rails of ±10 V, minus the forward voltage losses of the diodes. These losses are minimized by choosing Schottky-type diodes such as the BAT721S, which conveniently houses two of them in a single package. The result is approx. ±9 V. Ceramic capacitors are recommended for C2–C8; their low ESR results in low ripple, they do not degrade over time like electrolytics, and the required 10 µF capacities are nowadays inexpensively available.

2 The choice of a charge pump rather than a switched-mode power supply simplifies the design and eliminates inductors or transformers, which may emit undesirable electromagnetic noise.

ANALOG CIRCUITRY The analog circuitry is implemented using OPAx192 operational amplifiers. These relatively new op-amps from Texas Instruments[169] are high-precision, low offset voltage, low bias current, low-noise devices which have a wide supply voltage, rail-to-rail inputs and outputs, and a rather high output current. They closely approximate ideal op-amp behaviour, making them highly suitable for a measurement circuit like this where DC precision is of the utmost importance.

The core of the circuit is the control amplifier, U7A. It compares the voltage set by the DAC output to either the potentiostatic or the galvanostatic feedback voltage, and drives the working electrode of the cell until they are equal. To prevent oscillation, its bandwidth is limited by R5 and C24. The present component values yield a −3 dB frequency of approx. 3 kHz, which is still much faster than the typical measurement timescale. An additional "snubber"-type network consisting of R4 and C25 on its output pin increases stability towards capacitive loads. The cell switch K1 allows the electrochemical cell to be connected (this will later be referred to as the "`CELL ON`" state) or disconnected ("`CELL OFF`") from the output of U7A; in its disconnected state, the cell is not driven, but may still be measured.

Potentiostatic feedback is acquired through U7B, U7C, and U7D. U7B and U7D are unity-gain buffers which present very high input impedances on respectively the sense electrode and the reference electrode, satisfying the requirement of having nearly zero current flow between SE and RE.[3] The buffered voltages are then fed into U7C, which is configured as a differential amplifier by means of R6–R9. This amplifier implements the following operation:

$$V_{MEAS} = V_{REF} + (V_{SE} - V_{RE}) \times (R7/R6)$$
$$\text{(for } R8 = R6,\ R9 = R7\text{)}$$

With $V_{REF} = 2.500\,\text{V}$, $R7 = 75.0\,\text{k}\Omega$ and $R6 = 240\,\text{k}\Omega$, potential differences between SE and RE ranging from –8 V to +8 V are linearly scaled to output voltages V_{MEAS} ranging from 0 V to +5 V. In this way, the signal spans the same range as the DAC output (allowing it to be used as a feedback signal) and the ADC input (allowing it to be measured).

Galvanostatic feedback is acquired by making use of the shunt resistors R10, R11 or R12 to convert the CE current into a voltage (selectable by the ranging relays K2–K4), multiplying this voltage by a factor of exactly

3 The OPAx192 has a typical input impedance of $10^{13}\,\Omega$ and a typical input bias current of 5 pA.[169] Using e.g. a reference electrode with an impedance of 10 kΩ, this results in an error voltage of 50 nV – an insignificant quantity.

10 through the non-inverting amplifier U9A, and summing this voltage with V_{REF} using U9B. In the highest current range, a range of –25 mA $\rightarrow$ +25 mA is mapped linearly to the range of 0 $\rightarrow$ +5V, which is again suitable as a feedback signal and for acquisition by the ADC. The lower current ranges are respectively 100 times and 10 000 times more sensitive, resulting in ranges of resp. $\pm$250 µA and $\pm$2.5 µA.

The potentiostatic and galvanostatic feedback signals (labelled `V_MEAS` and `I_MEAS`) lead into the "normally closed" and "normally open" terminals of U8, a DG449 analog switch. When `MODE_SW` is low, the control amplifier receives the potentiostatic feedback signal; when high, it receives galvanostatic feedback. In this way, the circuit can quickly switch between the potentiostatic and galvanostatic control modes.

A/D CONVERSION The `V_MEAS` and `I_MEAS` signals are connected to U4 and U5, which are MCP3550 A/D converters, for data acquisition. The MCP3550 is a 22-bit delta-sigma ADC which offers high accuracy and low noise; in particular, it strongly rejects line noise at either 50 Hz (using the MCP3550-50 model) or 60 Hz (using the MCP3550-60 model).[170] This is highly desirable because it eliminates what is often the most important noise source in many lab environments; however, this comes at the cost of a fairly limited conversion rate of max. 12.5 samples/s. If faster conversion would be required, it could be directly replaced by the MCP3553 which samples at 60 samples/s but lacks the line noise filter. The inputs to the ADC's are additionally low-pass filtered by R1/C13 and R3/C15 to remove high-frequency switching noise; the present component values yield roll-off frequencies of approx. 1.6 kHz, well below the delta-sigma modulator's oversampling rate of 25600 samples/s (corresponding to a Nyquist frequency of 12.8 kHz) [170].

With 22-bit resolution, the potential is measured with a granularity of 3.8 µV. In the most sensitive current range, current is measured with a granularity of 1.2 pA; this figure increases to resp. 120 pA and 12 nA for the higher ranges.

D/A CONVERSION AND VOLTAGE REFERENCE The control amplifier receives its "setpoint" voltage from U6, a DAC1220 digital-to-analog converter. The DAC1220 is a 20-bit delta-sigma DAC which is inherently linear and contains an on-chip calibration function.[171] It receives its +2.500 V reference voltage V_{REF} (as do U4, U5 and the analog circuitry) from U3, an ADR421 voltage reference using XFET technology for low noise, high accuracy ($\sim$0.1%), and high stability.[172]

The 20-bit DAC resolution results in potential control with a granularity of 15.3 µV, or in current control with granularities of 4.8 pA, 480 pA or 48 nA, depending on the current range.

DIGITAL CONTROL The device connects to a host computer by an on-board USB interface. This function is implemented by U2, a PIC16F1459 microcontroller which has built-in USB capabilities and provides a sufficiently large number of general-purpose input/output pins for relay switching and SPI communication.[173] An ICSP header P3 is provided in order to load firmware onto the microcontroller. Its function is to receive commands from the host computer through USB, which may instruct it to either toggle a pin, read from the ADC, or set the DAC. It communicates with the ADC or DAC through a software-implemented SPI interface, and in case of a DAC read, it then sends back the acquired data to the host computer.

Status LEDs D3 and D4 provide some basic status indication. D3 provides the "`CELL ON`" indication; when D3 is illuminated, the cell is connected to the control amplifier. D4 is a dual-color LED which provides power-on and mode indication; it lights up green when the circuit is in the potentiostatic mode, and orange when it is in the galvanostatic mode.

A.1.2.2 *PCB design*

A compact, double-sided printed circuit board design was made in KiCad.[174] The design files are available in a github repository,[168] and a 3D rendering of the (populated and unpopulated) board is shown in figure A.4. The board is most easily fabricated by sending it off to a

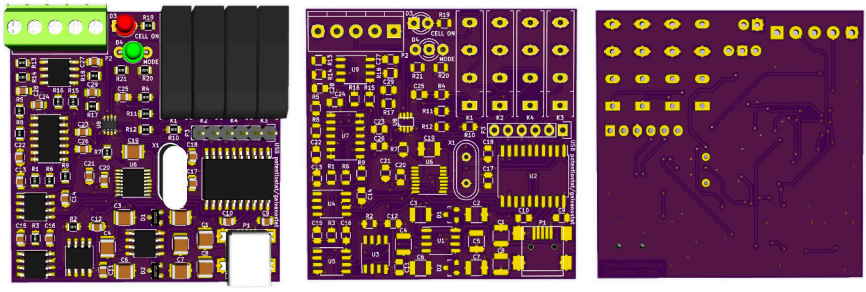

Figure A.4: 3D renders of the printed circuit board design, showing the populated board (left), the unpopulated board's front side (middle) and the unpopulated board's back side (right).

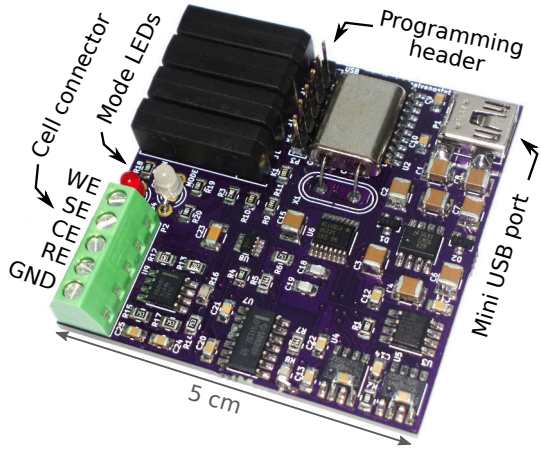

Figure A.5: Annotated photograph of the assembled potentiostat.

PCB prototyping service. Assembly can be carried out by either reflow soldering or hand-soldering.

Due to the small size of the PCB (approx. 5×5 cm), it may easily be put in a small enclosure, e.g. a mint tin, provided some openings are made to allow the mini-USB connection and the cell connection cables to pass through.

A bill of materials and a fabrication diagram (showing a top view of the PCB superimposed with the component values) may be found in the github repository[168] to aid component ordering and circuit assembly. The total cost of the device, including the components and a manufactured PCB, is well below $100. A photograph of the finished device is shown in figure A.5.

A.1.3 *The firmware*

The microcontroller firmware including the source code and a compiled .hex image may be found in the github repository.[168] Compilation and usage instructions may be found in the sections below.

A.1.3.1 *Compilation*

The source code is written in the C programming language and can be compiled using the Microchip MPLAB XC8 compiler. The provided Makefile allows easy compilation because it automatically provides the compiler with the necessary flags and include paths. On a Linux system, sim-

ply running the command `make all` will compile and link everything and produce the output file `firmware.hex`.

A.1.3.2 *Raw USB communication*

The microcontroller firmware makes use of Signal 11's "M-stack" open-source USB stack[175] to implement communication through raw USB bulk transfers. Commands are received as ASCII strings on EP1 OUT, are executed, and a reply is sent on EP1 IN. The following commands are supported:

- "`CELL ON`", "`CELL OFF`"
  Connects or disconnects the cell to the output of the control amplifier.
- "`POTENTIOSTATIC`", "`GALVANOSTATIC`"
  Switches between potentiostatic or galvanostatic control modes.
- "`RANGE x`" (where `x` = "`1`", "`2`", or "`3`")
  Switches between current ranges; range 1 is the highest (least sensitive) current range, increasing range numbers yield lower (more sensitive) ranges.
- "`DACSET xxx`" (`x` = one byte of data)
  Sets the DAC output code (three bytes).
- "`DACCAL`"
  Performs an automatic DAC calibration.
- "`DACCALSET xxxxxx`" (`x` = one byte of data)
  Sets the DAC calibration data; the first three bytes are proportional to the offset, the latter three bytes are proportional to the gain.[171]
- "`DACCALGET`"
  Returns six bytes, representing the current DAC calibration in the same format as above.
- "`ADCREAD`"
  Reads the potential and current from the ADC's, and returns six bytes if a previous conversion has finished. The first three bytes represent the potential ADC value, the latter three bytes represent the current ADC value. If a conversion is still ongoing, it returns the string "`WAIT`" instead.
- "`OFFSETSAVE xxxxxx`" (`x` = one byte of data)
  Saves six bytes to internal flash memory; these are used for potential/current offset removal.

- "`OFFSETREAD`"
  Retrieves the corresponding six bytes from internal flash memory and returns them.
- "`SHUNTCALSAVE xxxxxx`" (x = one byte of data)
  Saves six bytes to internal flash memory; these are used for fine-tuning the three current shunt resistors.
- "`SHUNTCALREAD`"
  Retrieves the corresponding six bytes from internal flash memory and returns them.

The host computer communicates with the potentiostat using a generic driver provided by the cross-platform libusb library.[176]

A.1.4 *The software*

A user-friendly GUI application allows the experimenter to easily perform typical electrochemical measurements. The program can be found in a github repository[168] and is written in Python 3. In addition to a working installation of Python, it requires NumPy[177] and SciPy[178] for data processing, PyUSB[179] for USB communication, PyQt[180] to provide the GUI, and PyQtGraph[181] for real-time plotting. These packages are freely available, and may be easily installed from the system software repositories on most Linux distributions. On Windows and Mac, it is recommended to use Anaconda[182]; it provides Python 3.6 along with all packages except PyQtGraph (which may be installed using conda) and PyUSB (which may be separately installed using pip). Only on Windows, a USB device driver is required upon connecting the device to the host computer; this driver may be generated by libusb[176] or downloaded from the github repository.[168]

After installing these dependencies, the program can be executed by running the command `python tdstatv3.py`. An application GUI similar to the one in Figure A.6a should then appear. The USB Vendor and Product IDs shown in the input fields should match the values in the microcontroller firmware source code; the default values are resp. `0xa0a0` and `0x0002`, but they can be adjusted if necessary. By clicking the "Connect" button, the application will start communicating with the potentiostat and will start displaying the measured potential and current; it does this both in numeric form (using the upper numeric indicators) and in graphical form (by plotting the potential and the current as a function of the time).

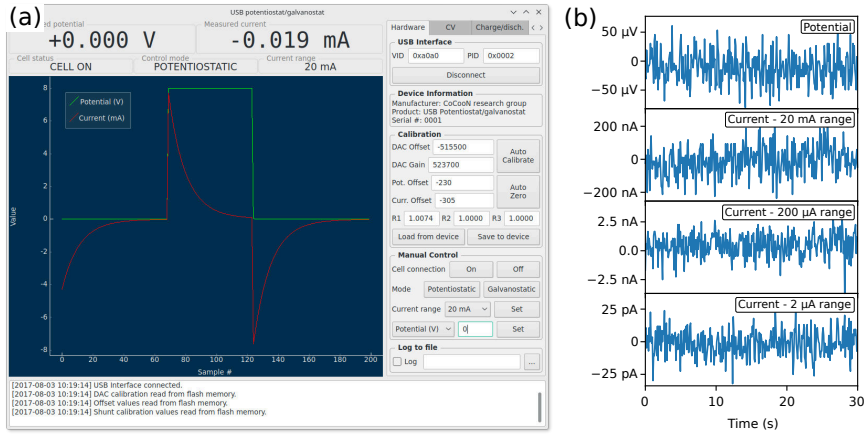

Figure A.6: (a) The user interface program running on the host computer in idle mode, showing the measured potential and current in real time. (b) Noise levels on the measured potential (with shorted sense and reference electrodes, i.e. zero potential) and on the measured current in the three current ranges (with the cell off, i.e. zero current).

A.1.4.1 *Calibration*

Even though the device will already be reasonably accurate without applying any calibration (thanks to the precision op-amps, precision resistors, and the inherent linearity of the ADCs and DAC), the remaining – small – offset and gain errors, typically in the order of respectively 0.01% of full-scale and 0.1% of the measured value, can be calibrated out by adjusting the values in the "Calibration" field under the "Hardware" tab. It is recommended that this be done by the following procedure:

- Short the SE and RE; leave WE and CE unconnected. Either adjust the potential offset and current offset manually until both the potential and the current are exactly zero, or wait at least 20 s (to have the device measure enough data points to average) and press the "Auto Zero" button.
- Connect SE to WE, and RE to CE. Press the "Auto Calibrate" button. Under "Manual Control", switch the cell on, and set a few different potentials. The measured potential should exactly match the set potential; if it does not, you can further fine-tune the calibration by making small adjustments to the DAC offset and DAC gain. Press "Save to device" to apply the values.

- Finally, the values R1–R3 represent relative fine adjustments to the shunt resistor values. If precise shunt resistors were used, they should not require adjustment, except for R1 (the lowest shunt resistor, used for the highest current range, having a nominal value of 10.00 Ω) which may have a slightly higher value due to the non-negligible contact resistance of the current ranging relay. To fine-adjust this value, connect SE and WE to one leg and WE and CE to the other leg of an accurate 1.000 kΩ resistor. Set a potential of e.g. 7.000 V, set potentiostatic mode, and turn the cell connection on; adjust the R1 value until the measured current is exactly 7.000 mA.
- By pressing the "Save to device" button, the calibration data is saved to the internal flash memory of the potentiostat, so that the correct values are automatically loaded upon the next application start-up. This is also useful in case the potentiostat is connected to a different host computer; the device will remember its own calibration settings.

To maintain the best accuracy, it is recommended to verify the calibration or repeat the calibration procedure if the device has been exposed to significant changes in ambient temperature or humidity.

A.1.4.2 *Measurement*

The user interface program can run a number of electrochemical techniques, which can be started from within the corresponding tab views. Figures A.8–A.12 illustrate these techniques using example measurements performed on a "dummy cell". The dummy cell consists of a series circuit of a 1.000 kΩ precision resistor and a 1000 µF (nominal) electrolytic capacitor, connected on one side to WE/SE and on the other side to RE/CE, and is drawn schematically in Figure A.7. The RC series circuit can be used to verify the correct operation of the potentiostat by comparing the measured potential and current to the expected behavior, which is governed by a first-order differential equation:

$$I = \frac{U_R}{R} = C\frac{dU_c}{dt} \tag{A.1}$$

$$U = U_R + U_C \tag{A.2}$$

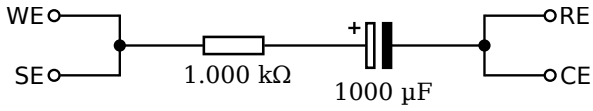

Figure A.7: Schematic diagram of the dummy cell.

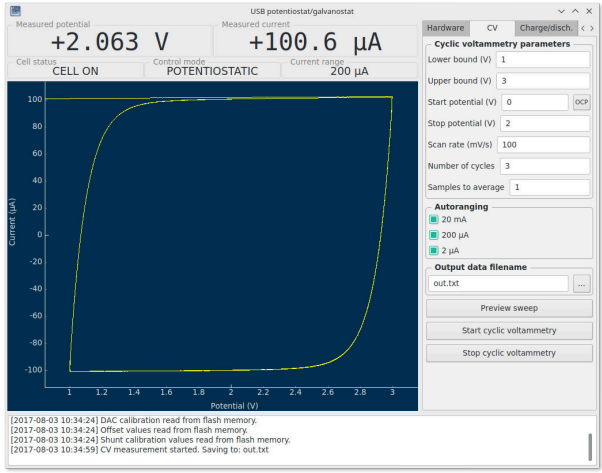

Figure A.8: Running a cyclic voltammetry measurement on the dummy cell using the "CV" tab.

CONSTANT POTENTIAL / CURRENT Using the manual controls in the "Hardware" tab, a fixed potential (in potentiostatic mode) or a fixed current (in galvanostatic mode) may be set. This makes it possible to use the device as a constant-voltage or constant-current source. Both the potential and current will be continuously measured and displayed. It is possible to log the data to a file by entering a filename and checking the "Log" checkbox. Figure A.6a shows the result of periodically changing the potential over the dummy cell between 0 V and +8 V (green curve), resulting in current spikes which decay exponentially as expected for an RC circuit (red curve). Figure A.6b shows the noise on the measured potential and current, using shorted leads (i.e. zero potential) and with the cell connection off (i.e. zero current). The RMS noise level on the potential is 28 µV, while the RMS noise levels on the current are respectively 88 nA, 1.1 nA, and 9.9 pA in the 20 mA, 200 µA, and 2 µA ranges.

CYCLIC VOLTAMMETRY Cyclic voltammetry (CV) is a versatile electrochemical measurement technique which finds application in many fields; the details can be found in literature,[35] but it is essentially based on the repeated application of a linear potential ramp, i.e. a "triangle waveform", while measuring the resulting current. In a typical CV plot, the current is then plotted as a function of the applied potential.

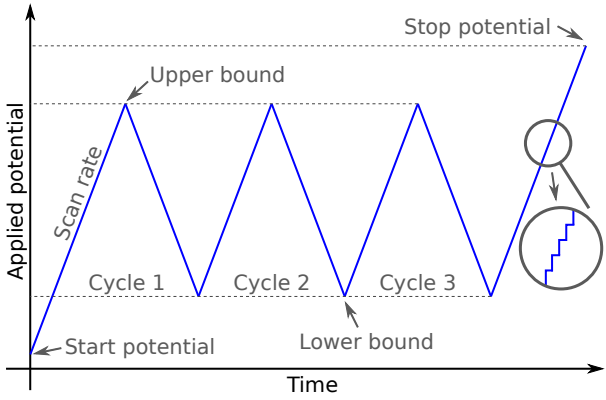

Figure A.9: Graphical illustration showing the applied potential waveform during a cyclic voltammetry measurement, and the parameters that determine its shape.

Before starting a CV measurement, a number of parameters must be set in the user interface program (Figure A.8). These parameters determine the nature of the applied triangular waveform and are graphically illustrated in Figure A.9. Because of the finite resolution (i.e. step size) in potential and time, the waveform is actually not truly linear but rather consists of a "staircase" shape; however, when the steps are sufficiently small, the results are equivalent to a truly linear ramp.

By clicking the "OCP" button next to the "Start potential" input field, the currently measured potential is copied into the input field; this is convenient when starting a CV measurement at the open-circuit potential (OCP) of the cell.

The "Samples to average" parameter is automatically calculated based on the scan rate, but can be overwritten. It determines how many samples are averaged for one measurement of potential and current. Samples are acquired every 90 ms; this means that a measurement containing n averaged samples will take $n \times 90$ ms. Averaging reduces noise, but also reduces the effective sampling rate; thus, $n > 1$ should only be used for sufficiently slow scan rates. Because the minimum sampling time is 90 ms, the maximum scan rate is limited to approx. 500 mV/s; at this scan rate, the height of the potential steps is 45 mV.

Because the resulting current is not known *a priori* and may span a large dynamic range, an autoranging feature is available: during the measurement, the device will automatically choose an appropriate current range

based on the actually measured current. This allows it to accurately measure currents ranging from nanoamps to max. 25 mA. If this is, for some reason, not desirable, a current range can be "disabled" (i.e. prevented from being selected by autoranging) by unticking its checkbox.

Before starting the measurement, the "Preview sweep" button may be used to make a potential vs. time plot based on the currently set CV parameters. This allows the experimenter to verify the CV settings. After setting an output filename, the measurement can be started by clicking "Start cyclic voltammetry". This will switch the device to potentiostatic mode and start applying the potential profile. During the measurement, the application shows a continuously updating CV plot and continuously writes the measurement data to the output file. The output file is formatted as ASCII text and contains three tab-separated columns representing resp. the elapsed time (in s), the measured potential (in V), and the measured current (in A). It may be imported in any plotting or data analysis tool.

The CV curve of the dummy cell (Figure A.8), acquired at a scan rate of 100 mV/s, reveals nearly horizontal plateaus at currents of $\pm 100.6\,\mu A$ (with the plus sign on the rising potential and the minus sign on the declining potential). This is expected; because the current through the capacitor is proportional to the rate of change of its voltage, and that (given a constant current) the voltage drop over the resistor is constant, the rate of change of the capacitor voltage is also equal to $\pm 100\,mV/s$. A straightforward calculation reveals that a $1006\,\mu F$ capacitance yields the measured constant current. This value is well within the tolerance of the (nominally) $1000\,\mu F$ capacitor in the dummy cell.

CONSTANT-CURRENT CHARGE/DISCHARGE Another commonly used electrochemical technique is to apply a constant current and to observe the evolution of the measured potential over time. In analytical redox chemistry, this method is known as coulometric titration. In the field of battery research, it can be used to determine the capacity of an electrode material. Using the galvanostatic mode of the potentiostat, such a measurement technique is easily implemented. Figure A.10 shows a charge/discharge measurement running on the dummy cell. Before starting a measurement, the following parameters need to be set in the "Charge/Disch." tab:

- Upper bound and lower bound: during the charging phase, the charge current is applied until the measured potential reaches the upper bound. This marks the end of the charging phase and the beginning of the discharging phase. During the discharging phase,

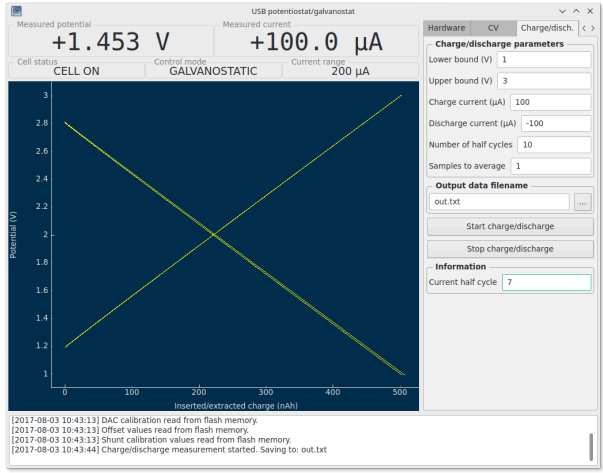

Figure A.10: Running a charge/discharge measurement on the dummy cell using the "Charge/Disch." tab.

the discharge current is applied until the measured potential reaches the lower bound. This marks the end of the discharging phase and the beginning of the next charging phase, thus repeating the cycle.

- Charge and discharge current: sets the applied currents (in µA) during the charge, resp. discharge phases.
- Number of half cycles: sets the total number of charge and discharge phases. As opposed to counting full cycles, this allows the experimenter to carry out e.g. a single charge measurement (one half cycle), or a charge/discharge/charge measurement (three half cycles).
- Samples to average: has the same function as explained earlier for cyclic voltammetry. Set it to the desired acquisition period, divided by 90 ms; higher values reduce noise, but result in slower data acquisition.

The meaning of these parameters in the context of a typical charge/discharge measurement is illustrated graphically in Figure A.11.

After setting the measurement parameters and choosing an output filename, clicking the "Start charge/discharge" button will start the charge/discharge process. During the measurement, the current half cycle is indicated in the "Information" box, and the plot window shows a continuously updating plot of the potential vs. the charge. The charge is calcu-

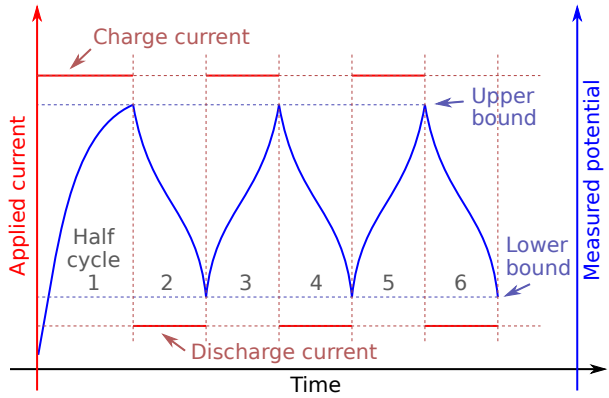

Figure A.11: Graphical illustration of the applied current (in red) during a charge/discharge measurement, assuming a fictive potential profile (in blue).

lated as the absolute value of the product of the (constant) current and the elapsed time.

For the dummy cell, the resulting measurement is shown in Figure A.10. In the charge phase, using a constant current I of +100 µA, the potential over the resistor U_R has a constant value of +100 mV, and the potential over the capacitor U_C increases linearly at a rate of $dU_C/dt = 100$ mV/s. This corresponds to the observed behavior. In the discharge phase, the same current is applied in the opposite direction. This causes the potential to decrease linearly at the same rate. The inserted/extracted charge over the 1.8 V potential window equals 100 µA × (1.8 V/0.1 V/s) = 1.8 mC = 500 nAh, which is in agreement with the value indicated on the horizontal axis.

RATE TESTING Specifically in battery research, the experimenter is often interested in the "rate behavior" of a test cell. This refers to the influence of the charge/discharge current on the measured cell capacity; typically, the capacity decreases with increasing current due to kinetic limitations. The current is expressed as a "C-rate", where 1C is defined as the current necessary to charge/discharge the cell to its theoretical capacity in exactly one hour.

Using the "Rate testing" feature which is accessible from the correspondingly named tab in the user interface program (see Figure A.12), the measurement of this rate behavior can be automated. For each C-rate (multiple

values may be separated by commas), a charge/discharge measurement is ran between the lower and upper potential bounds (as explained in the previous section) for a configurable number of cycles. The charge/discharge current is calculated as:

$$I\,[\mu\text{A}] = \pm C\,[\mu\text{Ah}] \times \text{C-rate} \tag{A.3}$$

with the positive sign for the charge current, and the negative sign for the discharge current.

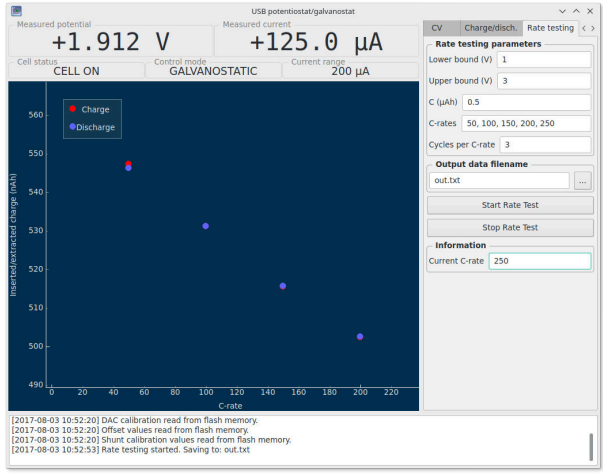

Figure A.12: Running a rate testing measurement on the dummy cell using the "Rate testing" tab.

During the measurement, the plot continuously updates itself to show the charge/discharge capacity measured in the final cycle as a function of the C-rate. The measurement on the dummy cell (Figure A.12) reveals a capacity which decreases linearly with the C-rate; indeed, the potential that is "lost" over the resistor is proportional to the applied current. The fact that the capacity decreases with the current, just like for a real battery, is no coincidence; in fact, the resistor in the dummy cell can be considered to represent the internal resistance encountered in real batteries.

A.1.5 *Use case: a thin-film lithium-ion battery electrode*

In the following section, the utility of this low-cost potentiostat will be demonstrated by an example use case in the context of thin-film lithium-ion batteries. A lithium-ion test cell was constructed using a PTFE body filled with electrolyte (1 M $LiClO_4$ in propylene carbonate) which was

clamped against a 40 nm anatase TiO_2 film on a TiN-coated silicon substrate, giving an active area of 0.95 cm^2. An electrical contact was made by applying conductive silver ink on the cleaved sides of the substrate in order to connect the TiN current collector layer to a piece of copper foil. This formed the working electrode. The counter electrode and reference electrode consisted of lithium metal strips dipped into the electrolyte.

As lithium-ion cells are incompatible with moisture and oxygen, the whole cell was constructed inside an argon glovebox. Thanks to its small size, the potentiostat could also be put inside the glovebox, needing only a USB cable feedthrough. Moving the potentiostat close to the test cell (inside the glovebox) greatly reduces noise and interference, compared to having it outside and extending the cell connection leads.

Cyclic voltammetry patterns were acquired at scan rates between 0.5 mV/s and 5 mV/s and are shown in Figure A.13. The cathodic and anodic peaks are clearly visible around resp. 1.7 V and 2.2 V, as is expected for anatase TiO_2.[183] As the scan rate increases, the available time for charge transfer decreases, causing the peak current to increase. The separation between the cathodic and anodic peak currents also increases; this is a kinetic effect, caused by the limited speed at which the lithium ions can diffuse through the TiO_2 film. This makes such a CV experiment useful to study the electrode kinetics. A thorough study can already be found in literature[183] and will not be repeated here.

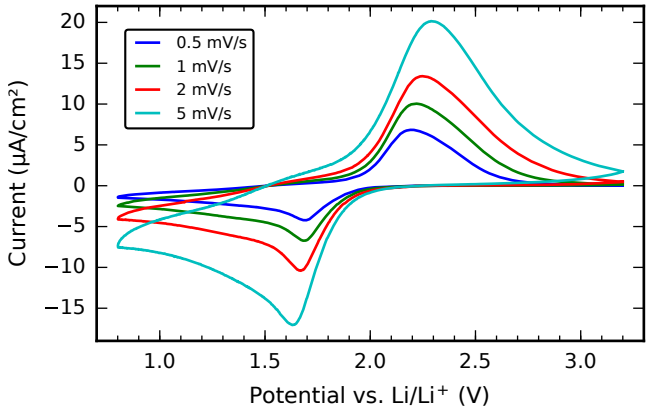

Figure A.13: Cyclic voltammogram of a 40 nm TiO_2 electrode acquired between 0.8 V and 3.2 V at scan rates between 0.5 mV/s and 5 mV/s.

The same electrode was subjected to charge/discharge cycling at a constant current of ± 0.18 $\mu A/cm^2$ (positive sign for charge, negative for dis-

charge) and between the same potential limits as in the CV experiment. The potential evolution, plotted as a function of the inserted/extracted charge, is shown in Figure A.14. It shows characteristic plateaus at 1.85 V (charge) and 1.75 V (discharge). The final capacities are 3.03 µAh/cm^2 (charge) and 3.09 µAh/cm^2 (discharge), yielding a coulombic efficiency (defined as the ratio between the delithiation and the lithiation capacities) of 98.1%. The measured capacity corresponds to the insertion/extraction of approx. 0.6 Li^+ per unit of TiO_2, according to the following calculation:

$$\#\mathrm{Li} = \frac{C_{\mathrm{measured}} \times M}{d\rho N_A q_e} \tag{A.4}$$

with $C_{\mathrm{measured}} \approx 0.011$ C/cm^2, $d = 40 \times 10^{-7}$ cm, $\rho = 3.8$ g/cm^3, $M = 79.9$ g/mol, N_A as Avogadro's constant, and q_e as the elementary electron charge.

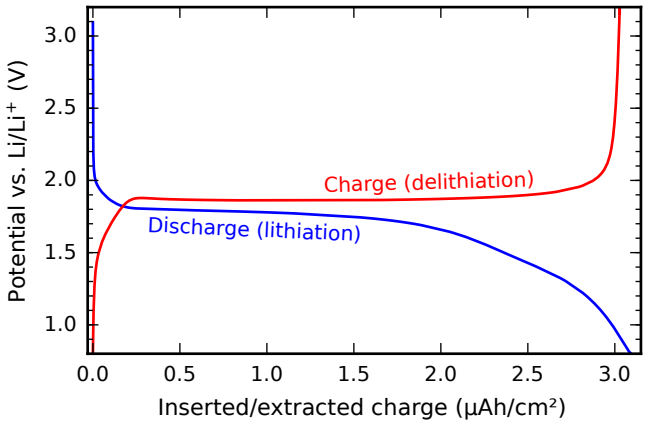

Figure A.14: Potential evolution during constant-current charging and discharging of a 40 nm TiO_2 electrode at a current density of ±0.18 µA/cm^2.

Taking the average of the measured charge and discharge capacity and defining 1C as 3.06 µAh/cm^2, the current density of ±0.18 µA/cm^2 can be equivalently expressed as a C-rate of approx. C/17, which is a rather slow rate. The charge/discharge measurements were repeated with increasingly higher currents using the rate testing mode of the potentiostat. The capacity was determined for each C-rate and the result is shown in Figure A.15. The results indicate that the capacity decreases quickly with an increasing C-rate, demonstrating the sluggish kinetics of the TiO_2 electrode. At a rate of C/2, only approx. 50% of the C/10 capacity remains. At very high C-rates (≥10C), the slope of the decline becomes flatter; in

this region, only a small pseudo-capacitive contribution to the capacity remains.

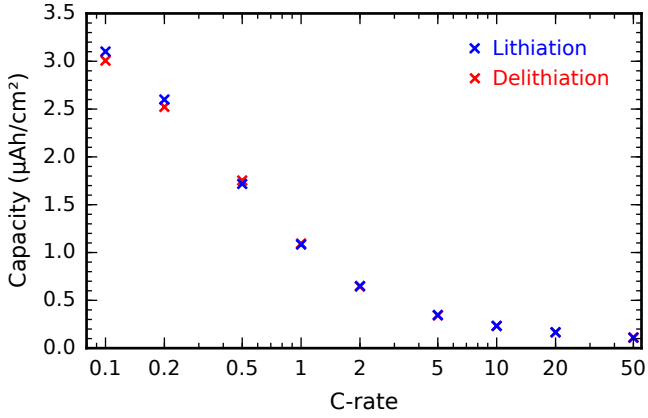

Figure A.15: Rate testing results on the 40 nm TiO_2 electrode, showing the measured capacity as a function of the C-rate.

A.1.6 *Limitations and possible modifications*

Although this potentiostat design may be used "as-is" for many applications, some may have requirements that exceed its capabilities in its current state. Because the design is fully open source, it is entirely possible to modify it in order to accommodate custom requirements. In particular:

- In the present design, the maximum current of 25 mA is limited by (1) the current that can be delivered by the charge pump, and (2) the maximum output current of the control amplifier U7A. A higher current could be achieved by (1) replacing the charge pump by an external $\pm 9\,V$ power supply (which must be able to supply the desired current), (2) including a high-current buffer stage (e.g. a pair of medium current transistors in a class AB amplifier configuration), and (3) adding a low-value current shunt resistor (e.g. 1Ω for a maximum current of 250 mA) and ranging relay.
- The sampling period of 90 ms may be too slow in case of fast electrochemical processes. It can be straighforwardly lowered to approx. 17 ms by replacing the MCP3550-type ADC's with the MCP3553 and adjusting the polling interval in the Python software. Even faster sampling would require more elaborate modifications.
- A new experimental technique may be required. As these are implemented in the software running on the host computer, it is relatively

straightforward to add a new technique by editing the Python source code.

BIBLIOGRAPHY

[1] R. L. Puurunen, "A Short History of Atomic Layer Deposition: Tuomo Suntola's Atomic Layer Epitaxy," Chem. Vap. Deposition **20**, 332–344 (2014).

[2] S. M. George, "Atomic Layer Deposition: An Overview," Chem. Rev. **110**, 111–131 (2010).

[3] R. W. Johnson, A. Hultqvist, and S. F. Bent, "A brief review of atomic layer deposition: from fundamentals to applications," Mater. Today **17**, 236–246 (2014).

[4] R. L. Puurunen, "Surface chemistry of atomic layer deposition: A case study for the trimethylaluminum/water process," J. Appl. Phys. **97**, 121301 (2005).

[5] R. L. Puurunen and W. Vandervorst, "Island growth as a growth mode in atomic layer deposition: A phenomenological model," J. Appl. Phys. **96**, 7686–7695 (2004).

[6] J. Dendooven, D. Deduytsche, J. Musschoot, R. L. Vanmeirhaeghe, and C. Detavernier, "Conformality of Al_2O_3 and AlN Deposited by Plasma-Enhanced Atomic Layer Deposition," J. Electrochem. Soc. **157**, G111–G116 (2010).

[7] H. B. Profijt, S. E. Potts, M. C. M. van de Sanden, and W. M. M. Kessels, "Plasma-Assisted Atomic Layer Deposition: Basics, Opportunities, and Challenges," J. Vac. Sci. Technol., A **29**, 050801 (2011).

[8] Plasma ALD guy, *Plasma enhanced atomic layer deposition publication database*, `http://www.plasma-ald.com`, [Online; accessed 08-March-2017].

[9] S. I. Kol'tsov, V. B. Aleskovskii, A. N Volkova, and V. Smirnov, "Change in the structure of silica gel in the process of the formation of a layer of phosphorus pentoxide on its surface," [In Russian], J. Appl. Chem. USSR **47**, 1292–1295 (1974).

[10] S. I. Kol'tsov, A. N Volkova, and V. B. Aleskovskii, "Preparation and investigation of the chemical composition of the products formed by successive chemisorption of titanium and phosphorus chlorides on the surface of silica gel," [In Russian], J. Appl. Chem. USSR **42**, 980–984 (1969).

[11] A. A. Malygin, S. I. Kol'tsov, and V. B. Aleskovskii, "Chemical composition of silica containing chromium and phosphorus synthesized by the molecular-stratification method," [In Russian], J. Gen. Chem. USSR **50**, 2121–2123 (1980).

[12] M. Nieminen, L. Niinistö, and R. Lappalainen, "Determination of P/Al ratio in phosphorus-doped aluminium oxide thin films by XRF, RBS and FTIR," Microchim. Acta **119**, 13–22 (1995).

[13] M. Tiitta, E. Nykänen, P. Soininen, L. Niinistö, M. Leskelä, and R. Lappalainen, "Preparation and characterization of phosphorus-doped aluminum oxide thin films," Mater. Res. Bull. **33**, 1315–1323 (1998).

[14] J. Hämäläinen, J. Holopainen, F. Munnik, M. Heikkilä, M. Ritala, and M. Leskelä, "Atomic layer deposition of aluminum and titanium phosphates," J. Phys. Chem. C **116**, 5920–5925 (2012).

[15] J. Liu, Y. Tang, B. Xiao, T.-K. Sham, R. Li, and X. Sun, "Atomic layer deposited aluminium phosphate thin films on N-doped CNTs," RSC Adv. **3**, 4492–4495 (2013).

[16] M. K. Wiedmann, D. H. K. Jackson, Y. J. Pagan-Torres, E. Cho, J. A. Dumesic, and T. F. Kuech, "Atomic layer deposition of titanium phosphate on silica nanoparticles," J. Vac. Sci. Technol., A **30**, 01A134 (2012).

[17] M. Putkonen, T. Sajavaara, P. Rahkila, L. Xu, S. Cheng, L. Niinistö, and H. J. Whitlow, "Atomic layer deposition and characterization of biocompatible hydroxyapatite thin films," Thin Solid Films **517**, 5819–5824 (2009).

[18] A. R. Ananda Sagari, J. Malm, M. Laitinen, P. Rahkila, M. Hongqiang, M. Putkonen, M. Karppinen, H. J. Whitlow, and T. Sajavaara, "Influence of titanium-substrate roughness on Ca–P–O thin films grown by atomic layer deposition," Thin Solid Films **531**, 26–31 (2013).

[19] J. Hämäläinen, J. Holopainen, F. Munnik, T. Hatanpää, M. Heikkilä, M. Ritala, and M. Leskelä, "Lithium phosphate thin films grown by atomic layer deposition," J. Electrochem. Soc. **159**, A259–A263 (2012).

[20] A. C. Kozen, A. J. Pearse, C.-F. Lin, M. Noked, and G. W. Rubloff, "Atomic Layer Deposition of the Solid Electrolyte LiPON," Chem. Mater. **27**, 5324–5331 (2015).

[21] H. H. Sønsteby, E. Østreng, H. Fjellvåg, and O. Nilsen, "Atomic layer deposition of $LaPO_4$ and Ca:$LaPO_4$**," Chem. Vap. Deposition **20**, 269–273 (2014).

[22] K. B. Gandrud, A. Pettersen, O. Nilsen, and H. Fjellvåg, "High-performing iron phosphate for enhanced lithium ion solid state batteries as grown by atomic layer deposition," J. Mater. Chem. A **1**, 9054–9059 (2013).

[23] J. Liu, B. Xiao, M. N. Banis, R. Li, T.-K. Sham, and X. Sun, "Atomic layer deposition of amorphous iron phosphates on carbon nanotubes as cathode materials for lithium-ion batteries," Electrochimica Acta **162**, 275–281 (2015).

[24] J. Liu, M. N. Banis, Q. Sun, A. Lushington, R. Li, T.-K. Sham, and X. Sun, "Rational Design of Atomic-Layer-Deposited $LiFePO_4$ as a High-Performance Cathode for Lithium-Ion Batteries," Adv. Mater. **26**, 6472–6477 (2014).

[25] M. N. Getz, P.-A. Hansen, H. Fjellvåg, and O. Nilsen, "Luminescent properties of europium titanium phosphate thin films deposited by atomic layer deposition," RSC Adv. **7**, 8051–8059 (2017).

[26] S. Knohl, A. K. Roy, R. Lungwitz, S. Spange, T. Mäder, D. J. Nestler, B. Wielage, S. Schulze, M. Hietschold, H. Wulff, C. A. Helm, F. Seidel, D. R. T. Zahn, and W. A. Goedel, "Nonaqueous atomic layer deposition of aluminum phosphate," ACS Appl. Mater. Interfaces **5**, 6161–6167 (2013).

[27] M. Nisula, Y. Shindo, H. Koga, and M. Karppinen, "Atomic Layer Deposition of Lithium Phosphorus Oxynitride," Chem. Mater. **27**, 6987–6993 (2015).

[28] A. J. Pearse, T. E. Schmitt, E. J. Fuller, F. El-Gabaly, C.-F. Lin, K. Gerasopoulos, A. C. Kozen, A. A. Talin, G. Rubloff, and K. E. Gregorczyk, "Nanoscale Solid State Batteries Enabled by Thermal Atomic Layer Deposition of a Lithium Polyphosphazene Solid State Electrolyte," Chem. Mater. **29**, 3740–3753 (2017).

[29] S. Shibata, "Thermal Atomic Layer Deposition of Lithium Phosphorus Oxynitride as a Thin-Film Solid Electrolyte," J. Electrochem. Soc. **163**, A2555–A2562 (2016).

[30] T. Dobbelaere, A. K. Roy, P. M. Vereecken, and C. Detavernier, "Atomic layer deposition of aluminum phosphate based on the plasma polymerization of trimethyl phosphate," Chem. Mater. **26**, 6863–6871 (2014).

[31] T. Dobbelaere, M. Minjauw, T. Ahmad, P. M. Vereecken, and C. Detavernier, "Plasma-enhanced atomic layer deposition of zinc phosphate," J. Non-Cryst. Solids **444**, 43–48 (2016).

[32] T. Dobbelaere, F. Mattelaer, J. Dendooven, P. M. Vereecken, and C. Detavernier, "Plasma-Enhanced Atomic Layer Deposition of Iron Phosphate as a Positive Electrode for 3D Lithium-Ion Microbatteries," Chem. Mater. **28**, 3435–3445 (2016).

[33] T. Dobbelaere, F. Mattelaer, A. K. Roy, P. M. Vereecken, and C. Detavernier, "Plasma-enhanced atomic layer deposition of titanium phosphate as an electrode for lithium-ion batteries," J. Mater. Chem. A **5**, 330–338 (2017).

[34] T. Dobbelaere, F. Mattelaer, P. M. Vereecken, and C. Detavernier, "Plasma-enhanced atomic layer deposition of vanadium phosphate as a lithium-ion battery electrode material," J. Vac. Sci. Technol., A **35**, 041513 (2017).

[35] A. J. Bard and L. R. Faulkner, *Electrochemical Methods: Fundamentals and Applications*, 2nd Edition (John Wiley & Sons, Inc., New York, Dec. 2000).

[36] G. G. Amatucci, J. M. Tarascon, and L. C. Klein, "CoO_2, The End Member of the Li_xCoO_2 Solid Solution," J. Electrochem. Soc. **143**, 1114–1123 (1996).

[37] K. Mizushima, P. C. Jones, P. J. Wiseman, and J. B. Goodenough, "Li_xCoO_2 ($0<x\leq1$): A new cathode material for batteries of high energy density," Mater. Res. Bull. **15**, 783–789 (1980).

[38] N. Nitta, F. Wu, J. T. Lee, and G. Yushin, "Li-ion battery materials: present and future," Mater. Today **18**, 252–264 (2015).

[39] A. K. Padhi, K. S. Nanjundaswamy, and J. B. Goodenough, "Phospho-olivines as positive-electrode materials for rechargeable lithium batteries," J. Electrochem. Soc. **144**, 1188–1194 (1997).

[40] A. K. Padhi, K. S. Nanjundaswamy, C. Masquelier, S. Okada, and J. B. Goodenough, "Effect of Structure on the Fe^{3+}/Fe^{2+} Redox Couple in Iron Phosphates," J. Electrochem. Soc. **144**, 1609–1613 (1997).

[41] Z. Zhang and S. S. Zhang, *Rechargeable Batteries: Materials, Technologies and New Trends* (Springer International Publishing, Switzerland, 2015).

[42] J. B Bates, N. J Dudney, B Neudecker, A Ueda, and C. D Evans, "Thin-film lithium and lithium-ion batteries," Solid State Ionics **135**, 33–45 (2000).

[43] P. H. L. Notten, F. Roozeboom, R. a. H. Niessen, and L. Baggetto, "3-D Integrated All-Solid-State Rechargeable Batteries," Adv. Mater. **19**, 4564–4567 (2007).

[44] P. M. Vereecken and C. Huyghebaert, "(Invited) Conformal Deposition for 3D Thin-Film Batteries," ECS Trans. **58**, 111–118 (2013).

[45] G. W. Rubloff and S. B. Lee, "New science at the meso frontier: Dense nanostructure architectures for electrical energy storage," Curr. Opin. Solid State Mater. Sci. **19**, 227–234 (2015).

[46] M. Roberts, P. Johns, J. Owen, D. Brandell, K. Edstrom, G. E. Enany, C. Guery, D. Golodnitsky, M. Lacey, C. Lecoeur, H. Mazor, E. Peled, E. Perre, M. M. Shaijumon, P. Simon, and P.-L. Taberna, "3D lithium ion batteries – from fundamentals to fabrication," J. Mater. Chem. **21**, 9876–9890 (2011).

[47] S. Ferrari, M. Loveridge, S. D. Beattie, M. Jahn, R. J. Dashwood, and R. Bhagat, "Latest advances in the manufacturing of 3D rechargeable lithium microbatteries," J. Power Sources **286**, 25–46 (2015).

[48] Y. Wang, B. Liu, Q. Li, S. Cartmell, S. Ferrara, Z. D. Deng, and J. Xiao, "Lithium and lithium ion batteries for applications in microelectronic devices: A review," J. Power Sources **286**, 330–345 (2015).

[49] L. Ma, R. B. Nuwayhid, T. Wu, Y. Lei, K. Amine, and J. Lu, "Atomic Layer Deposition for Lithium-Based Batteries," Adv. Mater. Interfaces **3**, 1600564 (2016).

[50] C. Liu, E. I. Gillette, X. Chen, A. J. Pearse, A. C. Kozen, M. A. Schroeder, K. E. Gregorczyk, S. B. Lee, and G. W. Rubloff, "An all-in-one nanopore battery array," Nat. Nanotechnol. **9**, 1031–1039 (2014).

[51] M. Létiche, E. Eustache, J. Freixas, A. Demortière, V. De Andrade, L. Morgenroth, P. Tilmant, F. Vaurette, D. Troadec, P. Roussel, T. Brousse, and C. Lethien, "Atomic Layer Deposition of Functional Layers for on Chip 3D Li-Ion All Solid State Microbattery," Adv. Energy Mater. **7**, 16011402 (2016).

[52] J.A. Woollam Co., Inc., *M-2000 brochure*, `http://www.jawoollam.com/download/pdfs/m-2000-brochure.pdf`, [Online; accessed 30-March-2017].

[53] R. E. March, "An introduction to quadrupole ion trap mass spectrometry," J. Mass Spectrom. **32**, 351–369 (1997).

[54] M. Juppo, A. Rahtu, M. Ritala, and M. Leskelä, "In Situ Mass Spectrometry Study on Surface Reactions in Atomic Layer Deposition of Al_2O_3 Thin Films from Trimethylaluminum and Water," Langmuir **16**, 4034–4039 (2000).

[55] A. J. M. Mackus, S. B. S. Heil, E. Langereis, H. C. M. Knoops, M. C. M. van de Sanden, and W. M. M. Kessels, "Optical emission spectroscopy as a tool for studying, optimizing, and monitoring plasma-assisted atomic layer deposition processes," J. Vac. Sci. Technol., A **28**, 77–87 (2010).

[56] G. Socrates, *Infrared and raman characteristic group frequencies: tables and charts*, 3rd ed. (John Wiley & Sons, Inc., Chichester, 2001).

[57] W. Knaepen, "Characterization of solid state reactions and crystallization in thin films using in-situ X-ray diffraction.," PhD thesis (Ghent University, 2010).

[58] M. Yasaka, "X-ray thin-film measurement techniques. V. X-ray reflectivity measurement," The Rigaku Journal **26** (2010).

[59] S. Hofmann, *Auger- and X-ray photoelectron spectroscopy in materials science: a user-oriented guide*, Springer Series in Surface Sciences (Springer, 2012).

[60] T. Alford, L. Feldman, and J. Mayer, *Fundamentals of nanoscale film analysis* (Springer, 2007).

[61] K. Mizohata, "Progress in elastic recoil detection analysis," PhD thesis (University of Helsinki, 2012).

[62] M. P. Seah and W. A. Dench, "Quantitative electron spectroscopy of surfaces: A standard data base for electron inelastic mean free paths in solids," Surf. Interface Anal. **1**, 2–11 (1979).

[63] P. Eaton and P. West, *Atomic force microscopy* (Oxford University Press, 2010).

[64] M. Yoshio, R. J. Brodd, and A. Kozawa, *Lithium-ion batteries: science and technologies* (Springer, New York, 2009).

[65] V. Miikkulainen, M. Leskelä, M. Ritala, and R. L. Puurunen, "Crystallinity of inorganic films grown by atomic layer deposition: overview and general trends," J. Appl. Phys. **113**, 021301 (2013).

[66] B. Kim, C. Kim, T.-G. Kim, D. Ahn, and B. Park, "The effect of AlPO4-coating layer on the electrochemical properties in LiCoO2 thin films," J. Electrochem. Soc. **153**, A1773–A1777 (2006).

[67] S. T. Meyers, J. T. Anderson, D. Hong, C. M. Hung, J. F. Wager, and D. A. Keszler, "Solution-processed aluminum oxide phosphate thin-film dielectrics," Chem. Mater. **19**, 4023–4029 (2007).

[68] G. Alberti, P. Cardini-Galli, U. Costantino, and E. Torracca, "Crystalline insoluble salts of polybasic metals–I Ion-exchange properties of crystalline titanium phosphate," J. Inorg. Nucl. Chem. **29**, 571–578 (1967).

[69] A. Clearfield and D. S. Thakur, "Zirconium and titanium phosphates as catalysts: a review," Appl. Catal. **26**, 1–26 (1986).

[70] N. Kuwata, N. Iwagami, Y. Tanji, Y. Matsuda, and J. Kawamura, "Characterization of thin-film lithium batteries with stable thin-film Li_3PO_4 solid electrolytes fabricated by ArF excimer laser deposition," J. Electrochem. Soc. **157**, A521–A527 (2010).

[71] D. R. Stull, "Vapor pressure of pure substances. Organic and inorganic compounds," Ind. Eng. Chem. **39**, 517–540 (1947).

[72] F. Hilt, D. Duday, N. Gherardi, G. Frache, J. Bardon, and P. Choquet, "Plasma deposition of an organophosphorus coating at atmospheric pressure," Plasma Processes Polym. **10**, 556–563 (2013).

[73] J.-G. Zhang, L. Meda, and E. Maxie, "System and method of producing thin-film electrolyte," pat. US6852139 B2 (Feb. 2005).

[74] H. K. Yasuda, *Plasma polymerization* (Academic Press, London, June 1985).

[75] I. Reva, A. SimÃčo, and R. Fausto, "Conformational properties of trimethyl phosphate monomer," Chem. Phys. Lett. **406**, 126–136 (2005).

[76] L. George, K. Sankaran, K. S. Viswanathan, and C. K. Mathews, "Matrix-isolation infrared spectroscopy of organic phosphates," Appl. Spectrosc. **48**, 7–12 (1994).

[77] K. G. Tokhadze, G. S. Denisov, M. Wierzejewska, and M. Drozd, "First example of the ABC îį(OH) absorption structure for both gaseous and crystalline phase: infrared studies of dimethylphosphinic acid," J. Mol. Struct. **404**, 55–62 (1997).

[78] K. Nakamoto, in *Infrared and raman spectra of inorganic and coordination compounds, 3rd ed.* (Wiley, New York, 1978), pp. 172–173.

[79] J. M. Campelo, J. M. Marinas, S. Mendioroz, and J. A. Pajares, "Texture and surface chemistry of aluminum phosphates," J. Catal. **101**, 484–495 (1986).

[80] Z. Katz-Tsameret and A. Raveh, "Characterization of aluminum based oxide layers formed by microwave plasma," J. Vac. Sci. Technol., A **13**, 1121–1127 (1995).

[81] M. H. Zahedi-Niaki, P. N. Joshi, and S. Kaliaguine, "Synthesis and characterization of AlPO-36, the missing end-member of ATS structure," Chem. Commun., 1373–1374 (1996).

[82] H. Graetsch, "Two forms of aluminium phosphate tridymite from X-ray powder data," Acta Crystallogr., Sect. C: Cryst. Struct. Commun. **56**, 401–403 (2000).

[83] A. Yamada, B. Sang, and M. Konagai, "Atomic layer deposition of ZnO transparent conducting oxides," Applied Surface Science **112**, 216–222 (1997).

[84] E. B. Yousfi, J. Fouache, and D. Lincot, "Study of atomic layer epitaxy of zinc oxide by in-situ quartz crystal microgravimetry," Applied Surface Science **153**, 223–234 (2000).

[85] S. Keun Kim, C. Seong Hwang, S.-H. Ko Park, and S. Jin Yun, "Comparison between ZnO films grown by atomic layer deposition using H2O or O3 as oxidant," Thin Solid Films **478**, 103–108 (2005).

[86] H. C. Knoops, J. W. Elam, J. A. Libera, and W. M. Kessels, "Surface Loss in Ozone-Based Atomic Layer Deposition Processes," Chem. Mater. **23**, 2381–2387 (2011).

[87] S.-H. K. Park, C.-S. Hwang, H.-S. Kwack, J.-H. Lee, and H. Y. Chu, "Characteristics of ZnO Thin Films by Means of Plasma-Enhanced Atomic Layer Deposition," Electrochem. Solid-State Lett. **9**, G299–G301 (2006).

[88] D. Kim, H. Kang, J.-M. Kim, and H. Kim, "The properties of plasma-enhanced atomic layer deposition (ALD) ZnO thin films and comparison with thermal ALD," Applied Surface Science **257**, 3776–3779 (2011).

[89] H. Yuan, B. Luo, S. A. Campbell, and W. L. Gladfelter, "Atomic Layer Deposition of p-Type Phosphorus-Doped Zinc Oxide Films Using Diethylzinc, Ozone and Trimethylphosphite," Electrochem. Solid-State Lett. **14**, H181–H183 (2011).

[90] T. Tynell, R. Okazaki, I. Terasaki, H. Yamauchi, and M. Karppinen, "Electron doping of ALD-grown ZnO thin films through Al and P substitutions," J. Mater. Sci. **48**, 2806–2811 (2012).

[91] L. B. Fletcher, J. J. Witcher, N. Troy, S. T. Reis, R. K. Brow, and D. M. Krol, "Direct femtosecond laser waveguide writing inside zinc phosphate glass," Opt. Express **19**, 7929 (2011).

[92] U. Caldiño, E. Álvarez, A. Speghini, and M. Bettinelli, "New greenish-yellow and yellowish-green emitting glass phosphors: Tb^{3+}/Eu^{3+} and $Ce^{3+}/Tb^{3+}/Eu^{3+}$ in zinc phosphate glasses," J. Lumin. **135**, 216–220 (2013).

[93] B. Tischendorf, J. U. Otaigbe, J. W. Wiench, M. Pruski, and B. C. Sales, "A study of short and intermediate range order in zinc phosphate glasses," J. Non-Cryst. Solids **282**, 147–158 (2001).

[94] C. Smith, "The structure and properties of ternary zinc phosphate glasses for optical applications," PhD thesis (Missouri University of Science and Technology, Jan. 2014).

[95] W. Knaepen, C. Detavernier, R. L. Van Meirhaeghe, J. Jordan Sweet, and C. Lavoie, "In-situ X-ray Diffraction study of Metal Induced Crystallization of amorphous silicon," Thin Solid Films **516**, 4946–4952 (2008).

[96] W. Knaepen, S. Gaudet, C. Detavernier, R. L. V. Meirhaeghe, J. J. Sweet, and C. Lavoie, "In situ X-ray diffraction study of metal induced crystallization of amorphous germanium," J. Appl. Phys. **105**, 083532 (2009).

[97] G. Rampelberg, M. Schaekers, K. Martens, Q. Xie, D. Deduytsche, B. De Schutter, N. Blasco, J. Kittl, and C. Detavernier, "Semiconductor-metal transition in thin VO_2 films grown by ozone based atomic layer deposition," Appl. Phys. Lett. **98**, 162902 (2011).

[98] Richard J. Lewis Sr., *Hawley's Condensed Chemical Dictionary*, 15th ed. (John Wiley & Sons, Inc., New York, 2007).

[99] G. Palavit, C. Mercier, L. Montagne, M. Drache, and Y. Abe, "Chemical Reactions of Ultraphosphate Glasses with Water at Various Temperatures," J. Am. Ceram. Soc. **81**, 1521–1524 (1998).

[100] I. Fanderlick, *Optical properties of glass* (Elsevier, New York, 1983).

[101] E. C. Onyiriuka, "Zinc phosphate glass surfaces studied by XPS," J. Non-Cryst. Solids **163**, 268–273 (1993).

[102] B. L. Ellis, K. T. Lee, and L. F. Nazar, "Positive electrode materials for Li-Ion and Li-batteries," Chem. Mater. **22**, 691–714 (2010).

[103] Y. Song, S. Yang, P. Y. Zavalij, and M. S. Whittingham, "Temperature-dependent properties of FePO4 cathode materials," Materials Research Bulletin **37**, 1249–1257 (2002).

[104] S. Okada, T. Yamamoto, Y. Okazaki, J.-i. Yamaki, M. Tokunaga, and T. Nishida, "Cathode properties of amorphous and crystalline FePO4," J. Power Sources **146**, 570–574 (2005).

[105] Y. J. Lee and A. M. Belcher, "Nanostructure design of amorphous $FePO_4$ facilitated by a virus for 3 V lithium ion battery cathodes," J. Mater. Chem. **21**, 1033–1039 (2011).

[106] J. Zhao, Z. Jian, J. Ma, F. Wang, Y.-S. Hu, W. Chen, L. Chen, H. Liu, and S. Dai, "Monodisperse Iron Phosphate Nanospheres: Preparation and Application in Energy Storage," ChemSusChem **5**, 1495–1500 (2012).

[107] V. Mathew, S. Kim, J. Kang, J. Gim, J. Song, J. P. Baboo, W. Park, D. Ahn, J. Han, L. Gu, Y. Wang, Y.-S. Hu, Y.-K. Sun, and J. Kim, "Amorphous iron phosphate: potential host for various charge carrier ions," NPG Asia Mater **6**, e138 (2014).

[108] X. Meng, X.-Q. Yang, and X. Sun, "Emerging Applications of Atomic Layer Deposition for Lithium-Ion Battery Studies," Adv. Mater. **24**, 3589–3615 (2012).

[109] R. K. Ramachandran, J. Dendooven, and C. Detavernier, "Plasma enhanced atomic layer deposition of Fe_2O_3 thin films," J. Mater. Chem. A **2**, 10662–10667 (2014).

[110] A. Guinier, *X-ray Diffraction in Crystals, Imperfect Crystals, and Amorphous Bodies* (W. H. Freeman and Company, 1963).

[111] P. M. A. Sherwood, "Introduction to Studies of Phosphorus-Oxygen Compounds by XPS," Surface Science Spectra **9**, 62–66 (2002).

[112] M. Descostes, F. Mercier, N. Thromat, C. Beaucaire, and M. Gautier-Soyer, "Use of XPS in the determination of chemical environment and oxidation state of iron and sulfur samples: constitution of a data basis in binding energies for Fe and S reference compounds and applications to the evidence of surface species of an oxidized pyrite in a carbonate medium," Appl. Surf. Sci. **165**, 288–302 (2000).

[113] C. Wagner, W. Riggs, L. Davis, J. Moulder, and G. Muilenberg, *Handbook of X-ray photoelectron spectroscopy: a reference book of standard data for use in x-ray photoelectron spectroscopy* (Perkin-Elmer Corporation, 1979).

[114] P. P. Prosini, M. Lisi, S. Scaccia, M. Carewska, F. Cardellini, and M. Pasquali, "Synthesis and Characterization of Amorphous Hydrated $FePO_4$ and Its Electrode Performance in Lithium Batteries," J. Electrochem. Soc. **149**, A297–A301 (2002).

[115] C. T. Cherian, J. Sundaramurthy, M. Kalaivani, P. Ragupathy, P. S. Kumar, V. Thavasi, M. V. Reddy, C. H. Sow, S. G. Mhaisalkar, S. Ramakrishna, and B. V. R. Chowdari, "Electrospun α-Fe_2O_3 nanorods as a stable, high capacity anode material for Li-ion batteries," J. Mater. Chem. **22**, 12198–12204 (2012).

[116] P. Verma, P. Maire, and P. Novák, "A review of the features and analyses of the solid electrolyte interphase in Li-ion batteries," Electrochim. Acta **55**, 6332–6341 (2010).

[117] K. B. Gandrud, O. Nilsen, and H. Fjellvåg, "Ultra-high power capabilities in amorphous $FePO_4$ thin films," J. Power Sources **306**, 454–458 (2016).

[118] G. Freiman, P. Barboux, J. Perrière, and K. Giannakopoulos, "Sequential Grafting of Dielectric Phosphates onto Silicon Oxide," Chem. Mater. **19**, 5862–5867 (2007).

[119] H. Wang, K. Huang, Y. Zeng, S. Yang, and L. Chen, "Electrochemical properties of TiP_2O_7 and $LiTi_2(PO_4)_3$ as anode material for lithium ion battery with aqueous solution electrolyte," Electrochim. Acta **52**, 3280–3285 (2007).

[120] Y. Uebou, S. Okada, M. Egashira, and J.-I. Yamaki, "Cathode properties of pyrophosphates for rechargeable lithium batteries," Solid State Ionics **148**, 323–328 (2002).

[121] W. Wu, S. Shanbhag, A. Wise, J. Chang, A. Rutt, and J. F. Whitacre, "High Performance TiP_2O_7 Based Intercalation Negative Electrode for Aqueous Lithium-Ion Batteries via a Facile Synthetic Route," J. Electrochem. Soc. **162**, A1921–A1926 (2015).

[122] M. Ritala, M. Leskelä, L. Niinistö, and P. Haussalo, "Titanium isopropoxide as a precursor in atomic layer epitaxy of titanium dioxide thin films," Chem. Mater. **5**, 1174–1181 (1993).

[123] Q. Xie, J. Musschoot, D. Deduytsche, R. L. V. Meirhaeghe, C. Detavernier, S. Van Den Berghe, Y.-L. Jiang, G.-P. Ru, B.-Z. Li, and X.-P. Qu, "Growth Kinetics and Crystallization Behavior of TiO_2 Films Prepared by Plasma Enhanced Atomic Layer Deposition," J. Electrochem. Soc. **155**, H688–H692 (2008).

[124] J. Lee, S. J. Lee, W. B. Han, H. Jeon, J. Park, W. Jang, C. S. Yoon, and H. Jeon, "Deposition temperature dependence of titanium oxide thin films grown by remote-plasma atomic layer deposition," Phys. Status Solidi A **210**, 276–284 (2013).

[125] K. L. Siefering and G. L. Griffin, "Kinetics of Low-Pressure Chemical Vapor Deposition of TiO2 from Titanium Tetraisopropoxide," J. Electrochem. Soc. **137**, 814–818 (1990).

[126] Y.-M. Wu, D. C. Bradley, and R. M. Nix, "Studies of titanium dioxide film growth from titanium tetraisopropoxide," Appl. Surf. Sci. **64**, 21–28 (1993).

[127] S. Tougaard, "Practical algorithm for background subtraction," Surf. Sci. **216**, 343–360 (1989).

[128] R. J. Ward and B. J. Wood, "A comparison of experimental and theoretically derived sensitivity factors for XPS," Surf. Interface Anal. **18**, 679–684 (1992).

[129] C. Detavernier, J. Dendooven, D. Deduytsche, and J. Musschoot, "Thermal Versus Plasma-Enhanced ALD: Growth Kinetics and Conformality," ECS Trans. **16**, 239–246 (2008).

[130] H. F. McMurdie, M. C. Morris, E. H. Evans, B. Paretzkin, W. Wong-Ng, Y. Zhang, and C. R. Hubbard, "Standard X-Ray Diffraction Powder Patterns from The JCPDS Research Associateship," Powder Diffr. **2**, 52 (1987).

[131] N. Aristov and A. Habekost, "Cyclic voltammetry – a versatile electrochemical method investigating electron transfer processes," World J. Chem. Educ. **3**, 115–119 (2015).

[132] J. Musschoot, D. Deduytsche, H. Poelman, J. Haemers, R. L. V. Meirhaeghe, S. V. d. Berghe, and C. Detavernier, "Comparison of Thermal and Plasma-Enhanced ALD/CVD of Vanadium Pentoxide," J. Electrochem. Soc. **156**, P122–P126 (2009).

[133] T. Blanquart, J. Niinistö, M. Gavagnin, V. Longo, M. Heikkilä, E. Puukilainen, V. R. Pallem, C. Dussarrat, M. Ritala, and M. Leskelä, "Atomic layer deposition and characterization of vanadium oxide thin films," RSC Adv. **3**, 1179–1185 (2012).

[134] V. E. Strempel, D. Löffler, J. Kröhnert, K. Skorupska, B. Johnson, R. N. d'Alnoncourt, M. Driess, and F. Rosowski, "Enhancing of catalytic properties of vanadia via surface doping with phosphorus using atomic layer deposition," J. Vac. Sci. Technol., A **34**, 01A135 (2015).

[135] N. Böckenfeld and A. Balducci, "On the use of lithium vanadium phosphate in high power devices," J. Power Sources **235**, 265–273 (2013).

[136] M. Y Saïdi, J Barker, H Huang, J. L Swoyer, and G Adamson, "Performance characteristics of lithium vanadium phosphate as a cathode material for lithium-ion batteries," J. Power Sources **119–121**, 266–272 (2003).

[137] T. Pagnier, M. Fouletier, and J. L. Souquet, "Electrochemical properties of phosphate based semi-conductive glasses," Solid State Ionics **9–10**, 649–653 (1983).

[138] Y. Sakurai, S. Okada, J. Yamaki, and T. Okada, "Electrochemical behaviour of amorphous V_2O_5(-P_2O_5) cathodes for lithium secondary batteries," J. Power Sources **20**, 173–177 (1987).

[139] Y. Sakurai and J.-i. Yamaki, "Correlation Between Microstructure and Electrochemical Behavior of Amorphous V_2O_5-P_2O_5 in Lithium Cells," J. Electrochem. Soc. **135**, 791–796 (1988).

[140] M. M. Ren, Z. Zhou, and X. P. Gao, "$LiVOPO_4$ as an anode material for lithium ion batteries," J. Appl. Electrochem. **40**, 209 (2010).

[141] B. Zhang, Y.-d. Han, J.-c. Zheng, J.-f. Zhang, C. Shen, L. Ming, X.-b. Yuan, and H. Li, "$VOPO_4$ nanosheets as anode materials for lithium-ion batteries," Chem. Commun. **50**, 11132–11134 (2014).

[142] Y. Zhang, X. J. Zhang, Q. Tang, D. H. Wu, and Z. Zhou, "Core-shell VPO_4/C anode materials for Li ion batteries: Computational investigation and sol-gel synthesis," J. Alloys Compd. **522**, 167–171 (2012).

[143] K. J. Gaskell, M. M. Smith, and P. M. A. Sherwood, "Valence band X-ray photoelectron spectroscopic studies of phosphorus oxides and phosphates," J. Vac. Sci. Technol., A **22**, 1331–1336 (2004).

[144] G. Silversmit, D. Depla, H. Poelman, G. B. Marin, and R. De Gryse, "Determination of the V2p XPS binding energies for different vanadium oxidation states (V^{5+} to V^{0+})," J. Electron Spectrosc. Relat. Phenom. **135**, 167–175 (2004).

[145] M. E. Donders, H. C. M. Knoops, M. C. M. van de Sanden, W. M. M. Kessels, and P. H. L. Notten, "Remote Plasma Atomic Layer Deposition of Co_3O_4 Thin Films," J. Electrochem. Soc. **158**, G92–G96 (2011).

[146] N. Barradas, C. Jeynes, and R. Webb, "Simulated annealing analysis of Rutherford backscattering data," Appl. Phys. Lett. **71**, 291–293 (1997).

[147] J. C Dupin, D Gonbeau, H Benqlilou-Moudden, P. Vinatier, and A Levasseur, "XPS analysis of new lithium cobalt oxide thin-films before and after lithium deintercalation," Thin Solid Films **384**, 23–32 (2001).

[148] G. X. Wang, Y. Chen, K. Konstantinov, J. Yao, J.-h. Ahn, H. K. Liu, and S. X. Dou, "Nanosize cobalt oxides as anode materials for lithium-ion batteries," J. Alloys Compd. **340**, L5–L10 (2002).

[149] J. Chae, H.-S. Park, and S.-w. Kang, "Atomic Layer Deposition of Nickel by the Reduction of Preformed Nickel Oxide," Electrochem. Solid-State Lett. **5**, C64–C66 (2002).

[150] H. L. Lu, G. Scarel, C. Wiemer, M. Perego, S. Spiga, M. Fanciulli, and G. Pavia, "Atomic Layer Deposition of NiO Films on Si(100) Using Cyclopentadienyl-Type Compounds and Ozone as Precursors," J. Electrochem. Soc. **155**, H807–H811 (2008).

[151] Strem Chemicals Product Blog, *The use of Cp2Ni as a precursor in ALD/CVD processes*, `https://www.strem.com/catalog/product_blog/61/1/the_use_of_cp2ni_as_a_precursor_in_ald_cvd_processes`, [Online; accessed 04-May-2017].

[152] H. Kumagai, M. Matsumoto, K. Toyoda, and M. Obara, "Preparation and characteristics of nickel oxide thin film by controlled growth with sequential surface chemical reactions," J. Mater. Sci. Lett. **15**, 1081–1083 (1996).

[153] H. L. Lu, G. Scarel, X. L. Li, and M. Fanciulli, "Thin MnO and NiO films grown using atomic layer deposition from ethylcyclopentadienyl type of precursors," J. Cryst. Growth **310**, 5464–5468 (2008).

[154] J. F. Callejas, C. G. Read, C. W. Roske, N. S. Lewis, and R. E. Schaak, "Synthesis, Characterization, and Properties of Metal Phosphide Catalysts for the Hydrogen-Evolution Reaction," Chem. Mater. **28**, 6017–6044 (2016).

[155] S. T. Oyama, "Novel catalysts for advanced hydroprocessing: transition metal phosphides," J. Catal. **216**, 343–352 (2003).

[156] M. D. Groner, F. H. Fabreguette, J. W. Elam, and S. M. George, "Low-Temperature Al_2O_3 Atomic Layer Deposition," Chem. Mater. **16**, 639–645 (2004).

[157] A. B. F. Martinson, M. J. DeVries, J. A. Libera, S. T. Christensen, J. T. Hupp, M. J. Pellin, and J. W. Elam, "Atomic Layer Deposition of Fe_2O_3 Using Ferrocene and Ozone," J. Phys. Chem. C **115**, 4333–4339 (2011).

[158] R. Puurunen, "Growth Per Cycle in Atomic Layer Deposition: A Theoretical Model," Chem. Vap. Deposition **9**, 249–257 (2003).

[159] R. Puurunen, "Growth Per Cycle in Atomic Layer Deposition: Real Application Examplesof a Theoretical Model," Chem. Vap. Deposition **9**, 327–332 (2003).

[160] S. Jakschik, U. Schroeder, T. Hecht, M. Gutsche, H. Seidl, and J. W. Bartha, "Crystallization behavior of thin ald–Al_2O_3 films," Thin Solid Films **425**, 216–220 (2003).

[161] B. B. Burton, F. H. Fabreguette, and S. M. George, "Atomic layer deposition of MnO using Bis(ethylcyclopentadienyl)manganese and H_2O," Thin Solid Films **517**, 5658–5665 (2009).

[162] O. Nilsen, H. Fjellvåg, and A. Kjekshus, "Growth of manganese oxide thin films by atomic layer deposition," Thin Solid Films **444**, 44–51 (2003).

[163] W. F. Howard and R. M. Spotnitz, "Theoretical evaluation of high-energy lithium metal phosphate cathode materials in Li-ion batteries," J. Power Sources **165**, 887–891 (2007).

[164] E. S. Friedman, M. A. Rosenbaum, A. W. Lee, D. A. Lipson, B. R. Land, and L. T. Angenent, "A cost-effective and field-ready potentiostat that poises subsurface electrodes to monitor bacterial respiration," Biosens. Bioelectron. **32**, 309–313 (2012).

[165] A. A. Rowe, A. J. Bonham, R. J. White, M. P. Zimmer, R. J. Yadgar, T. M. Hobza, J. W. Honea, I. Ben-Yaacov, and K. W. Plaxco, "CheapStat: An Open-Source, "Do-It-Yourself" Potentiostat for Analytical and Educational Applications," PLoS One **6**, e23783 (2011).

[166] M. D. M. Dryden and A. R. Wheeler, "DStat: A Versatile, Open-Source Potentiostat for Electroanalysis and Integration," PLoS One **10**, e0140349 (2015).

[167] Admiral Instruments, *Squidstat Solo*, `https://www.admiralinstruments.com/product-page/squidstat-solo`, [Online; accessed 23-August-2017].

[168] T. Dobbelaere, *Github repository*, `https://github.com/thomasdob/tdstatv3`, [Online; accessed 24-February-2017].

[169] Texas Instruments, *OPAx192 datasheet*, `http://www.ti.com/lit/gpn/opa192`, [Online; accessed 24-February-2017].

[170] Microchip Technology Inc., *Mcp3550/1/3 datasheet*, `http://ww1.microchip.com/downloads/en/DeviceDoc/20001950F.pdf`, [Online; accessed 24-February-2017].

[171] Texas Instruments, *DAC1220 datasheet*, http://www.ti.com/lit/gpn/dac1220, [Online; accessed 24-February-2017].

[172] Analog Devices, *ADR421 datasheet*, http://www.analog.com/media/en/technical-documentation/data-sheets/ADR420_421_423_425.pdf, [Online; accessed 24-February-2017].

[173] Microchip Technology Inc., *PIC16F1454/5/9 datasheet*, http://ww1.microchip.com/downloads/en/DeviceDoc/40001639B.pdf, [Online; accessed 24-February-2017].

[174] *KiCad EDA*, http://kicad-pcb.org/, [Online; accessed 24-February-2017].

[175] A. Ott, Signal 11 Software, *M-stack*, http://www.signal11.us/oss/m-stack/, [Online; accessed 24-February-2017].

[176] *Libusb*, http://libusb.info/, [Online; accessed 24-February-2017].

[177] *NumPy*, http://www.numpy.org/, [Online; accessed 23-August-2017].

[178] *SciPy*, https://www.scipy.org/, [Online; accessed 23-August-2017].

[179] *PyUSB*, https://github.com/walac/pyusb, [Online; accessed 24-February-2017].

[180] Riverbank Computing, *PyQt*, https://www.riverbankcomputing.com/software/pyqt/, [Online; accessed 24-February-2017].

[181] *PyQtGraph*, http://pyqtgraph.org/, [Online; accessed 24-February-2017].

[182] Continuum Analytics, *Anaconda*, https://www.continuum.io/downloads, [Online; accessed 23-August-2017].

[183] J. Wang, J. Polleux, J. Lim, and B. Dunn, "Pseudocapacitive Contributions to Electrochemical Energy Storage in TiO_2 (Anatase) Nanoparticles," J. Phys. Chem. C **111**, 14925–14931 (2007).

LIST OF PUBLICATIONS

- T. Dobbelaere, P. M. Vereecken, and C. Detavernier, "A USB-controlled potentiostat/galvanostat for thin-film battery characterization," HardwareX **2**, 34–49 (2017).
- J. Dendooven, R. K. Ramachandran, E. Solano, M. Kurttepeli, L. Geerts, G. Heremans, M. Minjauw, T. Dobbelaere, K. Devloo-Casier, J. A. Martens, A. Vantomme, S. Bals, G. Portale, A. Coati, and C. Detavernier, "Independent tuning of size and coverage of supported Pt nanoparticles using atomic layer deposition," Nature Communications, accepted.
- E. Solano, J. Dendooven, M. Minjauw, R. K. Ramachandran, K. Van De Kerckhove, T. Dobbelaere, D. Hermida-Merino, and C. Detavernier, "Key role of surface oxidation and reduction processes in the coarsening of Pt nanoparticles," Nanoscale **9**, 13159–13170 (2017).
- T. Dobbelaere, F. Mattelaer, P. M. Vereecken, and C. Detavernier, "Plasma-enhanced atomic layer deposition of vanadium phosphate as a lithium-ion battery electrode material," J. Vac. Sci. Technol., A **35**, 041513 (2017).
- T. Dobbelaere, F. Mattelaer, A. K. Roy, P. M. Vereecken, and C. Detavernier, "Plasma-enhanced atomic layer deposition of titanium phosphate as an electrode for lithium-ion batteries," J. Mater. Chem. A **5**, 330–338 (2017).
- J. Kuhs, T. Dobbelaere, Z. Hens, and C. Detavernier, "Plasma enhanced atomic layer deposition of zinc sulfide thin films," J. Vac. Sci. Technol., A **35**, 01B111 (2017)
- F. Mattelaer, K. Geryl, G. Rampelberg, T. Dobbelaere, J. Dendooven, and C. Detavernier, "Atomic layer deposition of vanadium oxides for thin-film lithium-ion battery applications," RSC Adv. **6**, 114658–114665 (2016)
- T. Dobbelaere, F. Mattelaer, J. Dendooven, P. M. Vereecken, and C. Detavernier, "Plasma-enhanced atomic layer deposition of iron and titanium phosphates as electrode materials for 3D-structured lithium-ion microbatteries," ECS Trans. **75**, 35–44 (2016)

- T. Dobbelaere, F. Mattelaer, J. Dendooven, P. M. Vereecken, and C. Detavernier, "Plasma-Enhanced Atomic Layer Deposition of Iron Phosphate as a Positive Electrode for 3D Lithium-Ion Microbatteries," Chem. Mater. **28**, 3435–3445 (2016)
- T. Dobbelaere, M. Minjauw, T. Ahmad, P. M. Vereecken, and C. Detavernier, "Plasma-enhanced atomic layer deposition of zinc phosphate," J. Non-Cryst. Solids **444**, 43–48 (2016)
- T. Dobbelaere, A. K. Roy, P. M. Vereecken, and C. Detavernier, "Atomic layer deposition of aluminum phosphate based on the plasma polymerization of trimethyl phosphate," Chem. Mater. **26**, 6863–6871 (2014)

DANKWOORD / ACKNOWLEDGEMENT

Dit doctoraatsproefschrift is het resultaat van vier jaar werk. Hoewel een doctoraat in de eerste plaats een persoonlijk traject inhoudt, zijn er gedurende die vier jaar talloze mensen in mijn leven geweest die dit voor mij op een positieve manier beïnvloed hebben. Via deze weg wil ik die mensen graag nog eens in het bijzonder bedanken, beginnende bij mijn promotor. Christophe, bedankt om mij de kans te geven om mijn masterthesis en doctoraat onder jouw begeleiding te maken, en voor de moeite die je gedaan hebt om steeds beschikbaar te zijn met raad en advies. Ik apprecieer de zorgvuldige manier waarop je mij enerzijds veel vrijheid gegeven hebt en anderzijds getracht hebt om het beste uit mij te halen. Ook mijn copromotor, Philippe, wil ik graag bedanken om mij te introduceren in de wondere wereld van batterijen en elektrochemie.

Davy, bedankt voor je geduld en voor je eeuwige behulpzaamheid met praktische zaken in het labo. Olivier, bedankt voor je hulp met de SEM. *Amit, thank you for coming up with the idea to do plasma-enhanced ALD of phosphates, which ended up as the foundation of my whole PhD!*

Dankzij de toffe collega's in S1 was het niet alleen een productieve, maar ook een leuke tijd. Ik denk hierbij aan Kilian, Shaoren, en Jakob voor de goede sfeer op ons bureau op de tweede verdieping. Maar ook aan Kilian, Christophe, Bob, Boris, Bartel, Arne, Mathias, Matthias, en Jonathan voor de aangename – en soms lange – lunchpauzes in het UZ, en aan Liesje, Felix, Jan, en Jevgenij voor de vele filmavonden in de vergaderzaal.

Af en toe was het ook nodig om eens even helemaal uit mijn onderzoek weg te zijn. Sander, An, Klaas, Isabelle, Hendrik, en Suzanne: bedankt voor jullie goede vriendschap en voor alle leuke feestjes, weekendjes en reizen die we samen gedaan hebben. Ik wil ook graag iedereen in Kojoko en Coro Maín bedanken voor al het muzikale plezier dat we samen beleefd hebben.

Bedankt aan de Vlaamse belastingbetaler; zonder uw trouwe bijdragen, maandelijks naar mij doorgesluisd via het FWO, had ik nooit vier jaar lang voltijds aan een dergelijk project kunnen werken.

Tenslotte: mama, papa, bedankt voor alles!

Thomas